

# **Applied Mathematics in Biomedical Sciences and Engineering**

Guest Editors: Chang-Hwan Im, Kiwoon Kwon, Venky Krishnan,  
and Pedro Serranho





---

# **Applied Mathematics in Biomedical Sciences and Engineering**

Journal of Applied Mathematics

---

# **Applied Mathematics in Biomedical Sciences and Engineering**

Guest Editors: Chang-Hwan Im, Kiwoon Kwon,  
Venky Krishnan, and Pedro Serranho



---

Copyright © 2012 Hindawi Publishing Corporation. All rights reserved.

This is a special issue published in "Journal of Applied Mathematics." All articles are open access articles distributed under the Creative Commons Attribution License, which permits unrestricted use, distribution, and reproduction in any medium, provided the original work is properly cited.

## Editorial Board

Said Abbasbandy, Iran  
Mina B. Abd-El-Malek, Egypt  
Mohamed A. Abdou, Egypt  
Subhas Abel, India  
Mostafa Adimy, France  
Pankaj Agarwal, India  
Carlos J. S. Alves, Portugal  
Mohamad Alwash, USA  
Igor Andrianov, Germany  
Francis T.K. Au, Hong Kong  
Olivier Bahn, Canada  
Roberto Barrio, Spain  
Alfredo Bellen, Italy  
J. Biazar, Iran  
Hester Bijl, The Netherlands  
Joke G. Blom, The Netherlands  
James Robert Buchanan, USA  
J. C. Butcher, New Zealand  
Xiao Chuan Cai, USA  
Weiming Cao, USA  
Alexandre Carvalho, Brazil  
Song Cen, China  
Qianshun Chang, China  
Tai-Ping Chang, Taiwan  
Ke Chen, UK  
Xinfu Chen, USA  
Jeng-Tzong Chen, Taiwan  
Jen-Tzung Chien, Taiwan  
Cheng-Sheng Chien, Taiwan  
M. S. H. Chowdhury, Malaysia  
C. Conca, Chile  
Vitor Costa, Portugal  
Livija Cveticanin, Serbia  
Mohamed Darouach, France  
Patrick De Leenheer, USA  
Eric de Sturler, USA  
Orazio Descalzi, Chile  
Kai Diethelm, Germany  
Vit Dolejsi, Czech Republic  
Salah M. El-Sayed, Egypt  
Meng Fan, China  
Ya Ping Fang, China

A. J. M. Ferreira, Portugal  
Michel Fliess, France  
M. A. Fontelos, Spain  
Luca Formaggia, Italy  
Victor A. Galaktionov, Russia  
Huijun Gao, China  
B. Geurts, The Netherlands  
Pablo González-Vera, Spain  
Laurent Gosse, Italy  
K. S. Govinder, South Africa  
Jose Luis Gracia, Spain  
Yuantong Gu, Australia  
Zhihong Guan, China  
Nicola Guglielmi, Italy  
F. G. Guimarães, Brazil  
Maoan Han, China  
Ferenc Hartung, Hungary  
Luis Javier Herrera, Spain  
Ying U. Hu, France  
Zhilong L. Huang, China  
Kazufumi Ito, USA  
Takeshi Iwamoto, Japan  
George Jaiani, Georgia  
Zhongxiao Jia, China  
Yehia Khulief, Saudi Arabia  
J. H. Kim, Republic of Korea  
Kazutake Komori, Japan  
Vadim A. Krysko, Russia  
Jin L. Kuang, Singapore  
Mirosław Lachowicz, Poland  
Hak-Keung Lam, UK  
Tak-Wah Lam, Hong Kong  
PGL Leach, Greece  
Yongkun Li, China  
Wan-Tong Li, China  
Jibin Li, China  
Chong Lin, China  
Leevan Ling, Hong Kong  
Fawang Liu, Australia  
Yansheng Liu, China  
Kang Liu, USA  
Chein-Shan Liu, Taiwan

Mingzhu Liu, China  
Jose Luis Lopez, Spain  
Julián López-Gómez, Spain  
Shiping Lu, China  
Gert Lube, Germany  
Nazim I. Mahmudov, Turkey  
F. M. Mahomed, South Africa  
O. D. Makinde, South Africa  
F. Marcellán, Spain  
Guiomar Martín-Herrán, Spain  
Nicola Mastronardi, Italy  
Michael Meylan, Australia  
Alain Miranville, France  
Jaime E. Munoz Rivera, Brazil  
Javier Murillo, Spain  
Roberto Natalini, Italy  
Srinivasan Natesan, India  
Khalida Inayat Noor, Pakistan  
D. O'Regan, Ireland  
Martin Ostoj-Starzewski, USA  
Turgut Öziş, Turkey  
Claudio Padra, Argentina  
R. Martinez Palhares, Brazil  
Bozenna Pasik-Duncan, USA  
Juan Manuel Peña, Spain  
Ricardo Perera, Spain  
Malgorzata Peszynska, USA  
James F. Peters, Canada  
Mark A. Petersen, South Africa  
Miodrag Petković, Serbia  
Vu Ngoc Phat, Vietnam  
Andrew Pickering, Spain  
Hector Pomares, Spain  
Maurizio Porfiri, USA  
Mario Primicerio, Italy  
Morteza Rafei, The Netherlands  
B. V. Rathish Kumar, India  
Jacek Rokicki, Poland  
Carla Roque, Portugal  
Debasish Roy, India  
Marcelo A. Savi, Brazil  
Wolfgang Schmidt, Germany



---

Eckart Schnack, Germany  
Mehmet Sezer, Turkey  
Naseer Shahzad, Saudi Arabia  
Fatemeh Shakeri, Iran  
Jian Hua Shen, China  
Hui-Shen Shen, China  
Fernando Simões, Portugal  
A. A. Soliman, Egypt  
Yuri N. Sotskov, Belarus  
P. J. C. Spreij, The Netherlands  
Niclas Strömberg, Sweden  
Ray KL Su, Hong Kong  
Wenyu Sun, China  
Jitao Sun, China  
Xianhua Tang, China

Marco Henrique Terra, Brazil  
Alexander Timokha, Norway  
Ch Tsitouras, Greece  
Kuppalapalle Vajravelu, USA  
Alvaro Valencia, Chile  
Nguyen Van Minh, USA  
E. S. Van Vleck, USA  
Ezio Venturino, Italy  
Jesus Vigo-Aguiar, Spain  
Junjie Wei, China  
Yimin Wei, China  
Li Weili, China  
Martin Weiser, Germany  
Adam Wittek, Australia  
Dongmei Xiao, China

Yuesheng Xu, USA  
Suh-Yuh Yang, Taiwan  
Jianke Yang, USA  
Jinyun Yuan, Brazil  
Alejandro Zarzo, Spain  
Guisheng Zhai, Japan  
Zhihua Zhang, China  
Jingxin Zhang, Australia  
Hongyong Zhao, China  
Shan Zhao, USA  
XiaoQiang Zhao, Canada  
Renat Zhdanov, USA  
J. Hoenderkamp, The Netherlands

# Contents

**Applied Mathematics in Biomedical Sciences and Engineering**, Chang-Hwan Im,  
Kiwoon Kwon, Venky Krishnan, and Pedro Serranho  
Volume 2012, Article ID 187252, 3 pages

**A Linear Transformation Approach for Estimating Pulse Arrival Time**, Dohyun Kim,  
Jong-Hoon Ahn, Jongshill Lee, Hoon Ki Park, and In Young Kim  
Volume 2012, Article ID 643653, 12 pages

**A New Weighted Correlation Coefficient Method to Evaluate Reconstructed Brain Electrical Sources**, Jong-Ho Choi, Min-Hyuk Kim, Luan Feng, Chany Lee, and Hyun-Kyo Jung  
Volume 2012, Article ID 251295, 11 pages

**Coupling of Point Collocation Meshfree Method and FEM for EEG Forward Solver**, Chany Lee,  
Jong-Ho Choi, Ki-Young Jung, and Hyun-Kyo Jung  
Volume 2012, Article ID 840593, 9 pages

**Phase- and GVF-Based Level Set Segmentation of Ultrasonic Breast Tumors**, Liang Gao,  
Xiaoyun Liu, and Wufan Chen  
Volume 2012, Article ID 810805, 22 pages

**The Second-Order Born Approximation in Diffuse Optical Tomography**, Kiwoon Kwon  
Volume 2012, Article ID 637209, 15 pages

**Selecting Negative Samples for PPI Prediction Using Hierarchical Clustering Methodology**,  
J. M. Urquiza, I. Rojas, H. Pomares, J. Herrera, J. P. Florido, and O. Valenzuela  
Volume 2012, Article ID 897289, 23 pages


**General Computational Model for Human Musculoskeletal System of Spine**, Kyungsoo Kim,  
Yoon Hyuk Kim, and SuKyoung Lee  
Volume 2012, Article ID 484759, 8 pages

**Personal Identification Based on Vectorcardiogram Derived from Limb Leads Electrocardiogram**, Jongshill Lee, Youngjoon Chee, and Inyoung Kim  
Volume 2012, Article ID 904905, 12 pages

**Monitoring Personalized Trait Using Oscillometric Arterial Blood Pressure Measurements**,  
Young-Suk Shin  
Volume 2012, Article ID 591252, 12 pages

**Qualitative and Computational Analysis of a Mathematical Model for Tumor-Immune Interactions**, F. A. Rihan, M. Safan, M. A. Abdeen, and D. Abdel Rahman  
Volume 2012, Article ID 475720, 19 pages

**Modeling of Brain Shift Phenomenon for Different Craniotomies and Solid Models**,  
Alvaro Valencia, Benjamin Blas, and Jaime H. Ortega  
Volume 2012, Article ID 409127, 20 pages



---

**Dynamical Models for Infectious Diseases with Varying Population Size and Vaccinations,**  
Peilin Shi and Lingzhen Dong  
Volume 2012, Article ID 824192, 20 pages

**Mathematical Issues in the Inference of Causal Interactions among Multichannel Neural Signals,** Young-Jin Jung, Kyung Hwan Kim, and Chang-Hwan Im  
Volume 2012, Article ID 472036, 14 pages

**Scanning Reduction Strategy in MEG/EEG Beamformer Source Imaging,** Jun Hee Hong and Sung Chan Jun  
Volume 2012, Article ID 528469, 19 pages



## *Editorial*

# **Applied Mathematics in Biomedical Sciences and Engineering**

**Chang-Hwan Im,<sup>1</sup> Kiwoon Kwon,<sup>2</sup>  
Venky Krishnan,<sup>3</sup> and Pedro Serranho<sup>4</sup>**

<sup>1</sup> Department of Biomedical Engineering, Hanyang University, 222 Wangsimni-ro, Seongdong-gu, Seoul 133-791, Republic of Korea

<sup>2</sup> Department of Mathematics, Dongguk University, Seoul 100-715, Republic of Korea

<sup>3</sup> Tata Institute of Fundamental Research, Centre for Applicable Mathematics, Bangalore 560065, India

<sup>4</sup> Department of Science and Technology, Open University, Campus TagusPark, Oeiras, Portugal

Correspondence should be addressed to Chang-Hwan Im, ich@hanyang.ac.kr

Received 26 March 2012; Accepted 26 March 2012

Copyright © 2012 Chang-Hwan Im et al. This is an open access article distributed under the Creative Commons Attribution License, which permits unrestricted use, distribution, and reproduction in any medium, provided the original work is properly cited.

Biomedical sciences and engineering are representative multidisciplinary research areas that have fulfilled the critical needs of modern medicine and biology. There is no doubt that applied mathematics has played a key role in developing new technologies in these emerging disciplines. For example, modern medical imaging systems such as magnetic resonance imaging (MRI) and computed tomography (CT) could not be materialized without the aid of advanced optimization theories and reconstruction algorithms. Progresses in numerical analysis and biostatistics have also contributed to the rapid advancement of physiological signal processing and computer-aided diagnosis of intractable diseases. Indeed, biomedical sciences and engineering have already become one of the most promising application areas of applied mathematics.

Considering the above-mentioned trends, it seems natural that this journal selected biomedical sciences and engineering as the theme of its Special Issue. This special issue includes fourteen high-quality peer-reviewed articles that might provide researchers in the field of applied mathematics with the current state-of-the-art knowledge of this emerging interdisciplinary research field.

In the paper “*Qualitative and computational analysis of a mathematical model for tumor-immune interactions*” by F. Rihan et al., a model of differential equations is provided for elucidating the dynamics of tumor growth and immunotherapy interactions, which can predict tumor dormancy and estimate the critical tumor-growth rate.

The paper *"Monitoring personalized trait using oscillometric arterial blood pressure measurements"* by Y. Shin suggests a new approach for monitoring personalized trait in oscillometric arterial blood pressure measurements. The proposed approach could offer more reliable blood pressure patterns than the broadly used principal component analysis.

The paper *"A linear transformation approach to estimate pulse arrival time"* by D. Kim et al. addresses a new mathematical framework for pulse arrival time estimation, combining local characteristics point methods with global parametric methods. The proposed linear method proved to be robust to noise as compared with standard approaches.

In the paper *"Modeling of brain shift phenomenon for different craniotomies and solid models"* by A. Valencia et al., the authors investigate mathematical models to compute brain displacement caused by craniotomy. The authors predict the displacements and stress levels for three models—elastic model, hyperelastic Ogden model, and hyperelastic Mooney-Rivlin model.

In the paper, *"Dynamical models for infectious diseases with varying population size and vaccinations"*, the authors, P. Shi and L. Dong, propose models for the spread of infectious diseases and vaccinations. They establish results for the existence and global stability of disease-free and endemic equilibria for two cases: susceptible populations are (a) vaccinated continuously and (b) vaccinated once per time period.

In the paper, *"Scanning reduction strategy in MEG/EEG beamformer source imaging"* by J. Hong and S. Jun, an efficient source scanning strategy in magnetoencephalography (MEG) and electroencephalography (EEG) beamformer imaging is proposed, leading to reduction in the number of scanning points while maintaining good spatial resolution. The efficacy of the new method is demonstrated through numerical and empirical experiments.

In the paper, *"Selecting negative samples for PPI prediction using hierarchical clustering methodology"* by J. Urquiza et al., a new protein-protein interaction (PPI) support vector machine (SVM) predictor model is proposed. The model is based on using a clustering approach to select a suitable negative data set. The new model is able to classify PPIs under various cases containing positive and negative datasets.

In the paper, *"A new weighted correlation coefficient method to evaluate reconstructed brain electrical sources"* by J. Choi et al., a novel evaluation metric to evaluate the accuracy of reconstructed MEG and EEG cortical sources is proposed. The new metric reflects the geometry of the cortical surface more accurately.

The paper *"Phase- and GVF-based level set segmentation of ultrasonic breast tumors"* by L. Gao et al. deals with the segmentation of ultrasonic breast tumors by combining a phase asymmetry approach and a new edge stopping function. They developed a method that can robustly cope with noise and extract the low contrast and/or concave boundaries with high accuracy.

The paper *"Mathematical Issues in the Inference of Causal Interactions among Multichannel Neural Signals"* by Y. Jung et al. is a well-organized review paper in which the authors described the current state-of-the-art technologies used for the causality inference in the field of neuroscience. It is expected that readers of this journal would be interested in the review paper, since the paper introduces a new interdisciplinary research topic to which their mathematical theories can be applied.

The paper *"The second-order born approximation in diffuse optical tomography"* by K. Kwon proposes a new numerical method based on the second-order Born approximation for better finding the solutions of diffuse optical tomography (DOT) reconstruction problems. Numerical implementation of the suggested method verifies that the new method has better convergence order than the conventional linearized method.

In the paper "*General computational model for human musculoskeletal system of spine*" by K. Kim et al., a general computational model of the human lumbar spine and trunk muscles including optimization formulations is provided. It is expected that the presented computational model and optimization technology can be fundamental tools to understand the control principle of human trunk muscles.

The paper "*Personal identification based on vectorcardiogram derived from limb leads electrocardiogram*" by J. Lee et al. propose a new method for personal identification using the derived vectorcardiogram (dVCG) from the limb leads electrocardiogram (ECG). The presented experimental results show that it is possible to identify a person by features extracted from a dVCG derived from limb leads only.

In the paper "*Coupling of point collocation meshfree method and FEM for EEG forward solver*" by C. Lee et al., MEG and EEG forward problems are solved using a new coupling method combining finite element method (FEM) and a point collocation meshfree method. Simulation results show that the hybrid method can be used for efficient computation of EEG and MEG forward problems.

## Acknowledgments

In closing this editorial, we would like to express our deepest gratitude to many reviewers, whose professional comments guaranteed the high quality of the selected papers. In addition, we would also like to express our appreciation to editorial board members of this journal, for their help and support throughout the preparation of this special issue. We hope you will find this special issue helpful for your future study.

Chang-Hwan Im  
Kiwoon Kwon  
Venky Krishnan  
Pedro Serranho

## Research Article

# A Linear Transformation Approach for Estimating Pulse Arrival Time

**Dohyun Kim,<sup>1</sup> Jong-Hoon Ahn,<sup>1</sup> Jongshill Lee,<sup>1</sup>  
Hoon Ki Park,<sup>2</sup> and In Young Kim<sup>1</sup>**

<sup>1</sup> Department of Biomedical Engineering, Hanyang University, 222 Wangsimni-ro Seongdong-gu, Seoul 133-791, Republic of Korea

<sup>2</sup> Family Medicine, College of Medicine, Hanyang University, 222 Wangsimni-ro Seongdong-gu, Seoul 133-791, Republic of Korea

Correspondence should be addressed to In Young Kim, iykim@hanyang.ac.kr

Received 31 October 2011; Revised 10 January 2012; Accepted 20 January 2012

Academic Editor: Pedro Serranho

Copyright © 2012 Dohyun Kim et al. This is an open access article distributed under the Creative Commons Attribution License, which permits unrestricted use, distribution, and reproduction in any medium, provided the original work is properly cited.

We propose a new mathematical framework for estimating pulse arrival time (PAT). Existing methods of estimating PAT rely on local characteristic points or global parametric models: local characteristic point methods detect points such as foot points, max points, or max slope points, while global parametric methods fit a parametric form to the anacrotic phase of pulse signals. Each approach has its strengths and weaknesses; we take advantage of the favorable properties of both approaches in our method. To be more precise, we transform continuous pulse signals into scalar timing codes through three consecutive transformations, the last of which is a linear transformation. By training the linear transformation method on a subset of data, the proposed method yields results that are robust to noise. We apply this method to real photoplethysmography (PPG) signals and analyze the agreement between our results and those obtained using a conventional approach.

## 1. Introduction

The importance of arterial stiffness as a cardiovascular disease index has been emphasized in recent years [1–6], because arterial stiffness can be acquired using inexpensive and noninvasive methods such as pulse wave velocity (PWV) [7, 8]. PWV is considered to be a good indicator for assessing arterial stiffness because it shows a strong correlation with cardiovascular events and mortality [1, 9–15]. Furthermore, PWV can be used for the continuous assessment of cardiovascular homeostasis and regulation [16].

One approach to assess PWV *in vivo* relies on tracking pressure pulses that arise from the onset of left ventricular ejection. This is the common method for acquiring PWV in

the arterial trees which uses ECG and two pressure pulses that are measured simultaneously. In general, pressure pulses are measured at the carotid and femoral arteries, respectively, and PWV is calculated as the distance between the two sites divided by the time for the pulse wave to travel that distance. The time that it takes the pulse pressure to travel from the carotid artery to the femoral artery is called pulse arrival time (PAT) [17].

To measure pressure pulses at the carotid and femoral arteries, a catheter is generally used. However, it is difficult to measure pressure pulses without clinical assistance because this is an invasive method. For this reason, intensive efforts have been made to improve the performance of external skin transducers that can measure PWV in recent years. Several techniques have been developed to record pressure pulses. Among these, photoplethysmography (PPG) is particularly popular as a noninvasive, nonobstructive technique that is based on the temporal patterns of light absorption in living tissues because morphological characteristics of PPG are similar to pressure pulse, especially in the arteries [18].

Pulse arrival time of PPG pulse is typically measured by detecting local characteristic points: the foot determined by the start point of the anacrotic phase (FOOT), the maximum-slope of the anacrotic phase (MS), and the maximum amplitude of the pulse (MAX) [15, 19, 20]. Unfortunately, however, these characteristic points often yield unstable and unreliable results when used to analyze PPG pulses with morphological variation due to underlying conditions [15]. Thus, the design of robust extraction techniques that are capable of estimating PAT from PPG pulses remains an unsolved problem. Solà and colleagues suggested that PAT could be estimated by parametric modeling of the anacrotic phase of pressure pulses in PPG. However, although their method produces robust and reliable results under noisy conditions, it is relatively computationally complex because of the need to fit a parametric function to every single pulse [21].

Therefore, our aim was to develop a method to measure PAT with accuracy and reliability using simple operations. In the next section, we outline the mathematical framework that we developed to estimate PAT.

## 2. Methods

### 2.1. Representation of PPG Signals in Vector Space

Let  $\Omega$  be the set of all continuous PPG signals measured from human arteries. We can define a sampling process  $\xi_M$  as follows:

$$\xi_M : \Omega \longrightarrow \mathbb{R}^M, \quad (2.1)$$

where  $\mathbb{R}^M$  is an  $M$ -dimensional Euclidean space. The mapping  $\xi_M$  reduces a continuous signal to an  $M$ -dimensional vector point. The vector point forms a lower-dimensional cluster in an  $M$ -dimensional space. Let us consider the cluster as being embedded by the manifold  $Y$ . Our goal in this paper is to find a mapping  $\tau$  between this manifold and PAT:

$$\tau : Y \longrightarrow \mathbb{R}^1. \quad (2.2)$$

Then, the parametric estimation of PAT is given by the composition of two mappings:  $\text{PAT} = \tau \circ \xi_M$ .

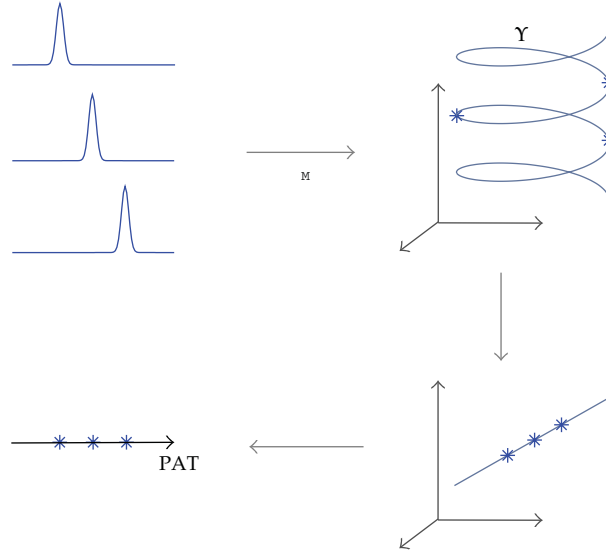


**Figure 1:** The estimation of PAT using a linear transformation approach.

However, manifolds constructed through normal sampling at a constant frequency are highly curved. Training this type of manifold and mapping PAT using this manifold are challenging [22]. Let us consider simple translations of Gaussian peaks, as shown in Figure 1. The manifold constructed using simple translations is spirally curved. If slight variation is added to Gaussian peaks, it is not feasible to parameterize the manifold with well-defined functions.

Now, suppose that we find the sampling process  $\xi_M$  such that the manifold  $Y$  can be flat and isometric along PAT. For instance, if three vectors  $f, g, h \in Y$  are collinear and have isometric timing codes  $t_f, t_g, t_h$ , that is,  $(t_h - t_g)f + (t_f - t_h)g + (t_g - t_f)h = 0$ , then we can always find the linear transformation  $\omega$  such that  $t_f = \omega^T f$ ,  $t_g = \omega^T g$ , and  $t_h = \omega^T h$ . This means that the special sampling process allows the mapping  $\tau$  to be the simplest form by  $\omega$ . However, we failed to find such a sampling process, regardless of the sampling frequencies applied to the continuous signals; convex combination of two different vectors  $f, g \in Y$  cannot be used to represent the human artery PPG signal.

In this context, we propose adding another transformation between  $\xi_M$  and  $\tau$ . By considering the new mapping, we intend to keep the mapping,  $\tau$ , the linear transformation. If we denote the novel mapping as  $\zeta$ , we can estimate the PAT of the PPG signals as

$$\text{PAT} = \tau \circ \zeta \circ \xi_M. \quad (2.3)$$

We refer to this as a linear transformation approach for estimating PAT. In following subsections, we describe the new transformation  $\zeta$  in more detail.

## 2.2. Conjugate Transformations

In the previous subsection, we framed a set of three transformations to change continuous pulse functions into scalar timing codes. The first transformation,  $\xi_M$ , is needed to reduce

continuous pulse functions into  $M$ -dimensional vector points, while the third transformation  $\tau$  is the linear transformation. The function of the second transformation,  $\zeta$ , will be fully discussed in this subsection, in which we consider a well-known transformation called the convex conjugate or Legendre transformation.

### 2.2.1. Convex Conjugate

The convex conjugate is a transformation that maps a convex function onto another convex function [23, 24]. A convex function always has its conjugate function: the conjugate function is also a convex function. First, we outline why we need convex functions. A Gaussian function, which was exemplified as a pulse in the previous subsection, is the starting point for developing our idea. Gaussian functions have a single peak and are nonnegative over the entire region. Such a Gaussian function can be derived from a convex function by differentiating the convex function twice. We can therefore consider convex functions instead of Gaussian functions. A general type of pulse function that has mixed-signed values, unlike Gaussian functions, will be discussed later.

Let us consider two arbitrary convex functions. When their first derivatives become inverses of each other, two functions are referred to as “convex conjugate”. If two functions  $f(t)$  and  $\tilde{f}(\tilde{t})$  have such a relation, then

$$\frac{df}{dt} \circ \frac{d\tilde{f}}{d\tilde{t}} = I = \frac{d\tilde{f}}{d\tilde{t}} \circ \frac{df}{dt}, \quad (2.4)$$

where  $I$  is an identity function, that is,  $I \circ t = t$  and  $I \circ \tilde{t} = \tilde{t}$ . To find an explicit expression for  $\tilde{f}$ , we assume

$$\tilde{t} = \frac{df}{dt} \circ t. \quad (2.5)$$

From (2.4) and (2.5), we obtain

$$I \circ t = \frac{d\tilde{f}}{d\tilde{t}} \circ \frac{df}{dt} \circ t \implies t = \frac{d\tilde{f}}{d\tilde{t}} \circ \tilde{t}. \quad (2.6)$$

Conversely, when we assume  $t = (d\tilde{f}/d\tilde{t}) \circ \tilde{t}$ , we also obtain  $\tilde{t} = (df/dt) \circ t$ . Thus, (2.4) gives the reciprocal expressions (2.5) and (2.6), which are referred to as variable change.

When we assume a finite domain  $\Omega$  on which a convex function is defined, the independent variable  $t$  on the domain can be changed into its conjugate variable  $\tilde{t}$  through convex conjugate. Then, the function form  $f$  can be changed into the form  $\tilde{f}$  by replacing  $t$  with  $\tilde{t}$ . To be precise, the explicit form of the convex conjugate from above relations is

$$\tilde{f}(\tilde{t}) = \sup \{ t\tilde{t} - f(t) \mid t \in \Omega \}, \quad (2.7)$$

where the conjugate variable  $\tilde{t}$  is expressed as the gradient of  $f$  at  $t$ . By differentiating  $t\tilde{t} - f(t)$  with regard to  $t$  and equating this result to zero, we can confirm that  $\tilde{t}$  is expressed as

the gradient of  $f$ . Conversely, the new convex function can be converted back to the original function in the same manner:

$$f(t) = \sup \{ \tilde{t} - f(t) \mid \tilde{t} \in \tilde{\Omega} \}. \quad (2.8)$$

In this case, the original variable  $t$  is expressed as the gradient of  $\tilde{f}$  at  $\tilde{t}$ . Variables  $t$  and  $\tilde{t}$  are basically conservative fields with regard to each other. Convex conjugation was originally derived from duality relationship between points and lines. The functional relationship specified by  $f(t)$  can be represented equally as well as a set of points  $t$ , or as a set of tangent lines specified by their gradients and intercept values.

### 2.2.2. Nonnegative Conjugate

Now, we introduce a new conjugate transformation termed *nonnegative conjugate*. This transformation is closely related to the former convex conjugate. If  $f$  is twice continuously differentiable and the domain is  $\Omega$ , then we can characterize a convex function as follows:

$$f \text{ is convex iff } f''(t) \geq 0 \text{ for } \Omega. \quad (2.9)$$

This is a link between convex conjugate and nonnegative conjugate based on the following definition.

*Definition 2.1.* Suppose that two convex functions  $f(t)$  and  $\tilde{f}(\tilde{t})$  are in convex conjugate for  $t \in \Omega$  and  $\tilde{t} \in \tilde{\Omega}$  and their second derivatives  $f''(t)$  and  $\tilde{f}''(\tilde{t})$  are denoted as  $I(t)$  and  $\tilde{I}(\tilde{t})$ , respectively. Then  $I(t)$  and  $\tilde{I}(\tilde{t})$  are said to be *nonnegative conjugate* of each other on domains  $\Omega$  and  $\tilde{\Omega}$ .

The two-dimensional conjugate transform that is analogous to this nonnegative conjugate has been applied to image morphing [25].

Let us calculate the second derivatives directly. As mentioned in (2.5) and (2.6), the first derivatives represent variable change between  $t$  and  $\tilde{t}$ . The second derivative of  $f(t)$  is given as

$$f''(t) = \frac{d^2 f(t)}{dt^2} = \frac{d\tilde{t}}{dt}. \quad (2.10)$$

Similarly, the second derivative of  $\tilde{f}''(\tilde{t})$  is given as

$$\tilde{f}''(\tilde{t}) = \frac{d^2 \tilde{f}(\tilde{t})}{d\tilde{t}^2} = \frac{dt}{d\tilde{t}}. \quad (2.11)$$

From (2.10) and (2.11), we obtain the following reciprocal relation between two second derivatives:

$$f''(t) \tilde{f}''(\tilde{t}) = 1. \quad (2.12)$$



If we denote  $f''(t)$  and  $\tilde{f}''(\tilde{t})$  as  $I(t)$  and  $\tilde{I}(\tilde{t})$ , the expression can be rewritten as  $I(t)\tilde{I}(\tilde{t}) = 1$ . Then, the nonnegative conjugate of  $I(t)$  can be expressed as

$$\begin{aligned}\tilde{I}(\tilde{t}) &= \frac{1}{I(t)} = \frac{1}{I(d\tilde{f}(\tilde{t})/d\tilde{t})} = \frac{1}{I\left(\left(d/d\tilde{t}\right) \sup\left\{\tilde{t}\tilde{t} - f(t) \mid t \in \Omega\right\}\right)} \\ &= \frac{1}{I\left(\left(d/d\tilde{t}\right) \sup\left\{\tilde{t}\tilde{t} - \int \int I(t)dt \mid t \in \Omega\right\}\right)}.\end{aligned}\quad (2.13)$$

Like variable change in the convex conjugate transformation, the variable  $t$  of the nonnegative function  $I(t)$  on the domain  $\Omega$  can be formally changed by using the nonnegative conjugate. This yields another nonnegative function  $\tilde{I}(\tilde{t})$  on the domain  $\tilde{\Omega}$  when the variable  $t$  is replaced with its conjugate variable  $\tilde{t}$ . Equation (2.13) has a very complex form, but the variable change between  $t$  and  $\tilde{t}$  has the following concise forms:

$$\tilde{t} = \int I(t)dt, \quad t = \int \tilde{I}(\tilde{t})d\tilde{t}. \quad (2.14)$$

Alternatively, the nonnegative conjugate can also be derived from the equidistribution principle. First, the conjugate variable  $\tilde{t}$  is introduced such that a nonnegative distribution  $I(t)$  becomes constant with 1 in the conjugate coordinate  $\tilde{t}$ :  $I(t)dt = d\tilde{t}$ . The conjugate function  $\tilde{I}(\tilde{t})$  also becomes constant with 1 in the original coordinate  $t$  by the same form:  $\tilde{I}(\tilde{t})d\tilde{t} = dt$ . As a result, we can obtain the reciprocal relation between  $I(t)$  and  $\tilde{I}(\tilde{t})$  and biconjugacy from the equidistribution principle, that is,  $I(t)\tilde{I}(\tilde{t}) = 1$  and  $\tilde{\tilde{I}} = I$ . This approach is equivalent to solving the Jacobian equation:

$$I(t) = \frac{d\tilde{t}}{dt}, \quad \tilde{I}(\tilde{t}) = \frac{dt}{d\tilde{t}}. \quad (2.15)$$

Note that equations in (2.15) are the same as (2.10) and (2.11), respectively.

### 2.2.3. Nonnegative Conjugate of a Nonnegative Vector

In the previous section, we described a method of transformation based on the convex conjugate. However, although the nonnegative conjugate transforms a continuous function into another continuous function, the transformation  $\zeta$  should map an  $M$ -dimensional vector onto another  $M$ -dimensional vector. Thus, we require a discrete version of the nonnegative conjugate.

Let us denote an  $M$ -dimensional column vector with nonnegative components as  $I$ , that is,  $I = (I_1 \cdots I_M)^T$  and  $I_i \geq 0$ . Then its nonnegative conjugate is denoted as  $\tilde{I}$ . To transform  $I$  into  $\tilde{I}$ , we have to link  $I$  with a continuous function  $I(t)$  by

$$I(t) \equiv I_{[t]}, \quad (2.16)$$

where the function  $[t]$  is a ceiling function that gives the smallest integer not less than  $t$ . Then  $I(t)$  is a continuous and nonnegative function defined from  $t = 0$  to  $t = M$ . If we denote a cumulative distribution  $\int_0^t I(t)dt$  as  $s(t)$ , we obtain  $\tilde{t} = s(t)$  from (2.14), and  $t$  is given by its inverse:

$$t = s^{-1}(\tilde{t}). \quad (2.17)$$

Then, from (2.13), we obtain

$$\tilde{I}(\tilde{t}) = \frac{1}{I(t)} = \frac{1}{I_{[t]}} = \frac{1}{I_{[s^{-1}(\tilde{t})]}}. \quad (2.18)$$

Finally, we can change it into the  $M$ -dimensional vector  $\tilde{I}$  by

$$\tilde{I}_i = \int_{i-1}^i \tilde{I}(\tilde{t}) d\tilde{t}. \quad (2.19)$$

Applying the same procedure to  $\tilde{I}$ , we can transform it back to the original vector  $I$ . However, this vector is not exactly same as the original vector. As the dimensionality of  $M$  increases, the error,  $I - \tilde{\tilde{I}}$ , converges to a zero vector.

### 2.3. Application to PPG Signals

All experiments and analyses were performed using ECG and PPG signals extracted from the publically available MIMIC database that contains data from intensive care unit patients admitted to Boston Beth Israel Hospital. ECG and PPG signals were measured to 500 and 125 samples per second, respectively. First,  $R$  peaks were detected from ECG based on the assumption that the  $R$  peak represents the onset time of left ventricular ejection. Therefore, the position of  $R$  peaks was used to segment single PPG pulses from the full PPG signals. Raw PPG signals were low-pass filtered at 15 Hz, then single PPG pulses were separated by synchronized  $R$  peaks. The extracted single PPG pulses were resampled to 500 Hz to improve accuracy, and then FOOT and MAX points of single PPG pulses were detected by the traditional method that detects characteristic points [26].

Each single PPG pulse was divided into two parts by the FOOT point: the front part from the  $R$  peak to the FOOT point, and the rear part from the FOOT point to the next  $R$  peak. The time difference at each part was calculated in different ways than that used to estimate PAT. The time difference  $t_a$  at the front part was derived by a simple translation to change the number of samples into time (seconds), and the time difference  $t_b$  at the rear part was calculated by the nonnegative conjugate transformation and linear projection, as shown in Figure 2.

Various single PPG pulses with different amplitudes, shapes, or pulse widths were represented as single points in an  $M$ -dimensional vector space after the nonnegative conjugate transformation. The points that corresponded to nonnegative conjugate vectors,  $\tilde{I}$ , were located on a same line in an  $M$ -dimensional vector space. This characteristic is referred to as collinearity.

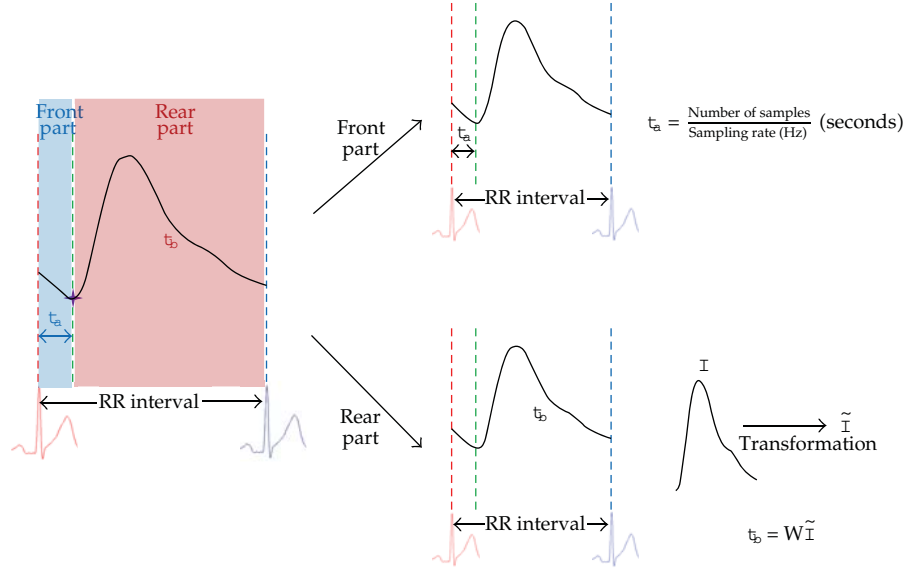


**Figure 2:** Single PPG pulse processing to estimate PAT.

### 2.3.1. Training a Projection Matrix $W$

To derive the matrix  $W$  that projects collinear points in an  $M$ -dimensional vector space into a one-dimensional time space, 10,000 different PPG pulses were extracted as the training set, and the linear projection matrix was trained according to the MAX point of the PPG pulse, because this is the most obvious characteristic point. Only rear parts of PPG pulses were used to train the linear projection matrix, which we derived by pseudoinverse operation between nonnegative conjugate transformed pulses and the known time information of MAX points as follows:

$$t_b = W\tilde{I}$$

$$\text{or } (t_b^1 \cdots t_b^N) = W(\tilde{I}^1 \cdots \tilde{I}^N). \quad (2.20)$$

The matrix  $W$  was calculated from the training samples by using the pseudo-inverse relationship

$$W = t_b \tilde{I}^T (\tilde{I} \tilde{I}^T)^{-1}, \quad (2.21)$$

where  $W = (w_1 \cdots w_M) \in \mathbb{R}^{1 \times M}$ ,  $t_b$  is the known time set from the R peaks to the MAX points,  $\tilde{I}$  is nonnegative conjugate transformed PPG pulse, and  $W$  is the derived linear projecting matrix.

### 2.3.2. PAT Estimation

Single PPG pulses extracted according to  $R$  peaks of ECG were divided into front and rear sections using the FOOT point, and time values were calculated for each section separately. First, the time of the front part,  $t_a$ , was calculated using the number of samples between the  $R$  peak and FOOT point divided by the sampling rate. Second, the time of the rear part,  $t_b$ , was acquired by linear operation between the linear projecting matrix ( $W$ ) and the nonnegative conjugate transformed pulse ( $\tilde{I}$ ). Finally, the PAT was obtained by simple summation of  $t_a$  and  $t_b$ :

$$\begin{aligned}
 t_a &= \frac{\text{Number of samples}}{\text{Sampling rate}} \text{ (seconds)}, \\
 t_b &= W\tilde{I}, \\
 t_b &= (w_1 \cdots w_M) \begin{pmatrix} \tilde{I}_1 \\ \vdots \\ \tilde{I}_M \end{pmatrix} \text{ (seconds)}, \\
 \text{PAT} &= t_a + t_b.
 \end{aligned} \tag{2.22}$$

## 3. Results and Discussion

To assess the agreement between the traditional method and our novel PAT estimation method, we evaluated a subset of data from the MIMIC database. This database is part of the Physionet platform and contains data from over 72 intensive care unit patients at the Boston Beth Israel Hospital, but we selected only those records for which nonsaturated and nonmissing ECG and PPG signals were simultaneously measured and available [27, 28].

We adopted the agreement analysis proposed by Bland and Altman: given two different estimating methods, their agreement can be assessed by computing the standard deviation of two sets of estimates. The proposed strategy computes the differences between measurements provided by two methods and then computes their dispersion. Two methods have good agreement if dispersion is minimal [29].

To acquire PAT estimates using our method, a linear projecting matrix was derived using a training process, and the derived linear projection matrix was applied to two test sets consisting of 2947 and 2890 PPG pulses, respectively. The mean difference and standard deviations of two sets of PAT estimates were calculated. Results of the agreement analysis are shown in Figure 3. The 95% limits of agreement were calculated as mean difference  $\pm 1.96 \times$  standard deviation at each set.

For the first test set, 98.9% of pulses were located between  $-34.3$  ms and  $28.3$  ms as the limits of agreement, while in the second test set, 96.2% of the pulses were located between  $-33.4$  ms and  $25.3$  ms.

The typical PAT estimation method, which detects characteristic points, is not accurate when applied to PPG pulse types with different morphologies. We therefore proposed a novel PAT estimation method that provides robust results by considering the morphological characteristics of PPG pulses according to the properties of blood vessels. We initially attempted to find a relation between a projecting factor and original PPG pulses,  $f$ , but were unsuccessful because of the broad dispersion of pulses in an  $M$ -dimensional vector space. We therefore decided to transform original PPG pulses into another form. We used

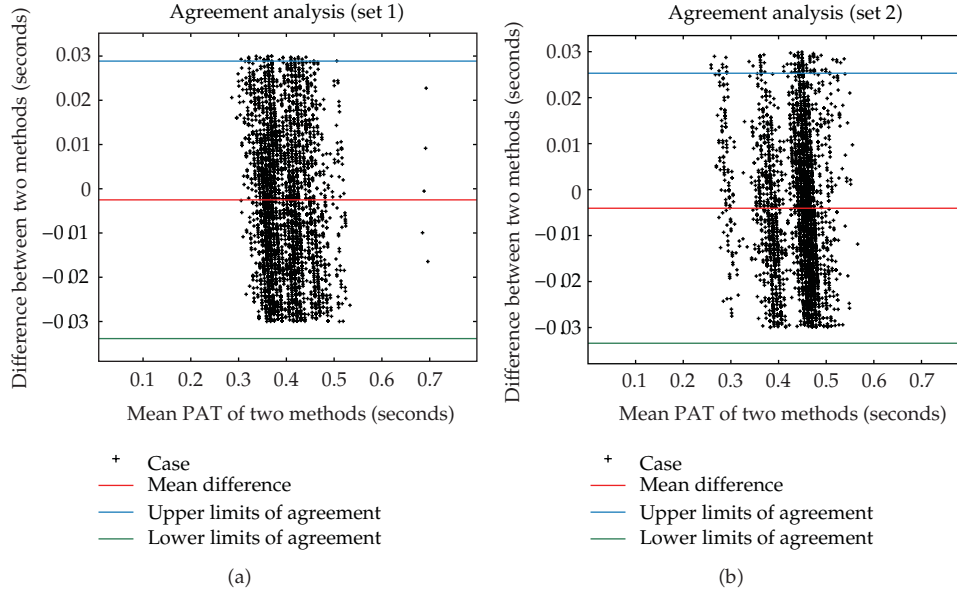


**Figure 3:** Agreement analysis between the two different PAT estimations.

the nonnegative conjugate transformation, because the nonnegative conjugate transformed signal,  $\tilde{I}$ , had the property of collinearity in an  $M$ -dimensional vector space and could be used to estimate the PAT by projection onto a one-dimensional time space. We derived a linear projection matrix through the training process for linear projection and applied this matrix to two different morphological PPG pulse sets. PAT values estimated from annotated MAX points and the proposed linear projecting method were in good agreement; over 95% of the data were included within the 95% limits of agreement.

Although our method provides results that appear to be highly accurate, it can show different results according to the linear projection matrix that is derived by different numbers of pulses and dimensionality. Therefore, an optimal combination that is applicable to a variety of morphological PPG pulse types should be determined. For instance, the size of the projecting matrix needs to be adjusted and the time delay caused by the nonnegative conjugate transformation needs to be addressed. Our novel approach still has some limitations in terms of its clinical application for real-time continuous monitoring of PAT as well as stiffness and blood pressure assessment using PPG; the linear projecting matrix needs to be optimized and the time delay caused by the nonnegative conjugate transformation needs to be addressed. Once these issues are addressed, however, our method has great potential in clinical practice to precisely assess cardiovascular risk associated with blood vessels.

#### 4. Conclusions

Various PAT estimation methods exist, most of which are based on unsupervised extraction of characteristic points in PPG signals. Despite the good performance of these PAT estimation techniques when applied to clean PPG signals, they are less reliable when used to analyze morphologically variable PPG signals. Thus, we designed a novel, simple linear model

based on the nonnegative conjugate transformation. This easy, stable PAT estimation method relies on training of the linear model using various samples. Because our method extracts information from various pressure pulse, it can be applied to different morphological signals without special conditions. In conclusion, we developed a novel method that can be used to estimate PAT robustly for a variety of PPG signals with different morphological characteristics.

## Authors' Contribution

D. kim and J-H. Ahn contributed equally to this paper and should be considered cofirst authors.

## Acknowledgment

This work was supported by the Research Fund of the Survivability Technology Defense Research Center of Agency for Defense Development of Korea (no. UD090090GD).

## References

- [1] M. F. O'Rourke, J. A. Staessen, C. Vlachopoulos, D. Duprez, and G. E. Plante, "Clinical applications of arterial stiffness; definitions and reference values," *American Journal of Hypertension*, vol. 15, no. 5, pp. 426–444, 2002.
- [2] S. J. Zieman, V. Melenovsky, and D. A. Kass, "Mechanisms, pathophysiology, and therapy of arterial stiffness," *Arteriosclerosis, Thrombosis, and Vascular Biology*, vol. 25, no. 5, pp. 932–943, 2005.
- [3] S. Laurent, J. Cockcroft, L. Van Bortel et al., "Expert consensus document on arterial stiffness: methodological issues and clinical applications," *European Heart Journal*, vol. 27, no. 21, pp. 2588–2605, 2006.
- [4] C. Vlachopoulos, K. Aznaouridis, and C. Stefanadis, "Clinical appraisal of arterial stiffness: the argonauts in front of the golden fleece," *Heart*, vol. 92, no. 11, pp. 1544–1550, 2006.
- [5] C. McEniery and J. Cockcroft, "Does arterial stiffness predict atherosclerotic coronary events?" *Advanced Cardiology*, vol. 44, pp. 160–172, 2007.
- [6] I. J. Kullo and A. R. Malik, "Arterial ultrasonography and tonometry as adjuncts to cardiovascular risk stratification," *Journal of the American College of Cardiology*, vol. 49, no. 13, pp. 1413–1426, 2007.
- [7] I. B. Wilkinson, J. R. Cockcroft, and D. J. Webb, "Pulse wave analysis and arterial stiffness," *Journal of Cardiovascular Pharmacology*, vol. 32, supplement 3, pp. S33–S37, 1998.
- [8] W. W. Nichols, "Clinical measurement of arterial stiffness obtained from noninvasive pressure waveforms," *American Journal of Hypertension*, vol. 18, no. 1, 2005.
- [9] K. Sutton-Tyrrell, R. H. Mackey, R. Holubkov, P. V. Vaitkevicius, H. A. Spurgeon, and E. G. Lakatta, "Measurement variation of aortic pulse wave velocity in the elderly," *American Journal of Hypertension*, vol. 14, no. 5, pp. 463–468, 2001.
- [10] I. B. Wilkinson, S. A. Fuchs, I. M. Jansen et al., "Reproducibility of pulse wave velocity and augmentation index measured by pulse wave analysis," *Journal of Hypertension*, vol. 16, no. 12, pp. 2079–2084, 1998.
- [11] J. Blacher, R. Asmar, S. Djane, G. M. London, and M. E. Safar, "Aortic pulse wave velocity as a marker of cardiovascular risk in hypertensive patients," *Hypertension*, vol. 33, no. 5, pp. 1111–1117, 1999.
- [12] J. Blacher, A. P. Guerin, B. Pannier, S. J. Marchais, M. E. Safar, and G. M. London, "Impact of aortic stiffness on survival in end-stage renal disease," *Circulation*, vol. 99, no. 18, pp. 2434–2439, 1999.
- [13] K. Cruickshank, L. Riste, S. G. Anderson, J. S. Wright, G. Dunn, and R. G. Gosling, "Aortic pulse-wave velocity and its relationship to mortality in diabetes and glucose intolerance: an integrated index of vascular function?" *Circulation*, vol. 106, no. 16, pp. 2085–2090, 2002.
- [14] S. Laurent, P. Boutouyrie, R. Asmar et al., "Aortic stiffness is an independent predictor of all-cause and cardiovascular mortality in hypertensive patients," *Hypertension*, vol. 37, no. 5, pp. 1236–1241, 2001.

- [15] Y. C. Chiu, P. W. Arand, S. G. Shroff, T. Feldman, and J. D. Carroll, "Determination of pulse wave velocities with computerized algorithms," *American Heart Journal*, vol. 121, no. 5, pp. 1460–1470, 1991.
- [16] J. Muehlsteff, J. Espina, M. A. A. Alonso, X. Aubert, and T. Falck, "Wearable body sensor network for continuous context- related pulse arrival time monitoring," in *Proceedings of the 6th IASTED International Conference on Biomedical Engineering*, pp. 378–383, February 2008.
- [17] P. Boutouyrie, M. Briet, C. Collin, S. Vermeersch, and B. Pannier, "Assessment of pulse wave velocity," *Artery Research*, vol. 3, no. 1, pp. 3–8, 2009.
- [18] J. Allen, "Photoplethysmography and its application in clinical physiological measurement," *Physiological Measurement*, vol. 28, no. 3, pp. R1–R39, 2007.
- [19] D. K. Jung, G. R. Kim, K. N. Kim et al., "Changes of pulse wave velocity in arm according to characteristic points of pulse wave," in *Proceedings of the 2nd International Conference on Convergent Information Technology (ICCIT '07)*, pp. 821–826, November 2007.
- [20] G. Ning, J. Du, Y. Li, J. Lu, and X. Zheng, "Comparison of pulse wave velocity computed by different characteristic points," in *Proceedings of the 3rd International Association of Science And Technology for Development*, pp. 335–340, 2005.
- [21] J. Solà, R. Vetter, P. Renevey, O. Chételat, C. Sartori, and S. F. Rimoldi, "Parametric estimation of pulse arrival time: a robust approach to pulse wave velocity," *Physiological Measurement*, vol. 30, no. 7, pp. 603–615, 2009.
- [22] D. Lee and S. Seung, "The manifold ways of perception," *Science*, vol. 290, no. 5500, pp. 2268–2269, 2000.
- [23] R. K. P. Zia, E. F. Redish, and S. R. McKay, "Making sense of the Legendre transform," *American Journal of Physics*, vol. 77, no. 7, pp. 614–622, 2009.
- [24] H. Touchette, "Legendre-Fenchel transforms in a nutshell," 2007, <http://www.maths.qmul.ac.uk/~ht/archive/lfth2.pdf>.
- [25] J. H. Ahn and J. H. Oh, "Unsupervised morphing by conjugate image processing," *Electronics Letters*, vol. 43, no. 21, pp. 1137–1138, 2007.
- [26] J. Pan and W. J. Tompkins, "A real-time QRS detection algorithm," *IEEE Transactions on Biomedical Engineering*, vol. 32, no. 3, pp. 230–236, 1985.
- [27] G. B. Moody and R. G. Mark, "A database to support development and evaluation of intelligent intensive care monitoring," *Computers in Cardiology*, pp. 657–660, 1996.
- [28] A. L. Goldberger, L. A. Amaral, L. Glass et al., "PhysioBank, physioToolkit, and physioNet: components of a new research resource for complex physiologic signals," *Circulation*, vol. 101, no. 23, pp. E215–220, 2000.
- [29] J. M. Bland and D. G. Altman, "Measuring agreement in method comparison studies," *Statistical Methods in Medical Research*, vol. 8, no. 2, pp. 135–160, 1999.



## Research Article

# A New Weighted Correlation Coefficient Method to Evaluate Reconstructed Brain Electrical Sources

**Jong-Ho Choi,<sup>1</sup> Min-Hyuk Kim,<sup>1</sup> Luan Feng,<sup>1</sup>  
Chany Lee,<sup>2</sup> and Hyun-Kyo Jung<sup>1</sup>**

<sup>1</sup> School of Electrical Engineering and Computer Science, College of Engineering, Seoul National University, Seoul 151744, Republic of Korea

<sup>2</sup> College of Medicine, Korea University, Seoul 136705, Republic of Korea

Correspondence should be addressed to Jong-Ho Choi, [cjhaha@gmail.com](mailto:cjhaha@gmail.com)

Received 28 October 2011; Accepted 18 January 2012

Academic Editor: Venky Krishnan

Copyright © 2012 Jong-Ho Choi et al. This is an open access article distributed under the Creative Commons Attribution License, which permits unrestricted use, distribution, and reproduction in any medium, provided the original work is properly cited.

Various inverse algorithms have been proposed to estimate brain electrical activities with magnetoencephalography (MEG) and electroencephalography (EEG). To validate and compare the performances of inverse algorithms, many researchers have used artificially constructed EEG and MEG datasets. When the artificial sources are reconstructed on the cortical surface, accuracy of the source estimates has been difficult to evaluate. In this paper, we suggest a new measure to evaluate the reconstructed EEG/MEG cortical sources more accurately. To validate the usefulness of the proposed method, comparison between conventional and proposed evaluation metrics was conducted using artificial cortical sources simulated under different noise conditions. The simulation results demonstrated that only the proposed method could reflect the source space geometry regardless of the number of source peaks.

## 1. Introduction

Noninvasive measurements of brain electrical activities with electroencephalography (EEG) and magnetoencephalography (MEG) enabled us to estimate the underlying cortical activities, thereby contributing to the rapid development of clinical and cognitive neuroscience. To estimate the cortical electrical activities from EEG and MEG, of which the process is often called EEG/MEG source imaging, highly underdetermined inverse problems have to be solved using linear or nonlinear inverse algorithms since the source estimation from EEG and MEG signals is an ill-posed problem, which generally produces blurry or inaccurately positioned source estimates [1]. Many mathematical approaches and techniques have been proposed to estimate accurate source locations and strengths. Among them, minimum-norm estimate (MNE) has been the most widely studied inverse algorithm as MNE is simple and has linearity [2]. MNE chooses a source distribution where the  $l_2$  norm of the current



distribution is minimized. On the contrary, minimum current estimate (MCE) selects a source where the  $l_1$  norm of the current is minimized [3]. Other than those two representative algorithms, there have been several modifications of norm minimization, for example, low-resolution electrical tomography (LORETA) algorithm [4] and the focal underdetermined system solution (FOCUSS) algorithm [5].

When a new source imaging algorithm is proposed, the performance of the inverse algorithm needs to be verified and compared with those of the existing ones. Since the reconstructed source distributions are hard to be verified using in vivo experiments, many researchers have used artificial EEG/MEG human skull phantoms [6] or realistically simulated EEG/MEG datasets. Since the use of simulated EEG/MEG data allows us to readily adjust and control noise levels and source configurations, that is, the number and size of source patches, most inverse algorithms are generally verified using simulated EEG/MEG data [2–5]. In recent simulation studies, the source spaces are generally constrained only on the interface between white and gray matter of the cerebral cortex, generally called cortical surface, considering neurophysiology. The orientations of the cortical sources are also assumed to be perpendicular to the cortical surface [7]. In such simulations, both the original source patches and the reconstructed sources are commonly distributed on the cortical surface generally tessellated with surface triangular elements.

For the evaluation of the reconstructed sources, evaluation metrics or error metrics need to be introduced to probe the similarity between the simulated and reconstructed sources. The well-known evaluation metrics are root mean square error (RMSE), shift of the maximum ( $S_{\max}$ ), shift of the center of mass ( $S_{\text{cm}}$ ), and the correlation coefficient (CC) [6]. Each metric has its own pros and cons. In contrast to the conventional geometric error metrics such as  $S_{\max}$  and  $S_{\text{cm}}$ , RMSE and CC do not reflect the geometry of the cortical surface. However, compared to  $S_{\max}$  and  $S_{\text{cm}}$ , RMSE and CC are reliable specifically when the source distributions are not concentrated to a single peak. For more accurate and robust estimation of the accuracy of reconstructed EEG/MEG sources, we modified CC by giving the geodesic distance weights to the reconstructed sources to reflect the geometric information of cortical surface. To validate the new evaluation metric, named weighted correlation coefficient (WCC), some representative examples were used.

## 2. Methods

### 2.1. EEG/MEG Inverse Problem

When a set of  $n$  possible source locations and  $m$  sensor positions is given, thanks to the linearity of Maxwell's equations, an EEG/MEG forward model can be described as  $\mathbf{b} = \mathbf{K}\mathbf{j} + \mathbf{s}$ , where  $\mathbf{K}$  is an  $m$  by  $n$  EEG/MEG lead field matrix,  $\mathbf{j}$  is an  $n$  by 1 unknown source vector,  $\mathbf{b}$  is an  $m$  by 1 recorded EEG/MEG data, and  $\mathbf{s}$  is the additional sensor noises. The inverse problem for estimating  $\mathbf{j}$  from  $\mathbf{b}$  has no unique solution. To estimate the possible solutions, MNE adopts the following minimization problem:

$$\min_{\mathbf{j}} \|\mathbf{j}\|_2 \quad \text{subject to } \mathbf{b} = \mathbf{K}\mathbf{j} + \mathbf{s}. \quad (2.1)$$

Then, the estimated solution  $\tilde{\mathbf{j}}$  can be written as

$$\tilde{\mathbf{j}} = \mathbf{K}^T [\mathbf{K}\mathbf{K}^T + \lambda \mathbf{I}]^{-1} \mathbf{b}, \quad (2.2)$$

where  $\lambda$  is a regularization parameter, which was determined using the generalized cross-validation method [8].

## 2.2. Conventional Evaluation Metrics

We assume that both the simulated true sources  $\mathbf{j}$  and the estimated sources  $\tilde{\mathbf{j}}$  are distributed on the 3D cortical surface. The dimension of both vectors is  $n$  by 1, where  $n$  is the number of nodes on the source space. We firstly summarize four conventional evaluation metrics, having been frequently used for assessing the accuracy of the source estimates.

### 2.2.1. Root Mean Square Error

The root mean square error (RMSE) is the most well-known and convenient way to measure the error between the actual source and the estimated source. RMSE is formulated as

$$\text{RMSE} = \sqrt{\frac{1}{n} \sum_{i=1}^n (j_i - \tilde{j}_i)^2}, \quad (2.3)$$

where  $j_i$  and  $\tilde{j}_i$  are the  $i$ th elements of  $\mathbf{j}$  and  $\tilde{\mathbf{j}}$  respectively.

This metric is easy to implement and can be used regardless of the shapes of the source distributions. However, RMSE does not reflect the geometry of the cortical surface since RMSE is computed with just vectored values.

### 2.2.2. Shift of the Maximum of the Estimate

The shift of the maximum of the estimate ( $S_{\max}$ ) is the simplest measure which reflects the geometry of the source space.  $S_{\max}$  indicates the distance between the locations where the maximum intensities of sources are generated. The maximum intensities of the actual and reconstructed source are assumed to be located at  $\mathbf{r}_{\max}$  and  $\tilde{\mathbf{r}}_{\max}$ ; respectively,

$$\mathbf{r}_{\max} = \max_{\mathbf{r}_i} j_i, \quad \tilde{\mathbf{r}}_{\max} = \max_{\mathbf{r}_i} \tilde{j}_i, \quad (2.4)$$

where  $\mathbf{r}_i$  is the coordinate of  $i$ th node, then  $S_{\max}$  is defined as

$$S_{\max} = \sqrt{(\mathbf{r}_{\max} - \tilde{\mathbf{r}}_{\max})^2} \quad (2.5)$$

and ranged from 0 to  $d_{\max}$ , the maximum distance within the brain.

This measure is reliable only when the actual source is concentrated around the location of the maximum source intensity because it does not consider the distributions of the cortical sources. When  $S_{\max}$  is adopted as a measure, the merit of distributed source modeling disappears. For example, even when the extents of the true source and the reconstructed sources are largely different, identical maximum location makes the  $S_{\max}$  value be 0.

### 2.2.3. Shift of the Center of Mass

The center of mass has been widely used for evaluating various algorithms adopted not only in EEG and MEG but also in other functional brain imaging techniques such as functional magnetic resonance imaging (fMRI) and positron emission tomography (PET). The center of mass of the actual source  $\mathbf{r}_{\text{cm}}$  and the center of mass of the reconstructed source  $\tilde{\mathbf{r}}_{\text{cm}}$  are computed as

$$\mathbf{r}_{\text{cm}} = \frac{\sum_{i=1}^n j_i \mathbf{r}_i}{\sum_{i=1}^n j_i}, \quad \tilde{\mathbf{r}}_{\text{cm}} = \frac{\sum_{i=1}^n \tilde{j}_i \mathbf{r}_i}{\sum_{i=1}^n \tilde{j}_i}. \quad (2.6)$$

As assuming the distributed source to be a dipole source placed on the center of mass of the source, the shift of center of mass ( $S_{\text{cm}}$ ) is defined as the distance between  $\mathbf{r}_{\text{cm}}$  and  $\tilde{\mathbf{r}}_{\text{cm}}$ :

$$S_{\text{cm}} = \sqrt{(\mathbf{r}_{\text{cm}} - \tilde{\mathbf{r}}_{\text{cm}})^2}. \quad (2.7)$$

$S_{\text{cm}}$  is similar to  $S_{\text{max}}$  in that the distributed source is considered as a point source placed at a single location. Therefore,  $S_{\text{cm}}$  is also reliable only when the simulated source is concentrated around  $\mathbf{r}_{\text{cm}}$ . If the distribution of the source has a radial symmetry,  $S_{\text{cm}}$  becomes equivalent to  $S_{\text{max}}$ .

### 2.2.4. Correlation Coefficient

The correlation coefficient (CC), a concept adopted from statistics, is a measure of linear dependency between two variables, and the value ranges between  $-1$  and  $1$ . It has been widely employed as a standard measure in various fields of engineering and sciences. The conventional CC is defined as the covariance of  $\mathbf{j}$  and  $\tilde{\mathbf{j}}$  divided by the product of their standard deviations:

$$\text{CC} = \frac{\text{cov}(\mathbf{j}, \tilde{\mathbf{j}})}{\sqrt{\text{cov}(\mathbf{j}, \mathbf{j}) \text{cov}(\tilde{\mathbf{j}}, \tilde{\mathbf{j}})}}, \quad (2.8)$$

where the covariance is defined as

$$\text{cov}(\mathbf{j}, \tilde{\mathbf{j}}) = \frac{1}{n} \sum_{i=1}^n (j_i - j^*) (\tilde{j}_i - \tilde{j}^*), \quad (2.9)$$

and  $j^*$  represents the mean value of the source  $\mathbf{j}$ :

$$j^* = \frac{1}{n} \sum_{i=1}^n j_i, \quad \tilde{j}^* = \frac{1}{n} \sum_{i=1}^n \tilde{j}_i. \quad (2.10)$$

If the distribution of the reconstructed sources is similar to that of the actual sources, the value of CC is close to 1; if the distribution of the reconstructed sources is different from

that of the actual sources, CC is close to  $-1$ . CC is reliable even when the source distribution is not concentrated to a single location or when the true source has many distinct peaks. However, similar to RMSE, CC cannot reflect the real geometry of the cortical surface.

### 2.3. New Algorithm: Weighted Correlation Coefficient

When we categorize four conventional measures mentioned in Section 2.2 in terms of geometric consideration, contrast to  $S_{\max}$  and  $S_{\text{cm}}$ , RMSE and CC do not reflect the geometry of the cortical surface. However, RMSE and CC are reliable compared to  $S_{\max}$  and  $S_{\text{cm}}$  when the source distribution is not concentrated to a single peak. To combine the advantages of both types of conventional measures, we modified CC by giving the source vector a weight reflecting geometrical information of cortical surface. The new evaluation measure, named weighted correlation coefficient (WCC), is defined as

$$\text{WCC} = \frac{\text{cov}(\mathbf{W}\mathbf{j}, \tilde{\mathbf{W}}\tilde{\mathbf{j}})}{\sqrt{\text{cov}(\mathbf{W}\mathbf{j}, \mathbf{W}\mathbf{j}) \text{cov}(\tilde{\mathbf{W}}\tilde{\mathbf{j}}, \tilde{\mathbf{W}}\tilde{\mathbf{j}})}}, \quad (2.11)$$

and  $\mathbf{W}$  is an  $n$  by  $n$  weighting matrix that can be computed as

$$\mathbf{W} = \frac{d_{\max} \mathbf{I}_n - \mathbf{D}}{d_{\max}}, \quad (2.12)$$

where  $\mathbf{I}_n$  is an  $n$  by  $n$  identity matrix.  $\mathbf{D}$  is an  $n$  by  $n$  distance matrix whose element is given as

$$D_{ij} = \|\mathbf{r}_i - \mathbf{r}_j\|_k \quad (2.13)$$

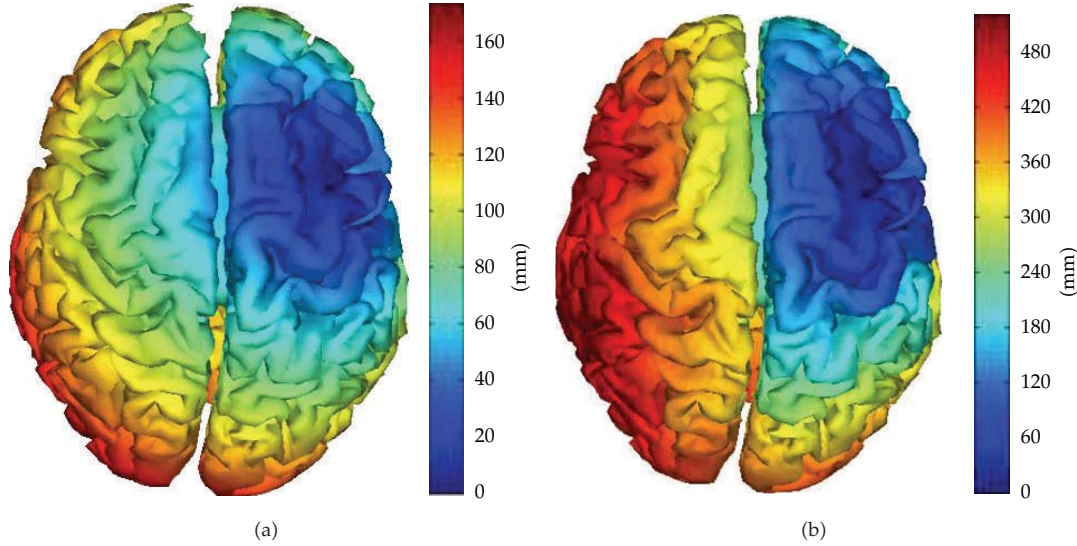
and  $d_{\max}$  is the maximum value in  $\mathbf{D}$ . If  $k = 2$ , the Euclidean distance is employed, and if  $k = \text{geo}$ , then the geodesic distance is employed to obtain the distance matrix. The geodesic distance was computed by solving the Eikonal equation on the tessellated cortical surface [9]. The main diagonal of the weight matrix  $\mathbf{W}$  was filled with 1, and the off-diagonal elements were filled with values between 0 and 1. By multiplying weight matrix  $\mathbf{W}$  to the source vector  $\mathbf{j}$ , the geometric information of cortical surface is considered.

Additionally, Euclidean or geodesic distance can be employed in the definition of the distance matrix  $\mathbf{D}$ . Since the cortical surface of a human brain is folded, the geodesic distance is more suitable to reflect the geometric information of the cortical surface than the Euclidean distance. The Euclidean distance is computed by the Cartesian coordinates regardless of the geometrical feature of the cortical surface. However, as the geodesic distance implies the minimum distance along the surface, the geodesic distance between the two adjacent gyri should be greater than the Euclidean distance. Figure 1 is an example of the Euclidean and geodesic distance between each cortical surface vertex and a reference point located at right dorsolateral prefrontal cortex, corresponding to a column of the distance matrix.

Once the distance matrix is computed, the weighting matrix is determined from (2.13). Figure 2 shows the Euclidean and geodesic weights corresponding to the Euclidean and

**Table 1:** The merits and demerits of measures.

Measures	Reflection of geometry	Multi-peaks	Bound	Unit
RMSE	no	Yes	$0 \sim \infty$	no unit
$S_{\max}$	yes	No	$0 \sim d_{\max}$	mm
$S_{\text{cm}}$	yes	No	$0 \sim d_{\max}$	mm
CC	no	Yes	$-1 \sim 1$	no unit
WCC	yes	Yes	$-1 \sim 1$	no unit

**Figure 1:** One column of (a) Euclidean and (b) geodesic distance matrix visualized on the cortical surface.

geodesic distance matrices exemplified in Figure 1. In contrast to Figure 1, as getting farther from the reference point, the weight is getting smaller.

The characteristics of the conventional and proposed measures are summarized in Table 1. Low values of RMSE,  $S_{\max}$ , or  $S_{\text{cm}}$  and high values of CC and WCC indicate the accurate reconstruction. Only WCC is applicable to the case of multipeak and can consider the geometry of source space.

### 3. Results

To compare and verify the conventional and proposed measures, a simple two-dimensional example was simulated as shown in Figure 3. The source space was defined as a two-dimensional rectangle. The actual source distribution  $\mathbf{x}$  is given in Figure 3(a), and five reconstructed sources are given in Figures 3(b)–3(f), each of which was denoted as  $\mathbf{y}_1$ ,  $\mathbf{y}_2$ ,  $\mathbf{y}_3$ ,  $\mathbf{y}_4$ , and  $\mathbf{y}_5$ . The source current intensities are indicated with different colors. If we evaluate the reconstructed sources based on visual inspection, anyone would agree that  $\mathbf{y}_1$  is the most accurate reconstruction and  $\mathbf{y}_2$  is the second best one.  $\mathbf{y}_5$  seem to be the worst reconstruction as the peak location is farthest from the actual one and no reconstructed source is overlapped with the actual one.  $\mathbf{y}_3$  and  $\mathbf{y}_4$  seems to be better matched than  $\mathbf{y}_5$ , but it is difficult to judge which result is better. The result  $\mathbf{y}_3$  has no commonly activated region with the actual

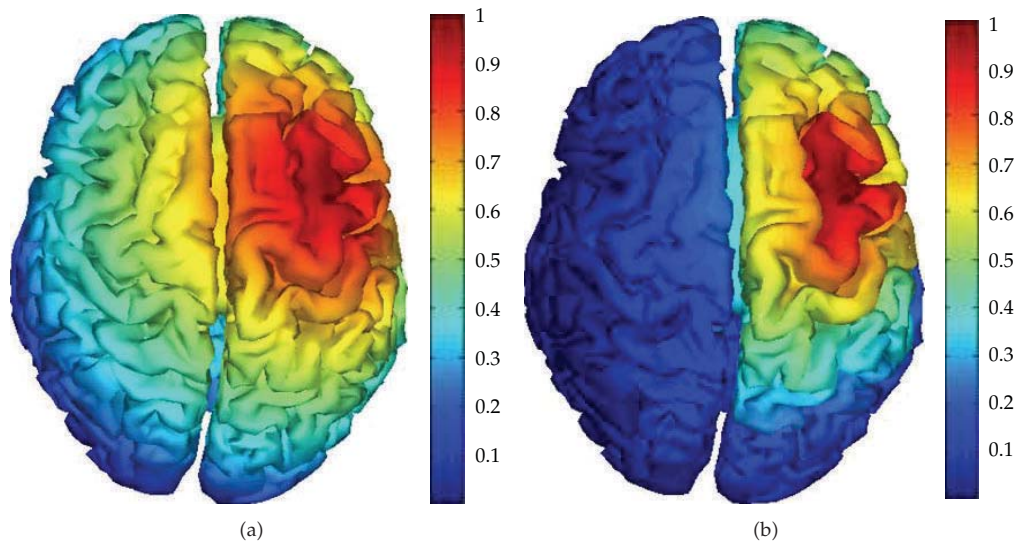


**Figure 2:** One column of (a) Euclidean and (b) geodesic weighted matrix visualized on the cortical surface.

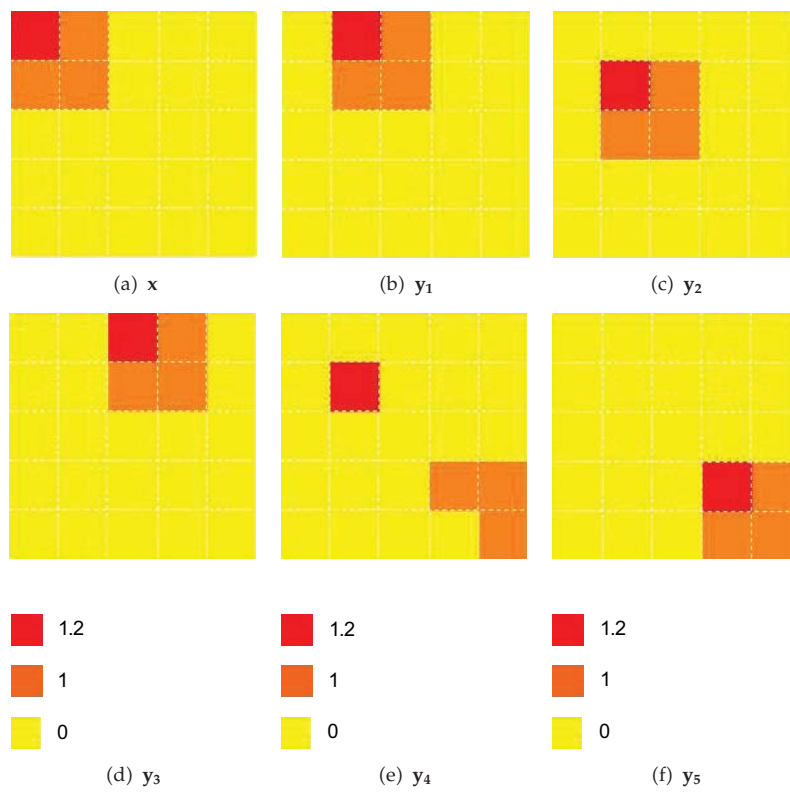


**Figure 3:** Example of a simulated two-dimensional source space: actual source distribution (a) and reconstructed sources (b)–(f).



**Table 2:** Evaluation of reconstructions depicted in Figure 1.

	$y_1$	$y_2$	$y_3$	$y_4$	$y_5$
RMSE	2.12	2.53	2.98	2.73	2.98
$S_{\max}$	1.00	1.41	2.00	1.41	4.24
$S_{\text{cm}}$	1.00	1.41	2.00	2.87	4.24
CC	0.40	0.13	-0.19	0.25	-0.19
WCC	0.89	0.80	0.48	-0.31	-0.79

**Table 3:** Evaluation of reconstructions depicted in Figure 4.

	$y_1$	$y_2$	$y_3$	$y_4$	$y_5$
RMSE	9.76	9.95	10.05	10.06	43.58
$S_{\max,E}$	10.07	21.94	31.39	59.54	20.07
$S_{\max,G}$	9.13	28.12	71.10	122.11	51.71
$S_{\text{cm},E}$	4.16	18.04	31.60	54.95	13.35
$S_{\text{cm},G}$	8.21	21.67	54.32	75.15	24.11
CC	0.32	0.09	0.00	0.00	0.00
$WCC_E$	0.92	0.89	0.82	0.60	0.58
$WCC_G$	0.95	0.86	0.43	0.36	0.35

source, but the distribution is close to the actual source distribution, whereas  $y_4$  has slightly overlapped region, but other regions are located far from the actual source location. If we assume visual inspection (VI) as a qualitative measure, the rank of the reconstructed sources can be expressed as  $VI(x, y_1) > VI(x, y_2) > VI(x, y_3) \geq VI(x, y_4) > VI(x, y_5)$ .

We then employed the conventional and proposed quantitative measures for the evaluation of the reconstructions depicted in Figure 1 and summarized the result in Table 2. All measures commonly indicated that  $y_1$  is the best reconstruction and  $y_5$  is the worst reconstruction. However, the different metrics showed different evaluation results for  $y_2$ ,  $y_3$ , and  $y_4$ . In the case of RMSE,  $y_3$  was evaluated as the worst reconstruction, and  $y_4$  and  $y_2$  had an identical RMSE value, which was because RMSE was affected by the commonly activated regions regardless of the source geometry. In the case of  $S_{\max}$ , which considers only the maximum location of the source, the results of  $y_2$  and  $y_4$  were equivalent. Similar to RMSE, CC classified  $y_3$  as the worst reconstruction and  $y_4$  and  $y_2$  had an identical CC value. Both  $S_{\text{cm}}$  and WCC evaluated the reconstruction results identically to the visual inspection results. However, if the actual source has multiple peaks,  $S_{\text{cm}}$  cannot be accurately evaluated.

We then applied the conventional and proposed evaluation metrics to the evaluation of distributed sources on the cortical surface. The cortical surface was extracted from a structural MRI of a standard brain atlas provided by the Montreal Neurological Institute (MNI). To extract and tessellate the cortical surface, we used CURRY6 for Windows (Compumedics, Inc., El Paso, TX). The actual source  $x$  defined on the cortical surface is given in Figure 4(a), and the reconstructed sources are given in Figures 4(b)–4(f), each of which was denoted as  $y_1$ ,  $y_2$ ,  $y_3$ ,  $y_4$  and  $y_5$ . If we verify the reconstructed sources by visual inspection,  $y_1$  seems to be the most accurate reconstruction and  $y_2$  seems to be the second best one. The two distributions  $y_4$  and  $y_5$  are very different from the actual source distribution. We can roughly estimate the rank of the reconstructed sources as  $VI(x, y_1) > VI(x, y_2) > VI(x, y_3) > VI(x, y_4) \geq VI(x, y_5)$ .

The quantitative evaluation results with conventional and proposed metrics are shown in Table 3. In the case of RMSE, the RMSE values corresponding to  $y_1$ – $y_4$  were increasing,

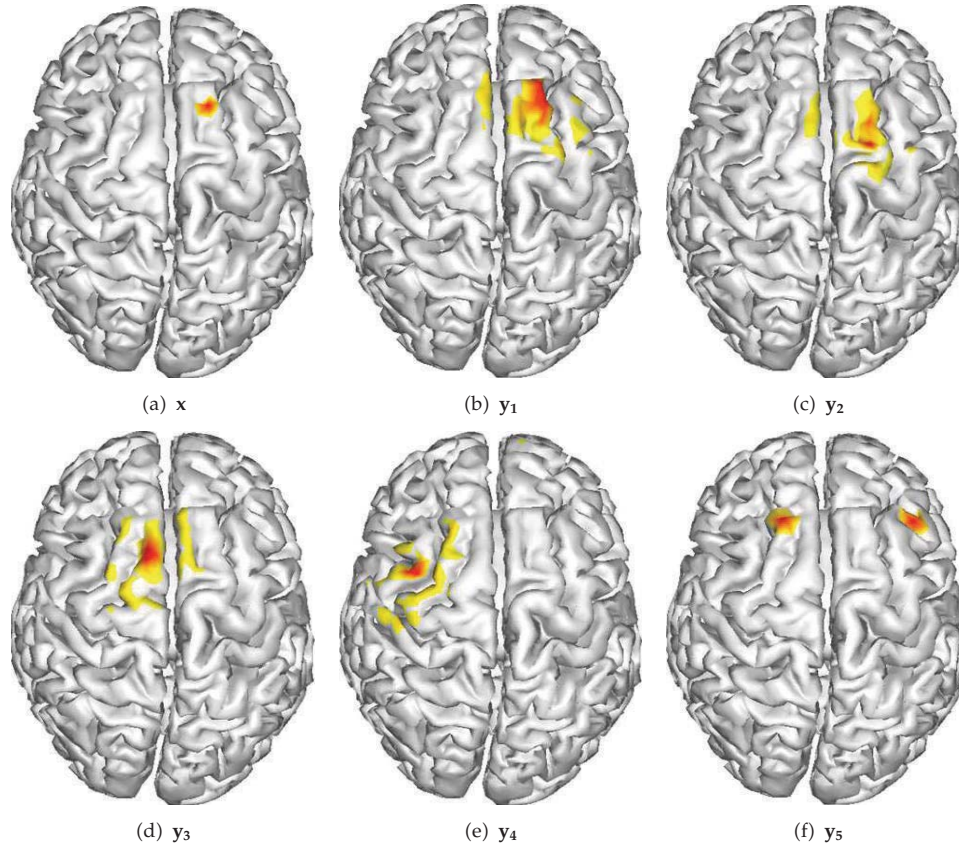


**Figure 4:** Simulation of three-dimensional cortical sources: actual source (a) and reconstructed sources (b)–(f).

which coincided with the visual inspection results, but the increment was very small compared to the absolute values of RMSE. The results of  $S_{\max,E}$  and  $S_{\max,G}$  showed that  $y_5$  is the better reconstruction than  $y_3$ . Moreover, since the center of mass of  $y_5$  was located near the actual source,  $S_{\text{cm},E}$  and  $S_{\text{cm},G}$  of  $y_5$  were less than those of  $y_2$ . Subscripted  $E$  and  $G$  indicate that the Euclidean and geodesic distance matrices were adopted, respectively. CC also could not distinguish the difference between  $y_3$  and  $y_4$ .  $WCC_E$  and  $WCC_G$  are the WCC results when the Euclidean and geodesic distance matrices were adopted, respectively, to construct the weighting matrix. Both  $WCC_E$  and  $WCC_G$  were proved to be reliable since both results coincided well with the visual inspection results. However, compared to  $WCC_G$ ,  $WCC_E$  could not reflect the large difference between  $y_2$  and  $y_3$ , which are located even in different hemispheres.

We performed extensive computer simulations to quantitatively compare the performance of the proposed measure with that of conventional measures. 2,000 locations on the cortical surface are selected randomly, and on each location a single constant source patch is generated. Consequently, our computer simulations used 2,000 cortical patches whose averaged radius is 6 mm ( $\pm 1.2$  mm). After solving the MEG forward problem with each cortical patch, different-level white Gaussian noise are added to the simulated MEG signal data. We set the signal-to-noise ratio (SNR) values from  $-10$  dB to  $30$  dB. The reconstructed source



**Table 4:** Evaluation of reconstructions with 2,000 randomly selected source patches.

dB	30	20	10	0	-10
RMSE	11.21	11.37	11.33	32.22	53.81
$S_{\max,E}$	12.71	12.54	21.17	19.29	20.63
$S_{\max,G}$	14.32	18.90	30.82	29.68	23.53
$S_{\text{cm},E}$	8.52	11.41	11.21	15.26	13.17
$S_{\text{cm},G}$	15.11	21.67	32.43	31.52	34.21
CC	0.54	0.12	0.01	0.01	0.01
$\text{WCC}_E$	0.93	0.85	0.74	0.63	0.52
$\text{WCC}_G$	0.94	0.86	0.65	0.56	0.42

is computed by the minimum norm method with each MEG signal then evaluated with different measures. Table 4 shows the averaged accuracies with conventional and proposed measures with respect to SNR. We expect that results of reconstruction to become more accurate as SNR is getting higher. In the case of RMSE, though the RMSE is increasing as SNR becomes lower, the difference between 10, 20, and 30 dB cases is not clear as much the cases of 0 and -10 dB. In the cases of geodesic measures ( $S_{\max,E}$ ,  $S_{\text{cm},E}$ ,  $S_{\max,G}$ ,  $S_{\text{cm},G}$ ), the relation of accuracy and SNR is not consistent with the expected tendency. Moreover, the accuracy of low SNR is occasionally greater than that of high SNR in geodesic measures. In the case of CC with high SNR (10, 0, and -10 dB), there is only a marginal difference compared to that of low SNR. Only the accuracy measured by WCC is consistently decreasing as the SNR becomes lower.

#### 4. Conclusion

The geometric measures ( $S_{\max}$ ,  $S_{\text{cm}}$ ) could reflect the geometry of the source space, while the statistical measures (RMSE, CC) could be applied regardless of the distribution characteristics of the sources. In this paper, a new evaluation metric named WCC was proposed to combine the advantages of both types of evaluation metrics and showed enhanced performances compared to the conventional metrics. From the extensive simulation, we could conclude that the proposed measure is very promising to evaluate accuracy of reconstructed sources or EEG/MEG inverse algorithms.

#### References

- [1] D. Cohen and E. Halgren, "Magnetoencephalography," in *Encyclopedia of Neuroscience*, L. R. Squire, Ed., pp. 615–622, Academic Press, Oxford, UK, 2009.
- [2] M. S. Hamalainen and R. J. Ilmoniemi, "Interpreting magnetic fields of the brain: minimum norm estimates," *Medical and Biological Engineering and Computing*, vol. 32, no. 1, pp. 35–42, 1994.
- [3] K. Uutela, M. Hämäläinen, and E. Somersalo, "Visualization of magnetoencephalographic data using minimum current estimates," *NeuroImage*, vol. 10, no. 2, pp. 173–180, 1999.
- [4] R. D. Pascual-Marqui, C. M. Michel, and D. Lehmann, "Low resolution electromagnetic tomography: a new method for localizing electrical activity in the brain," *International Journal of Psychophysiology*, vol. 18, no. 1, pp. 49–65, 1994.
- [5] I. F. Gorodnitsky, J. S. George, and B. D. Rao, "Neuromagnetic source imaging with FOCUSS: a recursive weighted minimum norm algorithm," *Electroencephalography and Clinical Neurophysiology*, vol. 95, no. 4, pp. 231–251, 1995.

- [6] S. Baillet, J. J. Rira, G. Main, J. F. Magin, J. Aubert, and L. Ganero, "Evaluation of inverse methods and head models for EEG source localization using a human skull phantom," *Physics in Medicine and Biology*, vol. 46, no. 1, pp. 77–96, 2001.
- [7] A. M. Dale and M. I. Sereno, "Improved localization of cortical activity by combining EEG and MEG with MRI cortical surface reconstruction: a linear approach," *Journal of Cognitive Neuroscience*, vol. 5, no. 2, pp. 162–176, 1993.
- [8] G. H. Golub, M. Heath, and G. Wahba, "Generalized cross-validation as a method for choosing a good ridge parameter," *Technometrics*, vol. 21, no. 2, pp. 215–223, 1979.
- [9] A. Bartesaghi and G. Sapiro, "A system for the generation of curves on 3D brain images," *Human Brain Mapping*, vol. 14, no. 1, pp. 1–15, 2001.

## Research Article

# Coupling of Point Collocation Meshfree Method and FEM for EEG Forward Solver

**Chany Lee,<sup>1</sup> Jong-Ho Choi,<sup>2</sup>  
Ki-Young Jung,<sup>1</sup> and Hyun-Kyo Jung<sup>1</sup>**

<sup>1</sup> College of Medicine, Korea University, 126-1 Anam-dong, Sungbuk-gu, Seoul 136-705, Republic of Korea

<sup>2</sup> School of Electrical Engineering and Computer Science, Seoul National University,  
Seoul 151-742, Republic of Korea

Correspondence should be addressed to Chany Lee, chan0511@hanmail.net

Received 15 November 2011; Accepted 28 December 2011

Academic Editor: Chang-Hwan Im

Copyright © 2012 Chany Lee et al. This is an open access article distributed under the Creative Commons Attribution License, which permits unrestricted use, distribution, and reproduction in any medium, provided the original work is properly cited.

For solving electroencephalographic forward problem, coupled method of finite element method (FEM) and fast moving least square reproducing kernel method (FMLSRLM) which is a kind of meshfree method is proposed. Current source modeling for FEM is complicated, so source region is analyzed using meshfree method. First order of shape function is used for FEM and second order for FMLSRLM because FMLSRLM adopts point collocation scheme. Suggested method is tested using simple equation using 1-, 2-, and 3-dimensional models, and error tendency according to node distance is studied. In addition, electroencephalographic forward problem is solved using spherical head model. Proposed hybrid method can produce well-approximated solution.

## 1. Introduction

Electroencephalography (EEG) is a technique to measure and analyze the scalp potential [1] and widely used for clinical applications and scientific researches because EEG has noninvasiveness and high temporal resolution [2, 3]. As electric potential on scalp is a reflection of neuronal activation in a brain [4], solving inverse problem of EEG, or reconstructing distribution of current source, is an important mathematical tool to investigate brain functions and diseases [5]. Because precise solution of forward problem is essential for accurate inverse solution, we proposed a new forward solver with high accuracy in this paper.

Solving forward problem of EEG is to obtain potential distribution of head due to neuronal electric current [1, 6, 7]. Although there are many methods to solve forward problem, finite element method (FEM) is frequently used because it can consider realistic head shape, inhomogeneity, and anisotropy [7–9]. However, according to Awada's research,

variation of dipole location in a first-order element cannot affect forward solution, which causes poor spatial resolution of FEM [9]. Furthermore, location of dipole is also a problem in node-based distributed source model. To overcome these limitations, we adopted a meshfree method for region near dipole.

Because meshfree methods do not need finite elements, mesh generation process is not required. So, difficult situation to generate finite elements such as small objects inside a large analysis domain [10], crack propagation [11], and moving objects [12] can be analyzed by meshfree methods. However, meshfree methods consume longer time to solve a system matrix than FEM does, because the number of nodes related with a certain node of meshfree method is more than that of FEM.

In this paper, a new hybrid method of meshfree method and FEM for forward solver is proposed. There were some tries to surmount disadvantages of FEM and meshfree method by combining two methods in previous studies [13–16]. While most meshfree methods with weak formulation and integration cells are studied for coupling with FEM [13–16], point collocation scheme is applied for this study because of its efficiency [17, 18]. Among many sorts of meshfree methods [19–23], fast moving least square reproducing kernel method (FMLSRLM) is adopted because FMLSRLM can evaluate all approximated derivatives of shape functions up to the order of the basis polynomials simultaneously, without additional computations [16, 17]. We explain FMLSRLM and its coupling with FEM in the next section. Then, using simple models, the suggested method is tested and error is evaluated. Moreover, EEG problem with 2D model is treated to show that the suggested method can be a forward solver with small error.

## 2. Combination of FEM and FMLSRLM

### 2.1. FMLSRLM

In FMLSRLM [10, 16, 17], an approximated solution  $u^h$  at  $\mathbf{x}$  near  $\bar{\mathbf{x}}$  can be determined using polynomial bases  $\mathbf{P}_m$  and their coefficient vector  $\mathbf{a}(\bar{\mathbf{x}})$ , like

$$u^h(\mathbf{x}, \bar{\mathbf{x}}) = \mathbf{P}_m\left(\frac{\mathbf{x} - \bar{\mathbf{x}}}{\rho}\right) \cdot \mathbf{a}(\bar{\mathbf{x}}), \quad (2.1)$$

where  $m$  is the highest order of polynomial and  $\rho$  is the dilation parameter which represents region of influence of  $u^h(\mathbf{x}, \bar{\mathbf{x}})$ . In order to obtain coefficient vector, localized error residual functional

$$J(\mathbf{a}(\bar{\mathbf{x}})) = \sum_{I=1}^{\text{NP}} \left| u(\mathbf{x}_I) - \mathbf{P}_m\left(\frac{\mathbf{x}_I - \bar{\mathbf{x}}}{\rho}\right) \cdot \mathbf{a}(\bar{\mathbf{x}}) \right|^2 \left( \frac{1}{\rho^n} \right) \Phi\left(\frac{\mathbf{x}_I - \bar{\mathbf{x}}}{\rho}\right), \quad (2.2)$$

should be minimized. Hence,

$$\mathbf{a}(\bar{\mathbf{x}}) = M^{-1}(\bar{\mathbf{x}}) \sum_{I=1}^{\text{NP}} \mathbf{P}_m\left(\frac{\mathbf{x}_I - \bar{\mathbf{x}}}{\rho}\right) u(\mathbf{x}_I) \Phi_\rho(\mathbf{x}_I - \bar{\mathbf{x}}), \quad (2.3)$$

$$M(\bar{\mathbf{x}}) = \sum_{I=1}^{\text{NP}} \mathbf{P}_m\left(\frac{\mathbf{x}_I - \bar{\mathbf{x}}}{\rho}\right) \mathbf{P}_m^T\left(\frac{\mathbf{x}_I - \bar{\mathbf{x}}}{\rho}\right) \Phi_\rho(\mathbf{x}_I - \bar{\mathbf{x}}), \quad (2.4)$$

where NP is the number of nodes in the local area. So, (2.1) can be rewritten as

$$u^h(\mathbf{x}, \bar{\mathbf{x}}) = \mathbf{P}_m^T \left( \frac{\mathbf{x} - \bar{\mathbf{x}}}{\rho} \right) M^{-1}(\bar{\mathbf{x}}) \sum_{I=1}^{NP} \mathbf{P}_m \left( \frac{\mathbf{x}_I - \bar{\mathbf{x}}}{\rho} \right) \Phi_\rho(\mathbf{x}_I - \bar{\mathbf{x}}) u(\mathbf{x}_I), \quad (2.5)$$

where

$$\Phi_\rho(\mathbf{x}_I - \bar{\mathbf{x}}) = \left( \frac{1}{\rho^n} \right) \Phi \left( \frac{\mathbf{x}_I - \bar{\mathbf{x}}}{\rho} \right) \quad (2.6)$$

is called window function, where

$$\Phi(\mathbf{x}) = \begin{cases} (1 - \|\mathbf{x}\|)^t, & \text{when } \|\mathbf{x}\| < 1, t > 0, \\ 0, & \text{otherwise.} \end{cases} \quad (2.7)$$

After moving least square scheme is applied, approximated solution (2.1) can be rewritten as

$$u(\mathbf{x}) = \sum_{I=1}^{NP} \Psi_I^{[\alpha]} u(\mathbf{x}_I), \quad (2.8)$$

where

$$\Psi_I^{[\alpha]} = \frac{\alpha!}{\rho^{|\alpha|}} \mathbf{e}_\alpha^T M^{-1}(\bar{\mathbf{x}}) \mathbf{P}_m \left( \frac{\mathbf{x} - \bar{\mathbf{x}}}{\rho} \right) \Phi_\rho(\mathbf{x}_I - \bar{\mathbf{x}}), \quad (2.9)$$

is the shape function of FMLSRKM.

## 2.2. Coupling of Shape Functions

For the sake of an explanation, in this section, 1-dimensional shape functions are considered. Because point collocation method is adopted for FMLSRKM, quadratic shape function is used. In FEM, influence of a shape function is confined in an element (see Figure 1(a)). In addition, the value of shape function is 1 at the node and 0 at the other node, and the sum of shape functions at any point is 1, which makes shape function the partition of unity. However, in the case of FMLSRKM, an area covered by a shape function of a node is usually larger than that of FEM (see Figure 1(b)). Furthermore, the value of shape function at the node is not 1 and shape function is not the partition of unity, so the approximated value inside two nodes is interpolated by more than two shape functions in many cases.

So, an interfacial area between FEM domain and FMLSRKM domain has one finite element shape function and many FMLSRKM shape functions. Hence, adequate weighting functions should be considered for shape functions of the hybrid method. While linear weighting functions are applied on both FEM and meshfree in the previous study [15], step functions are used for weight functions as shown in Figures 2(a) and 2(b).

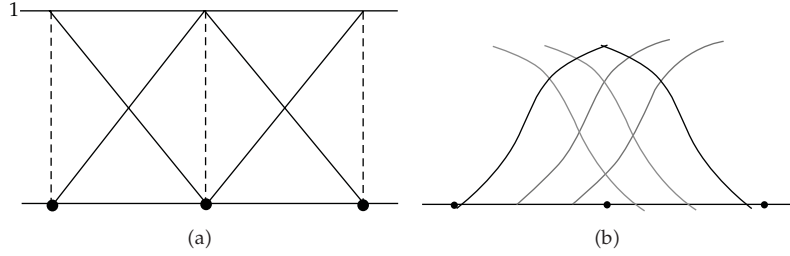


**Figure 1:** Shape functions of (a) FEM and (b) FMLSRKM. A shape function of FEM is a partition of unity, but that of FMLSRKM is not.

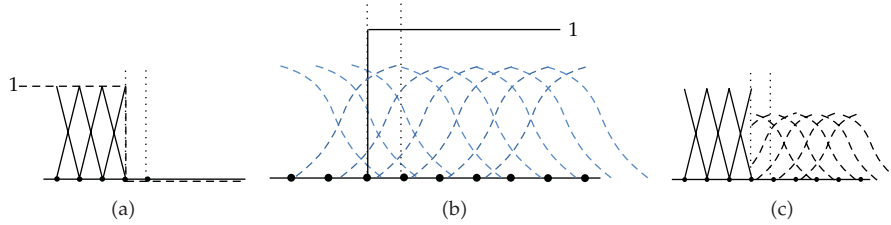


**Figure 2:** Combination of shape functions in an interfacial area of FEM and FMLSRKM. (a) Shape functions of FEM, (b) shape functions of FMLSRKM, and (c) shape functions of hybrid method. Shape function of FMLSRKM is fully adopted as shape function of the interfacial area (inside two vertical dotted lines).

Consequently, Figure 2(c) is shape functions for coupling method, because FMLSRKM with point collocation scheme uses quadratic polynomials as bases.

The suggested hybrid method has some advantages. First, the system matrix of the hybrid method is sparse almost same as that of FEM, if most of analysis domain can remain as finite element and meshfree region is well defined and specific. Second, adaptive approach is easy for meshfree region. In many cases, meshfree region may be a high-error area, because a region which is difficult to analyze is selected as meshfree region. Third, point collocation scheme is used for FMLSRKM, which makes applying boundary condition easy. Forth, the region of FMLSRKM has less error, since FMLSRKM of this paper has quadratic shape function.

### 3. Test and Result

Tests are performed using 1-, 2-, and 3-dimensional models with

$$\nabla^2 \phi = -1. \quad (3.1)$$

1D test model is shown in Figure 3(a). In this figure, a domain for FMLSRKM  $\Omega_{FM}$  is inside FEM domain  $\Omega_{FEM}$ , and their interfacial area  $\Omega_{IN}$  is surrounded by  $\Gamma_{FEM}$  and  $\Gamma_{FM}$ . At the ends, Dirichlet boundary conditions are applied as  $\phi = 0$ . In this test problem all boundaries are in FEM region. It is also possible that FMLSRKM region has boundaries, and applying boundary condition into FMLSRKM is even easier because FMLSRKM of this paper uses collocation scheme.

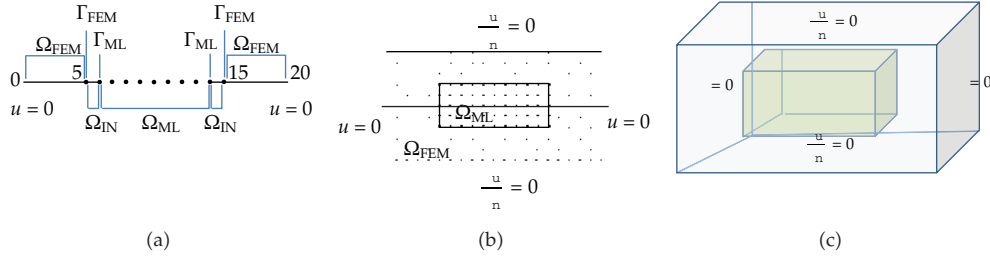


**Figure 3:** Test problems. In these problems, numbers, variables, and solutions are unitless. (a) 1D, (b) 2D. The solid line along  $y = 5$  is the cross-sectional line for error evaluation, and (c) 3D.

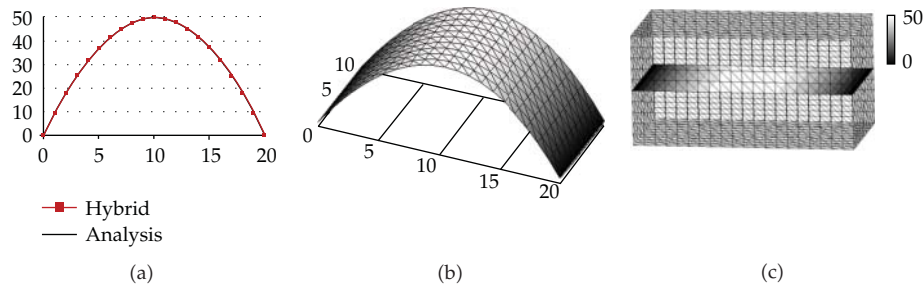


**Figure 4:** The results of the hybrid method. (a), (b), and (c) are the results of Figures 3(a), 3(b), and 3(c), respectively.

In Figures 3(b) and 3(c), test problems in 2D and 3D are shown, respectively. In these problems, domains for FMLSRKM are in the middle of the whole domains, and their boundary conditions are applied as shown in Figures 3(b) and 3(c), respectively. Hence, it is expected that the solutions of Figures 3(a), 3(b), and 3(c) are the same. Furthermore, these problems have analytic solution as

$$\phi = -\frac{1}{2}x^2 + 10x, \quad (3.2)$$

which can be compared to approximated solutions. The results of the hybrid method for Figures 3(a), 3(b), and 3(c) are shown in Figures 4(a), 4(b), and 4(c), respectively. All solutions are well approximated.

#### 4. Error Study

In this paper, error was evaluated using various intervals of nodes, or  $h$ . For evaluation of errors, the solid line along  $y = 5$  of Figure 3(b) is used. An error is defined as a difference between the exact solution and an approximated solution by the hybrid method. In Figure 4(a), it seems that the hybrid method generates the same result as the exact solution (3.2). However, actual error is not zero as shown in Figure 5. FEM region has higher error than FMLSRKM region because FEM uses 1st-order polynomials as shape functions while FMLSRKM uses 2nd-order ones. In FMLSRKM region, the error is nearly zero because 2nd-order FMLSRKM can describe (2.2) which is 2nd-order polynomials.

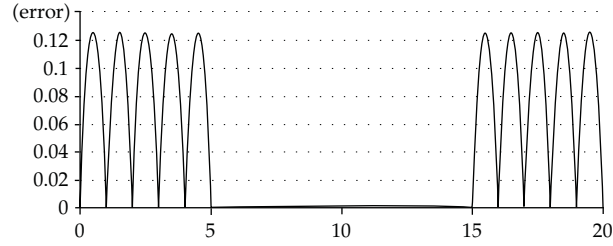


**Figure 5:** The error of approximation by the hybrid method. The error of FEM is higher than that of FMLSRKM because of the orders of bases for two methods.

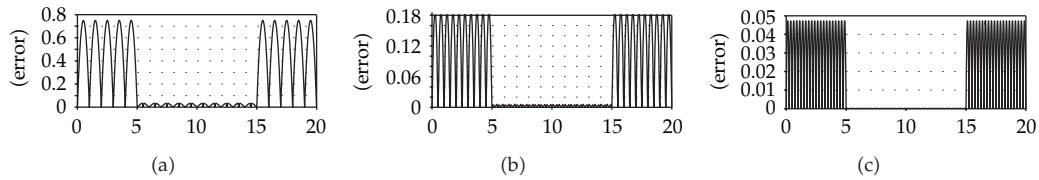


**Figure 6:** Errors of the hybrid method along  $y = 5$  of Figure 3(b). (a)  $h = 1$ , (b)  $h = 0.5$ , and (c)  $h = 0.25$ . The values of  $y$ -axis are absolute errors which decrease according to the size of  $h$ .

To investigate the error of FMLSRKM region, inhomogeneous forcing term should be applied. So,

$$\nabla^2 \phi = -0.6x, \quad (4.1)$$

is considered and the boundary conditions are the same as the previous example. In this case,

$$\phi = -0.1x^3 + 40x, \quad (4.2)$$

is the exact solution of (2.3). For this study, defining  $h$  as the interval of nodes,  $h = 1$ ,  $h = 0.5$ , and  $h = 0.25$  are used. The case of  $h = 1$  is as in Figure 3(b), and Figure 6(a) represents its absolute error which is evaluated along  $y = 5$ . In FMLSRKM region, the error at the middle of each interval is zero, while the error is not zero but the maximum in FEM region. Figure 7 explains the reason, and this phenomenon is caused by quadratic approximation of FMLSRKM. As shown in Figure 7(a), linear approximation of FEM is not capable of following the cubic solution and produces maximum error at the middle. On the other hand, because the quadratic approximation of FMLSRKM and the exact solution are the same at the two nodes ( $x = 7$  and  $8$  for Figure 7(b)), the quadratic approximation crosses the exact solution, which makes the error zero at the middle. For the cases of  $h = 0.5$  and  $0.25$ , the absolute errors are shown in Figures 6(b) and 6(c). The errors become smaller as the nodes become closer to next nodes. From Figure 6, tendency of relative errors is shown in Figure 8. Axes are drawn in logarithmic scale, and Figure 8 shows that the hybrid method has good characteristic of convergence.



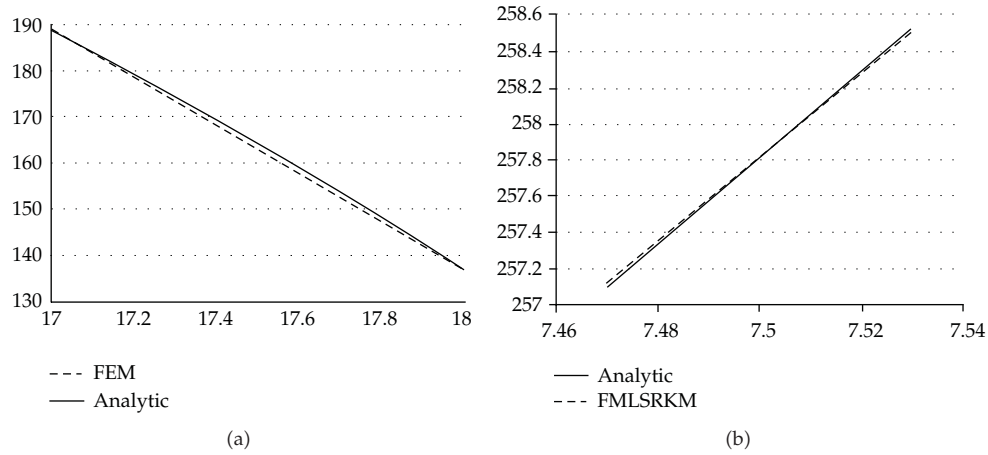


**Figure 7:** Examples of FEM and FMLSRKM. (a) Linear approximation of FEM shows maximum difference at the middle of the interval, and (b) Quadratic approximation of FMLSRKM crosses the exact solution.

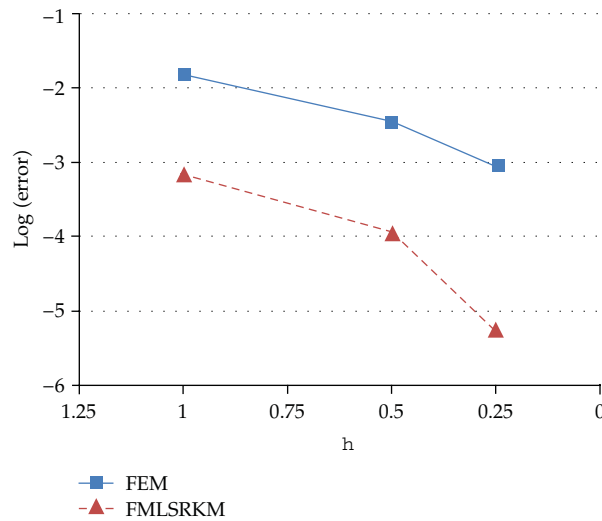


**Figure 8:** Relative error of FEM and FMLSRKM according to the interval of nodes.

## 5. EEG Forward Problem

Governing equation and boundary condition of EEG forward problem are

$$\begin{aligned} \nabla \cdot (\sigma \nabla V) &= \nabla \cdot \mathbf{J}_p \quad \text{in } \Omega, \\ \mathbf{n} \cdot \sigma \nabla V &= 0 \quad \text{on } \partial\Omega, \end{aligned} \quad (5.1)$$

where  $\sigma$ ,  $V$ ,  $\mathbf{J}_p$ , and  $\mathbf{n}$  are electric conductivity, potential, and primary current dipole, and unit vector normal to boundary, respectively. Test model and result are shown in Figure 9. Simple spherical head model as shown in Figure 9(a) is used, and a current dipole is in FMLSRKM

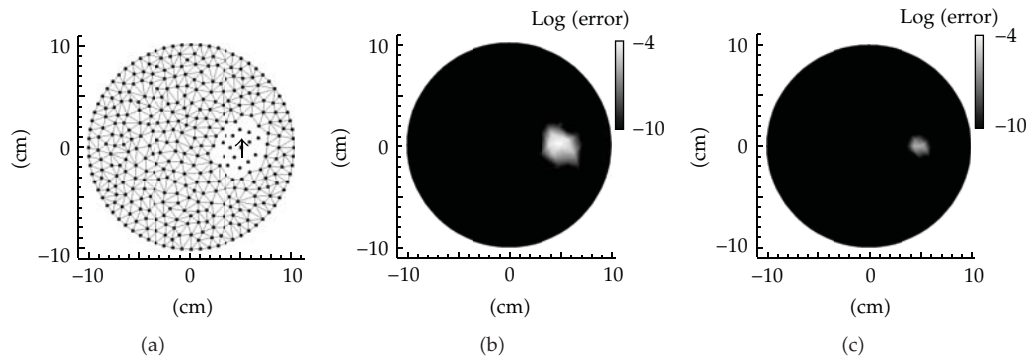


**Figure 9:** Test for EEG forward problem. (a) A dipole shown as an arrow is in the middle of FMLSRKM region, (b) result using FEM, and (c) result using the suggested hybrid method.

region. Because divergence of primary current of (5.1) can be represented as combination of one source and one sink [9], a node at dipole location should be divided into 2 nodes. In Figures 9(b) and 9(c), brighter region has larger error. Those figures show that the hybrid method can approximate the forward solution better than FEM.

## 6. Conclusion

A hybrid method of FMLSRKM and FEM is suggested in this paper, and it shows good result of 1-, 2-, and 3-dimensional boundary value problems. In addition, error of the hybrid method is studied, and proposed method shows good convergence in 2-dimensional model. In Figure 8, relative errors in amplitude are compared between FEM and FMLSRKM. From this figure, we want to say not that FMLSRKM is better method than FEM but that the hybrid method does not lose own error characteristic of each method.

We also tested the hybrid method for EEG forward problem and verified that the method can produce small-error solution. Actually, it is possible to reduce error of solution by *hp*-FEM [24]. However, adaptive strategy can be more adequate for meshfree methods than FEM, because new nodes are just placed on regions which have high error without generating new mesh structures [10, 19]. Hence, error estimation and adaptive scheme will be applied onto the proposed method.

This research shows that Poisson and Laplace equations were successfully handled by the suggested hybrid method. Therefore, realistic problems can be treated such as moving objects and singular points, and it is expected that the hybrid method will take its own role for problems with special conditions as well as EEG forward problem.

## Acknowledgment

This study was supported by a grant from the Korea Healthcare Technology R and D Project, Ministry for Health, Welfare and Family Affairs, Republic of Korea (A090794).

## References

- [1] H. Hallez, B. Vanrumste, R. Grech et al., "Review on solving the forward problem in EEG source analysis," *Journal of NeuroEngineering and Rehabilitation*, vol. 4, no. 1, article 46, 2007.

- [2] A. M. Dale and M. I. Sereno, "Improved localization of cortical activity by combining EEG and MEG with MRI cortical surface reconstruction: a linear approach," *Journal of Cognitive Neuroscience*, vol. 5, no. 2, pp. 162–176, 1993.
- [3] S. Baillet, J. C. Mosher, and R. M. Leahy, "Electromagnetic brain mapping," *IEEE Signal Processing Magazine*, vol. 18, no. 6, pp. 14–30, 2001.
- [4] D. Purves, "Principles of cognitive neuroscience," *Sinauer Associates*, vol. 83, no. 3, 757 pages, 2008.
- [5] C. H. Im, C. Lee, K. O. An, H. K. Jung, K. Y. Jung, and S. Y. Lee, "Precise estimation of brain electrical sources using anatomically constrained area source (ACAS) localization," *IEEE Transactions on Magnetics*, vol. 43, no. 4, pp. 1713–1716, 2007.
- [6] Z. Zhang, "A fast method to compute surface potentials generated by dipoles within multilayer anisotropic spheres," *Physics in Medicine and Biology*, vol. 40, no. 3, article 01, pp. 335–349, 1995.
- [7] J. C. Mosher, R. M. Leahy, and P. S. Lewis, "EEG and MEG: forward solutions for inverse methods," *IEEE Transactions on Biomedical Engineering*, vol. 46, no. 3, pp. 245–259, 1999.
- [8] C. H. Im, C. Lee, H. K. Jung, Y. H. Lee, and S. Kuriki, "Magnetoencephalography cortical source imaging using spherical mapping," *IEEE Transactions on Magnetics*, vol. 41, no. 5, pp. 1984–1987, 2005.
- [9] K. A. Awada, D. R. Jackson, J. T. Williams, D. R. Wilton, S. B. Baumann, and A. C. Papanicolaou, "Computational aspects of finite element modeling in EEG source localization," *IEEE Transactions on Biomedical Engineering*, vol. 44, no. 8, pp. 736–752, 1997.
- [10] C. Lee, C.-H. Im, H.-K. Jung, H.-K. Kim, and D. W. Kim, "A posteriori error estimation and adaptive node refinement for fast moving least square reproducing kernel (FMLSRLK) method," *Computer Modeling in Engineering & Sciences*, vol. 20, no. 1, pp. 35–41, 2007.
- [11] T. Belytschko, Y. Y. Lu, and L. Gu, "Crack propagation by element-free Galerkin methods," *Engineering Fracture Mechanics*, vol. 51, no. 2, pp. 295–315, 1995.
- [12] T. Rabczuk, R. Gracie, J.-H. Song, and T. Belytschko, "Immersed particle method for fluid-structure interaction," *International Journal for Numerical Methods in Engineering*, vol. 81, no. 1, pp. 48–71, 2010.
- [13] T. J. Barth and M. Field, *Meshfree Methods for Partial Differential Equations II*, Springer, 2003.
- [14] B. N. Rao and S. Rahman, "A coupled meshless-finite element method for fracture analysis of cracks," *International Journal of Pressure Vessels and Piping*, vol. 78, no. 9, pp. 647–657, 2001.
- [15] T. Rabczuk, S. P. Xiao, and M. Sauer, "Coupling of mesh-free methods with finite elements: basic concepts and test results," *Communications in Numerical Methods in Engineering*, vol. 22, no. 10, pp. 1031–1065, 2006.
- [16] D. W. Kim and H. K. Kim, "Point collocation method based on the FMLSRLK approximation for electromagnetic field analysis," *IEEE Transactions on Magnetics*, vol. 40, no. 2, pp. 1029–1032, 2004.
- [17] D. W. Kim and Y. Kim, "Point collocation methods using the fast moving least-square reproducing kernel approximation," *International Journal for Numerical Methods in Engineering*, vol. 56, no. 10, pp. 1445–1464, 2003.
- [18] C. Lee, D. W. Kim, S. H. Park, H. K. Kim, C. H. Im, and H. K. Jung, "Point collocation mesh-free method using FMLSRLK for solving axisymmetric Laplace equation," *IEEE Transactions on Magnetics*, vol. 44, no. 6, Article ID 4526930, pp. 1234–1237, 2008.
- [19] T. Belytschko, Y. Y. Lu, and L. Gu, "Element-free Galerkin methods," *International Journal for Numerical Methods in Engineering*, vol. 37, no. 2, pp. 229–256, 1994.
- [20] W.-K. Liu, S. Li, and T. Belytschko, "Moving least-square reproducing kernel methods. I. Methodology and convergence," *Computer Methods in Applied Mechanics and Engineering*, vol. 143, no. 1-2, pp. 113–154, 1997.
- [21] R. A. Gingold and J. J. Monaghan, "Smoothed particle hydrodynamics: theory and application to non-spherical stars," *Monthly Notices of the Royal Astronomical Society*, vol. 181, no. 2, pp. 375–389, 1977.
- [22] W. L. Nicomedes, R. C. Mesquita, and F. J. S. Moreira, "A meshless local Petrov-Galerkin method for three-dimensional scalar problems," *IEEE Transactions on Magnetics*, vol. 47, no. 5, pp. 1214–1217, 2011.
- [23] V. P. Nguyen, T. Rabczuk, S. Bordas, and M. Duflo, "Meshless methods: a review and computer implementation aspects," *Mathematics and Computers in Simulation*, vol. 79, no. 3, pp. 763–813, 2008.
- [24] R. Han, J. Liang, X. Qu et al., "A source reconstruction algorithm based on adaptive hp-FEM for bioluminescence tomography," *Optics Express*, vol. 17, no. 17, pp. 14481–14494, 2009.

## Research Article

# Phase- and GVF-Based Level Set Segmentation of Ultrasonic Breast Tumors

Liang Gao,<sup>1</sup> Xiaoyun Liu,<sup>1</sup> and Wufan Chen<sup>1,2</sup>

<sup>1</sup> School of Automation, University of Electronic Science and Technology of China, Chengdu 611731, China

<sup>2</sup> School of Biomedical Engineering, Southern Medical University, Guangzhou 510515, China

Correspondence should be addressed to Liang Gao, [lianlingjun168@hotmail.com](mailto:lianlingjun168@hotmail.com)

Received 17 September 2011; Revised 8 December 2011; Accepted 9 December 2011

Academic Editor: Kiwoon Kwon

Copyright © 2012 Liang Gao et al. This is an open access article distributed under the Creative Commons Attribution License, which permits unrestricted use, distribution, and reproduction in any medium, provided the original work is properly cited.

Automatically extracting breast tumor boundaries in ultrasound images is a difficult task due to the speckle noise, the low image contrast, the variance in shapes, and the local changes of image intensity. In this paper, an improved edge-based active contour model in a variational level set formulation is proposed for semi-automatically capturing ultrasonic breast tumor boundaries. First, we apply the phase asymmetry approach to enhance the edges, and then we define a new edge stopping function, which can increase the robustness to the intensity inhomogeneities. To extend the capture range of the method and provide good convergence to boundary concavities, we use the phase information to obtain an improved edge map, which can be used to calculate the gradient vector flow (GVF). Combining the edge stopping term and the improved GVF in the level set framework, the proposed method can robustly cope with noise, and it can extract the low contrast and/or concave boundaries well. Experiments on breast ultrasound images show that the proposed method outperforms the state-of-art methods.

## 1. Introduction

Breast cancer is one of the major causes of death among women [1]. The early detection is necessary and helpful to the diagnosis and treatment of breast cancer [2]. Both X-ray mammography and ultrasonic examination can be used for this purpose. The advantages of ultrasonic examination over mammography are its inexpensive, noninvasive, and cost-effect nature. Segmentation of breast ultrasound (US) images is essential for quantitative measurement of tumor characteristics. Manual segmentation is time consuming and it increases inter- and intraobserver variability. Fully automatic segmentation of US image is still a challenging task for two main reasons [3, 4]. First, US images have speckle noise, low contrast, and local changes of intensity [3]. Second, breast tumors have a great variation of their shapes, sizes and locations [4]. Particularly, when the tumors are malignant, they

generally have acute concave shapes. Therefore, developing a semiautomatic algorithm for segmentation of breast tumor in US images becomes urgent in clinical application.

Active contour models (also called snakes) have been proved to be very useful for image segmentation [5–19]. The desirable advantage of this semiautomatic method lies in its ability to facilitate the segmentation process with *a priori* knowledge and user interaction. Active contour models can be divided into two major classes: parametric [5–10] and geometric [11–19].

Parametric active contour models use parametric equation to explicitly represent the evolving curve. The problems of the traditional parametric active contour model are its limited capture range and its inability to handle concave boundaries. Xu and Prince [6, 7] proposed a gradient vector flow (GVF) field model to increase capture range and encourage convergence to boundary concavities. GVF snake has received a lot of attention in US image segmentation [8–10]. For example, Rodtook and Makhanov [8] developed an improved GVF approach based on the continuous force field analysis. They used the resulting vector field to generate a modified edge map and then used it to calculate a novel gradient-based source term. A comparison is made between their method and the conventional GVF type methods by using the reference segmentation results outlined by expert physicians. In their experiments, they claimed that their method can successfully solve the active contour convergence problem. They also obtained more accurate tumor segmentation result.

Geometric active contour models implicitly represent evolving curve as the zero-level set of a higher dimensional function, called level set function. Commonly, this function is defined by computing the closest distances between pixels and a given closed curve in an image domain. The points that have positive distances are inside the curve, and ones that have negative distances are outside the curve [11]. The curve is evolved using the partial differential equation [14] derived from the energy function. When the evolving curve maintains a steady status, that is, the curve stops evolving, the segmentation result is obtained as the zero-level set of the function. The partial differential equation [14], which sometimes can be derived from the energy function [13], describes a curve smoothing process. When the curve evolution stops, the zero-level set of the energy function refers to the segmentation result. Compared to the parametric models, level set methods can represent contour of complex topology and it can also deal naturally with topological changes by using the evolution of the level set function rather than the parametric curves. These properties lend themselves well in medical image segmentation where the anatomic structures split and merge through the pixels. One can see that this is especially useful when segmenting the breast tumors, which generally have complex and varying shapes. The level set method was first introduced by Osher and Sethian [11] and successfully applied to image segmentation by Malladi et al. [12] and Caselles et al. [13]. Caselles et al. developed the well-known geodesic active contour (GAC) model in [13]. However, in these methods, reinitialization of the level set function to a signed distance function is often required. Re-initialization is performed by periodically solving a partial differential equation, which is a computationally expensive operation. To address this problem, Li et al. [15] presented a variational level set method to eliminate the need for reinitialization by incorporating a penalty term into the energy functional. Unfortunately, this penalty term may cause an undesirable side effect on the level set function in some circumstances, which may affect the numerical accuracy. Recently, Li et al. [16] developed a more general variational level set formulation by incorporating a distance regularization term into the energy functional. Particularly, they investigated a double-well potential related to the distance regularization term to maintain a desired shape of the level set function. Accordingly, the undesirable side effect produced by the penalty term can be

completely avoided. They have demonstrated the capability of segmentation on artificial, natural and real medical images.

Using an additional edge stopping function (ESF) allows the active contour to stop at the edges [11–16]. In these models, ESF is related to a convolution of the intensity image with a Gaussian filter. However, the traditional ESF has at least two disadvantages. The first one is that the ESF is never equal to zero, and boundary leakage may occur, that is, the active contour may cross the object's boundaries. The second one is that the edge detection based on gradient is not appropriate for speckle noise, although it is generally effective for additive noise. In breast US images corrupted by multiplicative noise, using only the gradient information may detect false contours caused by noise, and consequently too many trivial contours may be obtained. An alternative approach to circumvent these problems is to use a stopping term based on the coefficient of variation [17]. This stopping term equals to zero at the edges and accommodates the speckle noise. An important advantage of using this stopping term is the capability of preventing the active contour from crossing the object's boundaries. Alternatively, Chan and Vese [18] proposed a method called C-V model, where their stopping term is based on a particular image segmentation result obtained by Mumford–Shah technique [19] rather than the image gradients. This segmentation model uses the intensity information of different region to minimize the energy function rather than using the edge information. Liu et al. [4] also proposed a model that considers the differences between the actual probability densities of the intensities in different regions and the corresponding estimated probability densities. Their model shows advantages over the C-V model [18] on breast US images with weak boundaries and low contrast.

In this paper, a novel segmentation method of ultrasonic breast tumor is proposed within the level set framework. First, we present a novel ESF, which is independent of the intensity gradient of image, as most of the active contour models do, but instead is related to local phase information obtained by using the phase asymmetry approach. The use of this ESF is more robust than the traditional gradient magnitude-based ESF because local phase is theoretically invariant to intensity magnitude. Subsequently, in order to increase the capture range of the method and its ability to move into acute concave boundaries, the improved gradient vector flow (GVF) field is adopted as external force and it is added to the proposed model. The results show that the proposed method can obtain better segmentation performance in comparison with some state-of-art methods [11, 16].

The rest of this paper is organized as follows. In Section 2, we first describe the traditional level set methods and the distance regularized level set method. Section 3 details the proposed method. Section 4 shows qualitative and quantitative experimental results on clinical breast US images. Section 5 summarizes our work.

## 2. Background

### 2.1. Traditional Level Set Methods

The basic idea of the level set methods is to implicitly represent a closed curve  $C(t)$  at time  $t$  by the zero-level set of function  $\phi$ , that is,

$$C(t) = \{(x, y) \mid \phi(x, y, t) = 0\}, \quad \text{with } \phi(x, y, 0) = C_0, \quad (2.1)$$

where  $C_0$  is the initial curve.

In the level set framework, the general evolution equation of the level set function  $\phi$  is

$$\frac{\partial \phi}{\partial t} + F|\nabla \phi| = 0, \quad (2.2)$$

where  $F$  is the speed function. For image segmentation,  $F$  is the external force which is dependent on some image information, such as image gradient and image intensity. This external force  $F$  attracts the curves toward the edges.  $F$  is commonly defined as follows:

$$F = F_{\text{image}} + F_{\text{geometry}}. \quad (2.3)$$

The first term  $F_{\text{image}}$  is the image force generated from image information. The second term  $F_{\text{geometry}}$  is the geometry force to smooth the curve.

## 2.2. Distance Regularized Level Set Method

In most of the traditional level set methods, reinitialization is used as a numerical remedy for keeping sound curve evolution and guaranteeing reliable results. The main problem with this procedure is its high computational cost. To avoid this problem, Li et al. [15] proposed a level set method without reinitialization by integrating a penalty term into the energy functional. However, this penalty term leads to undesirable side effect. More recently, by adding a distance regularization term into energy functional, Li et al. [16] presented a novel distance regularized level set evolution method, that is, DRLSE model. This model can not only completely eliminate the need for reinitialization but also avoid the undesirable side effect.

Let  $\Omega \subset \mathbb{R}^2$  be a bounded Lipschitz image domain. The energy functional  $E(\cdot)$  is written as

$$E(\phi) = \mu R_p(\phi) + E_{\text{ext}}(\phi), \quad (2.4)$$

where  $\phi$  is a level set function,  $\mu > 0$  is a constant, and  $R_p(\phi)$  is the distance regularization term defined by

$$R_p(\phi) = \int_{\Omega} p(|\nabla \phi|) dx, \quad (2.5)$$

where  $p$  is the potential function for  $R_p(\phi)$  [16], that is,

$$p(s) = \begin{cases} \frac{1}{(2\pi)^2} (1 - \cos(2\pi s)) & \text{if } s \leq 1, \\ \frac{1}{2} (s - 1)^2 & \text{if } s \geq 1. \end{cases} \quad (2.6)$$



In (2.4),  $E_{\text{ext}}(\phi)$  is the external energy, which is borrowed from the GAC model [13], that is,

$$E_{\text{ext}}(\phi) = \lambda L_g(\phi) + \alpha A_g(\phi) = \lambda \int_{\Omega} g \delta(\phi) |\nabla \phi| dx + \alpha \int_{\Omega} g H(-\phi) dx, \quad (2.7)$$

where  $\lambda$  and  $\alpha$  are constants,  $L_g(\phi)$  is the length of the interface,  $A_g(\phi)$  is the area of the region that the zero-level curve encloses,  $\delta(\cdot)$  is the Dirac delta function, and  $H(\cdot)$  is the Heaviside function.  $g$  is an ESF such that  $\lim_{t \rightarrow \infty} g(t) = 0$ ,

$$g = \frac{1}{1 + |\nabla G_{\sigma} * I|^2}, \quad (2.8)$$

where  $G_{\sigma}$  is a Gaussian function with the standard deviation  $\sigma$ ,  $I$  is a given 2D image, symbol  $*$  represents convolution,  $\nabla$  is the gradient operator, and  $|\cdot|$  is the modulus of the smoothed image gradients.

As can be seen, the level set function  $\phi$  will stop moving when  $g$  approaches zero. In other words, the resulting final contour will halt at where the image gray gradient is large enough to make  $g \rightarrow 0$ . A small value of  $\sigma$  may make the proposed method sensitive to noise, and the evolution will not be stable. On the other hand, a large value of  $\sigma$  may lead to boundary leakage, and the extracted boundary may not be accurate. The choice of  $\sigma$  is a dilemma, especially when the images have speckle noise and weak boundaries. This property makes the traditional ESF in (2.8) inappropriate for US images.

The associated Euler-Lagrange equations, obtained by minimizing function equation (2.4) with respect to  $\phi$ , is

$$\begin{aligned} \frac{\partial \phi}{\partial t} &= \mu \operatorname{div}(d_p(|\nabla \phi|) \nabla \phi) + \lambda \delta(\phi) \operatorname{div}\left(g \frac{\nabla \phi}{|\nabla \phi|}\right) + \alpha g \delta_{\varepsilon}(\phi), \\ \phi(x, y, 0) &= \phi_0(x, y), \end{aligned} \quad (2.9)$$

where  $\operatorname{div}(\cdot)$  is the divergence operator and  $d_p$  is a function given by

$$d_p(s) = \frac{p'(s)}{s}, \quad (2.10)$$

that satisfies  $|d_p(s)| < 1$ , for all  $s \in (0, \infty)$  and  $\lim_{s \rightarrow 0} d_p(s) = \lim_{s \rightarrow \infty} d_p(s) = 1$ .

In (2.9), the initial level set function  $\phi_0$  being a binary step function is given by

$$\phi_0(x, y) = \begin{cases} -d & \text{if } (x, y) \in \Omega_0, \\ d, & \text{otherwise,} \end{cases} \quad (2.11)$$

where  $d > 0$  is a constant and  $\Omega_0$  is a subset in the image domain  $\Omega$ .



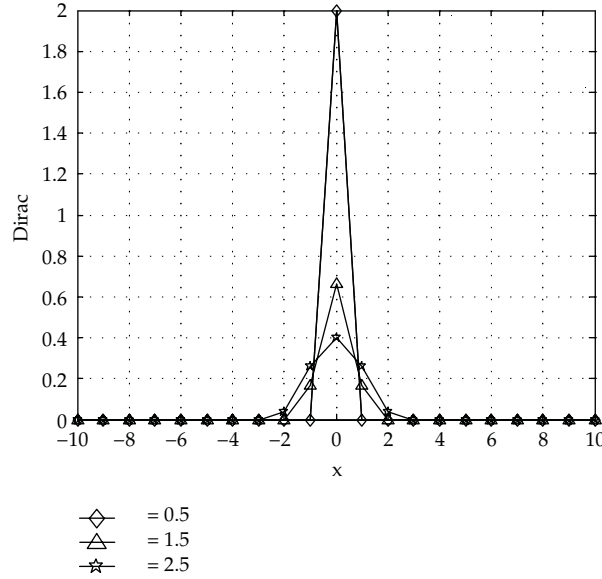


Figure 1: The Dirac function with different epsilon values.

In practice, the Dirac delta function  $\delta(\cdot)$  in (2.9) is replaced by the following function  $\delta_\varepsilon(\cdot)$ :

$$\delta_\varepsilon(x) = \begin{cases} \frac{1}{2\varepsilon} \left( 1 + \cos \frac{\pi x}{\varepsilon} \right), & |x| \leq \varepsilon, \\ 0, & |x| > \varepsilon, \end{cases} \quad (2.12)$$

where  $\varepsilon$  is a positive constant. As shown in Figure 1, if  $\varepsilon$  is too small, the values of  $\delta_\varepsilon(\cdot)$  are prone to approximately zero to make its effective range small, hence the energy functional can be easily trapped into a local minimum. On the contrary, if  $\varepsilon$  is large, the final contour location may be inaccurate, even if  $\delta_\varepsilon(\cdot)$  tends to achieve a global minimum. For all experiments in this paper, the parameter  $\varepsilon$  is set to 1.5.

### 3. Proposed Method

The goal of our method is to extract a breast tumor from a given US image. This method consists of three stages: ESF definition, improved GVF construction, and model generation. Figure 2 shows the block diagram of the proposed method. In the first stage, we first apply phase asymmetry approach to enhance the image edges and then define a novel phase-based ESF. At the second stage, we generate an edge map and use it to compute the GVF. At the last stage, we construct the model first by using a phase-based ESF and then by incorporating the improved GVF.



Figure 2: Block diagram of the proposed method for breast tumor segmentation.

### 3.1. Design of the ESF

The sine and cosine functions with specific amplitudes (energies) can represent any discrete signal. In the time domain, these functions cause a set of scaled waves, synthesizing the original signal. Morrone and Owens [20] gave a general definition of how to describe and detect signal features using the phase of the Fourier components.

Kovesi [21] proposed a low-level feature detector, named phase congruency model [20], in terms of the Fourier analysis. The phase congruency model is based on the assumption that features are perceived at points in an image where the Fourier components are maximally in phase, rather than assume a feature is a point of maximal intensity gradient. In other words, the phase of the sinusoidal components varies and a low phase congruency is achieved at all other nonfeature points. In practical applications, the local frequency, particularly, the phase information, is estimated via a bank of Cauchy filter tuned to various spatial frequencies (scales) rather than Log-Gabor filter. The main reason for this is that Log-Gabor filters are likely not a good choice in the event of feature detection [22, 23].

The measure of phase congruency provides inaccurate localization, noise sensitivity, and high computational cost. Motivated by the properties of the phase congruency, Kovesi considered that symmetries and asymmetries cause special phase patterns in the values of the image intensity [21]. At symmetric points, all Fourier series should have either maximum or minimum value. Kovesi proposed a modified measure to detect symmetry and asymmetry. The symmetric measure is

$$PS[n] = \frac{\sum_s [A_s[n] [|\cos(\phi_s[n])| - |\sin(\phi_s[n])|] - T_s]}{\sum_s A_s[n] + \varepsilon} = \frac{\sum_s [||\text{even}_s[n]| - |\text{odd}_s[n]|] - T_s]}{\sum_s A_s[n] + \varepsilon}, \quad (3.1)$$

and the asymmetric one is

$$PA[n] = \frac{\sum_s [||\text{odd}_s[n]| - |\text{even}_s[n]|] - T_s]}{\sum_s A_s[n] + \varepsilon}, \quad (3.2)$$

where  $\text{even}_s$  and  $\text{odd}_s$  are the responses of the even-symmetric (cosine) and odd-symmetric (sine) filters at scale  $s$ . At a point of symmetry, the absolute value of  $\text{even}_s$  is large while that of  $\text{odd}_s$  is small. At a point of asymmetry, the opposite is true.  $A_s[n]$  represents the magnitude of the responses of each quadrature pair of filters at a given scale  $s$  and point  $n$  in the image, that is,  $A_s[n] = \sqrt{(\text{odd}_s[n])^2 + (\text{even}_s[n])^2}$ . Symbol  $[\cdot]$  denotes zeroing of negative values,  $\varepsilon$  is a positive constant to avoid division by zero, and  $T_s$  is the scale specific noise threshold.

Extension to two-dimensional (2D) images uses the 1D analysis over several orientations and then combines the results to offer a single measure of the feature significance [24]. For a given breast US image, we first convolve a breast US image with a bank of Cauchy kernel filter in order to calculate the 2D phase asymmetry. In this paper, we yield

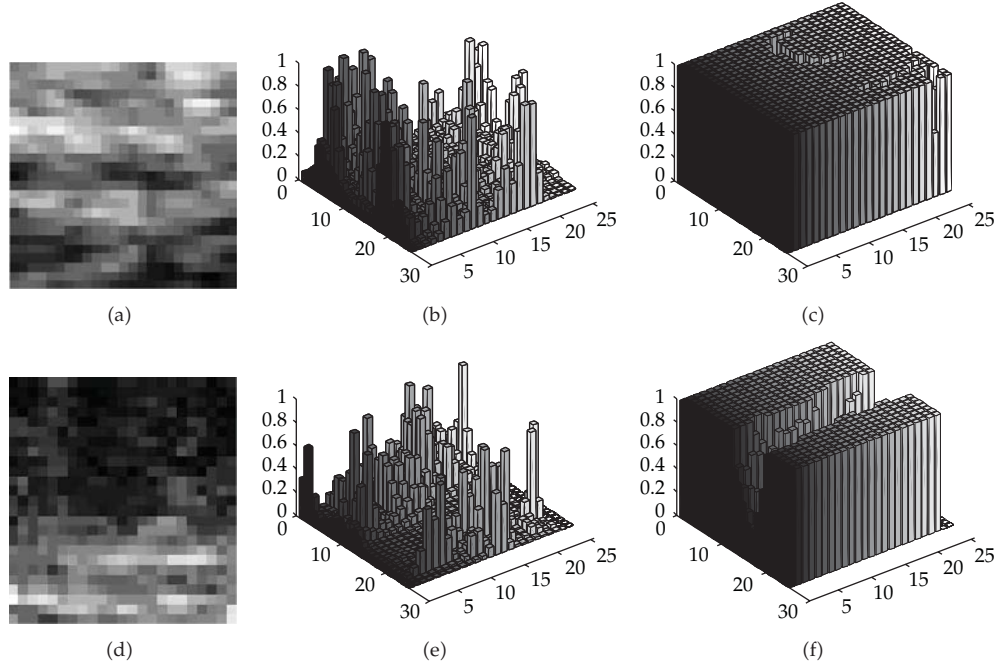


**Figure 3:** Comparison between gradient-based ESF and phase-based ESF of the US image. (a) Speckled homogeneous image; (b) and (c) are the gradient-based ESF and phase-based ESF of (a); (d) Speckled image with contour; (e) and (f) are the gradient-based ESF and phase-based ESF of (d).

the asymmetric measures over six orientations and four/five scales at each pixel. The values of  $PA$  range from 0 to 1, close to one in homogeneous region and close to zero in the vicinity of boundaries. Clearly,  $PA$  is a dimensionless quantity.

Based on the analysis mentioned above, one can see that  $PA \in [0, 1]$  is the feature asymmetry measure defined by (3.2) and can offer a better control on the edge detection quality. The main difference between this edge detection and the traditional edge detections is that it is invariant to the changes in image intensity or contrast. According to our knowledge of the breast US images, they are often intensity inhomogeneous and have high amounts of speckle noise. Thus, we apply  $PA$  to define ESF with sufficient robustness and accuracy in this paper. Since ESF is also an inverse edge indicator function, an appropriate definition of ESF is given by

$$g = \frac{1}{1 + (PA)^\alpha}, \quad (3.3)$$

where  $\alpha \in [0, 1]$  is a hyperparameter. The  $g$  takes values in  $[0, 1]$ , close to zero in the vicinity of boundaries and close to one in homogeneous regions. Particular advantage of this ESF over the gradient-based ESF (e.g., (2.8)) is its insensitivity to intensity inhomogeneity and speckle noise. Figure 3 illustrates this statement.

As can be seen from Figure 3, two situations are described. The first case, where there exists a single homogeneous region, is shown in Figure 3(a), and the second case, where two distinct homogeneous regions are separated by a sharp edge, is shown in Figure 3(d).

The gradient-based ESF and phase-based ESF are calculated on these two speckled images. Figures 3(b) and 3(e) show that the variance of the gradient-based ESF increases with the intensity in homogeneous regions. The multiplicative nature of speckle noise leads to this expected behavior. In contrast, the phase-based ESF has more homogeneous values, as shown in Figures 3(c) and 3(f). Consequently, the detected edges obtained using the phase-based ESF are better than those obtained using the gradient-based one. The very low values of ESF easily make curve stop at spurious edges which are caused by the speckle noise. Aiming at precise segmentation of US images, our proposed model prefers to use the phase-based ESF than the conventional gradient-based one.

### 3.2. Improved GVF Construction

Xu and Prince [6, 7] introduced the GVF as a bidirectional external force to capture the object's boundary from either sides and to deal with concave boundary. The construction of the GVF can be divided into two stages: the generation of edge map  $f$  from the image and the computation of the GVF from the edge map  $f$ . Clearly, the quality of edge map  $f$  is a crucial factor in the construction of GVF field. A classical choice is defined as

$$f = |\nabla G_\sigma * I|^2. \quad (3.4)$$

An obvious problem with this edge map is that the traditional GVF could be attracted to strong edges which are caused by noises in an inhomogeneous region with high gray values.

In order to eliminate this shortcoming, we define an edge map as

$$f(x, y) = g(x, y), \quad (3.5)$$

where  $g$  is given in (3.3).

The GVF field is defined by the vector field

$$V_{\text{GVF}}(x, y) = (u(x, y), v(x, y)), \quad (3.6)$$

that minimizes the following objective function [6, 7]:

$$E_{\text{GVF}}(u, v) = \frac{1}{2} \iint h_1(|\nabla f|) (u_x^2 + u_y^2 + v_x^2 + v_y^2) + h_2(|\nabla f|) |(u, v) - \nabla f|^2 dx dy, \quad (3.7)$$

where  $u_x, u_y, v_x, v_y$  are the first derivatives of the vector field,  $h_1(\cdot)$  and  $h_2(\cdot)$  are the weight functions depending on the gradient of the edge map  $\nabla f$ , and they are defined as

$$\begin{aligned} h_1(|\nabla f|) &= \exp\left(-\left(\frac{|\nabla f|}{K}\right)\right), \\ h_2(|\nabla f|) &= 1 - h_1(|\nabla f|), \end{aligned} \quad (3.8)$$

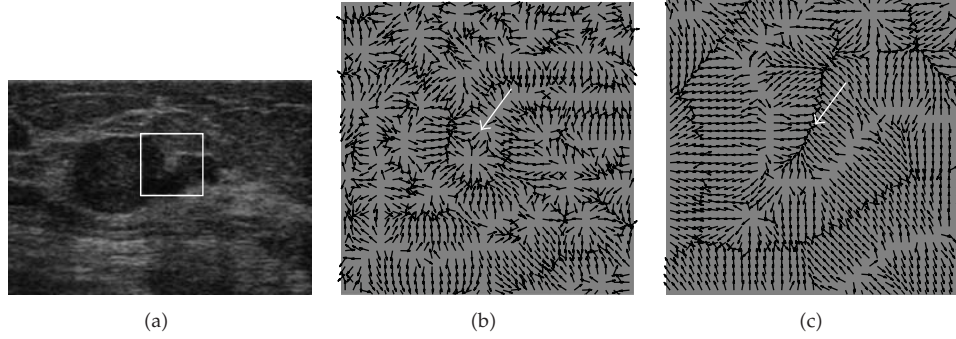


**Figure 4:** Comparison between original GVF field (Niter = 10) and improved GVF (Niter = 10) of the breast US image. (b) and (c) are zoomed-in views of the original GVF and improved GVF in square window marked in (a). As shown by the arrows, more gradient vectors in the improved GVF field point to the true boundaries.

where  $K$  is a nonnegative parameter which is used to control the smoothness of the resulting vector field  $V_{\text{GGVF}}$ .  $h_1(\cdot)$  and  $h_2(\cdot)$  should be monotonically decreasing and increasing functions of  $|\nabla f|$ , respectively.

The force vector field  $V_{\text{GGVF}}(x, y)$  can be solved from the following Euler equations:

$$\begin{aligned} h_1 \nabla^2 u - h_2 (u - f_x) &= 0, \\ h_1 \nabla^2 v - h_2 (v - f_y) &= 0, \end{aligned} \quad (3.9)$$

where  $f_x$  and  $f_y$  are the derivatives of  $f$  with respect to  $x$  and  $y$ .

For an example of breast US image, Figures 4(b) and 4(c) show the detailed original GVF field and improved GVF field of the window marked in Figure 4(a). It can be seen that more gradient vectors point to the true boundary obviously in the improved GVF field, with compared to the original GVF field.

The major difference between the traditional GVF and the improved GVF is that the former edge map is dependent on gradient magnitude while the latter is dependent on phase congruency. The advantage of the latter over the former is that it makes use of the phase information in the cure convolution and, thus, achieves better edge detection results for objects with intensity inhomogeneities or speckle noise.

### 3.3. Model Generation

Although most of the traditional level set methods require reinitialization, Li's method [16] does not require reinitialization and provides stable level set evolution. Therefore, based on the model in (2.9) presented by Li et al. [16], we propose an improved edge-based level set model in this paper. The main difference of the proposed model from the DRLSE model in (2.9) is that it uses the phased-based ESF previously constructed and simultaneously integrates the improved GVF.

The proposed model yields a level set evolution, called phase- and GVF-based level set evolution (PGBLSE). The PGBLSE model can be described by the following differential equations:

$$\frac{\partial \phi}{\partial t} = \mu \operatorname{div}(d_p(|\nabla \phi|) \nabla \phi) + ag\delta_\varepsilon(\phi) + \lambda\delta_\varepsilon(\phi) \operatorname{div}\left(g \frac{\nabla \phi}{|\nabla \phi|} \cdot [\hat{u}, \hat{v}]\right), \quad (3.10)$$

where  $\mu > 0$ ,  $a \in R$ ,  $\lambda \in R$  are the constants as the weights of the distance regularization term, the area term, and the length term,  $d_p(\cdot)$  is a function defined in (2.10),  $\delta_\varepsilon(\cdot)$  is the Dirac delta function in (2.12),  $g$  is the ESF defined in (3.3),  $\phi$  is the level set function,  $t$  represents time variable,  $\operatorname{div}(\cdot)$  is the divergence operator, and  $\nabla$  is the gradient operator.  $[\hat{u}, \hat{v}]$  is the normalized GVF field where  $\hat{u} = u/\sqrt{u^2 + v^2}$  and  $\hat{v} = v/\sqrt{u^2 + v^2}$ . The field normalization is responsible for obviating the dependency on the absolute value of the image intensity and providing sufficient information to guide the curve evolution.

Now assuming that  $\nabla \phi$  is negative inside the zero-level set and positive outside, the inward normal vector to the curve can be expressed as  $N = -\nabla \phi/|\nabla \phi|$ . The curve motion (shrinkage/expansion) is governed by the two vectors. This curve is expanded if the curve's normal aligns with the normalized GVF, or it is shrunk if the curve's normal and the normalized GVF are in the opposite directions and is not deformed if the curve's normal is orthogonal to the normalized GVF. Obviously, this flow increases the shrinking and expanding capability of curve evolution. This property is useful in concave boundaries.

## 4. Results and Discussions

### 4.1. Data Acquisition

This work was approved by Shanghai Sixth People's Hospital in China. Our method was developed using MATLAB and evaluated using 20 US images of breast tumors. Among these images, 10 were malignant tumors and 10 were benign tumors. The patients' ages are in the range from 18 and 75 years old. The images were collected by using three kinds of scanners with the linear transducers (7–14 MHz). The ultrasonic subimage of region of interest (ROI) was chosen by an expert radiologist. This area only was then used for image segmentation. An example of an extracted ROI subimage is illustrated in Figure 5.

### 4.2. Quantitative Measure

To evaluate the accuracy of the segmentation algorithms, we compared them with the gold standard, which was manually produced by an experienced radiologist. In addition to the golden standard segmentation, an error measure is required for evaluating object segmentation algorithms. Measures can be divided into region-based measures and boundary-based ones.

Region-based error measures are made by comparing the regions inside the contours. The overlapping area error [4] is represented by the three parameters including true positive

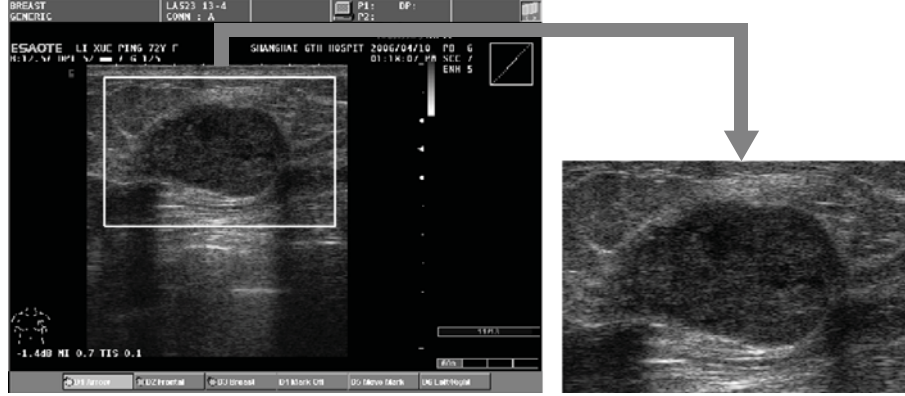


**Figure 5:** On the left is an US image captured from the sonographic scanner having a malignant tumor. On the right is the ROI subimage.

(TP), false positive (FP), and Jaccard similarity (JS). For a given image, let  $S_a$  and  $S_m$  be the obtained segmentation and golden standard, respectively. These three metrics are defined as

$$\begin{aligned} TP &= \frac{|S_m \cap S_a|}{|S_m|}, \\ FP &= \frac{|S_m \cup S_a - S_m|}{|S_m|}, \\ JS &= \frac{|S_m \cap S_a|}{|S_m \cup S_a|}, \end{aligned} \quad (4.1)$$

where  $\cup$  is the set union operator,  $\cap$  is the set intersection operator, and  $|\cdot|$  represents the number of pixels in the corresponding pixel set. The higher the TP value is, the more actual tumor regions the segmented tumor regions cover. The lower the FP value is, the fewer normal tissue regions the segmented tumor regions cover. The JS value ranges from 0 to 1. The closer the JS value is to 1, the better the segmentation is.

The Dice similarity coefficient [25] has also been widely used for comparing existing methods:

$$DSC = \frac{2JS}{1 + JS} = \frac{2|S_m \cap S_a|}{|S_m| + |S_a|}. \quad (4.2)$$

The closer the value of DSC is to 1, the better the segmentation is.

Boundary-based error measures evaluate segmentations based on the distance between two contours. The boundary error is defined as the average or max distance between two contours. We denote the golden standard boundary by  $A = \{a_1, \dots, a_m\}$  and the obtained boundary as  $B = \{b_1, \dots, b_n\}$ , where each element of  $A$  or  $B$  is a point on the corresponding



contour. For every point  $a_i$  on boundary  $A$ , a distance to boundary  $B$ , denoted as  $MD(a_i, B)$ , can be defined as the minimum distance of point  $a_i$  to all points in  $B$ :

$$MD(a_i, B) = \min_{j \in \{1, \dots, n\}} \|a_i - b_j\|, \quad (4.3)$$

where  $\|\cdot\|$  denotes the Euclidean distance.

The average minimum Euclidean distance (AMED) [26] is the average distance between two contours:

$$AMED(A, B) = \frac{\sum_{i=1}^m MD(a_i, B)}{2m} + \frac{\sum_{j=1}^n MD(b_j, A)}{2n}. \quad (4.4)$$

The Hausdorff distance (HD) [26], on the other hand, measures the max distance between two contours:

$$HD(A, B) = \max \left\{ \max_{i \in \{1, \dots, m\}} MD(a_i, B), \max_{j \in \{1, \dots, n\}} MD(b_j, A) \right\}. \quad (4.5)$$

For a perfect segmentation, the distances HD and AMED are equal to zero.

### 4.3. Comparison with Previous Methods

We compare our method, PGBLSE model (3.10), with two edge-based active contour models: GAC model [11] and DRLSE model [16]. The level set evolution in GAC model is

$$\frac{\partial \phi}{\partial t} = g |\nabla \phi| \operatorname{div} \left( \frac{\nabla \phi}{|\nabla \phi|} \right) + ag |\nabla \phi| + \nabla g \cdot \nabla \phi, \quad (4.6)$$

where  $a$  is a constant, which plays the similar role as in the PGBLSE model (3.10) and  $g$  is the ESF defined by (2.8).

The same initial contours are used in these methods. We use the following default setting of the parameters in our method:  $\mu = 0.2$ ,  $a = -1.1$ ,  $\lambda = 0.2$ . The parameters  $\alpha$  and  $s$  are not set to the same values in all experiments. If we have to detect tumors of weak boundaries or concave shapes, then parameters  $\alpha$  and  $s$  should be small. Conversely, if we have to detect tumors of strong boundaries and regular shapes, then parameters  $\alpha$  and  $s$  should be large. For the GAC and DRLSE models, we tuned the parameters for the best segmentation results for all images. Experiments 1–5 illustrate the comparison results on five US images of breast tumors.

Experiment 1 applies these three models to an US image which contains a malignant breast tumor with obvious intensity inhomogeneity and highly concave boundary as shown in Figure 6(a). The golden standard image was shown in Figure 6(b). The results obtained with the GAC [11], DRLSE [16], and the proposed PGBLSE models are illustrated in Figures 6(c), 6(d) and 6(e), respectively. The GAC model fails in concave region since there is no force that can pull the contour towards the concave portion of the tumor boundary. Although the DRLSE model produces a smoother contour, it also fails in a similar fashion. Obviously,



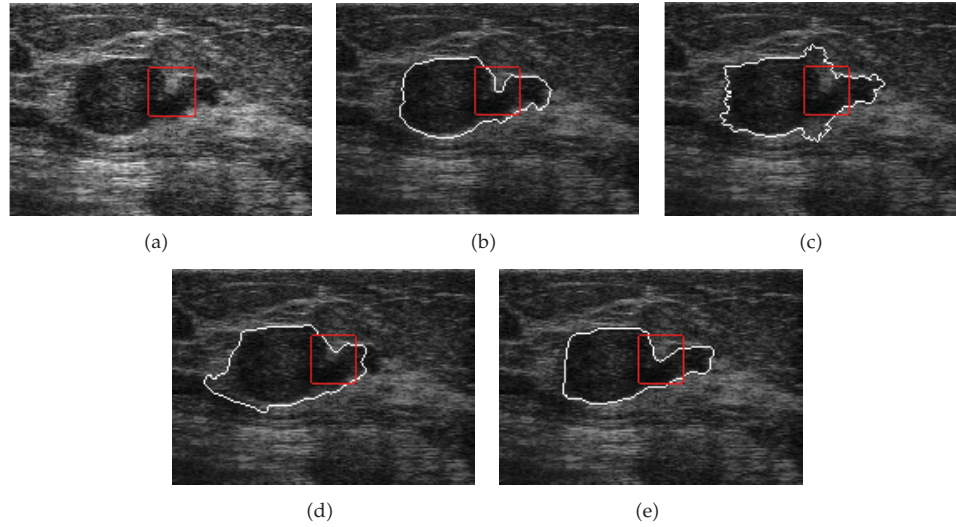


**Figure 6:** Segmentation of a malignant breast tumor with intensity inhomogeneity and highly concave boundary. (a) Original image. (b) Golden standard. Segmentation results of (c) GAC [11], (d) DRLSE [16], and (e) the proposed PGBLSE models.

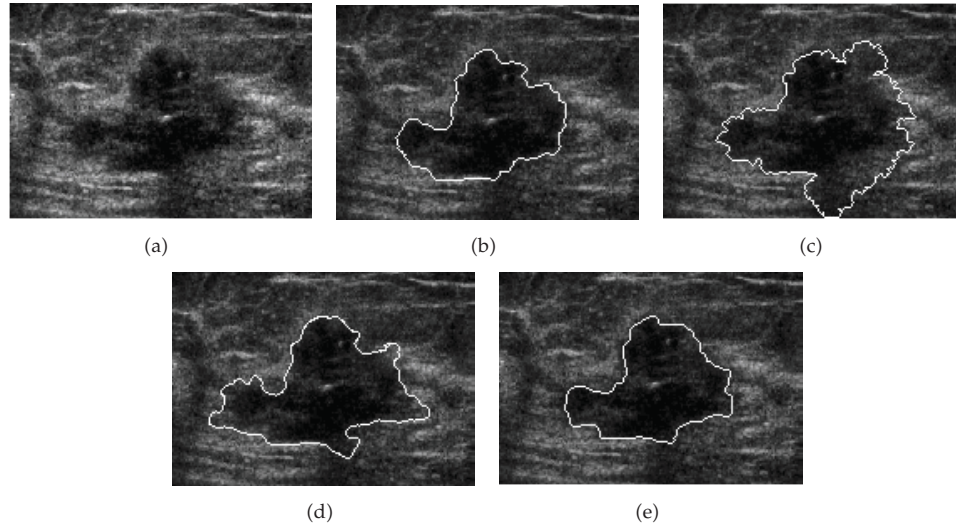


**Figure 7:** Segmentation of a malignant breast tumor having intensity inhomogeneity and weak boundaries. (a) Original image. (b) Golden standard. Segmentation results of (c) GAC [11], (d) DRLSE [16], and (e) the proposed PGBLSE models.

without gradient diffusion, the ability to capture concave boundary is limited. With the help of diffusion process, the proposed PGBLS method ( $\alpha = 0.1$ ,  $s = 4$ ) successfully extracts the concave part of the tumor. In addition, gradient diffusion is capable of removing the boundary effect of weak edges. This is the reason why some parts of the contours from the GAC and DRLSE models leak past weak boundary gradients while the PGBLSE model does not. This also supports the efficiency of the improved GVF.

In experiment 2, these three models are applied to an US image of the malignant tumor in Figure 7(a). This image is extremely challenging for edge-based active contour methods

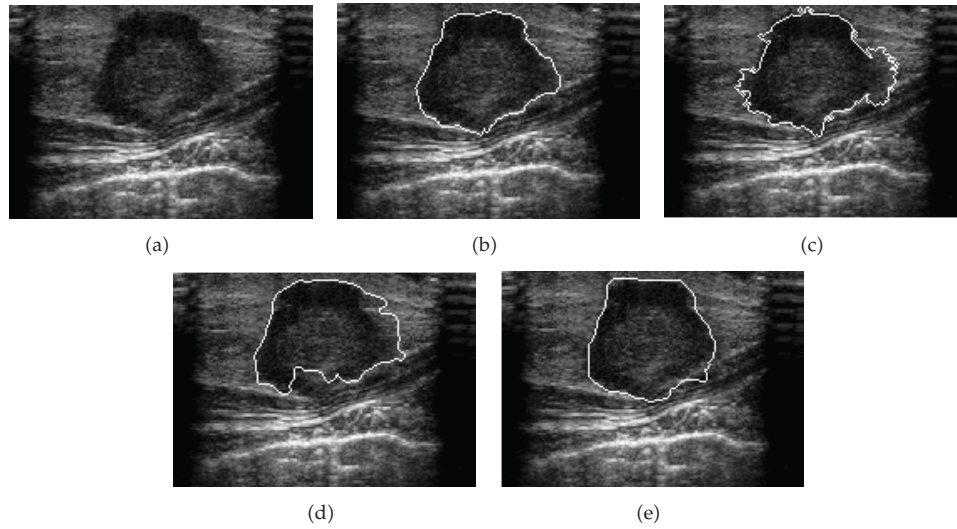


**Figure 8:** Segmentation of a malignant breast tumor intensity inhomogeneity and low contrast. (a) Original image. (b) Golden standard. Segmentation results of (c) GAC [11], (d) DRLSE [16], and (e) the proposed PGBLSE models.

since it contains a complex-shaped tumor. Besides, the boundaries between the tumor region and the surrounding normal tissue region are very weak, and the contrast is also low. The results of the GAC model [11], DRLSE model [16], and the proposed method are illustrated in Figures 7(c), 7(d), and 7(e), respectively. The GAC and DRLSE models capture the entire tumor when parts of the normal tissues are also identified as tumor. Since tumor region is surrounded by normal tissue regions with similar intensities and has local changes of intensity, the gradient-based stopping terms of GAC and DRLSE models are heavily affected and can be easily trapped into unsuitable local minima. In contrast, the proposed PGBLSE model ( $\alpha = 0.1$ ,  $s = 4$ ) uses a novel phase-based edge term; therefore, it can handle intensity inhomogeneity well. In addition, due to the efficiency of the improved GVF mentioned before (the ability to converge the concave boundaries is increased with sufficient gradient diffusion), the PGBLSE model can prevent the leakage through weak edges and extract the concave boundaries of tumor.

In experiment 3, Figure 8 illustrates the results using the GAC [11], DRLSE [16], and PGBLSE models in the segmentation of malignant breast tumor in an US image. The GAC model fails to segment the tumor in that the surrounding normal tissues of the tumor are included as shown in Figure 8(c). It is also difficult to use the DRLSE model to successfully extract the tumor; Figure 8(d) illustrates that some parts of the contour leak past weak boundary gradients while other parts are confined inside the tumor. The PGBLSE model ( $\alpha = 0.5$ ,  $s = 5$ ) separates the real tumor from normal tissue regions, as illustrated in Figure 8(e). That is, a successful segmentation is obtained.

Experiment 4 applies these three methods on an US image of a benign breast tumor, as shown in Figure 9(a). It can be seen that the tumor image has gradually changing intensity and the boundaries between the tumor region and its surrounding normal tissue are very weak. The GAC model cannot deal with weak boundary, and the resulting contour leaks at where there are relatively weak boundary gradients, as depicted in Figure 9(c). The DRLSE model also cannot handle weak boundaries well, and the contour leaks into the surrounding

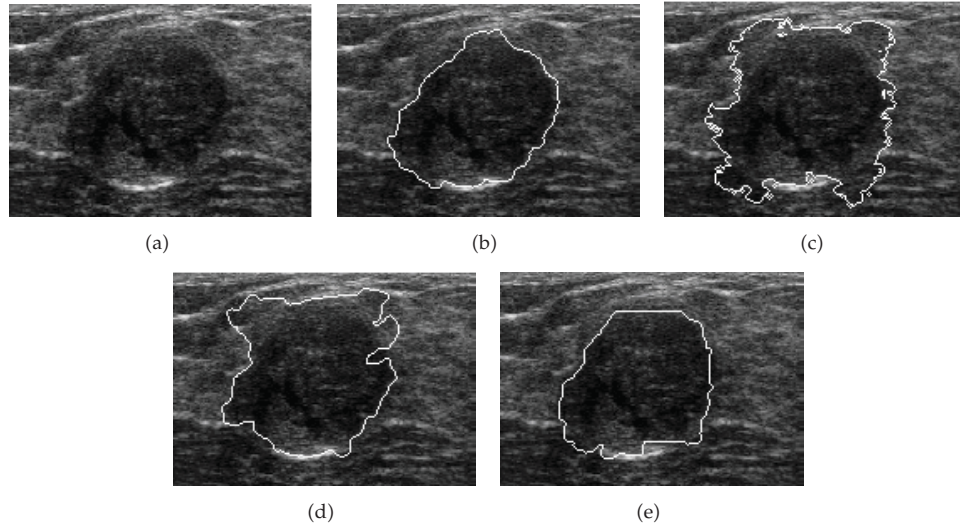


**Figure 9:** Segmentation of a benign breast tumor having low contrast and weak boundaries. (a) Original image. (b) Golden standard. Segmentation results of (c) GAC [11], (d) DRLSE [16], and (e) the proposed PGBLSE models.

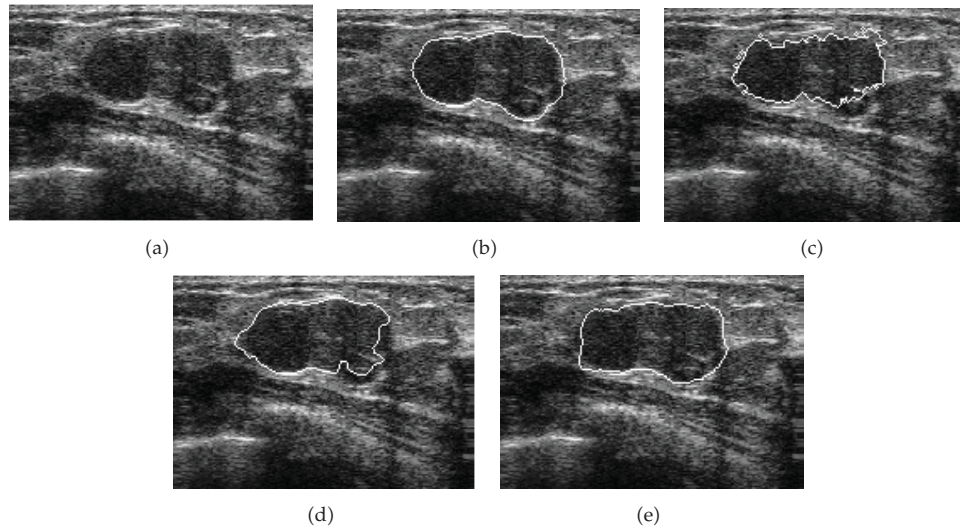


**Figure 10:** Segmentation of a benign breast tumor with low contrast and high speckle noise. (a) Original image. (b) Golden standard. Segmentation results of (c) GAC [11], (d) DRLSE [16], and (e) the proposed PGBLSE models.

normal tissues, as shown in Figure 9(d). In contrast, the proposed model ( $\alpha = 0.1$ ,  $s = 4$ ) uses the edge map based on phase information to calculate the gradients, which helps to prevent the contour from leaking into normal tissues. Therefore, the proposed model is more immune to leaking effect and the generated tumor contour is very close to the golden standard, as shown in Figure 9(e).

Experiment 5 illustrates the application of the proposed method to a relatively smooth benign breast tumor as shown in Figure 10(a). We analyze the GAC and DRLSE models. The



US image suffers from speckle noise. The classical GAC model cannot yield smooth contour even for the round shape, as shown in Figure 10(c). In addition, the GAC contour is confined inside by small clusters of noise with large intensity magnitudes. Even though the DRLSE model generates smoother contour, the resulting contour is still confined inside the tumor region as illustrated in Figure 10(d). On the contrary, Figure 10(e) shows that the proposed PGBLSE model ( $\alpha = 0.5$ ,  $s = 5$ ) is the most accurate among these three methods.

Clearly, the GAC and DRLSE models are sensitive to the noise which seriously affects the gradient-based stopping terms. Therefore, these two models yield many comparatively strong gradients throughout the whole image including the homogeneous regions, which distracts the evolution contours from the real boundaries. This problem can be solved by using the phase-based stopping term because this term is theoretically intensity invariant.

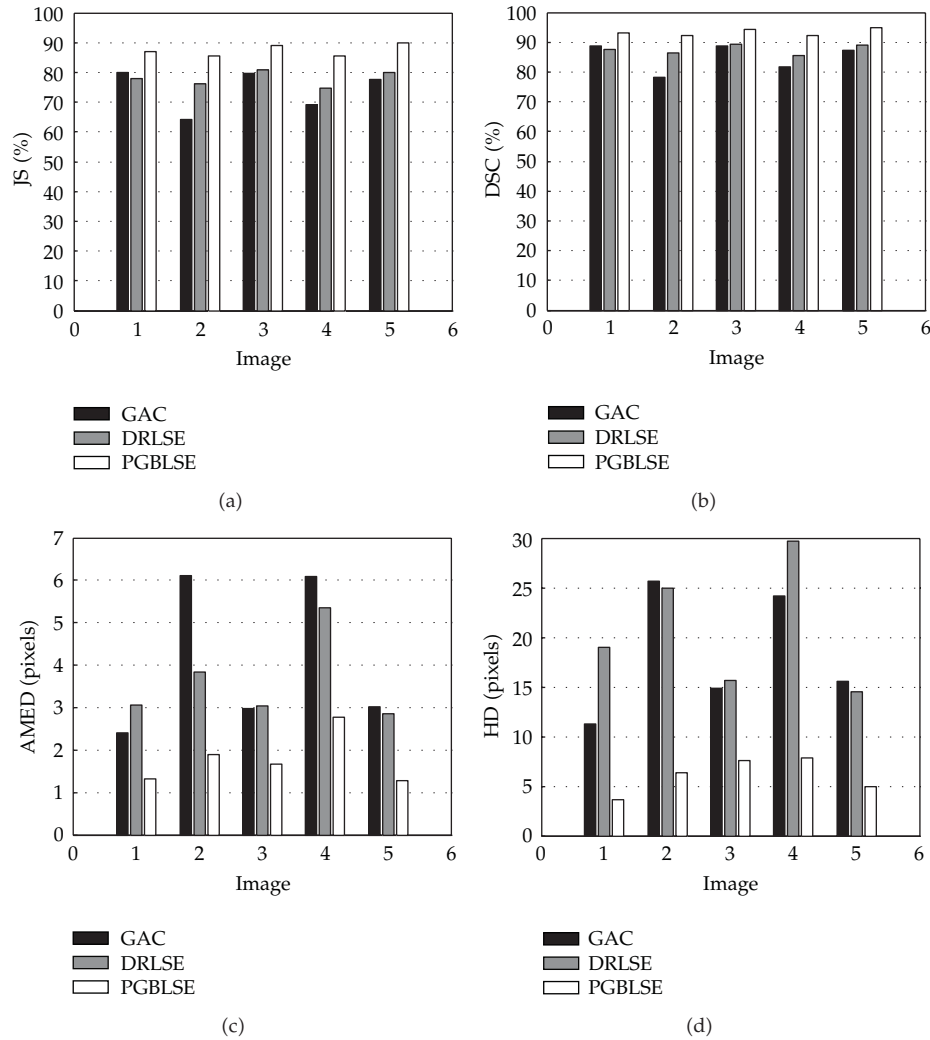
Experiments 1–5 illustrate the comparison results on five US images of breast tumors in comparison with the GAC model [11], the DRLSE model [16], and the golden standard. The results suggest that the tumor contours extracted from our proposed PGBLSE model are better than those from the other two models [11, 16], and they are very close to the golden standard. This conclusion is also supported by the details shown in Figure 11.

Figure 11 shows that the proposed PGBLSE model obtains better accuracy than the GAC and DRLSE models in terms of the JS and DSC measures. Moreover, the PGBLSE model is superior to the GAC and DRLSE models in terms of the AMED and HD measures. Particularly, the PGBLSE model is almost 2 times better than the GAC model in terms of the HD measure.

Figures 6–10 demonstrate that the proposed model is the most accurate comparing with the other models in the study. Finally, we evaluated our approach on the dataset of 20 US images of breast tumors. For these studied images, Figure 12 shows six box plot graphics using the TP, FP, JS, DSC, AMED, and HD measures for the three segmentation models.

From Figure 12(a), a phenomenon is observed that the GAC model and the DRLSE model performed slightly better than the proposed PGBLSE model in terms of the TP measure. This advantage has been visualized in the box plot showing the large median values of the TP. However, their segmentation results are not accurate, and the higher values of FP also imply this. As shown in Figure 12(b), the median FP values of the GAC and DRLSE models are very high (17.74% and 19.74%, resp.). On the contrary, the proposed PGBLSE model obtains a much lower median value of FP (4.19%), which demonstrates that there are fewer normal tissue regions mistakenly included in tumor regions and thus the segmentation is more reliable. Like the cases in Figures 7 and 9, although the GAC and DRLSE models approximately include the entire real tumor regions, they simultaneously cover a lot of unsatisfied normal tissue regions. Figure 12(c) illustrates that the median values of JS for these models are, respectively, 79.73%, 80.08%, and 86.30%. It is observed that the proposed PGBLSE model presents the best median value, while the GAC and DRLSE models have lower median values, which suggests worst segmentation performance. The GAC model (from 81.63% to 85.1%) and the DRLSE model (from 81.51% to 85.95%) have the upper quartile in a lower position when compared to the position of the same quartile of the proposed PGBLSE model (from 87.74% to 90.04%), which suggests a lower performance of the GAC and DRLSE models. This is also verified by the DSC measure (Figure 12(d)).

As can be seen from Figure 12(f), the median value of HD for our PGBLSE model is around 7 pixels, whereas the median values for the GAC and DRLSE models are all above 16 pixels. High HD value means high disagreement between the segmented contour and the golden standard. Besides, it is observed that our model offers a smaller dispersion range while the GAC and DRLSE models provide large dispersion ranges. Although the median



**Figure 11:** Bar plots of segmentation errors among the GAC, DRLSE, and PGBLSE models. (a) JS error. (b) DSC error. (c) AMES error. (d) HD error. The  $x$ -axis represents five images in Figures 6(a)–10(a) in the same order.

values of AD for the three models are not very different from each other, the GAC and DRLSE models have more outliers and larger dispersion range of values as illustrated in Figure 12(e).

As can be seen from Figure 13, the results are then assessed on 20 clinical US images of breast tumors using the tumor areas that tumor contour enclosed. They are displayed in Bland-Altman [27] plots. The  $x$ -axis is golden standard area and the  $y$ -axis represents the tumor area difference between the three segmentation models and golden standard. For the 20 breast US images, using the GAC and DRLSE models, 95% of the point pairs (19 images) are with  $\pm 2SD$  (95% confidence intervals). Using the proposed PGBLSE model, 100% of the point pairs (20 images) are with  $\pm 2SD$  (100% confidence intervals). The mean differences are 568, 369, and  $-202.4$  pixels for the GAC, DRLSE, and proposed PGBLSE models, respectively.

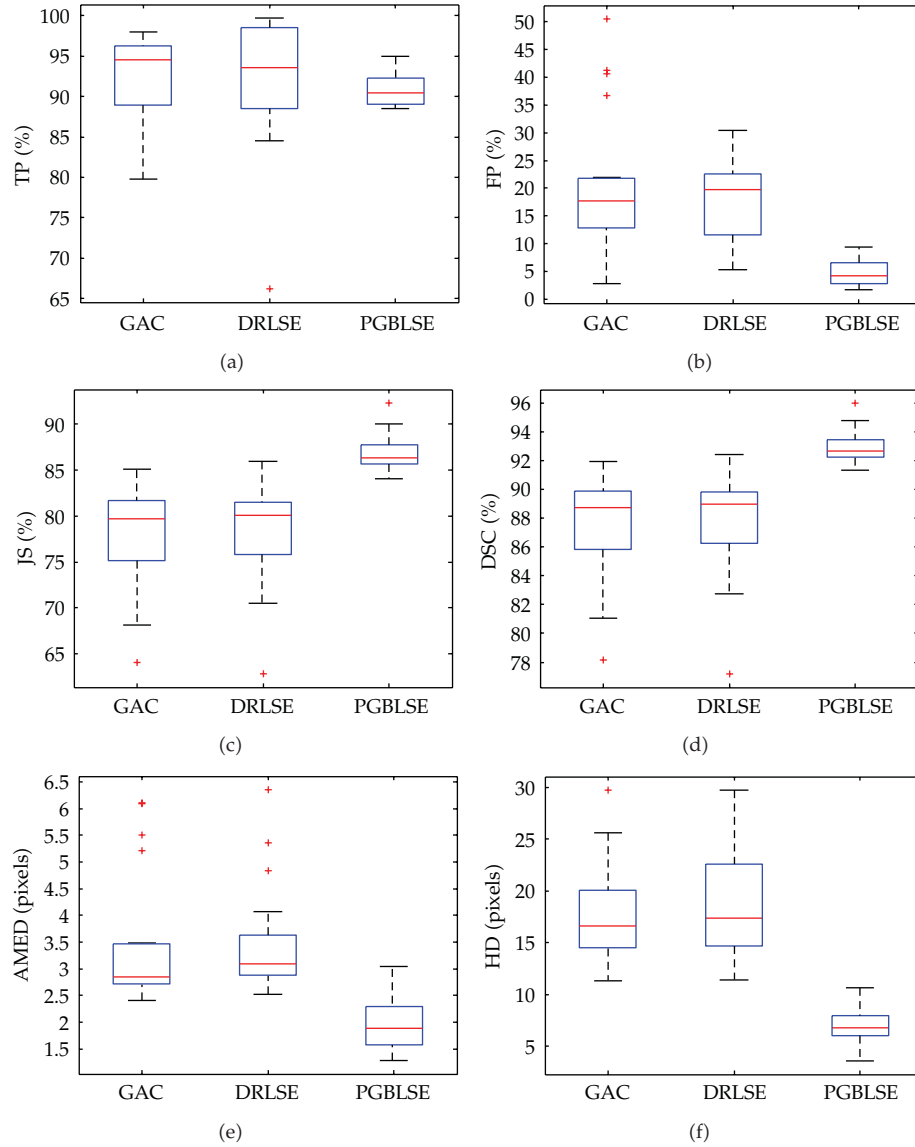


**Figure 12:** Box plots of segmentation errors among the GAC, DRLSE, and PGBLSE models on 20 clinical US images of breast tumors. (a)TP, (b) FP, (c) JS, (d) DSC, (e) AMED, and (f) HD.

The goal of this particular experiment is twofold. On the one hand, we demonstrate that tumor areas of the GAC and DRLSE models are larger than those of the proposed PGBLSE model, and, therefore, large values of TP are obtained. On the other hand, some nontumor regions are also incorrectly covered by the GAC and DRLSE models, and, therefore, large values of FP are achieved.

In our experiments, all figures (i.e., Figures 6–13) show, among the three models, that the best agreement is between the proposed PGBLSE model and the golden standard.

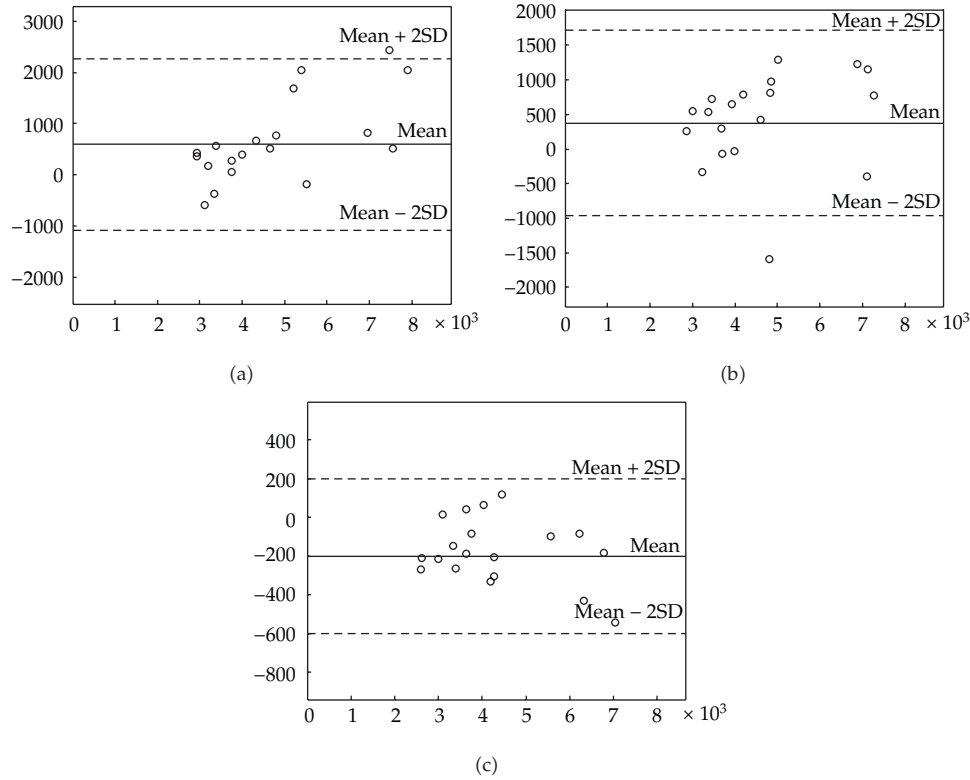


**Figure 13:** Bland-Altman plots for the comparison of the tumor areas on clinical US images of breast tumors, assessed by three segmentation models and by the golden standard: (a) GAC [11], (b) DRLSE [16], and (c) the proposed PGBLSE models.

## 5. Conclusions

We have presented in this paper a new approach for the segmentation of the ultrasonic breast tumors. For the first time, phase asymmetry approach, which can enhance the boundaries, is used to segment the ultrasonic breast tumors. In a level set framework, we integrate the use of a novel ESF and the improved GVF, both constructed using the output of phase asymmetry. This model shows significant improvements, particularly, in robustness against the speckle noise, as well as in handling intensity inhomogeneities and capturing concave boundaries.

The performance of the proposed PGBLSE model is demonstrated on clinical US images of breast tumors. Qualitative and quantitative results show that the PGBLSE model outperforms the classical intensity-based GAC and DRLSE models. The further work will focus on developing a hybrid level set active contour model by investigating the addition of a region-based term, in order to improve the performance of the method.

## Acknowledgment

This work was supported by National Basic Research Program of China, the 973 Program (Grant no. 2010CB732501).

## References

- [1] B. Liu, H. D. Cheng, J. Huang, J. Tian, X. Tang, and J. Liu, "Fully automatic and segmentation-robust classification of breast tumors based on local texture analysis of ultrasound images," *Pattern Recognition*, vol. 43, no. 1, pp. 280–298, 2010.
- [2] E. Paci, "Mammography and beyond: developing technologies for the early detection of breast cancer," *Breast Cancer Research*, vol. 4, pp. 123–125, 2002.
- [3] J. A. Noble and D. Boukerroui, "Ultrasound image segmentation: a survey," *IEEE Transactions on Medical Imaging*, vol. 25, no. 8, pp. 987–1010, 2006.
- [4] B. Liu, H. D. Cheng, J. Huang, J. Tian, X. Tang, and J. Liu, "Probability density difference-based active contour for ultrasound image segmentation," *Pattern Recognition*, vol. 43, no. 6, pp. 2028–2042, 2010.
- [5] M. Kass, A. Witkin, and D. Terzopoulos, "Snakes: active contour models," *International Journal of Computer Vision*, vol. 1, no. 4, pp. 321–331, 1988.
- [6] C. Xu and J. L. Prince, "Snakes, shapes, and gradient vector flow," *IEEE Transactions on Image Processing*, vol. 7, no. 3, pp. 359–369, 1998.
- [7] C. Xu and J. L. Prince, "Generalized gradient vector flow external forces for active contours," *Signal Processing*, vol. 71, no. 2, pp. 131–139, 1998.
- [8] A. Rodtook and S. S. Makhanov, "Continuous force field analysis for generalized gradient vector flow field," *Pattern Recognition*, vol. 43, no. 10, pp. 3522–3538, 2010.
- [9] H. Zhou, G. Schaefer, M. E. Celebi, F. Lin, and T. Liu, "Gradient vector flow with mean shift for skin lesion segmentation," *Computerized Medical Imaging and Graphics*, vol. 35, no. 2, pp. 121–127, 2011.
- [10] X. Zhu, P. Zhang, J. Shao, Y. Cheng, Y. Zhang, and J. Bai, "A snake-based method for segmentation of intravascular ultrasound images and its in vivo validation," *Ultrasonics*, vol. 51, no. 2, pp. 181–189, 2011.
- [11] S. Osher and J. A. Sethian, "Fronts propagating with curvature-dependent speed: algorithms based on Hamilton-Jacobi formulations," *Journal of Computational Physics*, vol. 79, no. 1, pp. 12–49, 1988.
- [12] R. Malladi, J. A. Sethian, and B. C. Vemuri, "Shape modeling with front propagation: a level set approach," *IEEE Transactions on Pattern Analysis and Machine Intelligence*, vol. 17, no. 2, pp. 158–175, 1995.
- [13] V. Caselles, R. Kimmel, and G. Sapiro, "Geodesic Active Contours," *International Journal of Computer Vision*, vol. 22, no. 1, pp. 61–79, 1997.
- [14] G. Sapiro, *Geometric Partial Differential Equations and Image Analysis*, chapter 2, Cambridge University Press, Cambridge, UK, 2001.
- [15] C. Li, C. Xu, C. Gui, and M. D. Fox, "Level set evolution without re-initialization: a new variational formulation," in *Proceedings of the IEEE Computer Society Conference on Computer Vision and Pattern Recognition (CVPR '05)*, pp. 430–436, San Diego, Calif, USA, June 2005.
- [16] C. M. Li, C. Xu, C. Gui, and M. D. Fox, "Distance regularized level set evolution and its application to image segmentation," *IEEE Transactions on Image Processing*, vol. 19, no. 12, pp. 3243–3254, 2010.
- [17] M. Mora, C. Tauber, and H. Batatia, "Robust level set for heart cavities detection in ultrasound images," in *Proceedings of the Computers in Cardiology*, pp. 235–238, Lyon, France, September 2005.
- [18] T. F. Chan and L. A. Vese, "Active contours without edges," *IEEE Transactions on Image Processing*, vol. 10, no. 2, pp. 266–277, 2001.
- [19] D. Mumford and J. Shah, "Optimal approximations by piecewise smooth functions and associated variational problems," *Communications on Pure and Applied Mathematics*, vol. 42, no. 5, pp. 577–685, 1989.
- [20] M. C. Morrone and R. A. Owens, "Feature detection from local energy," *Pattern Recognition Letters*, vol. 6, no. 5, pp. 303–313, 1987.
- [21] P. Kovess, "Phase congruency: a low-level image invariant," *Psychological Research*, vol. 64, no. 2, pp. 136–148, 2000.
- [22] D. Boukerroui, J. A. Noble, and M. Brady, "On the choice of band-pass quadrature filters," *Journal of Mathematical Imaging and Vision*, vol. 21, no. 1, pp. 53–80, 2004.
- [23] D. Boukerroui, J. A. Noble, and M. Brady, "Frontiers in robotics research," in *On the Selection of Band-Pass Quadrature Filters*, M. A. Denket, Ed., pp. 67–111, Nova Publishing, New York, NY, USA, 2006.
- [24] K. Rajpoot, J. A. Noble, V. Grau, and N. Rajpoot, "Feature detection from echocardiography images using local phase information," in *Proceedings of 12th Medical Image Understanding and Analysis*, pp. 1–5, Scotland, UK, 2008.



- [25] X. Liu, D. L. Langer, M. A. Haider, Y. Yang, M. N. Wernick, and I. S. Yetik, "Prostate cancer segmentation with simultaneous estimation of Markov random field parameters and class," *IEEE Transactions on Medical Imaging*, vol. 28, no. 6, pp. 906–915, 2009.
- [26] J. Zhang, Y. Wang, and X. Shi, "An improved graph cut segmentation method for cervical lymph nodes on sonograms and its relationship with node's shape assessment," *Computerized Medical Imaging and Graphics*, vol. 33, no. 8, pp. 602–607, 2009.
- [27] X. Xu, Y. Zhou, X. Cheng, E. Song, and G. Li, "Ultrasound intima-mediasegmentation using Hough transform and dual snake model," *Computerized Medical Imaging and Graphics*. In press.

## Research Article

# The Second-Order Born Approximation in Diffuse Optical Tomography

**Kiwoon Kwon**

*Department of Mathematics, Dongguk University, Seoul 100715, Republic of Korea*

Correspondence should be addressed to Kiwoon Kwon, kwkwon@dongguk.edu

Received 21 October 2011; Accepted 8 December 2011

Academic Editor: Chang-Hwan Im

Copyright © 2012 Kiwoon Kwon. This is an open access article distributed under the Creative Commons Attribution License, which permits unrestricted use, distribution, and reproduction in any medium, provided the original work is properly cited.

Diffuse optical tomography is used to find the optical parameters of a turbid medium with infrared red light. The problem is mathematically formulated as a nonlinear problem to find the solution for the diffusion operator mapping the optical coefficients to the photon density distribution on the boundary of the region of interest, which is also represented by the Born expansion with respect to the unperturbed photon densities and perturbed optical coefficients. We suggest a new method of finding the solution by using the second-order Born approximation of the operator. The error analysis for the suggested method based on the second-order Born approximation is presented and compared with the conventional linearized method based on the first-order Born approximation. The suggested method has better convergence order than the linearized method, and this is verified in the numerical implementation.

## 1. Introduction

Diffuse optical tomography involves the reconstruction of the spatially varying optical properties of a turbid medium. It is usually formulated as inverse problem with respect to the forward problem describing photon propagation in the tissue for given optical coefficients [1].

The forward model is described by the photon diffusion equation with the Robin boundary condition. In the frequency domain, it is given by

$$\begin{aligned} -\nabla \cdot (\kappa \nabla \Phi) + \left( \mu_a + \frac{i\omega}{c} \right) \Phi &= q \quad \text{in } \Omega, \\ \Phi + 2a\nu \cdot (\kappa \nabla \Phi) &= 0 \quad \text{on } \partial\Omega, \end{aligned} \tag{1.1}$$

where  $\Omega$  is a Lipschitz domain in  $\mathbb{R}^n$ ,  $n = 2, 3, \dots$ ,  $\partial\Omega$  is its boundary,  $\nu$  is the unit outward normal vector on the boundary,  $\Phi$  is the photon density,  $q$  is a source term,  $a$  is a refraction

parameter, and  $\mu_a$ ,  $\mu'_s$ , and  $\kappa = 1/3(\mu_a + \mu'_s)$  are the absorption, reduced scattering, and diffusion coefficients, respectively. Assume that  $a$  is a constant and  $\kappa$ ,  $\mu_a$ ,  $\mu'_s$  are scalar functions satisfying

$$0 < L \leq \kappa, \mu_a, \mu'_s, a \leq U \quad (1.2)$$

for positive constants  $L$  and  $U$ . The unique determination of the optical coefficients is studied in electrical impedance tomography problem [2–5] and some elliptic problem [6], which is applicable to diffuse optical tomography problem also. Let us denote  $x = (\mu_a, \kappa)$  and  $\Phi = \Phi(x)$  to emphasize the dependence of  $\Phi$  on the optical coefficient  $x$ .

Assuming we know some a priori information  $x_0$  about the structural optical coefficients  $x$  and the perturbation of the optical coefficients  $\delta x = x - x_0$ , the diffuse optical tomography problem is to find the perturbation of the optical coefficients  $\delta x$  from the difference  $\Phi(x + \delta x) - \Phi(x)$  between the perturbed and unperturbed photon density distribution on the boundary  $\partial\Omega$ . The relation between  $\delta x$  and  $\Phi(x + \delta x) - \Phi(x)$  is given by the following Born expansion [7, 8]:

$$\Phi(x + \delta x) - \Phi(x) = \mathcal{R}^1(x, \delta x) + \mathcal{R}^2(x, (\delta x)^2) + \cdots, \quad (1.3)$$

where

$$\begin{aligned} \mathcal{R}^0(x) &= \Phi(x), \\ \mathcal{R}^i((\delta x)^i) &= \mathcal{R}(\delta x, \mathcal{R}^{i-1}((\delta x)^{i-1}, f)), \quad i = 1, 2, \dots, \\ \mathcal{R}(\delta x, f) &= \mathcal{R}_{\mu_a}(\delta x, f) + \mathcal{R}_{\kappa}(\delta x, f), \\ \mathcal{R}_{\mu_a}(\delta x, f) &= \int_{\Omega} \delta \mu_a(\eta) R(\cdot, \eta) f(\eta) d\eta, \\ \mathcal{R}_{\kappa}(\delta x, f) &= \int_{\Omega} \delta \kappa(\eta) \nabla R(\cdot, \eta) \cdot \nabla f(\eta) d\eta, \end{aligned} \quad (1.4)$$

and  $R(\cdot, \eta)$  is the Robin function for a source at  $\eta$ , which is the solution of (1.1) for the optical coefficient  $x$  when  $q$  is the Dirac delta function. By definition of (1.4), the operator  $\mathcal{R}$  and  $\mathcal{R}^1$  are different in the following sense:

$$\mathcal{R}^1(\delta x) = \mathcal{R}(\delta x, \mathcal{R}^0) = \mathcal{R}(\delta x, \Phi). \quad (1.5)$$

Let the perturbation of the coefficients be  $\delta x^\dagger$  when we neglect second-order terms and higher in the Born expansion (1.3). We can then formulate the linearized diffuse optical tomography problem to find  $\delta x^\dagger$  from the following equation, which is the first-order Born approximation:

$$\mathcal{R}^1(\delta x^\dagger) = \Phi(x + \delta x) - \Phi(x). \quad (1.6)$$

This linearized diffuse optical tomography problem is simple to implement and widely used [9, 10].

In this paper, a new method, which is more accurate than the linearized method, will be suggested (1.6), which is based on the second-order Born approximation. And the method is faster than the full nonlinear method [11]. Let the solution of the proposed method in this paper be  $\delta x^B$ , and let  $\delta x$  be sufficiently small. Then, the error for the linearized solution  $\delta x^\dagger$  and the proposed solution  $\delta x^B$  is given by

$$\|\delta x^\dagger - \delta x\|_{\mathcal{A}} \leq C^\dagger \|\delta x\|_{\mathcal{A}}^2, \quad (1.7a)$$

$$\|\delta x^B - \delta x\|_{\mathcal{A}} \leq C^B \|\delta x\|_{\mathcal{A}}^3, \quad (1.7b)$$

where  $\mathcal{A} = L^\infty(\Omega) \times L^\infty(\Omega)$  and  $C^\dagger$  and  $C^B$  are constants which are independent of  $\delta x$ . Hence, the error of the proposed solution  $x^B$  in (1.7b) is of the order  $O(\|\delta x\|_{\mathcal{A}}^3)$ , which is higher than the order of the error of the linearized solution  $x^\dagger$ ,  $O(\|\delta x\|_{\mathcal{A}}^2)$ .

The detailed statement with proof will be proved in Section 2. Numerical algorithm involving the detailed computation of the second-order term is given in Section 3. Numerical implementation of the proposed method and the linearized method is given in Section 4, and the conclusion of the paper is given in Section 5.

## 2. Error Analysis

Instead of solving linearized solution  $\delta x^\dagger$  in (1.6), we suggest the second order solution  $\delta x^B$  satisfying

$$\mathcal{R}^1(\delta x^B) = (\Phi(x + \delta x) - \Phi(x)) - \mathcal{R}^2(\delta x^\dagger)^2, \quad (2.1)$$

or equivalently,

$$\mathcal{R}^1(\delta x^B - \delta x^\dagger) = -\mathcal{R}^2(\delta x^\dagger)^2. \quad (2.2)$$

In this section, we analyze the error for the linearized solution  $\delta x^\dagger$  and the suggested solution  $\delta x^B$ .

Let  $\mathcal{B} = H^1(\Omega)$ ; then, the operator  $\mathcal{R}$  and  $\mathcal{R}^i$ ,  $i = 1, 2, \dots$ , are considered to be the operators from  $\mathcal{A} \times \mathcal{B} \rightarrow \mathcal{B}$  and  $\mathcal{A}^i (= \overbrace{\mathcal{A} \times \dots \times \mathcal{A}}^{i \text{ times}}) \rightarrow \mathcal{B}$ , respectively, by the definition given in (1.4). For the detailed explanation about the definitions of higher-order Fréchet derivative in diffuse optical tomography and its relation to the Born expansion, see [7].

**Proposition 2.1.** *Let  $\Phi$  be the solution of (1.1) for the given optical coefficients  $\mu_a, \kappa$ , source  $q$ , and modulating frequency  $\omega$ . Then one gets the following relation between the operators between  $\mathcal{R}$  and  $\mathcal{R}^i$ ,  $i = 1, 2, \dots$ :*

$$\|\mathcal{R}^i\|_{\mathcal{A}^i \rightarrow \mathcal{B}} \leq \|\mathcal{R}\|_{\mathcal{A} \times \mathcal{B} \rightarrow \mathcal{B}}^i \|\Phi\|_{\mathcal{B}} \quad (2.3)$$

for  $i = 1, 2, \dots$

*Proof.* By the induction argument on  $i = 1, 2, \dots$  and using (1.5), we get the following inequality:

$$\|\mathcal{R}^1\|_{\mathcal{A} \rightarrow \mathcal{B}} \leq \|\mathcal{R}\|_{\mathcal{A} \times \mathcal{B} \rightarrow \mathcal{B}} \|\Phi\|_{\mathcal{B}}, \quad (2.4)$$

which is (2.3) for  $i = 1$ . Suppose that (2.3) holds for  $i = 1, 2, \dots, I - 1$ . Then we obtain

$$\begin{aligned} \|\mathcal{R}^I(\delta x)^I\|_{\mathcal{B}} &\leq \|\mathcal{R}\|_{\mathcal{A} \times \mathcal{B} \rightarrow \mathcal{B}} \|\delta x\|_{\mathcal{A}} \|\mathcal{R}^{I-1}(\delta x)^{I-1}\|_{\mathcal{B}} \\ &\leq \|\mathcal{R}\|_{\mathcal{A} \times \mathcal{B} \rightarrow \mathcal{B}} \|\delta x\|_{\mathcal{A}} \|\mathcal{R}^{I-1}\|_{\mathcal{A}^{I-1}} \|\delta x\|_{\mathcal{A}}^{I-1} \\ &\leq \|\mathcal{R}\|_{\mathcal{A} \times \mathcal{B} \rightarrow \mathcal{B}}^I \|\delta x\|_{\mathcal{A}}^I \|\Phi\|_{\mathcal{B}}. \end{aligned} \quad (2.5)$$

Using (2.5) and the definition of the operator norm  $\|\cdot\|_{\mathcal{A}^I \rightarrow \mathcal{B}}$ , we obtain (2.3) for  $i = I$ . Therefore, by the induction argument, we have proved (2.3) for  $i = 1, 2, \dots$   $\square$

By [7],  $\|\mathcal{R}\|_{\mathcal{A} \times \mathcal{B} \rightarrow \mathcal{B}}$  is bounded, and thus  $\|\mathcal{R}^i\|_{\mathcal{A}^i \rightarrow \mathcal{B}}$ ,  $i = 1, 2, \dots$ , are also bounded by Proposition 2.1. Let us assume that there exists a bounded operator  $(\mathcal{R}^1)^\dagger$  from  $\mathcal{B}$  to  $\mathcal{A}$  such that  $(\mathcal{R}^1)^\dagger(\mathcal{R}^1) = id_{\mathcal{A}}$ .  $(\mathcal{R}^1)^\dagger$  is usually called the left inverse of  $\mathcal{R}^1$ . Let us denote

$$\begin{aligned} \|\delta x\| &:= \|\delta x\|_{\mathcal{A}}, \\ \|\Phi(x)\| &:= \|\Phi(x)\|_{\mathcal{B}}, \\ \|\mathcal{R}\| &:= \|\mathcal{R}\|_{\mathcal{A} \times \mathcal{B} \rightarrow \mathcal{B}}, \\ \|\mathcal{R}^i\| &:= \|\mathcal{R}^i\|_{\mathcal{A}^i \rightarrow \mathcal{B}}, \quad i = 1, 2, \dots, \\ \|(\mathcal{R}^1)^\dagger\| &:= \|(\mathcal{R}^1)^\dagger\|_{\mathcal{B} \rightarrow \mathcal{A}}, \end{aligned} \quad (2.6)$$

for brevity.

Using Proposition 2.1 and the assumption on the left inverse, the main theorem of this paper is given as follows.

**Theorem 2.2.** *Assume that there exists  $(\mathcal{R}^1)^\dagger$  such that  $(\mathcal{R}^1)^\dagger \mathcal{R}^1 = id$  and  $\|(\mathcal{R}^1)^\dagger\|$  is bounded, and let*

$$\|\delta x\| \leq \frac{1}{2\|\mathcal{R}\|}. \quad (2.7a)$$

Then,

$$\|\delta x^\dagger - \delta x\| \leq C^\dagger \|\delta x\|^2, \quad (2.7b)$$

$$\|\delta x^B - \delta x\| \leq C^B \|\delta x\|^3, \quad (2.7c)$$

where

$$\begin{aligned} C^\dagger &:= 2 \left\| \left( \mathcal{R}^1 \right)^\dagger \right\| \|\mathcal{R}\|^2 \|\Phi\|, \\ C^B &:= \frac{(C^\dagger)^3}{4\|\mathcal{R}\|} + (C^\dagger)^2 + \|\mathcal{R}\|C^\dagger = C^\dagger \|\mathcal{R}\| \left( \frac{C^\dagger}{2\|\mathcal{R}\|} + 1 \right)^2. \end{aligned} \quad (2.8)$$

*Proof.* By (1.3) and (1.6), we obtain

$$\mathcal{R}^1(\delta x^\dagger - \delta x) = \mathcal{R}^2(\delta x)^2 + \mathcal{R}^3(\delta x)^3 + \dots. \quad (2.9)$$

Therefore we arrive at (2.7b) by the following inequality:

$$\left\| \delta x^\dagger - \delta x \right\| \leq \left\| \left( \mathcal{R}^1 \right)^\dagger \right\| \frac{(\|\mathcal{R}\| \|\delta x\|)^2 \|\Phi\|}{1 - (\|\mathcal{R}\| \|\delta x\|)} \leq C^\dagger \|\delta x\|^2. \quad (2.10)$$

From (2.7a) and (2.7b), we obtain the following upper bound of  $\|\delta x^\dagger\|$ :

$$\left\| \delta x^\dagger \right\| \leq (1 + C^\dagger \|\delta x\|) \|\delta x\| \leq \left( 1 + \left\| \left( \mathcal{R}^1 \right)^\dagger \right\| \|\mathcal{R}\| \|\Phi\| \right) \|\delta x\|. \quad (2.11)$$

Using (2.2) and (2.9), we obtain

$$\mathcal{R}^1(\delta x - \delta x^B) = \mathcal{R}^2(\delta x)^2 - \mathcal{R}^2(\delta x^\dagger)^2 + \mathcal{R}^3(\delta x)^3 + \mathcal{R}^4(\delta x)^4 + \dots. \quad (2.12)$$

The second-order term on the righthand side of (2.12) is analyzed as follows:

$$\begin{aligned} \mathcal{R}^2(\delta x)^2 - \mathcal{R}^2(\delta x^\dagger)^2 &= \mathcal{R}(\delta x, \mathcal{R}(\delta x, \Phi)) - \mathcal{R}(\delta x^\dagger, \mathcal{R}(\delta x^\dagger, \Phi)) \\ &= \mathcal{R}(\delta x, \mathcal{R}(\delta x - \delta x^\dagger, \Phi)) + \mathcal{R}(\delta x - \delta x^\dagger, \mathcal{R}(\delta x^\dagger, \Phi)). \end{aligned} \quad (2.13)$$

From (2.12), we obtain

$$\left\| \delta x - \delta x^B \right\| \leq \left\| \left( \mathcal{R}^1 \right)^\dagger \right\| \left[ \left\| \mathcal{R}^2(\delta x)^2 - \mathcal{R}^2(\delta x^\dagger)^2 \right\| + \left\| \mathcal{R}^3(\delta x)^3 + \mathcal{R}^4(\delta x)^4 + \dots \right\| \right]. \quad (2.14)$$

- (I) Compute the solution  $\Phi(x)$  and the Robin function  $R(x)$  and its first and second derivatives.  
 (II) Find  $\delta x^\dagger$  by solving  $\mathcal{R}^1(\delta x^\dagger) = \Phi(x + \delta x) - \Phi(x)$  as in (1.6).  
 (III) Find  $\delta x^\Delta = \delta x^B - \delta x^\dagger$  by solving  $\mathcal{R}^1(\delta x^\Delta) = -\mathcal{R}^2(\delta x^\dagger)$  as in (2.2).  
 (IV) Compute  $\delta x^B$  by adding  $\delta x^\dagger$  and  $\delta x^\Delta$ .

**Algorithm 1:** Numerical algorithm (continuous version).

By using (2.3), (2.10), (2.11), (2.13), and the definition of  $C^\dagger$ , (2.7c) is achieved from (2.14) as follows:

$$\begin{aligned}
 \|\delta x - \delta x^B\| &\leq \|(\mathcal{R}^1)^\dagger\| \|\Phi\| \left[ \|\mathcal{R}\|^2 \|\delta x - \delta x^\dagger\| (\|\delta x\| + \|\delta x^\dagger\|) + \frac{(\|\mathcal{R}\| \|\delta x\|)^3}{1 - \|\mathcal{R}\| \|\delta x\|} \right] \\
 &\leq \|(\mathcal{R}^1)^\dagger\| \|\Phi\| \|\mathcal{R}\|^2 \|\delta x\|^3 \left[ C^\dagger \left( 2 + \|(\mathcal{R}^1)^\dagger\| \|\mathcal{R}\| \|\Phi\| \right) + 2\|\mathcal{R}\| \right] \\
 &\leq C^\dagger \|\delta x\|^3 \left[ C^\dagger \left( 1 + \frac{C^\dagger}{4\|\mathcal{R}\|} \right) + \|\mathcal{R}\| \right] \\
 &\leq C^B \|\delta x\|^3.
 \end{aligned} \tag{2.15}$$

□

### 3. Numerical Algorithm

Assume that we can measure the photon density distribution  $\Phi(x + \delta x)$  and  $\Phi(x)$  on the entire boundary  $\partial\Omega$ . That is to say, we have infinite detectors and one source. Then, the numerical algorithm is given as follows.

The detailed computation of the integral operators  $\mathcal{R}^1$  and  $\mathcal{R}^2$ , which is introduced in (1.5), is as follows:

$$\mathcal{R}^1(\delta x) = \mathcal{R}_{\mu_a}(\delta \mu_a, \Phi) + \mathcal{R}_\kappa(\delta \kappa, \Phi), \tag{3.1a}$$

$$\begin{aligned}
 \mathcal{R}^2(\delta x) &= \mathcal{R}_{\mu_a}(\delta \mu_a, \mathcal{R}_{\mu_a}(\delta \mu_a, \Phi)) + \mathcal{R}_{\mu_a}(\delta \mu_a, \mathcal{R}_\kappa(\delta \kappa, \Phi)), \\
 &\quad + \mathcal{R}_\kappa(\delta \kappa, \mathcal{R}_{\mu_a}(\delta \mu_a, \Phi)) + \mathcal{R}_\kappa(\delta \kappa, \mathcal{R}_\kappa(\delta \kappa, \Phi)).
 \end{aligned} \tag{3.1b}$$

#### 3.1. Discretization

Algorithm 1 is based on one source and infinite detectors. However, for practical reasons, we need to discretize Algorithm 1 to obtain the numerical algorithm for finite sources and finite detectors for finite frequencies. The following notations will be used for the discretization:

- (i)  $N_d$  detector positions:  $r_{i_d}$  for  $i_d = 1, 2, \dots, N_d$ ,
- (ii)  $N_s$  source functions:  $q_{i_s} = \delta_{i_s}$  (Dirac delta function) for  $i_s = 1, 2, \dots, N_s$ ,
- (iii)  $N_\omega$  frequencies:  $\omega_{i_\omega}$  for  $i_\omega = 1, 2, \dots, N_\omega$ ,

- (iv)  $N_e$  elements:  $T_{i_e}$  for  $i_e = 1, 2, \dots, N_e$ ,
- (v)  $N_n$  nodes:  $t_{i_n}$  for  $i_n = 1, 2, \dots, N_n$ ,
- (vi) the measurement index:  $j = (i_\omega - 1)N_s N_d + (i_s - 1)N_d + i_d$ ,
- (vii) the optical coefficient index:  $k = (i_{\mu\kappa} - 1)N_e + i_e$ , where  $i_{\mu\kappa}$  is 1 (the absorption coefficient) or 2 (the diffusion coefficient).

If we use piecewise linear or bilinear finite element method, the finite element solution is represented by

$$u_h(x) = \sum_{i_n=1}^{N_n} u_h(i_n) \phi_{i_n}(x), \quad (3.2)$$

where  $\phi_{i_n}$  is the piecewise linear or the bilinear function which is 1 on the  $i_n$ th node and 0 on all the other nodes. Assume  $\mu_a$  and  $\kappa$  are piecewise constant function, which is constant for each  $N_e$  finite elements. Therefore, in diffuse optical tomography inverse problem, we have  $N_\omega N_s N_d$  measurement information contents and  $2N_e$  variables to find.

We should discretize  $\mathcal{R}^1$  and  $\mathcal{R}^2$  to obtain a discretized version of Algorithm 1. Let the Jacobian and Hessian matrices, which is the discretization of integral operators  $\mathcal{R}^1$  and  $\mathcal{R}^2$ , be  $J$  and  $H$ . The relation between higher order derivatives for the diffusion operator and higher order terms of Born expansions including  $\mathcal{R}^1$  and  $\mathcal{R}^2$  is analyzed in [7].

Firstly, let us discretize  $\delta x$ ,  $\Phi$ , and the Robin function  $R$  as follows:

$$\delta x \approx \left( \sum_{i_e=1}^{N_e} \delta \mu_{i_e} \chi_{T_{i_e}}, \sum_{i_e=1}^{N_e} \delta \kappa_{i_e} \chi_{T_{i_e}} \right), \quad (3.3a)$$

$$\Phi^{i_\omega, i_s} \approx \sum_{i_n=1}^{N_n} \Phi_{i_n}^{i_\omega, i_s} \phi_{i_n}, \quad (3.3b)$$

$$R^{i_\omega}(\cdot, r_{i_s}) \approx \sum_{i_n=1}^{N_n} R_{i_n}^{i_\omega, i_s} \phi_{i_n}. \quad (3.3c)$$

Since we chose the source function  $q_s$  as the Dirac delta function at the  $i_s$ th source point,  $\Phi^{i_\omega, i_s} = R^{i_\omega}(\cdot, r_{i_s})$ . However, we will discriminate these two functions in this paper, since they are different for general source function  $q$  which is different from the Dirac delta function. We will use  $\delta \mu$  instead of  $\delta \mu_a$  for notational convenience.

Let the vector  $\gamma_0$  which corresponds to the discretization of  $\delta x$  in (3.3a) be defined as

$$\gamma_0 = (\delta \mu_1, \delta \mu_2, \dots, \delta \mu_{N_e}, \delta \kappa_1, \delta \kappa_2, \dots, \delta \kappa_{N_e}). \quad (3.4)$$

By the adjoint method [12],  $R^{i_\omega}(r_{i_d}, \cdot) = (R^{i_\omega}(\cdot, r_{i_d}))^*$ , where  $*$  denotes complex conjugate. Likewise for (3.3a), let  $\gamma$ ,  $\gamma^\dagger$ ,  $\gamma^\Delta$ , and  $\gamma^B$  be the discretization of  $\delta x$ ,  $\delta x^\dagger$ ,  $\delta x^\Delta$ , and  $\delta x^B$ , respectively.



For a function  $f$  and a measurable set  $T$ , let us denote  $f \in T$  if the intersection of the support of  $f$  and  $T$  is not empty. The discretization of the linearized solution  $\gamma^\dagger$  is attained by solving the following equation:

$$J\gamma^\dagger = b, \quad (3.5)$$

where

$$\begin{aligned} J(j, k) &= \sum_{\phi_{i_{n1}} \in T_{i_e}} \sum_{\phi_{i_{n2}} \in T_{i_e}} \left( R_{i_{n1}}^{i_\omega, i_d} \right)^* E_{i_e}(i_{n1}, i_{n2}) \Phi_{i_{n2}}^{i_\omega, i_s} \quad \text{when } i_{\mu\kappa} = 1, \\ J(j, k) &= \sum_{\phi_{i_{n1}} \in T_{i_e}} \sum_{\phi_{i_{n2}} \in T_{i_e}} -3 \left( R_{i_{n1}}^{i_\omega, i_d} \right)^* \kappa_{i_e}^2 F_{i_e}(i_{n1}, i_{n2}) \Phi_{i_{n2}}^{i_\omega, i_s} \quad \text{when } i_{\mu\kappa} = 2, \\ b(j) &= \Phi^{i_\omega, i_s}(x + \delta x)(r_{i_d}) - \Phi^{i_\omega, i_s}(x)(r_{i_d}), \\ E_{i_e}(i_{n1}, i_{n2}) &= \int_{T_{i_e}} \phi_{i_{n1}}(\xi) \phi_{i_{n2}}(\xi) d\xi, \\ F_{i_e}(i_{n1}, i_{n2}) &= \int_{T_{i_e}} \nabla \phi_{i_{n1}}(\xi) \cdot \nabla \phi_{i_{n2}}(\xi) d\xi. \end{aligned} \quad (3.6)$$

The discretized solution  $\gamma^\Delta$  is obtained by solving the following equation:

$$J\gamma^\Delta = \left( \gamma^\dagger \right)^t H \gamma^\dagger, \quad (3.7)$$

where

$$H(j, i_{e1}, i_{e2}) = \sum_{\phi_{i_{n1}} \in T_{i_{e1}}} \sum_{\phi_{i_{n2}} \in T_{i_{e2}}} \left( R_{i_{n1}}^{i_\omega, i_d} \right)^* (H_{\mu\mu} + H_{\mu\kappa} + H_{\kappa\mu} + H_{\kappa\kappa})(i_{e1}, i_{e2}; i_{n1}, i_{n2}) \Phi_{i_{n2}}^{i_\omega, i_s}, \quad (3.8)$$

where  $H_{\mu\mu}$ ,  $H_{\mu\kappa}$ ,  $H_{\kappa\mu}$ , and  $H_{\kappa\kappa}$  are the discretization of corresponding terms in (3.1b) such that

$$\begin{aligned} H_{\mu\mu}(i_{e1}, i_{e2}; i_{n1}, i_{n2}) &= \int_{T_{i_{e1}}} \int_{T_{i_{e2}}} \phi_{i_{n1}}(\xi) R^{i_\omega}(\xi, \eta) \phi_{i_{n2}}(\eta) d\xi d\eta, \\ H_{\mu\kappa}(i_{e1}, i_{e2}; i_{n1}, i_{n2}) &= \int_{T_{i_{e1}}} \int_{T_{i_{e2}}} \phi_{i_{n1}}(\xi) \nabla_\eta R^{i_\omega}(\xi, \eta) \cdot \nabla_\eta \phi_{i_{n2}}(\eta) d\xi d\eta, \\ H_{\kappa\mu}(i_{e1}, i_{e2}; i_{n1}, i_{n2}) &= \int_{T_{i_{e1}}} \int_{T_{i_{e2}}} \nabla_\xi \phi_{i_{n1}}(\xi) \cdot \nabla_\xi (R^{i_\omega}(\xi, \eta)) \phi_{i_{n2}}(\eta) d\xi d\eta, \\ H_{\kappa\kappa}(i_{e1}, i_{e2}; i_{n1}, i_{n2}) &= \int_{T_{i_{e1}}} \int_{T_{i_{e2}}} \nabla_\xi \phi_{i_{n1}}(\xi) \cdot \left[ \nabla_\xi \nabla_\eta R^{i_\omega}(\xi, \eta) \right] \nabla_\eta \phi_{i_{n2}}(\eta) d\xi d\eta. \end{aligned} \quad (3.9)$$

- (I) Compute the solution  $\Phi(\gamma_0)_{i_n}^{i_\omega, i_s}$  and the Robin function  $R(\gamma_0)_{i_d, i_n}^{i_\omega}$  for  $i_\omega = 1, \dots, N_\omega, i_s = 1, \dots, N_s, i_n = 1, \dots, N_n$  as in (3.3b) and (3.3c), respectively.
- (II) Find  $\gamma^\dagger$  by solving the equation (3.5).
- (III) Find  $\gamma^\Delta$  by solving the equation (3.7).
- (IV) Compute  $\gamma^B$  by adding  $\gamma^\dagger$  and  $\gamma^\Delta$ .

**Algorithm 2:** Numerical algorithm (discretized version).

Even though the Hessian is not discretized, we obtain the following discretized numerical algorithm (Algorithm 2), expecting the Hessian is simply discretized and approximated in the next subsection:

### 3.2. Approximation of Hessian

In this subsection we approximate  $H_{\mu\mu}$ , by assuming  $\kappa$  and  $\mu'_s$  are constant in  $\Omega$ . The approximation is progressed in three ways.

First, we approximate the Robin function  $R(\xi, \eta)$  when  $(\xi, \eta) \in \Omega \setminus \partial\Omega$  by its leading term  $R_0(\xi, \eta)$  defined by

$$R_0(\xi, \eta) = \begin{cases} \frac{1}{(p-2)g_p\kappa(\eta)} |\xi - \eta|^{2-p} & p \geq 3, \\ \frac{1}{\omega_2\kappa(\eta)} \log\left(\frac{2S}{|\xi - \eta|}\right) & p = 2, \end{cases} \quad (3.10)$$

where  $g_p$  is the hypersurface area of the unit sphere in  $\mathbb{R}^p$ ,  $p = 2, 3, \dots$  and  $S = \sup_{\xi, \eta \in \Omega} |\xi - \eta|$ . Some important relations between  $R$  and  $R_0$  are found in [13].

Second, when  $i_{e1} \neq i_{e2}$ , the Robin function  $R$  and  $\phi_{i_n}$  are approximated by constant values  $R_0(c(i_{e1}), c(i_{e2}))$  and  $\phi_{i_n}(c(i_e))$  in  $T_{i_e}$ , respectively, where  $c(i_e)$  of the center of the element  $T_{i_e}$ . That is to say, when  $i_{e1} \neq i_{e2}$ , (3.9) is approximated as follows:

$$H_{\mu\mu}(i_{e1}, i_{e2}; i_{n1}, i_{n2}) = R_0(c(i_{e1}), c(i_{e2})) \int_{T_{i_{e1}}} \phi_{i_{n1}}(\xi) d\xi \int_{T_{i_{e2}}} \phi_{i_{n2}}(\eta) d\eta. \quad (3.11)$$

Third, when  $i_{e1} = i_{e2}$ , we use the following lemma.

**Lemma 3.1.** *Let the measurable set  $T$  be contained in  $\mathbb{R}^p$ ,  $p = 2, 3, \dots$ , and  $0 < m < p$ ; then, the following inequality holds for  $T$ :*

$$\iint_T |\xi - \eta|^{-m} d\xi d\eta \leq \frac{p^{1-m/p}}{p-m} g_p^{m/p} |T|^{2-m/p}, \quad p \geq 2, \quad (3.12a)$$

$$\iint_T \log\left(\frac{2S}{|\xi - \eta|}\right) d\xi d\eta \leq \frac{1}{4\pi} \left(1 + \log\left(\frac{4S^2\pi}{|T|}\right)\right) |T|^2, \quad p = 2, \quad (3.12b)$$

where  $|T|$  is the volume of  $T$ .

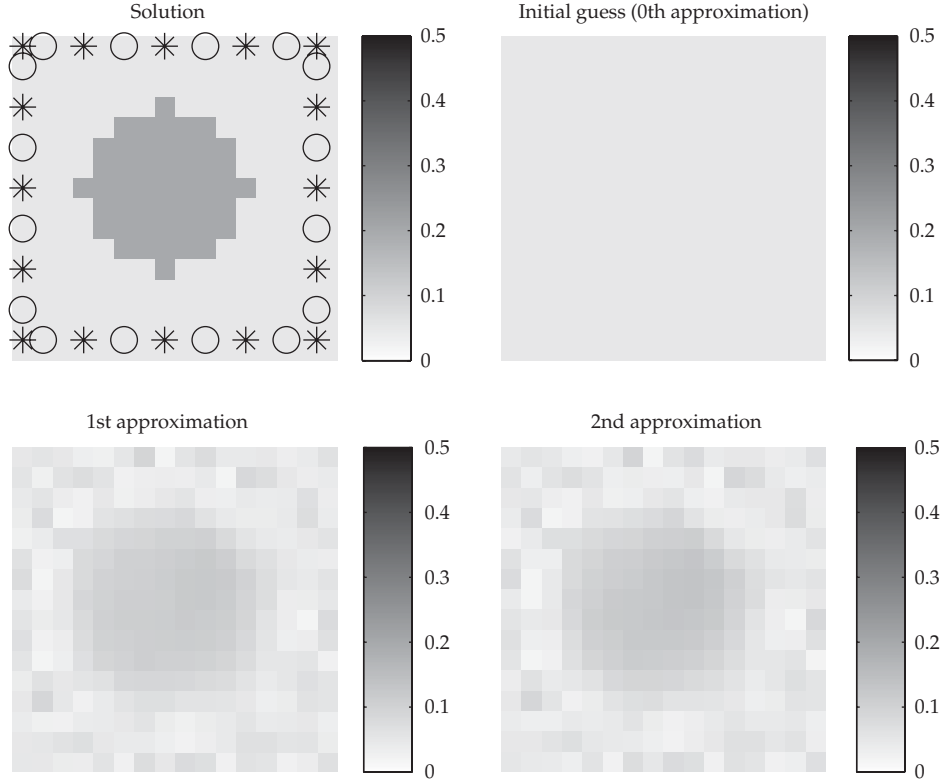


**Figure 1:**  $J_{index} = Nx * Ny * 0.4$ ,  $J_{alpha} = 6.4920e - 009$ , 10% noise, sources (\*), and detectors (o).

*Proof.* If a ball with a radius  $r$  has the same volume as  $T$ , we have

$$r = \left( |T| \frac{p}{g_p} \right)^{1/p} \quad (3.13)$$

for the space dimensions  $p = 2, 3, \dots$ . Let the ball of radius  $r$  with center  $\xi \in T$  be  $B_\xi$ . Let  $T_0 = T \cap B_\xi$ ,  $T^+ = T \setminus B_\xi$ , and  $T^- = B_\xi \setminus T$ . Noting that  $|T^+| = |T^-|$ , we obtain

$$\begin{aligned} \int_T |\xi - \eta|^{-m} d\eta &= \int_{T_0} |\xi - \eta|^{-m} d\eta + \int_{T^+} |\xi - \eta|^{-m} d\eta \\ &\leq \int_{T_0} |\xi - \eta|^{-m} d\eta + \int_{T^-} |\xi - \eta|^{-m} d\eta = \int_{B_\xi} |\xi - \eta|^{-m} d\eta \\ &\leq \int_0^r \rho^{p-m-1} g_p d\rho = \frac{g_p}{p-m} r^{p-m} \\ &\leq \frac{g_p}{p-m} \left( |T| \frac{p}{g_p} \right)^{1-m/p} \end{aligned} \quad (3.14)$$

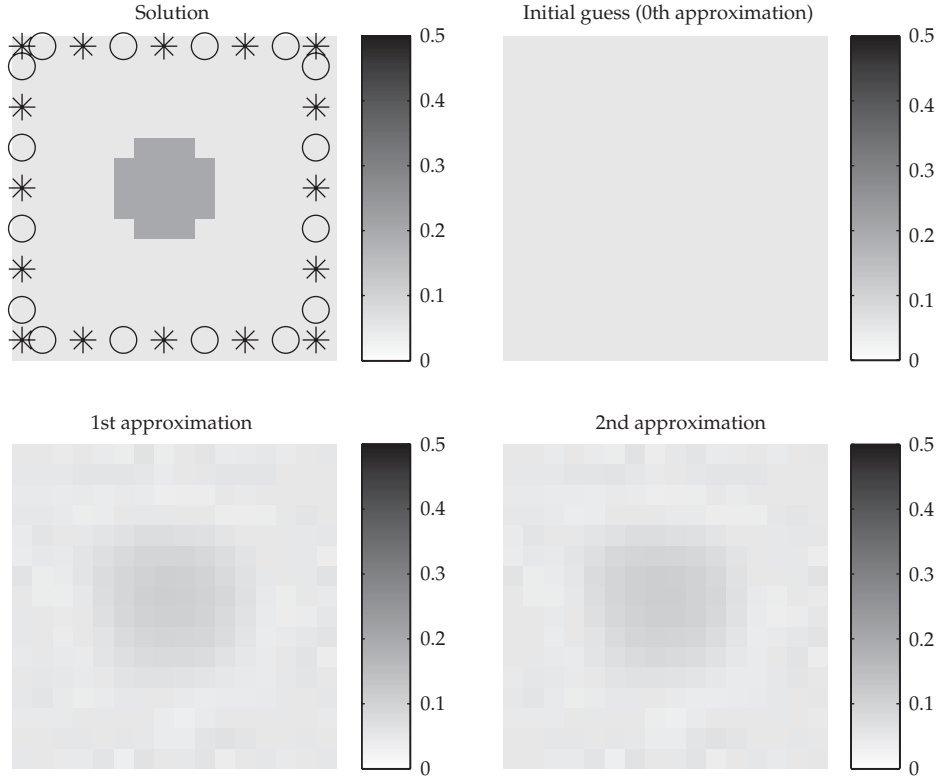


**Figure 2:**  $Jindex = Nx * Ny * 0.4$ ,  $Jalpha = 6.5711e - 009$ , 10% noise, sources (\*), and detectors (o).

for all  $\xi \in T$ . Therefore,

$$\iint_T |\xi - \eta|^{-m} d\eta d\xi \leq \frac{g_p |T|}{p - m} \left( |T| \frac{p}{g_p} \right)^{1-m/p} = \frac{p^{1-m/p}}{p - m} g_p^{m/p} |T|^{2-m/p}. \quad (3.15)$$

Equation (3.12b) is derived in the same manner.  $\square$

Therefore, when  $i_{e1} = i_{e2}$ , (3.9) is approximated using the inequality in Lemma 3.1 as follows:

$$H_{\mu\mu}(i_{e1}, i_{e1}; i_{n1}, i_{n2}) \approx \phi_{i_{n1}}(c_{i_{e1}}) \phi_{i_{n2}}(c_{i_{e1}}) \cdot \begin{cases} \frac{p^{2/p} |T_{i_{e1}}|^{1+2/p}}{2(p-2) g_p^{2/p} \kappa(c(i_{e1}))} & p \geq 3, \\ \frac{1}{8\pi^2 \kappa(c(i_{e1}))} \left( 1 + \log \left( \frac{4S^2 \pi}{|T_{i_{e1}}|} \right) \right) |T_{i_{e1}}|^2 & p = 2. \end{cases} \quad (3.16)$$

#### 4. Numerical Implementation

In the numerical implementation, the following parameters are used:

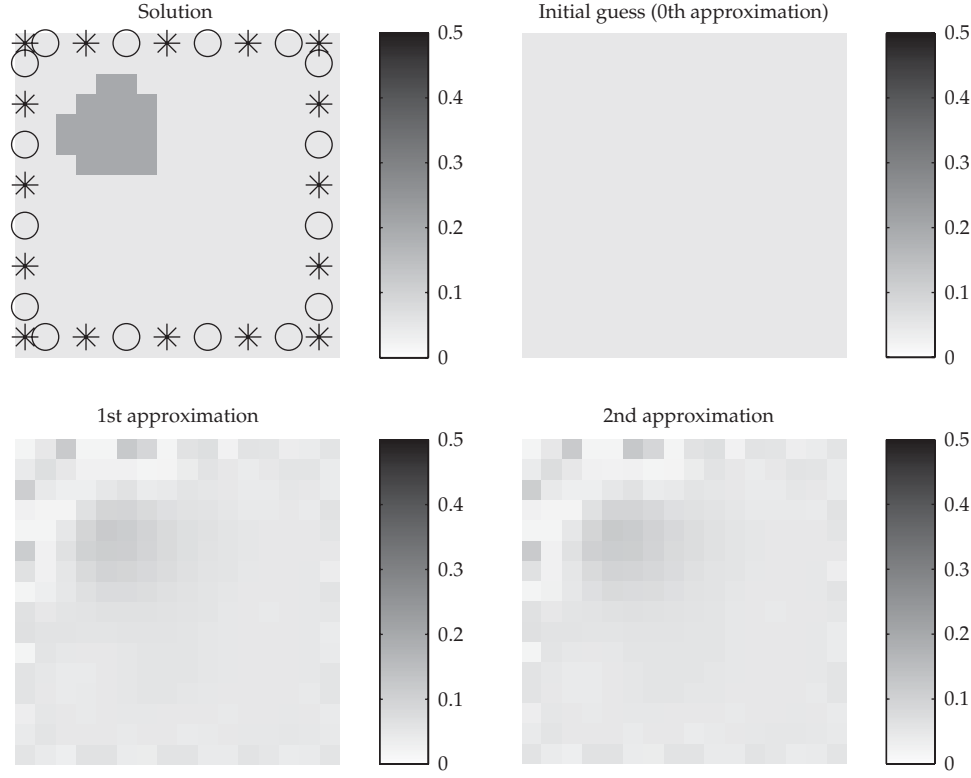


**Figure 3:**  $J_{index} = Nx * Ny * 0.3$ ,  $J_{alpha} = 1.8227e - 7$ , 10% noise, sources (\*) and detectors (o).

- (i)  $\Omega = [0, 6] \times [0, 6] \text{ (cm}^2\text{)},$
- (ii)  $N_d = 16,$
- (iii)  $N_s = 16,$
- (iv)  $N_\omega = 1,$
- (v)  $Nx = Ny = 16,$
- (vi)  $N_e = Nx * Ny,$
- (vii)  $N_n = (Nx + 1) * (Ny + 1),$
- (viii)  $\mu_a = 0.05 + (0.2 - 0.05)\chi_D \text{ (cm}^{-1}\text{)},$
- (ix)  $\mu'_s = 8 \text{ (cm}^{-1}\text{)},$
- (x)  $\kappa = 1/3 * (\mu_a + \mu'_s) = 1/3 * (0.05 + 8),$
- (xi)  $\omega = 2\pi * 300 \text{ MHz},$
- (xii)  $a = 1,$
- (xiii)  $J_{index} = Nx * Ny * 0.4.$

Since the diffusion coefficient  $\kappa$  is constant, the right-hand side  $b$  is a  $N_s * N_d$  column vector, Jacobian  $J$  is a  $(N_s * N_d) \times N_e$  matrix, the Hessian  $H$  is a  $N_e \times (N_s * N_d) \times N_e$  third-order tensor, and  $(\gamma^\dagger)^t H \gamma^\dagger$  is  $N_s * N_d$  column vector in (3.5) and (3.7).  $H = H_{\mu\mu}$  is approximated by (3.11) and (3.16).

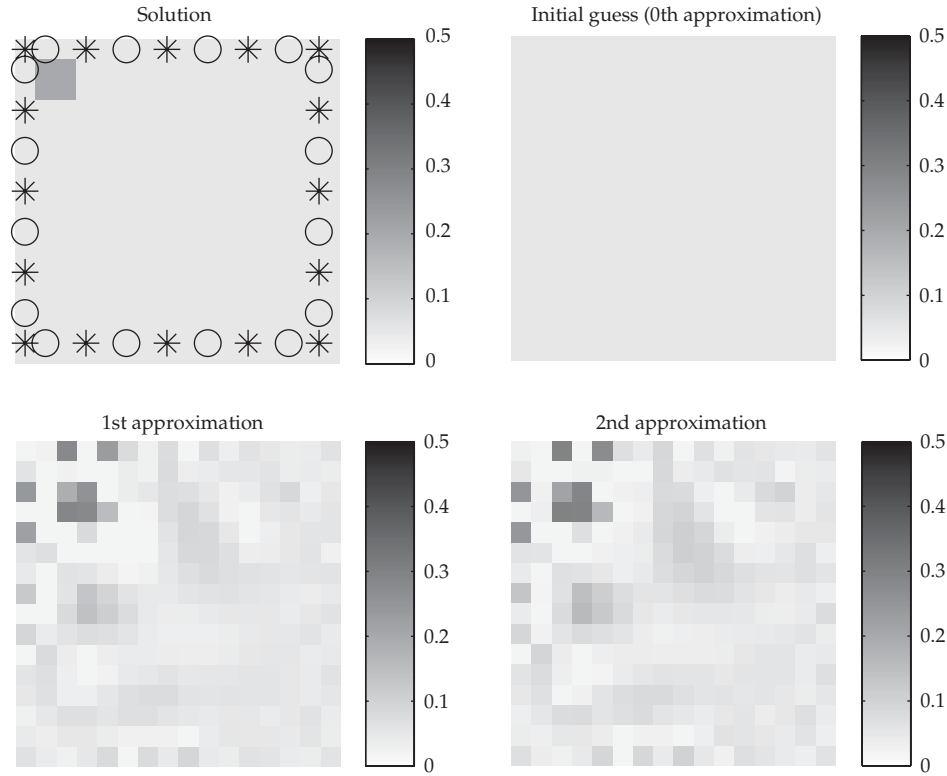


**Figure 4:**  $Jindex = Nx * Ny * 0.4$ ,  $Jalpha = 6.5029e - 009$ , 10% noise, sources (\*), and detectors (o).

In the above setting, we reconstruct the obstacle  $D$  which has different absorption coefficient ( $0.2 \text{ cm}^{-1}$ ) compared to the background absorption coefficient ( $0.05 \text{ cm}^{-1}$ ). Four cases of the obstacle  $D$  are considered in Figures 1, 2, 3, and 4. The reconstruction of the absorption coefficient  $\mu_a = 0.05 + (0.2 - 0.05)\chi_D \text{ (cm}^{-1}\text{)}$  is implemented using two algorithms. One is the suggested Algorithm 2 based on the second-order Born approximation. The other is linearized method based on the first-order Born approximation, which is equivalent to the step I and II in Algorithm 2. We denoted these two methods in the figures: the 2nd order approximation and the 1st-order approximation, respectively. On the upper-left part of the figures, original  $\mu_a$  and source/detector locations are plotted. The initial guess ( $\mu_{a0}$  or  $\gamma_0$ ) for the absorption coefficient is plotted on the upper-right part of the figures. In the lowerleft and lowerright part of each figure, reconstructed absorption coefficients by the first approximation ( $\mu_a^\dagger$  or  $\gamma^\dagger$ ) and the second approximation ( $\mu_a^B$  or  $\gamma^B$ ) are plotted, respectively.

In all four cases, 10% noise is added. Truncated singular value decomposition(SVD) is used.  $Jindex$  is the number of largest singular values used in the truncated SVD method. We used the Tikhonov regularization parameter  $Jalpha$  as the value of the  $Jindex$ th largest singular values.

As is shown in the figure, the discrimination between background and the obstacle is clearer in the second-order approximation than the first-order approximation. The reconstructed image resolution depends on the distance from the boundary of the tissue, which is verified by comparing Figures 1 and 2 with Figures 3 and 4. And the resolution also depends on the size of obstacle, which is verified by comparing Figures 1 and 3 with Figures 2

and 4. Due to the diffusion property of near infrared light, the reconstructed image is much blurred especially in Figure 3. The sensitivity to the noise made some kind of irregular checkboard pattern near the boundary (Figures 1, 3, and 4).

## 5. Conclusions

We derived a new numerical method based on the second-order Born approximation. The method is a method of order 3, which is more accurate than the well-known linearized method based on the first-order Born approximation. The error analysis for the method is proved, and the computation of the second-order term is explained using some approximation and integral inequalities. The comparison between the suggested and the linearized method is implemented for four different kinds of absorption coefficients. In the implementation, the suggested method shows more discrimination between the optical obstacle and the background than the linearized method. If more accurate numerical quadrature with more efficient approximation of the Robin function is used, the efficiency of the present method will be elaborated. The simultaneous reconstruction of the absorption and the reduced scattering coefficients based on the proper approximation on the second derivatives of the Robin function would be an interesting topic.

## Acknowledgment

This research was supported by Basic Science Research Program through the National Research Foundation of Korea (NRF) funded by the Ministry of Education, Science and Technology (2010-0004047).

## References

- [1] S. R. Arridge and J. C. Schotland, "Optical tomography: forward and inverse problems," *Inverse Problems*, vol. 25, pp. 1–59, 2009.
- [2] V. Isakov, "On uniqueness in the inverse transmission scattering problem," *Communications in Partial Differential Equations*, vol. 15, no. 11, pp. 1565–1587, 1990.
- [3] K. Kwon, "Identification of anisotropic anomalous region in inverse problems," *Inverse Problems*, vol. 20, no. 4, pp. 1117–1136, 2004.
- [4] K. Kwon and D. Sheen, "Anisotropic inverse conductivity and scattering problems," *Inverse Problems*, vol. 18, no. 3, pp. 745–756, 2002.
- [5] J. Sylvester and G. Uhlmann, "A global uniqueness theorem for an inverse boundary value problem," *Annals of Mathematics*, vol. 125, no. 1, pp. 153–169, 1987.
- [6] H. Kang, K. Kwon, and K. Yun, "Recovery of an inhomogeneity in an elliptic equation," *Inverse Problems*, vol. 17, no. 1, pp. 25–44, 2001.
- [7] K. Kwon and B. Yazıcı, "Born expansion and Fréchet derivatives in nonlinear diffuse optical tomography," *Computers & Mathematics with Applications*, vol. 59, no. 11, pp. 3377–3397, 2010.
- [8] V. A. Markel and J. C. Schotland, "Inverse problem in optical diffusion tomography. I. Fourier-Laplace inversion formulas," *Journal of the Optical Society of America A*, vol. 18, no. 6, pp. 1336–1347, 2001.
- [9] G. Murat, K. Kwon, B. Yazıcı, E. Giladi, and X. Intes, "Effect of discretization error and adaptive mesh generation in diffuse optical absorption imaging: I," *Inverse Problems*, vol. 23, no. 3, pp. 1115–1133, 2007.
- [10] G. Murat, K. Kwon, B. Yazıcı, E. Giladi, and X. Intes, "Effect of discretization error and adaptive mesh generation in diffuse optical absorption imaging. II," *Inverse Problems*, vol. 23, no. 3, pp. 1135–1160, 2007.
- [11] K. Kwon, B. Yazıcı, and M. Guven, "Two-level domain decomposition methods for diffuse optical tomography," *Inverse Problems*, vol. 22, no. 5, pp. 1533–1559, 2006.

- [12] S. R. Arridge, "Optical tomography in medical imaging," *Inverse Problems*, vol. 15, no. 2, pp. R41–R93, 1999.
- [13] C. Miranda, *Partial Differential Equations of Elliptic Type*, Springer, New York, NY, USA, 1970.



## Research Article

# Selecting Negative Samples for PPI Prediction Using Hierarchical Clustering Methodology

**J. M. Urquiza,<sup>1</sup> I. Rojas,<sup>1</sup> H. Pomares,<sup>1</sup> J. Herrera,<sup>1</sup>  
J. P. Florido,<sup>1</sup> and O. Valenzuela<sup>2</sup>**

<sup>1</sup> Department of Computer Architecture and Computer Technology, University of Granada, 18017 Granada, Spain

<sup>2</sup> Department of Applied Mathematics, University of Granada, 18017 Granada, Spain

Correspondence should be addressed to J. M. Urquiza, [jurquiza@atc.ugr.es](mailto:jurquiza@atc.ugr.es)

Received 12 September 2011; Accepted 17 November 2011

Academic Editor: Venky Krishnan

Copyright © 2012 J. M. Urquiza et al. This is an open access article distributed under the Creative Commons Attribution License, which permits unrestricted use, distribution, and reproduction in any medium, provided the original work is properly cited.

Protein-protein interactions (PPIs) play a crucial role in cellular processes. In the present work, a new approach is proposed to construct a PPI predictor training a support vector machine model through a mutual information filter-wrapper parallel feature selection algorithm and an iterative and hierarchical clustering to select a relevance negative training set. By means of a selected suboptimum set of features, the constructed support vector machine model is able to classify PPIs with high accuracy in any positive and negative datasets.

## 1. Introduction

Protein-protein interactions (PPIs) play a greatly important role in almost any biological function carried out within the cell [1, 2]. In fact, an enormous effort has already been made to study biological protein networks in order to understand the main cell mechanisms [3–5]. The development of new technologies has improved the experimental techniques for detecting PPIs, such as coimmunoprecipitation (CoIP), yeast two-hybrid (Y2H), or mass spectrometry studies [6–9]. However, computational approaches have been implemented for predicting PPIs because of cost and time requirements associated with the experimental techniques [5].

Therefore, different computational methods have been applied in PPI prediction, some methods are Bayesian approaches [10–12], maximum likelihood estimation (MLE) [13, 14], maximum specificity set cover (MSSC) [4], decision trees [15, 16], and support vector machines (SVM) [15–18]. Many computational approaches use information from diverse sources at different levels [5]. In this way, predicting PPI models [4, 13, 15, 16, 19] have been built

using domain information. Since interacting proteins are usually coexpressed and collocated in the same subcellular compartment [10], cell location patterns are also considered to be a valid criterion in prediction works. In other works, authors use functional similarity to predict interacting proteins [20]. Likewise, the concept of homology has been already used to generate prediction models [19, 21], homologs interactions databases [11], and negative datasets [22].

In the past years, these experimental methods [23] and computational approaches [22] have provided interactions for several organisms such as *Saccharomyces cerevisiae* (*S. cerevisiae* or Baker's yeast or simply yeast) [24–27], *Caenorhabditis elegans* (*C. elegans*) [28, 29], *Drosophila melanogaster* (*D. melanogaster* or fruit fly) [30, 31], including *Homo Sapiens* (*H. sapiens*) [3, 6, 32].

In spite of obtaining a huge amount of interaction data through high-throughput technologies, it is still difficult to compare them as they contain a large number of false positives [11, 22]. Some authors provide several reliable interaction sets, including diverse confidence levels. With this context, supervised learning methods used in PPI prediction require complete and reliable datasets formed by positive and negative samples. However, noninteracting pairs are rarely reported by experimentalists motivated by the difficulties associated in demonstrating noninteraction under all possible conditions. In fact, negative datasets have traditionally been created by randomly paired proteins [15, 33, 34] or by selecting pairs of proteins that are not sharing the same subcellular compartment [10]. Nonetheless, other works suggest that negative sets created on the basis of cell location alone lead to biased estimations in the predictive interacting models [17]. To solve this problem, Wu et al. [35] proposed a predictive interacting method by means of similarity semantic measures [36], based on gene ontology (GO) annotations [37], although they did not specify which ontology contributed most to the process of obtaining negative interactions. For this reason, Saeed and Deane [22] introduced a novel method to generate negative datasets, based on functional data, location, expression, and homology. These authors considered noninteracting pairs to be two proteins showing no overlapping between any of the features under consideration. In another work, Yu et al. [38] demonstrated that the accuracy of the PPI prediction works is significantly overestimated. The accuracy reported by the prediction model strongly depends on the structure of the selected training and testing datasets. The chosen negative pairs in the training data have a variable impact on the accuracy, and it can be artificially inflated by a bias towards dominant samples in the positive data [38]. In this way, Yu et al. [38] also presented a method for the selection of unbiased negative examples based on the frequency of the proteins involved in positive interactions in the dataset.

In this work, a novel method is presented for constructing an SVM classifier for PPI prediction, selecting negative dataset through clustering approach applied to 4 million negative pairs from Saeed and Deane [22]. This clustering approach is applied in an effort to avoid the impact of negative dataset on the accuracy of the classifier model. This new method is based on a new feature extraction and selection using well-known databases, applied specifically to a yeast organism model, since yeast is the most widely analysed organism and the one in which it is easiest to find data. New similarity semantic measures calculated from the features are proposed, and they demonstrate that their use improves the predictive power of trained classifiers. In addition, this classifier may return a confidence score for each PPI prediction through a modification of the SVM implementation. Firstly, features are extracted for positive and negative samples; then, a clustering approach is performed in order to obtain high-reliable noninteracting representative samples. Subsequently a parallel filter-wrapper feature technique selects the most relevance extracted features in order to obtain a reliable

model. The algorithm called mRMR (minimal-redundancy-maximal-relevance criterion) [39] is used as filter and is based on the statistical concept of mutual information. This reduction in the number of features allows for a better training efficiency as the search space for most of the parameters of the model is also reduced [40, 41].

In a second part, with the purpose of validating the generalisation capability of our model, a group of highly reliable external datasets from [9] were classified using our method. These datasets to be validated were extracted using computational and experimental approaches together with information from the literature. The used models are SVM classifiers built using the most relevance selected features that characterise the protein-protein interaction as explained. They were trained using three training sets, the positive examples were kept, but the negative set was changed, each negative set was obtained by a specific method: (1) hierarchical clustering method presented in this paper, (2) randomly selection, and (3) using the approach proposed by Yu et al. [38].

The testing datasets were filtered for assessment to prevent biased results, that is, without any overlapping between the datasets used during the training stage. High sensitivity and specificity are obtained in both parts using this proposed approach, that is, the model trained using the negative set by the proposed hierarchical clustering method. The presented approach leads to the possibility of becoming a guide for experimentation, being a useful tool to save money and time.

## 2. Material and Methods

### 2.1. Material

Two types of datasets were used: training datasets to construct the models and testing datasets to assess the goodness of predictions. A supervised learning classifier as SVM requires positive and negative samples for training data. The positive and negative examples were extracted from Saeed and Deane [22], where authors provide a positive dataset composed of 4809 high-reliability interacting pairs of proteins and a high-quality negative set formed by more than 4 million noninteracting pairs. Two negative subsets of the size similar to that of the positive dataset were extracted from this negative set: one dataset is composed of randomly selected noninteraction pairs (4894) and the other one is created by means of the proposed hierarchical clustering approach presented in this paper in order to select the most representative negative samples (4988). The main goal of this negative dataset of clustered samples is to represent the whole negative space of more than 4 million examples avoiding biased results in PPI prediction. The third negative set used in this paper is created using the method proposed by Yu et al. [38], which is “balanced” to the taken positive set. A comparison of the PPI classification results training three models using these negative datasets is shown Section 3. During the training phase, the positive dataset is called gold standard positive (GSP) set and the used negative dataset is called gold standard negative (GSN) set.

In the case of testing datasets, these were selected for the sake of validating the generalisation capability of the proposed approach in PPI prediction. A group of reliable binary interaction datasets (LC-multiple, binary-GS, Uetz-screen, and Ito-core) were taken from Yu et al. [34]. These datasets have been obtained using several approaches from experimentally, computationally, and grouping datasets well known in the literature. These datasets can be freely downloaded from the website <http://interactome.dfci.harvard.edu/>. Besides, another group of used negative testing datasets is also described here. So all proposed testing datasets are the following.

- (i) The LC-Multiple Dataset. It is composed of literature-curated interactions supported by two or more publications. There are 2855 positive interactions.
- (ii) Binary-GS dataset. It is a binary gold standard set that was assembled through a computational quality reexamination that includes well-established complexes, as well as conditional interactions and well-documented direct physical interactions in the yeast proteome. There are 1253 positive interactions.
- (iii) Uetz-screen. It is the union of sets found by Uetz et al. in a proteome-scale all-by-all screen [24]. There are 671 positive interactions.
- (iv) Ito-core. It is Interactions found by Ito et al. that appear three times or more [25]. There are 829 positive interactions.
- (v) *Random Negative Dataset 1, 2*. Due to the low number of noninteracting protein data within the RRS set, three negative subsets of similar size of the proposed GSP have been utilised. These set are denoted, random dataset negative 1 (4896 pairs) and random dataset negative 2 (4898 pairs), and were also randomly selected from the Saeed and Deane negative set [22].
- (vi) *Negative Datasets Obtained Using the Proposed Hierarchical Clustering Approach*. The negative datasets obtained in the last step of the hierarchical clustering process were used as testing negative datasets. In total there are 9 datasets of 5000 examples (see Section 3).

For all the datasets, a feature extraction process was applied and the data obtained through this process were normalised in the range  $[0, 1]$  to apply the proposed method. Furthermore, in a previous step to the evaluation of our model, those interactions from every testing dataset were filtered out to remove overlapping with the training set. In this way, the possible overestimated classification accuracy is prevented through a clustering process selecting a representative negative dataset and a filtering step.

## 2.2. Feature Extraction

Feature extraction process for the proposed datasets was applied using well-known databases in proteomics, especially for yeast model organism. The calculated features cover different proteomic information integrating diverse databases: Gene Ontology Annotation (GOA) Database [42], MIPS Comprehensive Yeast Genome Database (MIPS CYGD) [43], Homologous Interactions database (HINTdb) [11], 3D Interacting Domains database (3did) [44], and SwissPfam (SwissPfam is an annotated description of how Pfam domains map to possibly multidomain SwissProt entries) [45].

Essentially, the presented approach in this paper integrates distinct protein features to design a reliable classifier of PPIs. The importance of protein domains in predicting PPIs has been already proved [4, 13, 19], so the use of SwissPfam and 3did databases was included in this process. The MIPS CYGD catalogues that cover functional, complexes, phenotype, proteins, and subcellular compartments information about yeast make it a very useful tool in PPI analysis [10, 11]. Likewise, GO data has been successfully applied in classification models [46] and so has the usage of similarity measures supporting PPI prediction [35]. Furthermore, the “interlogs” concept helps to design new approaches in proteomics such as PPI prediction, classification, and creation of reliable PPI databases [11, 22, 28]. Therefore, the HINTdb database was included in our study.

The main step in this process is the extraction of a set of features that can be associated with all possible combinations of pairs of proteins. The fundamental idea about feature extraction here consists of computing how many common terms are shared between two proteins (a given pair) in any given database. Those features would be our “basic” features, with every feature being calculated as the number of common terms that are shared by a pair of proteins in a specific database.

Although the extraction process integrates several information sources, these features in themselves do not provide enough information to estimate whether any given pair of proteins are very likely to interact [10]. Thus, reinforcing the predictive power of classification models through a specific combination of features, two new similarity measures called local and global were incorporated in this process as “extended” features. The definition of these two similarity measures would be the following.

Given a pair of proteins ( $protA$ ,  $protB$ ) and letting  $A$  be the set of all terms linked for protein  $protA$  and  $B$  the set of terms linked for protein  $protB$  in a specific database, the local similarity measure for ( $protA$ ,  $protB$ ) is defined as

$$\text{sim}_{\text{local}} = \frac{\#(A \cap B)}{\#(A \cup B)}, \quad (2.1)$$

where  $\#(A \cap B)$  represents the number of common terms in a specific database for ( $protA$ ,  $protB$ ) and  $\#(A \cup B)$  is the total number of all terms in the union of sets  $A$  and  $B$ .

In a similar way, the global similarity measure is calculated as the ratio of common terms shared by a given pair ( $protA$ ,  $protB$ ) with respect to the sum of all terms in a specific database. This measure is calculated as

$$\text{sim}_{\text{global}} = \frac{\#(A \cap B)}{\#C}, \quad (2.2)$$

where  $C$  is the total number of terms in the complete database.

Hence, a further description of each considered database detailing the feature calculation and extraction for a given pair of proteins is summarised in Table 4. For the sake of clarity, in the following enumeration, the same information indicating between parenthesis the type of data (integer or real) and the order in the feature list is also explained.

- (i) Gene Ontology Annotation (GOA) Database [42] that provides high-quality annotation of gene ontology (GO) [37]. The GO project was developed to give a controlled vocabulary for the annotations of molecular attributes in different model organisms. These annotations are classified in GOA into three structured ontologies that describe molecular function (F), biological process (P), and cellular component (C). Each ontology is organised as a directed acyclic graph (DAG). We extract the IDs (identifiers) of the GO terms associated with each protein calculating the common GO annotation terms between both proteins in the three ontologies (P, C, and F) (1st integer) and their local and global similarity measures (12th real, 13th real). Moreover, we considered each ontology separately (4th P integer, 5th C integer, and 6th F integer) and their respective local (15th real, 16th real, and 17th real) and global similarity measures (18th real, 19th real, and 20th real).
- (ii) Homologous Interactions database (HINTdb) [11] is a collection of protein-protein interactions and their homologs in one or more model organisms. Homology refers

to any similarity between characteristics that is because of their shared ancestry. The number of homologs between both proteins obtained from HintDB is the 2nd feature (integer).

- (iii) MIPS Comprehensive Yeast Genome Database (MIPS CYGD) [43] gathers information on molecular structure and functional network in yeast. All catalogues are considered: functional, complexes, phenotype, proteins, and subcellular compartments. Considering each MIPS catalogue separately, the number of common terms (using the catalogue identifier) is calculated between both proteins (functional 7th integer, complexes 8th integer, proteins 9th integer, phenotypes 10th integer, and subcellular compartments 11th integer). Moreover, their local similarity measures are considered (21st real, 22nd real, 23rd real, 24th real, 25th real).
- (iv) 3D Interacting Domains database (3did) [44] is a collection of domain-domain interactions in proteins for which high-resolution three-dimensional structures are known in the Protein Data Bank (PDB) [47]. 3did exploits structural information to support critical molecular details necessary for better understanding how interactions occur. This database also provides an overview of how similar in structure are interactions between different members of the same protein family. The database also stores gene ontology-based functional annotations and interactions between yeast proteins from large-scale interaction discovery analysis. The 3rd feature (integer) is calculated as the common Pfam domains between both proteins, extracted from SwissPfam, which are found in the 3did database. The 3rd feature divided by the total Pfam domains that are associated with both proteins is the 14th feature (real).
- (v) SwissPfam [45] from UniProt database [48] is a compilation of domain structures from SWISSPROT and TrEMBL [45] according to Pfam [49]. Pfam is a database of protein families that stores their annotations and multiple sequence alignments created using hidden Markov models (HMM). No feature is directly associated with this database, but it is used in combination with the 3did database to calculate the 3rd and 14th features.

### 2.3. Feature Selection: Mutual Information and mRMR Criterion

In pattern recognition theory, patterns are represented by a set of variables (features) or measures. Such pattern is a point in an  $n$ -dimensional features space. The main goal is to select features that distinguish uniquely between patterns of different classes. Normally, the optimal set of features is unknown and commonly has an irrelevant number or redundant features. In this way, through a pattern recognition process, these irrelevant or redundant features are filtered out greatly improving the learning performance of classifiers [40, 41]. This reduction in the number of features, also known as *feature selection*, allows to simplify the model complexity, as it gives a better visualisation and understanding of used data [50]. In this work, we consider the PPI prediction as a classification problem, so each sample point represents a pair of proteins that must be classified into one out of two possible classes: noninteracting or interacting pair.

The feature selection algorithm can be classified in two groups: filter and wrapper [50, 51]. The filter methods choose a subset of features by means of a preprocessed step independently of used machine learning algorithm. The wrapper methods use the classifier performance to assess the goodness of the features subset. Other authors have utilised



a combination of filter and wrapper algorithms [39]; in fact, in this work, a combination between filter and wrapper is used. First, a filter method is applied in order to obtain the relevance of features and subsequently a wrapper method is performed using support vector machine models from the obtained relevance order.

Different criteria have been applied to evaluate the goodness of a feature [50, 52]. In this case, the proposed filter features selection method is based on mutual information as relevance measure and redundancy between the features through minimal-redundancy-maximal-relevance criterion (mRMR) proposed by Peng et al. [39].

Let  $X$  and  $Y$  be two random continuous variables with marginal pdfs  $p(x)$  and  $p(y)$ , respectively, and joint probability density function (pdf)  $p(x, y)$ . The mutual information between  $X$  and  $Y$  can be represented as [50, 53].

$$I(X, Y) = \iint p(x, y) \log \frac{p(x, y)}{p(x)p(y)} dx dy. \quad (2.3)$$

In the case of discrete variables, the integral operation is reduced to a summation operation. Let  $X$  and  $Y$  be two discrete variables with mathematical alphabets  $\mathcal{X}$  and  $\mathcal{Y}$ , marginal probabilities  $p(x)$  and  $p(y)$ , respectively, and a joint probability mass function  $p(x, y)$ . The MI between  $X$  and  $Y$  is expressed as [50]

$$I(X, Y) = \sum_{x \in \mathcal{X}} \sum_{y \in \mathcal{Y}} p(x, y) \log \frac{p(x, y)}{p(x)p(y)}. \quad (2.4)$$

The mutual information (MI) has two principal properties that make it different from other dependency measures: (1) the capacity of measuring any relationship between variables and (2) its invariance under space transformations [50, 54].

For mRMR, authors considered mutual-information-based feature selection for both discrete and continuous data [39]. The MI for continuous variables was estimated using the Panzer Gaussian windows [39]. Peng et al. show that using a first-order incremental search (as a feature is selected in a time), the mRMR criterion is equal to maximum dependence, or, in other words, estimating the mutual information  $I(C, S)$  between class variable  $C$  and subset of selected features  $S$ . In Peng et al. [39], for minimizing the classification error in the incremental search algorithm, mRMR method is combined with two wrapper schemes. In a first stage, the method is used with the purpose of finding the candidate feature set. In a second stage, backward and forward selections were applied in order to find the compact feature set through the candidate feature set that minimises the classification error.

Given class variable  $C$ , the initial set of features  $F$ , an individual feature  $f_i \in F$ , and a subset of selected features  $S \subset F$ , the mRMR criterion for the first-order incremental search can be expressed as the optimisation of the following condition [39, 50]:

$$I(C; f_i) = \frac{1}{|S|} \sum_{f_s \in S} I(f_s; f_i), \quad (2.5)$$

where  $|S|$  is the cardinality of the selected feature set  $S$ ,  $f_s \in S$ .



This filter mRMR method is a fast and efficient method because of its incremental nature, showing better feature selection and accuracy in classifier including wrapper approach [39, 50].

In this work, mRMR criterion method was used as filter algorithm with the purpose of obtaining the relevance of proposed features. Subsequently, an SVM model is trained for each incremental combination of features in ascending order of relevance. Such combination of features is applied adding a feature in a time according to the relevance, starting from the most relevant one, and adding the next most relevant one until feature 25. In total, 25 SVM models are trained using grid search to estimate the hyperparameters. A parallel approach was implemented for this filter-wrapper proposal because of memory and computational requirements, reducing the time to obtain the best combination of features that minimises the error classification.

## 2.4. Support Vector Machine

In machine learning theory, support vector machine (SVM) is related to supervised learning methods that analyse data and recognise patterns in regression analysis and classification problems. In fact, a support vector machine (SVM) is a classification and regression paradigm originally invented by Vladimir Vapnik [55, 56]. In the literature, the SVM is quite popular above all in classification and regression problems mainly due to its good generalisation capability and its good performance [57]. Although SVM method was originally designed for binary-class classification, a multiclass classification methodology was presented in Wu et al. [58]. In the case of this PPI classification, it is straightforward to apply the binary-class classification between interacting and noninteracting pairs of proteins.

For a given training set of instance-label pairs  $\{\mathbf{x}_i, y_i\}$ ,  $i = 1, \dots, N$ , with input data  $\mathbf{x}_i \in \mathbb{R}^n$  and labelled output data  $y_i \in \{-1, +1\}$ , a support vector machine resolves the next optimisation problem:

$$\begin{aligned} \min_{\mathbf{w}, b, \xi} \quad & \frac{1}{2} \mathbf{w}^T \mathbf{w} + C \sum_{i=1}^N \xi_i, \\ \text{subject to} \quad & y_i (\mathbf{w}^T \phi(\mathbf{x}_i) + b) \geq 1 - \xi_i, \xi_i \geq 0. \end{aligned} \quad (2.6)$$

So the training data vectors  $\mathbf{x}_i$  are mapped into a higher-dimensional space through the  $\phi$  function.  $C$  is the hyperparameter called penalty parameter of the error term, that is, it is a real positive constant that controls the amount of misclassification allowed in the model.

Taking the problem given in (2.6) into account, the dual form of an SVM can be obtained

$$\begin{aligned} \min_{\alpha} \quad & \frac{1}{2} \alpha^T Q \alpha - \mathbf{e}^T \alpha, \\ \text{subject to} \quad & \mathbf{y}^T \alpha = 0, \\ & 0 \leq \alpha_i \leq C, \quad i = 1, \dots, N, \end{aligned} \quad (2.7)$$

where  $\mathbf{e}$  is a vector composed of all ones (all-ones vector).  $Q$  is an  $N$  by  $N$  positive semi-definite matrix given by  $Q_{ij} \equiv y_i y_j K(\mathbf{x}_i, \mathbf{x}_j)$ .  $K(\mathbf{x}_i, \mathbf{x}_j) \equiv \phi(\mathbf{x}_i)^T \phi(\mathbf{x}_j)$  is called the *kernel function* and allows the SVM algorithm to fit a maximum-margin hyperplane in a transformed feature space.

The classifier is a hyperplane in the high-dimensional feature space that may be non-linear in the original input space. In this case, for the general nonlinear SVM classifier, the decision function can be expressed as

$$y(x) = \text{sign} \left[ \sum_{i=1}^N \alpha_i y_i K(x, x_i) + b \right], \quad (2.8)$$

where parameters  $\alpha_i$  correspond to the solution of the quadratic programming problem that solves the maximum-margin optimisation problem. The training data points corresponding to nonzero  $\alpha_i$  values are called *support vectors* [59] because they are the ones that are really required to define the separating hyperplane.

The most common kernel utilised in the literature is the radial basis function (RBF) or the Gaussian kernel [60]. It can be defined as

$$K(x, x_i) = \exp(-\gamma \|x - x_i\|^2), \quad \gamma > 0, \quad (2.9)$$

where parameter  $\gamma$  controls the region of influence of every support vector.

Training an SVM implies the optimization of the  $\alpha_i$  and of the so-called hyperparameters of the model. These hyperparameters are usually calculated using gridsearch and cross-validation [59]. In the case of the RBF kernel, the hyperparameters  $C$  and  $\gamma$  are required to be optimised.

Furthermore, a score is proposed in the presented work for PPI prediction. This score is estimated using the difference of probabilities in absolute value returned by SVM model for each pair of proteins.

This score would be used as a measure of confidence in PPI classification. SVM classifies the pairs reporting two probability values that express the chance to belong to an interacting pair class or noninteracting pair class. These probabilities are obtained by the particularisation of the multiclass classification methodology introduced by Wu et al. [58] in the problem of PPI prediction (binary classification). In a general problem, given the observation  $\mathbf{x}$  and the class label  $y$ , it is assumed that the estimated pairwise class probabilities  $\mu_{ij} = P(y = i | y = i \text{ or } j, \mathbf{x})$  are available. Following the setting of the one-against-one approach for the general problem of multiclass problem with  $k$  classes, firstly, the pairwise class probabilities are estimated by  $r_{ij}$  with

$$r_{ij} \approx P(y = i | y = i \text{ or } j, \mathbf{x}) \approx \frac{1}{1 + e^{A\hat{f} + B}}, \quad (2.10)$$

where  $A$  and  $B$  are estimated by minimizing the negative log-likelihood function using known training data and  $\hat{f}$  are their decision values for these training data. In Zhang et al. [61], it is recalled that SVM decision can be easily clustered at  $\pm 1$ , making the estimate probability in (2.10) inaccurate. Therefore, ten-fold cross-validation was applied to obtain

decision values in the experimental results. The next step is obtaining  $p_i$  from these  $r_{ij}$ , solving the following optimisation problem presented in Wu et al. [58].

The implementation for SVM was taken from the library LIBSVM [62] for Matlab (in this case R2010a). Specifically, C-SVM and RBF kernel was used in the development of the presented work.

## 2.5. Clustering Methodology

A clustering approach was applied to the negative dataset proposed by Saeed and Deane [22] in order to obtain a relevant, representative, and significant negative subset for training reliable SVM models. Saeed and Deane provide more than 4 million high-quality negative pairs. Therefore, after the feature extraction process applied to this large set of pairs, the set of data to consider would be represented as a matrix whose size is more than 4 million pairs (rows) and 25 features (columns). However, such amount of data is not feasible to train a model, and there is also an overrepresentation of negative data that hides the positive samples effect.

In order to reduce this amount of negative samples to select the most relevant noninteracting pairs, a “hierarchical” clustering approach is proposed in this section which is a iterative  $k$ -means process. Due to memory and computational requirements, the clustering data of 4 million noninteracting pairs were divided into subsets which are suitable to be computed by  $k$ -means. The  $k$ -means algorithm is applied to every subset. For each  $k$ -means, the  $k$  nearest samples to centroid are taken as the most representative pairs of that specific subset. Then, these representatives are joined again creating a number of new subsets. Thus, the same process of  $k$ -means for each subset is applied in an iterative procedure as explained below.

Therefore, in the following lines, a definition of classic  $k$ -means is given. In data mining,  $k$ -means clustering [63] is a method of cluster analysis that assigns  $n$  observations into  $k$  clusters where each observation belongs to the cluster with the nearest mean. Given a set of observations  $(x_1, x_2, \dots, x_n)$ , where each observation or point is a  $d$ -dimensional real vector,  $n$  observations are then assigned into  $k$  sets ( $k \leq n$ )  $S = S_1, S_2, \dots, S_k$  minimising the within-cluster sum of squares (WCSS) [63]:

$$\arg \min_S \sum_{i=1}^k \sum_{x_j \in S_i} \|x_j - \mu_i\|^2, \quad (2.11)$$

where  $\mu_i$  is the mean of points in  $S_i$ .

Here, in the application of  $k$ -means, the used distance measure is the classical squared Euclidean distance and the clustering data is actually a matrix whose rows represent a pair of noninteracting proteins and columns represent the 25 considered features. The initial cluster centroid positions are randomly chosen from samples. Likewise,  $k$  is set to 5000 because it is a value similar to the size of the considered positive set (GSP) and also for computational performance of this “hierarchical” clustering approach.

In practice, the 4 million set was divided in subsets of 50000 pairs approximately (49665 samples) creating 84 subsets of negative samples. This division was carried out due to memory requirements of the available computing system, using the maximum allowed limit. A classical  $k$ -means clustering algorithm [63] was applied to each subset obtaining the 5000 most representative samples, that is, reducing 10% of data. Then, new subsets of 50000 negative samples were created adding the 5000 respective samples in order. And again

the  $k$ -means algorithm is applied to the new subsets obtaining the 5000 most representative samples. This process is repeated until the last 5000 most representative samples that have a similar size to the proposed positive set (see Figure 1) are obtained. This approach is a “hierarchical” and iterative  $k$ -means-based clustering algorithm that can be run in a parallel computing platform (see Section 2.6) considering the  $k$ -means clustering independently in every iteration.

More formally, if we pay attention to Figure 1, we can see that in Iteration 1, given an initial group of subsets of 50000 pairs approximately  $\mathbf{C} = C_1^1, C_2^1, \dots, C_1^{84}$ . As commented, the proposed “hierarchical” clustering approach is an iterative  $k$ -means process applied for each  $C_i^j$  where  $i$  is the iteration and  $j$  is the subset order. The resulting set for the  $k$ -means method is called  $R_i^j$  using the same indices  $i$  and  $j$  from the input subset  $C_i^j$ . Thus,  $R_i^j$  is formed by the set of the 5000 most representative negative samples from  $C_i^j$  selected by  $k$ -means. In the next iterations,  $C_{i+1}^j$  is the subset formed by the summation of the 10 sets of the 5000 most representative negative samples  $R_i^j$ . When it is not possible to apply the summation of every 10 subsets  $R_i^j$  because there is an inferior number of subsets, the summation is composed by the maximum number of subsets until completing all considered data. In general,  $C_i^j = \sum_{m=(j-1)*10+1}^{j*10} R_{i-1}^m$  given the iteration  $i$  and the subset  $j$ . In this paper, 3 iterations were executed until obtaining the set of the 5000 most representative negative samples from the whole set of more than 4 million negative samples. Iteration 2 shows that there were 9 subsets  $C_2^1, C_2^2, \dots, C_2^9$  where  $C_2^9$  contains 20000 pairs. The resulting subsets by  $k$ -means  $R_2^1, R_2^2, \dots, R_2^9$  create a new  $C_3^1$  of 45000 elements. In the final step,  $R_3^1$  is obtained in Iteration 3, which will be used as part of a training set as a representation of the negative space from the whole negative set. The  $R_2^1, R_2^2, \dots, R_2^9$  will be used as testing set in Section 3, and after a filtering process from the training set, they are called  $R_3^{\text{test.1}}, R_3^{\text{test.2}}, R_2^{\text{test.3}}, R_3^{\text{test.4}}, R_3^{\text{test.5}}, R_3^{\text{test.6}}, R_3^{\text{test.7}}, R_3^{\text{test.8}},$  and  $R_3^{\text{test.9}}$ .

With this process, the main goal of obtaining a representative negative dataset and not biased from a high-quality negative set is fulfilled.

## 2.6. Parallelism Approach

The filter/wrapper feature selection proposed in this work demands high computational resources. The classical and simple master-slave approach was adopted [64], a master process sends tasks and data to the slave process, and the master process receives results from slaves and controls the finalisation of the tasks. In our case, the tasks are to train SVM model including grid search for hyperparameters. Therefore, the master process sends the next data for slave processes: the selected features and the training and testing datasets. In addition, the “hierarchical”  $k$ -means clustering algorithm from the previous section could be implemented in a parallel computing platform using this approach.

The implementation of this approach was carried out using MPIMEX [65], a new interface that allows MATLAB standalone applications to call MPI (message passing interface) standard routines (it was developed in our research group). MPI is a library specification for message passing, proposed as a standard by a broadly based committee of vendors, implementers, and users as defined in <http://www.mcs.anl.gov/research/projects/mpi/>.

This parallel approach was running in a cluster of computers. This cluster was formed by 13 nodes with dual processors Intel Xeon E5320 2.86 GHz, 4 GB RAM memory, and 250 GB HDD. All nodes are connected using Gigabit Ethernet. The installed operating system is

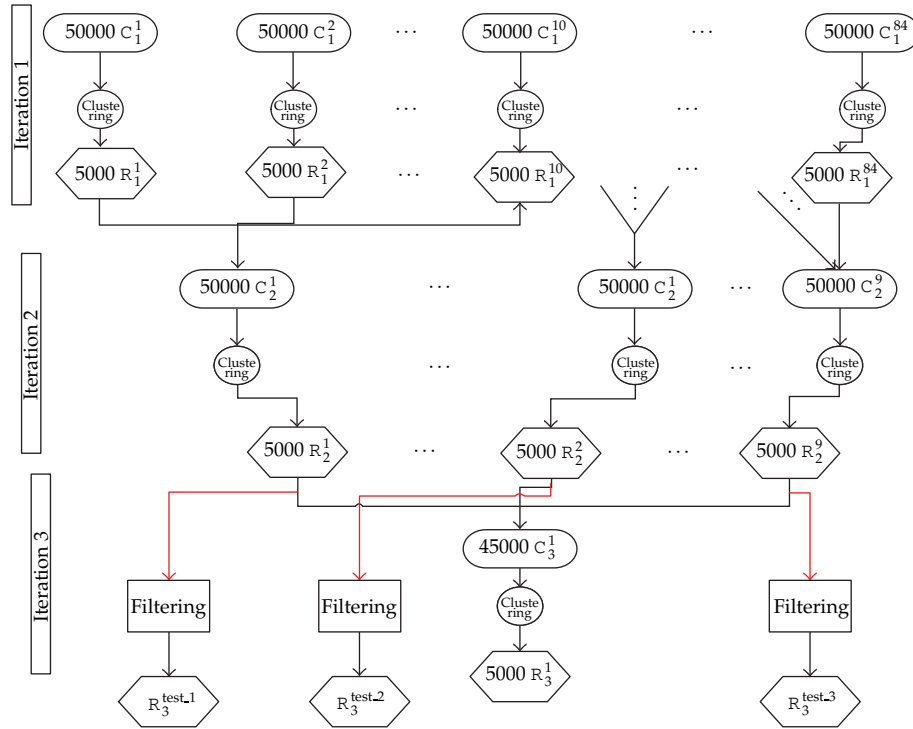


**Figure 1:** Diagram for the proposed “hierarchical”  $k$ -means-based clustering algorithm applied. It is an iterative  $k$ -means process. The application in this problem would be the selection of the 5000 most representative negative samples of the whole set.

Linux CentOS 4.6 (rocks). This cluster was purchased using public funds from the Spanish Ministry of Education Project TIN 2007-60587. The time of execution was reduced from 16 days in a single computer to 32 hours to train all the SVM models.

### 3. Results and Discussion

The results consist of two parts. In the first part, a “suboptimal” set of features is selected through the filter/wrapper feature selection process using the parallel approach. The training data for RBF-SVM model is composed by a GSP set and for a GSN set which is the set which resulted from applying iterative clustering approach as explained in section Material and Methods. In the second part, taking this suboptimal set of features, three RBF-SVM classifiers are constructed using three training sets, respectively. All training sets have the same GSP set for positive examples. In one case, the GSN set is the negative set obtained using the hierarchical clustering method from the first part and, in a second case, the GSN set is a randomly selected negative set as commented. In the third case, the GSN set was created using the approach proposed by Yu et al. [38], it is a “balanced” set to GSP. Subsequently, a comparison of the results obtained of three RBF-SVM classifiers trained with all the proposed negative datasets is discussed.

Previously the filter/wrapper feature selection process, the feature extraction process is applied to all available datasets. The 25 features were also extracted for the 4 million

negative set from Saeed and Deane [22], but, due to computational requirements, the whole set was divided into 84 subsets of 50000 samples approximately. In order to obtain a representative negative dataset of the whole negative space, the iterative  $k$ -means clustering approach was applied to these 84 subsets as explained in the Section 2.5. In total, three iterations selecting 5000 negative representative samples were realized using the clustering approach. In the first iteration, the Euclidean  $k$ -means method was applied to the 84 subsets creating 5000 centroids, and 9 new subsets (8 subsets of 50000 and the last one of 20000 negative examples) were obtained adding the selected 5000 negative representative samples of each previous subset. In the second iteration, the  $k$ -means was applied again to the 9 new subsets taking 5000 new negative representative samples of each subset and creating another new subset of 45000 samples (the representatives of 9-subset summation). In the third and last iteration, the last 5000 most representative negative samples taken as GSN set for training data were obtained from clustering the previous subset. The taken negative pairs were selected using the minimum Euclidean distance to the centroid of each cluster. A diagram of this process is represented in Figure 1.

In this way, the considered data (GSP and clustered GSN sets) was used to apply the presented paralleled filter/wrapper feature selection process. Because of memory requirements in the construction of the 25 SVM models, this data was randomly divided into 70% for training SVM and 30% for testing the performance of obtained models. Hence, four random divisions of data as 4 training/test datasets were used in this feature selection approach in a cluster of computers as commented in Section 2.6. In order to obtain the best hyperparameters for SVM models, gridsearch and 10-fold cross-validation were implemented. In Figure 2, the accuracy, sensitivity, and specificity obtained using the order of feature relevance reported by mRMR filter method are shown for all 25 SVM models. It can be observed that an excess of information may lead to overfitting, that is, the interaction information decreases when adding more features to the models, specially for testing case. The last added features were considered for mRMR method as more irrelevant or redundant than the features in the first positions. In Figure 2, it can be observed that the performance does not significantly improve after reaching 6 features, it even gets worse due to an excess of information, so the suboptimum selected set is composed of those 6 features: 13th referring to *global similarity measure for 1st feature*, *common GO terms using all ontologies*, 3rd referring to *number of SwissPfam domains for a pair in 3did*, 10th referring to *common terms for the two proteins in MIPS phenotype catalogue*, 8th referring to *common terms for the two proteins in MIPS functional catalogue*, 7th referring to *common terms for the two proteins in MIPS complexes catalogue*, and 2nd referring to *number of shared homologous proteins between a pair of proteins*.

In the selected suboptimum set, the features concerning protein complex, phenotypes, and functional data from MIPS CYGD catalogues have already been used successfully and proved themselves to be reliable in interacting prediction analysis [10, 35, 66–69]. Note that global similarity measures were also included in this suboptimum set of features with the purpose of improving the performance of the classifier in PPI prediction. At the same time, domain information (3rd feature) has provided a suitable framework in PPI prediction works [4, 13]. Moreover, the second feature refers to homology whose relevance has been shown in previous publications [11, 19, 21, 22].

In order to check if the SVM models trained with 6 features are significant, a ROC (receiver operating characteristic) was plotted using the confidence score presented in this work, previously explained in Section 2. The ROC curve shows the sensitivity values with respect to 1-specificity values. The used statistics to measure the goodness of the classification was the widely extended AUC (area under curve) [70, 71]. This statistics represents the probability



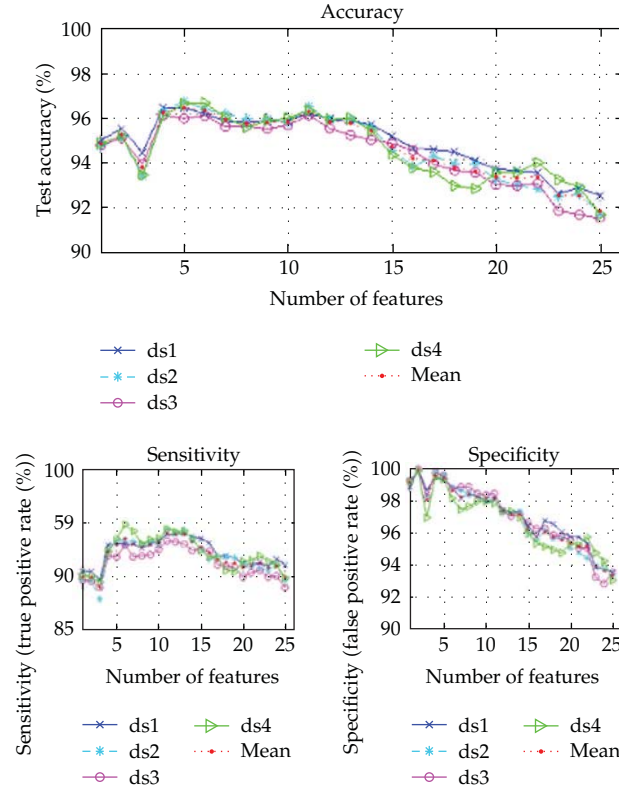


**Figure 2:** Sensitivity, specificity, and test accuracy for the four randomly partitioned datasets and their average values.

**Table 1:** Results for ROC: Area Under Curve (AUC).

Training and test group	6-feature SVM	25-feature SVM
1st	0.808	0.672
2nd	0.812	0.725
3rd	0.836	0.698
4th	0.846	0.619
Mean	0.826	0.678
Std. deviation	0.016	0.039

The ROC curve was constructed using our proposed confidence score for the four randomised sets (70% training, 30% test). The RBF kernel SVMs were trained using 6 features and 25 features. Std. standard.

that a classifier will rank a randomly chosen positive instance higher than a randomly chosen negative one. In Figure 3 and Table 1, the results for 6-feature SVM model and 25-feature SVM model showing better performance of the SVM trained with a suboptimum set are shown. As we mentioned, this reduction in the number of features implies a significant saving in memory, calculation, and other computational requirements, obtaining an overfitting utilising the whole set.

In the second part, the behaviour of our approach is tested using the selected subset of the six most relevant characteristics. Three RBF-SVM models are built with three training sets, sharing the same GSP but with a different GSN. In one case, the GSN is the negative set from



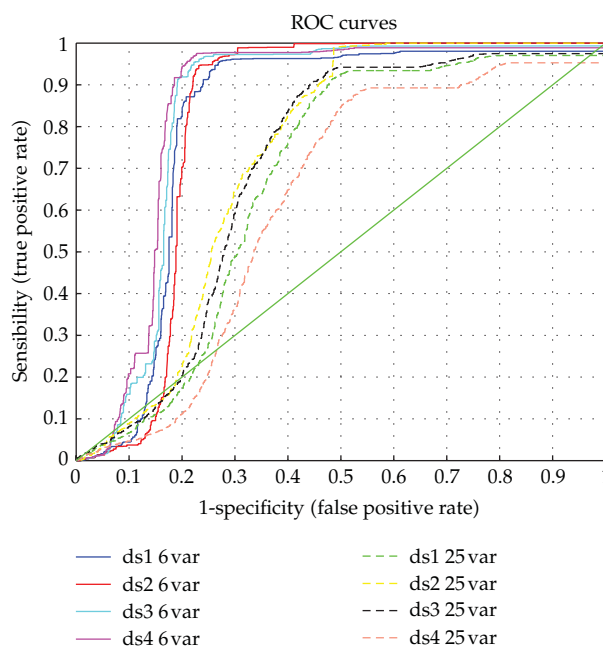


**Figure 3:** ROC curve for the four randomly partitioned groups (6 and 26 features).

the first part created using the proposed hierarchical clustering approach presented in this paper (it is also called clustered training dataset). In the second case, the GSN is a randomly selected negative set (called random training dataset), and, in the last case, the GSN is a negative set “balanced” to GSP set obtained using the approach by Yu et al. [38]. This third GSN is created using a selection of unbiased negative examples based on the frequency of the proteins in the positive set. The testing datasets, detailed in Section 2, cover both positive and negative sets and they were obtained in different ways: experimentally, from the literature, and computationally. Additionally, in order to make a reliable comparison, previous to the evaluation of our models, the interactions for each testing dataset were filtered out to avoid overlapping with the respective training set. The new sizes of the testing datasets are shown in Table 2.

Therefore, the results of these models are shown in Table 3 and Figure 4 for positive datasets and Figure 5 for negative datasets. In general, the SVM model trained using the negative set generated by the proposed hierarchical clustering approach presented in this paper has a better performance in comparison with the rest of models, that is, the models that used the randomly selected negative set and the balanced negative set. Globally, the obtained results were slightly worse in the experimental datasets than in the computational and literature datasets. The models classify the literature-extracted dataset “LC-multiple” with a range between 93 and 95% of accuracy. For the computationally obtained “binary-GS” dataset, the classifiers obtain a range of accuracy between 92 and 95%. Between the experimental datasets “Uetz-screen” [24] and “Ito-core” [25], the reported accuracies are slightly lower than for the previous datasets with ranges of 72–81% and 76–80%, respectively, for the case of the models trained with the negative set from the clustering approach and the negative set from the random selection. Nevertheless, in the case of the model trained using the “balanced” negative set, the accuracies for both datasets are about 50%. However, if we can consider the nature

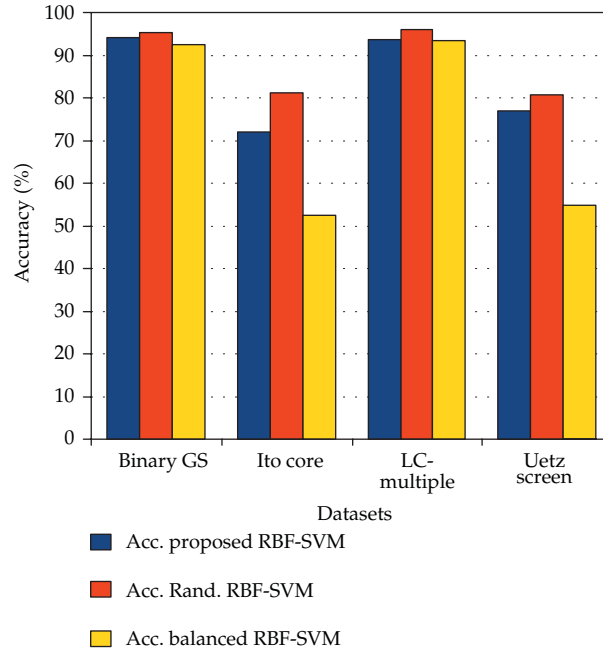


**Figure 4:** Comparison of accuracy obtained in positive datasets for the three trained models: the SVM model trained using the training set formed by the GSP set and the GSN set obtained using the proposed hierarchical clustering method (clustered), the SVM model trained using the training set where the GSN set was randomly selected (Rand. RBF-SVM) and the balanced RBF-SVM is the SVM model trained using the training set formed by the GSP set and the GSN set obtained using the approach to create a “balanced” negative set by Yu et al. [38].

**Table 2:** New sizes of datasets after filtering process.

Datasets	Size of filtering training set with GSN set obtained using the presented hierarchical clustering	Size of filtering training set with randomly selected GSN set	Size of filtering training set with “balanced” GSN set obtained from the approach by Yu et al. [38]
Binary-GS	933	937	987
Ito-core	680	686	700
LC-multiple	2362	2380	2468
Uetz-screen	574	584	594
Random negative dataset 1	4893	4894	4894
Random negative dataset 2	4895	4894	4898
$R_3^{\text{test.1}}$	4735	4995	4992
$R_3^{\text{test.2}}$	4788	4995	4994
$R_3^{\text{test.3}}$	4814	4991	4991
$R_3^{\text{test.4}}$	4844	4987	4992
$R_3^{\text{test.5}}$	4854	4983	4986
$R_3^{\text{test.6}}$	4816	4991	4994
$R_3^{\text{test.7}}$	4837	4985	4990
$R_3^{\text{test.8}}$	4797	4994	4994
$R_3^{\text{test.9}}$	4873	4994	4996

**Table 3:** Accuracy using the 6 most relevant features for three RBF-SVM models.

Datasets	Acc. Our proposal RBF-SVM	Acc. Rand. RBF-SVM	Acc. "balanced" RBF-SVM	% relative difference for our proposal versus "Rand" model	% relative difference for our proposal versus "balanced" model
Binary-GS	94,111	95,411	92,401	-1,381	1,817
Ito-core	72,059	81,195	52,571	-12,678	27,045
LC-multiple	93,750	95,924	93,517	-2,319	0,249
Uetz-screen	76,857	80,822	54,882	-5,159	28,592
Random negative dataset 1	72,211	38,353	6,537	46,888	90,947
Random negative dataset 2	71,951	37,937	37,444	47,274	47,959
$R_3^{\text{test.1}}$	58,184	29,349	1,883	49,558	96,764
$R_3^{\text{test.2}}$	63,596	30,150	1,882	52,591	97,041
$R_3^{\text{test.3}}$	96,469	69,365	1,683	28,096	98,255
$R_3^{\text{test.4}}$	62,221	31,061	1,522	50,080	97,554
$R_3^{\text{test.5}}$	61,248	29,862	1,364	51,244	97,773
$R_3^{\text{test.6}}$	64,992	33,120	1,702	49,040	97,381
$R_3^{\text{test.7}}$	64,441	31,454	1,824	51,189	97,170
$R_3^{\text{test.8}}$	94,705	67,821	1,702	28,387	98,203
$R_3^{\text{test.9}}$	64,334	31,237	1,061	51,446	98,351

Acc. is the accuracy of the RBF SVM model. *Our proposal RBF-SVM* is the SVM model trained using the training set formed by the GSP set and the GSN set obtained using the proposed hierarchical clustering method. *Rand. RBF-SVM* is the SVM model trained using the training set where the GSN set was randomly selected. *"balanced" RBF-SVM* is the SVM model trained using the training set formed by the GSP set and the GSN set obtained using the approach to create a "balanced" negative set by Yu et al. [38]. % relative difference is the percentage of relative difference using "our proposal RBF-SVM" as basis.

and complexity of the filtering in experimental data, the obtained accuracy is still satisfactory at least in the case of the model trained using the negative set from the clustering approach. Referring to the different negative datasets in the training data, the model trained using the negative set extracted by clustering method attained better results than the model trained using a randomly selected negative set. The obtained minimum relative difference is about 28% compared to the randomly selected negative set, and the maximum difference is about 90% in the case of the model trained using the "balanced" negative set. The negative set obtained by the "hierarchical" approach has a relevant representation of the negative search space from a large high-reliability negative set from Saeed and Deane [22]. But in the case of the "balanced" negative set, this is not happening, the negative set is "balanced" to the positive side in the training data but it is not enough to recognise any negative case. Hence, the obtained results of the model predicting negative datasets are worse than the results in the classification of positive datasets. Nonetheless, the difficulty and complexity to predict negatives make the results still acceptable. It can be observed that the relative difference in positive datasets is better for the model trained with the randomly selected negative set but that difference is not so strong, it can even be a slightly overestimation. The accuracy could be artificially inflated by a bias towards dominant samples in the positive data as Yu et al. showed [38]. With such a suboptimum set of features, an SVM model is able to classify PPIs with relative notorious accuracy in any positive and negative datasets.

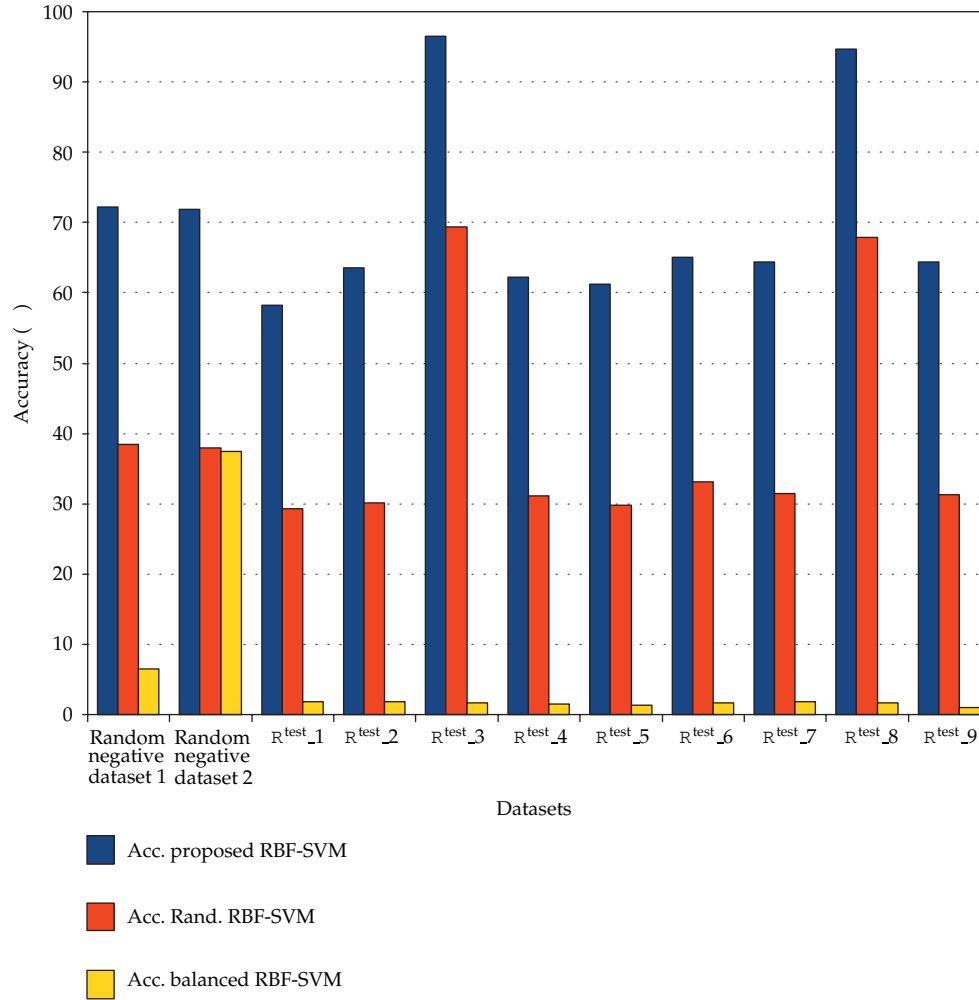


**Figure 5:** Comparison of accuracy obtained in negative datasets for the two trained models: the SVM model trained using the training set formed by the GSP set and the GSN set obtained using the proposed hierarchical clustering method (clustered) and the SVM model trained using the training set where the GSN set was randomly selected (Rand. RBF-SVM) and the balanced RBF-SVM is the SVM model trained using the training set formed by the GSP set and the GSN set obtained using the approach to create a “balanced” negative. Please note that  $R^{\text{test}}_1, R^{\text{test}}_2, R^{\text{test}}_3, R^{\text{test}}_4, R^{\text{test}}_5, R^{\text{test}}_6, R^{\text{test}}_7, R^{\text{test}}_8$ , and  $R^{\text{test}}_9$  correspond to:  $R_3^{\text{test}.1}, R_3^{\text{test}.2}, R_2^{\text{test}.3}, R_3^{\text{test}.4}, R_3^{\text{test}.5}, R_3^{\text{test}.6}, R_3^{\text{test}.7}, R_3^{\text{test}.8}$ , and  $R_3^{\text{test}.9}$ . And the “balanced” negative set is created using the approach by Yu et al. [38].

First, in Patil and Nakamura [19], the authors used a Bayesian approach, previously proposed by Jansen et al. [10] with only three features for the filtering out of high-throughput datasets of the organisms *Saccharomyces cerevisiae* (Yeast), *Caenorhabditis elegans*, *Drosophila melanogaster*, and *Homo sapiens*. Their model was able to obtain a sensibility of 89.7% and a specificity of 62.9%, being only capable of attaining a prediction accuracy of 56.3% for true interactions for the datasets Y2H, external to the model. For two datasets called “Ito” and “Uetz” (see Table 3), the presented model trained with the negative set from clustering method reported classification rates between 76 and 93%. In Jiang and Keating [72], a mixed framework is proposed combining high-quality data filtering with decision trees in PPI prediction,

**Table 4:** Description of the 25 extracted features.

Number	Description	Type
1st	$\#(A_{GOA} \cap B_{GOA})$ from GOA DB taking 3 ontologies together (P,F,C)	Integer
2nd	Number of homologs for $(protA, ProtB)$ from HINTdb	integer
3rd	$\#[(A_{SPFAM} \cap 3DID) + (B_{SPFAM} \cap 3DID)]$ , $A$ and $B$ are domains extracted from SwissPfam, 3DID is 3did database	Integer
4th	$\#(A_{GOA-P} \cap B_{GOA-P})$ from GOA DB taking Biological Process ontology	Integer
5th	$\#(A_{GOA-C} \cap B_{GOA-C})$ from GOA DB taking Cellular Compartment ontology	integer
6th	$\#(A_{GOA-F} \cap B_{GOA-F})$ from GOA DB taking Molecular Function ontology	integer
7th	$\#(A_{MIPS-F} \cap B_{MIPS-F})$ from functional MIPS catalogue identifiers	integer
8th	$\#(A_{MIPS-C} \cap B_{MIPS-C})$ from complexes MIPS catalogue identifiers	integer
9th	$\#(A_{MIPS-P} \cap B_{MIPS-P})$ from proteins MIPS catalogue identifiers	integer
10th	$\#(A_{MIPS-FE} \cap B_{MIPS-FE})$ from phenotypes MIPS catalogue identifiers	integer
11th	$\#(A_{MIPS-FCC} \cap B_{MIPS-FCC})$ from subcellular compartments MIPS catalogue identifiers	integer
12th	Local similarity of 1st feature	real
13th	Global similarity of 1st feature	real
14th	$\#[((A_{SPFAM} \cap 3DID) + (B_{SPFAM} \cap 3DID))]/\#(A_{SPFAM} \cup B_{SPFAM})$	Real
15th	Local similarity of 4th feature	real
16th	Local similarity of 5th feature	real
17th	Local similarity of 6th feature	real
18th	Global similarity of 4th feature	real
19th	Global similarity of 5th feature	Real
20th	Global similarity of 6th feature	Real
21th	Local similarity of 7th feature	Real
22th	Local similarity of 8th feature	Real
23th	Local similarity of 9th feature	Real
24th	Local similarity of 10th feature	Real
25th	Local similarity of 11th feature	Real

Symbol # indicates the number of elements in a set. See (2.1) and (2.2).

taking as the base the notation of all GO ontologies, aiming an accuracy in a range of 65–78%. From there, we incorporated that information in combination with other features to improve the generalisation of our approach. Other similarity measures have been proposed, mainly based on the GO annotations, for example, the works by Wu et al. [35] that were able to detect the 35% of the cellular complexes from the MIPS CYGD catalogues or the work by Wang et al. [36] for the validation of gene expression analysis. Nevertheless, the authors did not take into account the cellular component ontology because it was considered that this ontology includes ambiguous annotations that may lead to error. In this paper, we opted for proposing a set of similarity measures that permit their generalisation to a wide range of databases in the obtaining of our prediction model.

## 4. Conclusion

In this work, a new approach to build an SVM classifier in PPI prediction is presented. The approach has several notorious processes: a feature extraction using well-known databases,

a new filter-wrapper feature selection implemented in a master-slave parallel approach, and a reliable and representative negative dataset for training by the means of “hierarchical”  $k$ -means clustering. The filter method is based on the statistical concept of mutual information using mRMR criterion, which is a reliable and quick method. In addition, a confidence score is presented through a modification of SVM model implementation. A comparison between a randomly selected negative dataset, a “balanced” negative set obtained using Yu et al. approach [38], and a negative dataset obtained using the “hierarchical”  $k$ -means clustering method presented in this paper is done where the model training using the set resulted by the clustering approach has better performance. This comparison also allowed us to check the generalisation capacity of the presented approach for the sake of the evaluation of previously filtered external datasets. Hence, a fair negative selection method is presented avoiding the overestimation in the classification of PPIs.

For further work, a hierarchical parallel clustering could improve the performance of a classifier with the purpose of obtaining a balanced negative dataset using a more complex clustering algorithm. We consider applying this approach to other model organisms as *Homo sapiens*. A parallel approach was applied, which, by making a better load balancing, would be suitable to reduce time computation in the filter/wrapper feature selection approach.

In summary, we conclude that by combining data from several databases, using reliable positive and clustered negative samples for training, supporting a set of widely applicable similarity measures to the feature extraction process, and using mutual information methods for feature selection and RBF-SVM models capable of returning a confidence score, we have presented a reliable approach to the validation of protein-protein interaction datasets.

## Acknowledgments

J. M. Urquiza is supported by the FPU Research Grant AP2006-01748 from the Spanish Ministry of Education. This paper has been partially supported by the Spanish CICYT Project SAF2010-20558 and by the Regional Excellence Projects P07-TIC-02768 and P09-TIC-175476.

## References

- [1] V. Deshmukh, C. Cannings, and A. Thomas, “Estimating the parameters of a model for protein-protein interaction graphs,” *Mathematical Medicine and Biology*, vol. 23, no. 4, pp. 279–295, 2006.
- [2] D. J. Higham, G. Kalna, and J. K. Vass, “Spectral analysis of two-signed microarray expression data,” *Mathematical Medicine and Biology*, vol. 24, no. 2, pp. 131–148, 2007.
- [3] J. F. Rual, K. Venkatesan, T. Hao et al., “Towards a proteome-scale map of the human protein-protein interaction network,” *Nature*, vol. 437, no. 7062, pp. 1173–1178, 2005.
- [4] C. Huang, F. Morcos, S. P. Kanaan, S. Wuchty, D. Z. Chen, and J. A. Izaguirre, “Predicting protein-protein interactions from protein domains using a set cover approach,” *IEEE/ACM Transactions on Computational Biology and Bioinformatics*, vol. 4, no. 1, pp. 78–87, 2007.
- [5] A. J. González and L. Liao, “Predicting domain-domain interaction based on domain profiles with feature selection and support vector machines,” *BMC Bioinformatics*, vol. 11, article 537, 2010.
- [6] U. Stelzl, U. Worm, M. Lalowski et al., “A human protein-protein interaction network: a resource for annotating the proteome,” *Cell*, vol. 122, no. 6, pp. 957–968, 2005.
- [7] K. Venkatesan, J. F. Rual, A. Vazquez et al., “An empirical framework for binary interactome mapping,” *Nature Methods*, vol. 6, no. 1, pp. 83–90, 2009.
- [8] P. Braun, M. Tasan, M. Dreze et al., “An experimentally derived confidence score for binary protein-protein interactions,” *Nature Methods*, vol. 6, no. 1, pp. 91–97, 2009.
- [9] J. Yu and R. L. Finley, “Combining multiple positive training sets to generate confidence scores for protein-protein interactions,” *Bioinformatics*, vol. 25, no. 1, pp. 105–111, 2009.

- [10] R. Jansen, H. Yu, D. Greenbaum et al., "A bayesian networks approach for predicting protein-protein interactions from genomic data," *Science*, vol. 302, no. 5644, pp. 449–453, 2003.
- [11] A. Patil and H. Nakamura, "HINT—a database of annotated protein-protein interactions and their homologs," *Biophysics*, vol. 1, pp. 21–24, 2005.
- [12] I. Kim, Y. Liu, and H. Zhao, "Bayesian methods for predicting interacting protein pairs using domain information," *Biometrics*, vol. 63, no. 3, pp. 824–833, 2007.
- [13] M. Deng, S. Mehta, F. Sun, and T. Chen, "Inferring domain-domain interactions from protein-protein interactions," *Genome Research*, vol. 12, no. 10, pp. 1540–1548, 2002.
- [14] I. Iossifov, M. Krauthammer, C. Friedman et al., "Probabilistic inference of molecular networks from noisy data sources," *Bioinformatics*, vol. 20, no. 8, pp. 1205–1213, 2004.
- [15] L. V. Zhang, S. L. Wong, O. D. King, and F. P. Roth, "Predicting co-complexed protein pairs using genomic and proteomic data integration," *BMC Bioinformatics*, vol. 5, article no. 38, 2004.
- [16] Y. Liu, I. Kim, and H. Zhao, "Protein interaction predictions from diverse sources," *Drug Discovery Today*, vol. 13, no. 9–10, pp. 409–416, 2008.
- [17] A. Ben-Hur and W. S. Noble, "Kernel methods for predicting protein-protein interactions," *Bioinformatics*, vol. 21, no. 1, pp. i38–i46, 2005.
- [18] R. A. Craig and L. Liao, "Improving protein-protein interaction prediction based on phylogenetic information using a least-squares support vector machine," *Annals of the New York Academy of Sciences*, vol. 1115, pp. 154–167, 2007.
- [19] A. Patil and H. Nakamura, "Filtering high-throughput protein-protein interaction data using a combination of genomic features," *BMC Bioinformatics*, vol. 6, article no. 100, 2005.
- [20] F. Azuaje, H. Wang, H. Zheng, O. Bodenreider, and A. Chesneau, "Predictive integration of gene ontology-driven similarity and functional interactions," in *Proceedings of the 6th IEEE International Conference on Data Mining*, pp. 114–119, 2006.
- [21] C. M. Deane, L. Salwiński, I. Xenarios, and D. Eisenberg, "Protein interactions: two methods for assessment of the reliability of high throughput observations," *Molecular and Cellular Proteomics*, vol. 1, no. 5, pp. 349–356, 2002.
- [22] R. Saeed and C. Deane, "An assessment of the uses of homologous interactions," *Bioinformatics*, vol. 24, no. 5, pp. 689–695, 2008.
- [23] M. Pellegrini, D. Haynor, and J. M. Johnson, "Protein interaction networks," *Expert Review of Proteomics*, vol. 1, no. 2, pp. 239–249, 2004.
- [24] P. Uetz, L. Glot, G. Cagney et al., "A comprehensive analysis of protein-protein interactions in *Saccharomyces cerevisiae*," *Nature*, vol. 403, no. 6770, pp. 623–627, 2000.
- [25] T. Ito, T. Chiba, R. Ozawa, M. Yoshida, M. Hattori, and Y. Sakaki, "A comprehensive two-hybrid analysis to explore the yeast protein interactome," *Proceedings of the National Academy of Sciences of the United States of America*, vol. 98, no. 8, pp. 4569–4574, 2001.
- [26] A. C. Gavin, M. Bösch, R. Krause et al., "Functional organization of the yeast proteome by systematic analysis of protein complexes," *Nature*, vol. 415, no. 6868, pp. 141–147, 2002.
- [27] Y. Ho, A. Gruhler, A. Heilbut et al., "Systematic identification of protein complexes in *Saccharomyces cerevisiae* by mass spectrometry," *Nature*, vol. 415, no. 6868, pp. 180–183, 2002.
- [28] A. J. M. Walhout, R. Sordella, X. Lu et al., "Protein interaction mapping in *C. elegans* Using proteins involved in vulval development," *Science*, vol. 287, no. 5450, pp. 116–122, 2000.
- [29] S. Li, C. M. Armstrong, N. Bertin et al., "A map of the interactome network of the metazoan *C. elegans*," *Science*, vol. 303, no. 5657, pp. 540–543, 2004.
- [30] L. Giot, J. S. Bader, C. Brouwer et al., "A protein interaction map of *Drosophila melanogaster*," *Science*, vol. 302, no. 5651, pp. 1727–1736, 2003.
- [31] E. Formstecher, S. Aresta, V. Collura et al., "Protein interaction mapping: a *Drosophila* case study," *Genome Research*, vol. 15, no. 3, pp. 376–384, 2005.
- [32] T. Bouwmeester, A. Bauch, H. Ruffner et al., "A physical and functional map of the human TNF- $\alpha$ /NF- $\kappa$ B signal transduction pathway," *Nature Cell Biology*, vol. 6, no. 2, pp. 97–105, 2004.
- [33] Y. Qi, J. Klein-Seetharaman, and Z. Bar-Joseph, "Random forest similarity for protein-protein interaction prediction from multiple sources," in *Proceedings of the Pacific Symposium on Biocomputing*, pp. 531–542, 2005.
- [34] H. Yu, P. Braun, M. A. Yildirim et al., "High-quality binary protein interaction map of the yeast interactome network," *Science*, vol. 322, no. 5898, pp. 104–110, 2008.
- [35] X. Wu, L. Zhu, J. Guo, D. Y. Zhang, and K. Lin, "Prediction of yeast protein-protein interaction network: insights from the Gene Ontology and annotations," *Nucleic Acids Research*, vol. 34, no. 7, pp. 2137–2150, 2006.



- [36] H. Wang, F. Azuaje, O. Bodenreider, and J. Dopazo, "Gene expression correlation and gene ontology-based similarity: an assessment of quantitative relationships," in *Proceedings of the IEEE Symposium on Computational Intelligence in Bioinformatics and Computational Biology (CIBCB '04)*, pp. 25–31, 2004.
- [37] G. O. Consortium, "The gene ontology (GO) database and informatics resource," *Nucleic Acids Research*, vol. 32, pp. D258–D261, 2004.
- [38] J. Yu, M. Guo, C. J. Needham, Y. Huang, L. Cai, and D. R. Westhead, "Simple sequence-based kernels do not predict protein-protein interactions," *Bioinformatics*, vol. 26, no. 20, Article ID btq483, pp. 2610–2614, 2010.
- [39] H. Peng, F. Long, and C. Ding, "Feature selection based on mutual information: criteria of Max-Dependency, Max-Relevance, and Min-Redundancy," *IEEE Transactions on Pattern Analysis and Machine Intelligence*, vol. 27, no. 8, pp. 1226–1238, 2005.
- [40] P. Block, J. Paern, E. Hüllermeier, P. Sanschagrin, C. A. Sottriffer, and G. Klebe, "Physicochemical descriptors to discriminate protein-protein interactions in permanent and transient complexes selected by means of machine learning algorithms," *Proteins: Structure, Function and Genetics*, vol. 65, no. 3, pp. 607–622, 2006.
- [41] M. J. Mizianty and L. Kurgan, "Modular prediction of protein structural classes from sequences of twilight-zone identity with predicting sequences," *BMC Bioinformatics*, vol. 10, article 414, 2009.
- [42] E. Camon, M. Magrane, D. Barrell et al., "The gene ontology annotation (GOA) database: sharing knowledge in uniprot with gene oncology," *Nucleic Acids Research*, vol. 32, pp. D262–D266, 2004.
- [43] U. Güldener, M. Münsterkötter, G. Kastenmüller et al., "CYGD: the comprehensive yeast genome database," *Nucleic Acids Research*, vol. 33, pp. D364–D368, 2005.
- [44] A. Stein, R. B. Russell, and P. Aloy, "3did: interacting protein domains of known three-dimensional structure," *Nucleic Acids Research*, vol. 33, pp. D413–D417, 2005.
- [45] B. Boeckmann, A. Bairoch, R. Apweiler et al., "The SWISS-PROT protein knowledgebase and its supplement TrEMBL in 2003," *Nucleic Acids Research*, vol. 31, no. 1, pp. 365–370, 2003.
- [46] R. Roslan, R. M. Othman, Z. A. Shah et al., "Utilizing shared interacting domain patterns and Gene Ontology information to improve protein-protein interaction prediction," *Computers in Biology and Medicine*, vol. 40, no. 6, pp. 555–564, 2010.
- [47] H. M. Berman, J. Westbrook, Z. Feng et al., "The protein data bank," *Nucleic Acids Research*, vol. 28, no. 1, pp. 235–242, 2000.
- [48] T. U. Consortium, "The universal protein resource (UniProt)," *Nucleic Acids Research*, vol. 35, pp. D193–D197, 2007.
- [49] R. D. Finn, J. Tate, J. Mistry et al., "The Pfam protein families database," *Nucleic Acids Research*, vol. 36, no. 1, pp. D281–D288, 2008.
- [50] P. A. Estévez, M. Tesmer, C. A. Perez, and J. M. Zurada, "Normalized mutual information feature selection," *IEEE Transactions on Neural Networks*, vol. 20, no. 2, pp. 189–201, 2009.
- [51] G. John, R. Kohavi, and K. Pfleger, "Irrelevant features and the subset selection problem," in *Proceedings of the International Conference on Machine Learning*, pp. 121–126, 1994.
- [52] J. Bins and B. A. Draper, "Feature selection from huge feature sets," in *Proceedings of the 8th International Conference on Computer Vision*, vol. 2, pp. 159–165, July 2001.
- [53] T. M. Cover and J. A. Thomas, *Elements of Information Theory*, John Wiley & Sons, Hoboken, NJ, USA, Second edition, 2006.
- [54] S. Kullback, *Information Theory and Statistics*, Dover Publications, Mineola, NY, USA, 1997.
- [55] C. Cortes and V. Vapnik, "Support-vector networks," *Machine Learning*, vol. 20, no. 3, pp. 273–297, 1995.
- [56] L. J. Herrera, H. Pomares, I. Rojas, A. Guillén, A. Prieto, and O. Valenzuela, "Recursive prediction for long term time series forecasting using advanced models," *Neurocomputing*, vol. 70, no. 16–18, pp. 2870–2880, 2007.
- [57] A. Statnikov, L. Wang, and C. F. Aliferis, "A comprehensive comparison of random forests and support vector machines for microarray-based cancer classification," *BMC Bioinformatics*, vol. 9, article 319, 2008.
- [58] T. Wu, C. Lin, and R. C. Weng, "Probability estimates for multi-class classification by pairwise coupling," *Journal of Machine Learning Research*, vol. 5, pp. 975–1005, 2004.
- [59] J. A. K. Suykens, T. V. Gestel, J. D. Brabanter, B. D. Moor, and J. Vandewalle, *Least Squares Support Vector Machines*, World Scientific Publishing Company, 2003.
- [60] I. Rojas, H. Pomares, J. Gonzáles et al., "Analysis of the functional block involved in the design of radial basis function networks," *Neural Processing Letters*, vol. 12, no. 1, pp. 1–17, 2000.

- [61] T. Zhang, "Statistical behavior and consistency of classification methods based on convex risk minimization," *The Annals of Statistics*, vol. 32, no. 1, pp. 56–85, 2004.
- [62] C. Chang and C. Lin, LIBSVM: a Library for Support Vector Machines, 2001, <http://www.csie.ntu.edu.tw/~main.php>.
- [63] J. Macqueen, "Some methods for classification and analysis of multivariate observations," in *Proceedings of the 5th Berkeley Symposium on Mathematical Statistics and Probability*, pp. 281–297, University of California Press, Berkeley, Calif, USA, 1967.
- [64] A. Guillén, H. Pomares, J. González, I. Rojas, O. Valenzuela, and B. Prieto, "Parallel multiobjective memetic RBFNNs design and feature selection for function approximation problems," *Neurocomputing*, vol. 72, no. 16–18, pp. 3541–3555, 2009.
- [65] A. Guillen, D. Sovilj, A. Lendasse, F. Mateo, and I. Rojas, "Minimising the delta test for variable selection in regression problems," *International Journal of High Performance Systems Architecture*, vol. 1, no. 4, pp. 269–281, 2008.
- [66] A. Kumar, S. Agarwal, J. A. Heyman et al., "Subcellular localization of the yeast proteome," *Genes and Development*, vol. 16, no. 6, pp. 707–719, 2002.
- [67] F. Browne, H. Wang, H. Zheng, and F. Azuaje, "Supervised statistical and machine learning approaches to inferring pairwise and module-based protein interaction networks," in *Proceedings of the 7th IEEE International Conference on Bioinformatics and Bioengineering*, pp. 1365–1369, 2007.
- [68] H. Zheng, H. Wang, and D. H. Glass, "Integration of genomic data for inferring protein complexes from global protein-protein interaction networks," *IEEE Transactions on Systems, Man, and Cybernetics Part B*, vol. 38, no. 1, pp. 5–16, 2008.
- [69] F. Browne, H. Wang, H. Zheng, and F. Azuaje, "A knowledge-driven probabilistic framework for the prediction of protein-protein interaction networks," *Computers in Biology and Medicine*, vol. 40, no. 3, pp. 306–317, 2010.
- [70] J. Fogarty, R. S. Baker, and S. E. Hudson, "Case studies in the use of ROC curve analysis for sensor-based estimates in human computer interaction," in *Proceedings of the Graphics Interface (GI '05)*, pp. 129–136, Canadian Human-Computer Communications Society, Victoria, Canada, 2005.
- [71] J. A. Hanley and B. J. McNeil, "A method of comparing the areas under receiver operating characteristic curves derived from the same cases," *Radiology*, vol. 148, no. 3, pp. 839–843, 1983.
- [72] T. Jiang and A. E. Keating, "AVID: an integrative framework for discovering functional relationship among proteins," *BMC Bioinformatics*, vol. 6, article 136, 2005.

## Research Article

# General Computational Model for Human Musculoskeletal System of Spine

**Kyungsoo Kim,<sup>1</sup> Yoon Hyuk Kim,<sup>2,3</sup> and SuKyoung Lee<sup>4</sup>**

<sup>1</sup> Department of Mathematics, Kyonggi University, Suwon 443-760, Republic of Korea

<sup>2</sup> Department of Mechanical Engineering, Kyung Hee University, Yongin 446-701, Republic of Korea

<sup>3</sup> e-Spine Center, Kyung Hee University, Yongin 446-701, Republic of Korea

<sup>4</sup> Department of Computer Science, Yonsei University, Seoul 120-749, Republic of Korea

Correspondence should be addressed to Yoon Hyuk Kim, yoonhkim@khu.ac.kr

Received 30 September 2011; Accepted 14 November 2011

Academic Editor: Chang-Hwan Im

Copyright © 2012 Kyungsoo Kim et al. This is an open access article distributed under the Creative Commons Attribution License, which permits unrestricted use, distribution, and reproduction in any medium, provided the original work is properly cited.

A general computational model of the human lumbar spine and trunk muscles including optimization formulations was provided. For a given condition, the trunk muscle forces could be predicted considering the human physiology including the follower load concept. The feasibility of the solution could be indirectly validated by comparing the compressive force, the shear force, and the joint moment. The presented general computational model and optimization technology can be fundamental tools to understand the control principle of human trunk muscles.

## 1. Introduction

The human lumbar spine can support large loads during daily activities such as standing, walking, running, and lifting, where the loads are up to several thousand Newtons [1, 2]. However, it has been reported in experimental studies [3, 4] that an intact ligamentous lumbar spine buckled at the load less than 100 N when a load was applied at the superior end in the vertical direction. Although the trunk muscles have been known to play an important role to withstand external loads [5–7], the principle of trunk muscle activation to obtain such load-carrying capacity of the spine has not been elucidated. Recent experimental studies [4, 8] have demonstrated that the load-carrying capacity of the human spine significantly increased as the load applied to the spine was transferred along a path that approximates its curvature, which is called a follower load path originated from the field of mechanical engineering to solve the problems associated with the stability of columns [9, 10] since the 1950s. In the follower load case, a nearly compressive force was produced in the spine with a small shear force. The follower load concept is a possible principle of muscle activation pattern.

It is not easy to directly investigate trunk muscle activations because there have been difficulties in the in vivo measurements of the activated muscle forces, and the responses of the lumbar spine, such as the intradiscal pressure, resultant joint forces and moments at each vertebral joint. Thus, the computational modeling of the human musculoskeletal system is indispensable to predict the forces of the muscles and the responses of the lumbar spine. Several computational models of the lumbar spine and trunk muscles have been developed to estimate the trunk muscle forces [5, 11–21]. Although the follower load concept was considered in [14, 16–21], it is necessary to improve the generality of model to reflect the physiological conditions of the human spine. In this study, a general computational model of the human lumbar spine and trunk muscles including optimization formulations was provided to predict muscle forces based on the follower load. A three-dimensional numerical example was tested to validate the given model.

## 2. Preliminaries

### 2.1. Finite Element Model of the Spine and Trunk Muscles

In this paper, the fundamental definitions and notations were based on [17]. A part of the human spine consisting of  $N$  vertebrae and  $M$  trunk muscles is considered. Each spinal motion segment consisting of vertebra-intervertebral disc vertebra is modeled as a linear elastic beam element located at the vertebral body centers. Position vector of the  $i$ th vertebral body center is given as a node by  $\mathbf{p}_i$ ,  $i = 1, 2, \dots, N$ . Let  $F_k^m$  and  $PCSA_k$  be the  $k$ th muscle force and the physiological cross-sectional area of the  $k$ th muscle for  $k = 1, 2, \dots, M$ . Assume that there are  $M_i$  muscles acting on  $i$ th vertebra among  $M$  trunk muscles and  $F_{i,j}^m$ ,  $j = 1, 2, \dots, M_i$ , denotes the  $j$ th muscle force vector starting from the attachment point in  $i$ th vertebra. Let  $\mathbf{p}_{i,j}$  be the position vector of the attachment point of  $j$ th muscle acting on  $i$ th vertebra. Geometric data such as vertebral positions and locations of muscle attachment points can be obtained from published anatomical data of the human spine and muscles [11, 22].

### 2.2. Static Equilibrium Equations

Let us assume that the spinal system is in static equilibrium. The displacements including translations and rotations of each beam element are related with the forces and the moments acting on the vertebral body centers. Let us call these forces and moments motion segment forces and motion segment moments, respectively. The relation between the motion segment forces and the motion segment moments, and the displacements at vertebral nodes, could be defined as

$$\begin{bmatrix} \mathbf{F}_1^{ms} \\ \vdots \\ \mathbf{F}_N^{ms} \\ \mathbf{M}_1^{ms} \\ \vdots \\ \mathbf{M}_N^{ms} \end{bmatrix} = \mathbf{K} \cdot \begin{bmatrix} \mathbf{d}_1 \\ \mathbf{d}_2 \\ \vdots \\ \mathbf{d}_N \end{bmatrix}, \quad (2.1)$$

where  $\mathbf{F}_i^{ms}$ ,  $\mathbf{M}_i^{ms}$ , and  $\mathbf{d}_i$ , denote the motion segment force, the motion segment moment, and the displacement vectors at  $i$ th vertebral body center, respectively.  $\mathbf{K}$  represents the stiffness matrix describing linear elasticity of the spine model. The stiffness matrix  $\mathbf{K}$  of the motion segment can be obtained from experimental studies such as [23, 24]. The displacement vector  $\mathbf{d}_i$  at  $i$ th node consists of the translation components,  $d_{i,k}^t$ ,  $k = 1, 2, \dots, K$ , and the rotation components,  $d_{i,l}^r$ ,  $l = 1, 2, \dots, L$ , where  $K$  and  $L$  are the number of translational and rotational degrees of freedom at each node, respectively.

Then, for given external forces  $\mathbf{F}_i^e$  and moments  $\mathbf{M}_i^e$  applied at  $i$ th vertebral body center, the static equilibrium equations at the vertebral nodes can be formulated by

$$\sum_{j=1}^{M_i} \mathbf{F}_{i,j}^m - \mathbf{F}_i^{ms} + \mathbf{F}_i^e = \mathbf{0}, \quad i = 1, 2, \dots, N, \quad (2.2)$$

$$\sum_{j=1}^{M_i} \mathbf{r}_{i,j} \times \mathbf{F}_{i,j}^m - \mathbf{M}_i^{ms} + \mathbf{M}_i^e = \mathbf{0}, \quad i = 1, 2, \dots, N, \quad (2.3)$$

where  $\mathbf{r}_{i,j} = \mathbf{p}_i - \mathbf{p}_{i,j}$  for all  $i$  and  $j$ , represents the moment arm of the muscle force.

### 2.3. Resultant Joint Force and Resultant Joint Moment

The resultant joint force at each vertebra is the sum of all the muscle forces, the applied external forces, and the force transmitted from the upper vertebra. Hence, the resultant joint force,  $\mathbf{F}_i^{jt}$ , at  $i$ th vertebra is calculated iteratively: for  $i = 1, 2, \dots, N$ ,

$$\mathbf{F}_i^{jt} = \sum_{j=1}^{M_i} \mathbf{F}_{i,j}^m + \mathbf{F}_i^e + \mathbf{F}_{i-1}^{jt} = \mathbf{F}_i^{ms} + \mathbf{F}_{i-1}^{jt} \quad (2.4)$$

with  $\mathbf{F}_0^{jt} = \mathbf{0}$ .

The follower load path direction at each node was defined in order to decompose the resultant joint force into the compressive force and the shear force. Let the compressive force direction vector  $\mathbf{c}_i$  at  $i$ th node be

$$\mathbf{c}_i = \frac{\mathbf{p}_i - \mathbf{p}_{i-1}}{\|\mathbf{p}_i - \mathbf{p}_{i-1}\|}, \quad i = 1, 2, \dots, N, \quad (2.5)$$

under the assumption that  $\mathbf{p}_0 = \mathbf{0}$ , which indicates the direction of  $i$ th beam element.

Then,  $\mathbf{F}_i^{jt}$  can be decomposed into two perpendicular compressive forces  $\mathbf{F}_i^c = (\mathbf{F}_i^{jt} \cdot \mathbf{c}_i)\mathbf{c}_i$  and shear force  $\mathbf{F}_i^s = \mathbf{F}_i^{jt} - (\mathbf{F}_i^{jt} \cdot \mathbf{c}_i)\mathbf{c}_i$  at  $i$ th node for  $i = 1, 2, \dots, N$  (Figure 1) as

$$\mathbf{F}_i^{jt} = (\mathbf{F}_i^{jt} \cdot \mathbf{c}_i)\mathbf{c}_i + (\mathbf{F}_i^{jt} - (\mathbf{F}_i^{jt} \cdot \mathbf{c}_i)\mathbf{c}_i) = \mathbf{F}_i^c + \mathbf{F}_i^s. \quad (2.6)$$

The resultant joint moment  $\mathbf{M}_i^{jt}$  at  $i$ th node for  $i = 1, 2, \dots, N$  is the same to the motion segment moment  $\mathbf{M}_i^{ms}$ .

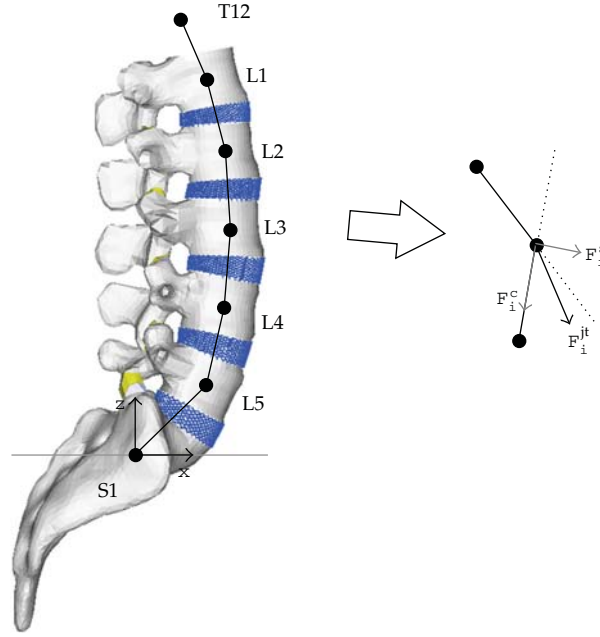


Figure 1: Decomposition of joint force  $F_i^{jt}$  into the compressive force  $F_i^c$  and the shear force  $F_i^s$ .

### 3. Formulation of Optimization Scheme

#### 3.1. Assumptions for Physiology

In this study, the displacement vector  $\mathbf{d}_i$  at  $i$ th vertebral body center for  $i = 1, 2, \dots, N$  and the  $k$ th muscle force  $F_k^m$  for  $k = 1, 2, \dots, M$  were unknowns. Since the number of unknowns is substantially larger than that of equilibrium equations (2.2) and (2.3), an optimization scheme is necessary to predict nodal displacements and muscle forces. To formulate the optimization scheme, requirements from human physiology for the spine must be considered. First, the compressive forces, the shear forces, and the joint moments at vertebral body centers should be minimized in order to avoid injuries or damages to soft tissues such as intervertebral discs or ligaments in the spine region [25]. The square sum of muscle forces and the cubic sum of muscle stresses should be minimized in order to increase the efficiency of muscle activation and to decrease the fatigue of muscles, respectively [11, 12], where the muscle stress is defined by the ratio of the muscle force to the physiological cross-sectional area of muscle. Finally, the follower load concept to minimize the shear force in comparison to the compressive force at each vertebra should be considered [25]. These multiple issues can be formulated in a multiobjective cost function as

$$f(\mathbf{d}_1, \dots, \mathbf{d}_N, F_1^m, \dots, F_M^m) = w_1 \sum_{i=1}^N \|F_i^c\|^2 + w_2 \sum_{i=1}^N \|F_i^s\|^2 + w_3 \sum_{i=1}^N \|M_i^{jt}\|^2 + w_4 \sum_{k=1}^M |F_k^m|^2 + w_5 \sum_{k=1}^M \left| \frac{F_k^m}{PCSA_k} \right|^3, \quad (3.1)$$

where  $w_1, w_2, w_3, w_4$ , and  $w_5$  are weight factors.

To find the relevant solution of the given optimization problem, the weight factors must be selected based on the quantitative relationships between physiological characteristics. However, there is little information regarding the quantitative relationships due to difficulties in experimental measurement of such in vivo characteristics. Thus, it is necessary to reduce the number of terms in the objective function under feasible assumptions. Since (2.2), (2.3), and (2.4) indicate that the resultant joint forces and moments are dependent on the muscle forces, and the square sum of muscle forces and the cubic sum of muscle stresses are calculated from the muscle forces, the objective function can be modified as

$$f(\mathbf{d}_1, \dots, \mathbf{d}_N, F_1^m, \dots, F_M^m) = w_1 \sum_{i=1}^N \|\mathbf{F}_i^c\|^2 + w_2 \sum_{i=1}^N \|\mathbf{F}_i^s\|^2 + w_3 \sum_{i=1}^N \|\mathbf{M}_i^{jt}\|^2, \quad (3.2)$$

$$f(\mathbf{d}_1, \dots, \mathbf{d}_N, F_1^m, \dots, F_M^m) = \sum_{k=1}^M |F_k^m|^2, \quad (3.3)$$

or

$$f(\mathbf{d}_1, \dots, \mathbf{d}_N, F_1^m, \dots, F_M^m) = \sum_{k=1}^M \left| \frac{F_k^m}{PCSA_k} \right|^3. \quad (3.4)$$

In addition, the follower load concept can be formulated by a constraint as

$$\|\mathbf{F}_i^c\| \leq \alpha \|\mathbf{F}_i^s\|, \quad (3.5)$$

where  $\alpha$  is a restriction coefficient for the follower load concept. The physiologically feasible upperbounds for the displacements of vertebrae and the muscle forces must also be presented.

The optimization scheme can then be formulated as follows.

Minimize

$$f(\mathbf{d}_1, \dots, \mathbf{d}_N, F_1^m, \dots, F_M^m) \quad (3.6)$$

s. t.



(1)  $\mathbf{F}^m - \mathbf{K} \cdot \mathbf{d} + \mathbf{F}^e = \mathbf{0}$ , where

$$\mathbf{F}^m = \begin{bmatrix} \sum_{j=1}^{M_1} \mathbf{F}_{1,j}^m \\ \vdots \\ \sum_{j=1}^{M_N} \mathbf{F}_{N,j}^m \\ \sum_{j=1}^{M_1} \mathbf{r}_{1,j} \times \mathbf{F}_{1,j}^m \\ \vdots \\ \sum_{j=1}^{M_N} \mathbf{r}_{N,j} \times \mathbf{F}_{N,j}^m \end{bmatrix}, \quad \mathbf{d} = \begin{bmatrix} \mathbf{d}_1 \\ \vdots \\ \vdots \\ \vdots \\ \mathbf{d}_N \end{bmatrix}, \quad \mathbf{F}^e = \begin{bmatrix} \mathbf{F}_1^e \\ \vdots \\ \mathbf{F}_N^e \\ \mathbf{M}_1^e \\ \vdots \\ \mathbf{M}_N^e \end{bmatrix}, \quad (3.7)$$

and  $\mathbf{K}$  is the stiffness matrix defined in (2.1);

- (2)  $\|\mathbf{F}_i^c\| \leq \alpha \|\mathbf{F}_i^s\|, i = 1, 2, \dots, N$ ;
- (3)  $|\mathbf{F}_k^m / PCSA_k| \leq \sigma, k = 1, 2, \dots, M$  where  $\sigma$  is the maximum muscle stress;
- (4)  $0 \leq |d_{i,k}^t| \leq d_{i,k,\max}^t$  and  $0 \leq |d_{i,l}^r| \leq d_{i,l,\max}^r, i = 1, 2, \dots, N$  where  $d_{i,k,\max}^t$  and  $d_{i,l,\max}^r$  denote the upper bounds of  $k$ th translation component and of  $l$ th rotation component of  $\mathbf{d}_i$ .

#### 4. Numerical Tests

A three-dimensional problem of the spine from T12 to S1 is tested to confirm the developed computational model and the formulation of the optimization scheme predicting the muscle forces ( $N = 7$ ). Here, 117 pairs of trunk muscles were considered ( $M = 234$ ): 5 longissimus pars lumborum, 4 iliocostalis pars lumborum, 12 longissimus pars thoracis, 8 iliocostalis pars thoracis, 11 psoas, 5 quadratus lumborum, 6 external oblique, 6 internal oblique, 1 rectus abdominus, 12 thoracic multifidus, 20 lumbar multifidus, 6 interspinales, 10 intertransversarii, and 11 rotatores. The anatomical data at the initial position of the vertebrae, muscle attachments, and physiological cross-sectional areas were obtained from the literature and medical images [11, 19–22]. The stiffness matrix  $\mathbf{K}$  was obtained from previous experimental studies [23, 24].

In this test, (3.2) was used for the objective function. The weight factors  $w_1, w_2$ , and  $w_3$  are supposed to be 3, 3, and 1, respectively, since 3 N of force and 1 Nmm of moment are considered equally based on the presumed safe limits of intervertebral loads being approximately 3000 N for forces and 9000 Nmm for moments as shown in [12]. The restriction coefficient  $\alpha$  was selected to be 0.25 based on [20] and the maximum muscle stress  $\sigma$  was assumed to be 0.46 MPa based on [26]. The upperbounds of all translation component and rotation component were 20.0 mm and 10.0°, respectively. An upright standing posture was considered for the external loading as 300 N of the upper body weight, 3 Nm of the resulting flexion moment applied to T12, and a vertebral weight of 10 N was added to each lumbar vertebra from L1–L5.

The muscle force distribution satisfying the formulated optimization problem was obtained using MATLAB (MathWorks Inc., USA). The number of activated muscles according to the ratio of muscle force to maximum muscle force was summarized in Table 1. The maximum compressive force and the maximum shear force were 691.1 N and 172.8 N while

**Table 1:** The number of activated muscles according to the ratio of muscle force to maximum muscle force.

Ratio of muscle force to maximum muscle force	Number of activated muscles
0%–20%	7
20%–40%	7
40%–60%	6
60%–80%	2
80%–100%	20
Total	42

the maximum joint moment was 2271 Nmm. The previous in vivo studies reported that the maximum compressive force, shear force, and joint moment were about 650 N, 190 N, and 8400 Nmm, respectively, in the upright standing posture [1, 14, 15, 27]. The validity of our results seems to be indirectly achieved since the models in [1, 14, 15, 27] were not exactly same to our model.

## 5. Conclusion

In this study, a general computational model of the human lumbar spine and trunk muscles including optimization formulations was provided. For a given condition, the trunk muscle forces could be predicted. The feasibility of the solution could be indirectly validated by comparing the compressive force, the shear force, and the joint moment. The presented general computational model and optimization technology can be fundamental tools to understand the control principle of human trunk muscles.

## Acknowledgments

This research was supported by Basic Science Research Program through the National Research Foundation of Korea (NRF) funded by the Ministry of Education, Science and Technology (2010-0005167), and 2009 National Agenda Project (NAP) funded by Korea Research Council of Fundamental Science & Technology (P-09-JC-LU63-C01).

## References

- [1] A. Nachemson, "Lumbar intradiscal pressure," in *The Lumbar Spine and Back Pain*, M. I. V. Jayson, Ed., chapter 9, pp. 191–203, 1987.
- [2] A. Schultz, "Loads on the lumbar spine," in *The Lumbar Spine and Back Pain*, M. I. V. Jayson, Ed., chapter 10, pp. 205–214, 1987.
- [3] J. J. Crisco, M. M. Panjabi, I. Yamamoto, and T. R. Oxland, "Euler stability of the human ligamentous lumbar spine. Part II: experiment," *Clinical Biomechanics*, vol. 7, no. 1, pp. 27–32, 1992.
- [4] A. G. Patwardhan, R. M. Havey, K. P. Meade, B. Lee, and B. Dunlap, "A follower load increases the load-carrying capacity of the lumbar spine in compression," *Spine*, vol. 24, no. 10, pp. 1003–1009, 1999.
- [5] J. J. Crisco and M. M. Panjabi, "The intersegmental and multisegmental muscles of the lumbar spine: a biomechanical model comparing lateral stabilizing potential," *Spine*, vol. 16, no. 7, pp. 793–799, 1991.
- [6] H. J. Wilke, S. Wolf, L. E. Claes, M. Arand, A. Wiesend, and T. Bendix, "Stability increase of the lumbar spine with different muscle groups: a biomechanical in vitro study," *Spine*, vol. 20, no. 2, pp. 192–198, 1995.
- [7] H. J. Wilke, A. Rohlmann, S. Neller, F. Graichen, L. Claes, and G. Bergmann, "A Novel approach to determine trunk muscle forces during flexion and extension: a comparison of data from an in vitro Experiment and in vivo measurements," *Spine*, vol. 28, no. 23, pp. 2585–2593, 2003.

- [8] A. G. Patwardhan, R. M. Havey, A. J. Ghanayem et al., "Load-carrying capacity of the human cervical spine in compression is increased under a follower load," *Spine*, vol. 25, no. 12, pp. 1548–1554, 2000.
- [9] M. Beck, "Die Knicklast des einseitig eingespannten, tangential gedrückten Stabes," *Zeitschrift für Angewandte Mathematik und Physik*, vol. 3, no. 6, pp. 476–477, 1952.
- [10] G. Herrmann, "Stability of equilibrium of elastic systems subjected to nonconservative forces," *Applied Mechanics Reviews*, vol. 20, pp. 103–108, 1967.
- [11] I. A. Stokes and M. Gardner-Morse, "Lumbar spine maximum efforts and muscle recruitment patterns predicted by a model with multijoint muscles and joints with stiffness," *Journal of Biomechanics*, vol. 28, no. 2, pp. 173–186, 1995.
- [12] I. A. F. Stokes and M. Gardner-Morse, "Lumbar spinal muscle activation synergies predicted by multi-criteria cost function," *Journal of Biomechanics*, vol. 34, no. 6, pp. 733–740, 2001.
- [13] A. G. Patwardhan, K. P. Meade, and B. Lee, "A frontal plane model of the lumbar spine subjected to a follower load: implications for the role of muscles," *Journal of Biomechanical Engineering*, vol. 123, no. 3, pp. 212–217, 2001.
- [14] A. Shirazi-Adl and M. Parnianpour, "Load-bearing and stress analysis of the human spine under a novel wrapping compression loading," *Clinical Biomechanics*, vol. 15, no. 10, pp. 718–725, 2000.
- [15] N. Arjmand and A. Shirazi-Adl, "Model and in vivo studies on human trunk load partitioning and stability in isometric forward flexions," *Journal of Biomechanics*, vol. 39, no. 3, pp. 510–521, 2006.
- [16] Y. H. Kim and K. Kim, "Numerical analysis on quantitative role of trunk muscles in spinal stabilization," *JSME International Journal Series C*, vol. 47, no. 4, pp. 1062–1069, 2004.
- [17] Y. H. Kim and K. Kim, "Computational modeling of spine and trunk muscles subjected to follower force," *Journal of Mechanical Science and Technology*, vol. 21, no. 4, pp. 568–574, 2007.
- [18] K. Kim, Y. H. Kim, and S. K. Lee, "Increase of load-carrying capacity under follower load generated by trunk muscles in lumbar spine," *Journal of Engineering in Medicine*, vol. 221, no. 3, pp. 229–235, 2007.
- [19] K. Kim and Y. H. Kim, "Role of trunk muscles in generating follower load in the lumbar spine of neutral standing posture," *Journal of Biomechanical Engineering*, vol. 130, no. 4, Article ID 041005, 2008.
- [20] K. Kim, Y. H. Kim, and S. Lee, "Shear force allowance in lumbar spine under follower load in neutral standing posture," *Acta of Bioengineering and Biomechanics*, vol. 12, no. 4, pp. 47–51, 2010.
- [21] K. Kim, Y. H. Kim, and S. Lee, "Investigation of optimal follower load path generated by trunk muscle coordination," *Journal of Biomechanics*, vol. 44, no. 8, pp. 1614–1617, 2011.
- [22] I. A. F. Stokes and M. Gardner-Morse, "Quantitative anatomy of the lumbar musculature," *Journal of Biomechanics*, vol. 32, no. 3, pp. 311–316, 1999.
- [23] M. M. Panjabi, R. A. Brand, and A. A. White, "Three dimensional flexibility and stiffness properties of the human thoracic spine," *Journal of Biomechanics*, vol. 9, no. 4, pp. 185–192, 1976.
- [24] M. G. Gardner-Morse, J. P. Laible, and I. A. F. Stokes, "Incorporation of spinal flexibility measurements into finite element analysis," *Journal of Biomechanical Engineering*, vol. 112, no. 4, pp. 481–483, 1990.
- [25] A. A. White III and M. M. Panjabi, *Clinical Biomechanics of the Spine*, Lippincott Williams & Wilkins, Philadelphia, Pa, USA, 1990.
- [26] A. B. Schultz, "Biomechanical analyses of loads on the lumbar spine," in *The Lumbar Spine*, pp. 160–171, W. B. Saunders, Philadelphia, Pa, USA, 1990.
- [27] H. J. Wilke, P. Neef, M. Caimi, T. Hoogland, and L. E. Claes, "New in vivo measurements of pressures in the intervertebral disc in daily life," *Spine*, vol. 24, no. 8, pp. 755–762, 1999.

## Research Article

# Personal Identification Based on Vectorcardiogram Derived from Limb Leads Electrocardiogram

Jongshill Lee,<sup>1</sup> Youngjoon Chee,<sup>2</sup> and Inyoung Kim<sup>1</sup>

<sup>1</sup> Department of Biomedical Engineering, Hanyang University, Seoul 133-791, Republic of Korea

<sup>2</sup> School of Electrical Engineering, College of Engineering, University of Ulsan, Ulsan 680-749, Republic of Korea

Correspondence should be addressed to Inyoung Kim, iykim@hanyang.ac.kr

Received 28 October 2011; Accepted 23 November 2011

Academic Editor: Chang-Hwan Im

Copyright © 2012 Jongshill Lee et al. This is an open access article distributed under the Creative Commons Attribution License, which permits unrestricted use, distribution, and reproduction in any medium, provided the original work is properly cited.

We propose a new method for personal identification using the derived vectorcardiogram (dVCG), which is derived from the limb leads electrocardiogram (ECG). The dVCG was calculated from the standard limb leads ECG using the precalculated inverse transform matrix. Twenty-one features were extracted from the dVCG, and some or all of these 21 features were used in support vector machine (SVM) learning and in tests. The classification accuracy was 99.53%, which is similar to the previous dVCG analysis using the standard 12-lead ECG. Our experimental results show that it is possible to identify a person by features extracted from a dVCG derived from limb leads only. Hence, only three electrodes have to be attached to the person to be identified, which can reduce the effort required to connect electrodes and calculate the dVCG.

## 1. Introduction

Human identification has potential applications in many different areas where the identity of a person needs to be determined, and to obtain even higher security levels, more complex system are required. Specific features of human beings need to be selected to recognize a person. Much work has been carried out on human face identification [1, 2]. These methods require a high-resolution computer vision system to collect facial features, which are generally anthropometric face structures. Other methods used in this area include: voice recognition [3] and palm recognition [4], with the most common being finger print identification. The human eye also contains specific features in both the retina and the iris that may be used for recognition [5].

Although most of these identification methods have gained wide acceptance, one of the problems with them is the fact that a specific biometric belonging to a certain person can

still be used, even if the owner of the biometric is not present or has died. Therefore, many biometric hardware systems include a liveness testing measure. This can be obtained by measuring the body temperature, moisture, oxygen level, reflection or absorbance of light or other radiation, or the presence of a natural spontaneous signal such as a pulse, the contraction of a pupil in response to light, and muscular contraction in response to an electrical stimulus. In most cases, such liveness testing is difficult to measure [6], and still it is needed to develop the reliable and efficient method to test the “liveness” of an applicant’s biometric.

The electrocardiogram (ECG) signal is an alternative inherent liveness biometric because of the significant fact that an ECG signal does not exist if the subject is not alive. Recently, the feasibility of using ECG as a new biometric measure for personal identification has been explored. Biel et al. [7] explained that automatic human identification can be achieved by analyzing the 30 features extracted from a standard 12-lead ECG. Shen et al. [8] investigated the feasibility of ECG as a biometric by applying template matching and a decision-based neural network to the seven features extracted from a single-lead ECG. Kyoso and Uchiyama [9] developed a human identification engine based on the four feature parameters of a sampled ECG data sequence on a beat-to-beat basis. Israel et al. [10] proposed a set of ECG descriptors that characterize the trace of a heartbeat to identify a person. 15 features have been selected from each heartbeat.

All of these researchers used time intervals (e.g., P wave duration, PQ interval, QRS interval, QT interval, and so on) or amplitude as important features in their studies. These features from the time domain have some limitations as the temporal features of interval and amplitude can vary depending on variables such as the time of day of the measurement or the physical condition of the subject. Noise and positioning of the electrode can also decrease the accuracy. In contrast, the spatial features of the cardiac electric vector, represented by the vectorcardiogram (VCG), are not affected by the variables mentioned above. It is also expected that the vectorcardiographic loops will differ in shape and orientation from person to person. It is possible to identify a person by features extracted from a VCG. We have investigated the feasibility of the VCG, which is derived from a standard 12-lead ECG, as a new biometric for personal identification in our previous study [11], and the experimental results have shown that it is applicable to identify a person. The drawback of this approach is the considerable effort required to connect many electrodes to the person, including six leads to the chest, which is inconvenient in a real environment.

In this work, we investigated a novel approach for identifying a person using the dVCG that was derived from limb leads only. For limb-lead recording, only three electrodes are attached to the wrist and ankle, which is much easier than 12-lead recording. By comparing the performances from limb-lead recordings and from 12-lead recordings, we analyzed the feasibility of using VCG from limb-lead recording for personal identification. First, we derived a VCG from a limb-lead ECG and extracted features from the derived VCG. To remove some redundant features and to analyze the effect of each feature, we performed feature selection using the Relief-F algorithm. Finally, we performed personal identification using a support vector machine (SVM).

## **2. Materials and Methods**

### **2.1. Vectorcardiogram**

VCG have been widely investigated in the diagnosis of heart diseases, such as atrial fibrillation [12], premature ventricular contraction [13], and early ventricular repolarization [14].

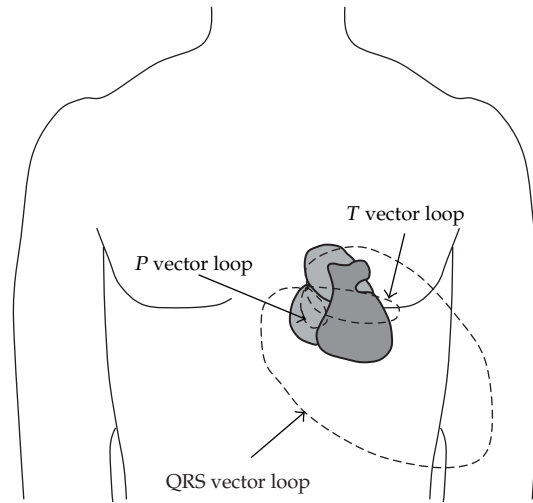


**Figure 1:** Vectorcardiogram.

VCG is a graphic representation of the magnitude and orientation of the heart's electrical activity during a cardiac cycle in the form of a vector loop. In contrast to ECG, which represents the electrical potential in any one single axis, VCG displays the same heart's electrical events along two or three perpendicular axes. VCG provides a vectorial representation of the distribution of electrical potentials generated by the heart and produces loop-type patterns (Figure 1). The magnitude and orientation of the P, QRS, and *T* vector loops are determined according to an individual heart's characteristics. Because of the high amplitude associated with QRS, loops from the QRS complex predominate.

The electrode positions of leads for the traditional VCG are different from those of a 12-lead ECG and must first be deduced by the recording technicians. Therefore, the method for calculating VCG from a conventional 12-lead ECG is more appealing [12, 15].

## 2.2. Derived VCG

From a standard 12-lead ECG, the derived VCG can be easily calculated using a method based on inverse Dower matrix [16] as shown in (2.1). Each of the orthogonal leads, *X*, *Y*, and *Z* used to plot the VCG are linear combinations of the eight independent leads (*I*, *II*, and *V1* – *V6*) of a standard 12-lead ECG

$$\begin{bmatrix} X \\ Y \\ Z \end{bmatrix} = D_0^{-1} [I \ II \ V1 \ V2 \ V3 \ V4 \ V5 \ V6]^T, \quad (2.1)$$

$$D_0^{-1} = \begin{bmatrix} -0.172 & -0.074 & 0.122 & 0.231 & 0.239 & 0.194 & 0.156 & -0.010 \\ 0.057 & -0.019 & -0.106 & -0.022 & 0.041 & 0.048 & -0.227 & 0.887 \\ -0.229 & -0.310 & -0.246 & -0.063 & 0.055 & 0.108 & 0.022 & 0.102 \end{bmatrix}.$$

To derive the limb ECG from vectorcardiographic leads, Dower et al. described a method using a transform matrix where each lead (I, II, and III) in the ECG was expressed as a linear function of the leads X, Y, and Z [17, 18]. The transformation matrix for the limb leads (I, II and III) is shown in (2.2).

$$\begin{bmatrix} \text{I} \\ \text{II} \\ \text{III} \end{bmatrix} = \begin{bmatrix} 0.632 & -0.235 & 0.059 \\ 0.235 & 1.066 & -0.132 \\ -0.397 & 1.301 & -0.191 \end{bmatrix} \begin{bmatrix} \text{X} \\ \text{Y} \\ \text{Z} \end{bmatrix}. \quad (2.2)$$

The transformation between the vectorcardiographic and limb-lead systems is a simple matrix operation:

$$S_{\text{ECG}} = DS_{\text{VCG}}, \quad (2.3)$$

where  $S_{\text{ECG}}$  is the ECG signal,  $S_{\text{VCG}}$  is the VCG signal, and  $D$  is the transformation matrix.

To calculate a VCG signal from a limb-lead system, we need the inverse of  $D$ , but there is no inverse matrix because  $D$  is singular ( $\text{II} = \text{I} + \text{III}$ ). Therefore, we use the pseudo inverse (or Moore-Penrose inverse) [19]. The pseudoinverse of  $D$  can be determined by the singular value decomposition ( $D = U\Sigma V^T$ ). Because matrix  $D$  has rank 2,  $\Sigma$  has two positive singular values ( $\sigma_1, \sigma_2$ ) along the main diagonal extending from the upper left-hand corner, and the remaining components of  $\Sigma$  are zero. Then,  $D^\dagger$  (the pseudo inverse matrix of  $D$ ) =  $(U\Sigma V^T)^\dagger = (V^T)^\dagger \Sigma^\dagger U^\dagger = V\Sigma^\dagger U^T$  since  $(V^T)^\dagger = V$  and  $U^\dagger = U^T$  because of their orthogonality. The matrix  $\Sigma^\dagger$  takes the following form:

$$\Sigma^\dagger = \begin{bmatrix} \frac{1}{\sigma_1} & 0 & 0 \\ 0 & \frac{1}{\sigma_2} & 0 \\ 0 & 0 & 0 \end{bmatrix}. \quad (2.4)$$

Therefore, the pseudo inverse matrix of  $D$  is shown as follows:

$$D^\dagger = \begin{bmatrix} 1.0808 & 0.7038 & -0.3770 \\ 0.0790 & 0.4663 & 0.3874 \\ 0.0367 & -0.0315 & -0.0682 \end{bmatrix}. \quad (2.5)$$

Finally, we calculated the dVCG from the limb-lead ECG using

$$\begin{bmatrix} \text{X} \\ \text{Y} \\ \text{Z} \end{bmatrix} = D^\dagger \begin{bmatrix} \text{I} \\ \text{II} \\ \text{III} \end{bmatrix}. \quad (2.6)$$



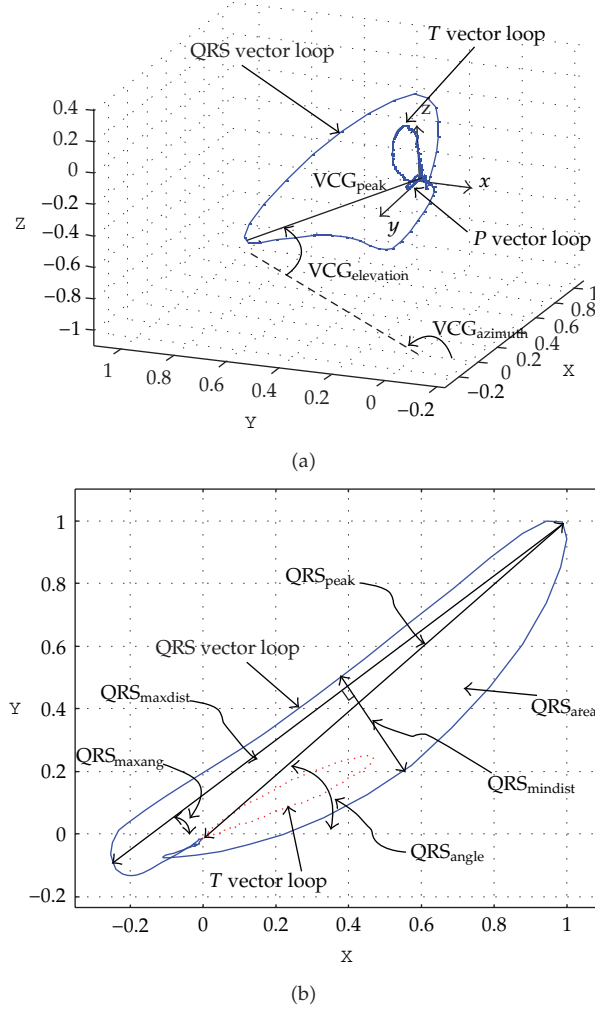


**Figure 2:** Feature extraction (a) from the dVCG in 3D space, and (b) from the QRS and T vector loops in the frontal plane.

The pseudoinverse of  $D(D^+)$  is an approximation matrix because  $D$  has deficient rank. Therefore, the dVCG derived from the limb leads has different patterns than the dVCG from the standard 12-lead ECG.

Because the three-dimensional space (3D) and the frontal (XY) plane of the dVCG provide useful information, such as shape and direction [11], as shown in Figure 2, we used the dVCG in 3D space and the frontal plane. In the frontal plane, the large vector loop (QRS vector loop) represents the QRS complex and the small vector loop (T vector loop) represents the T wave of the ECG. The P vector loop has such a small shape that we did not consider it.

### 2.3. Feature Extraction

Since the dVCG data taken from all of the recorded heartbeats produced similar patterns for each subject, the average values were taken from each beat's dVCG trace. Twenty-one features

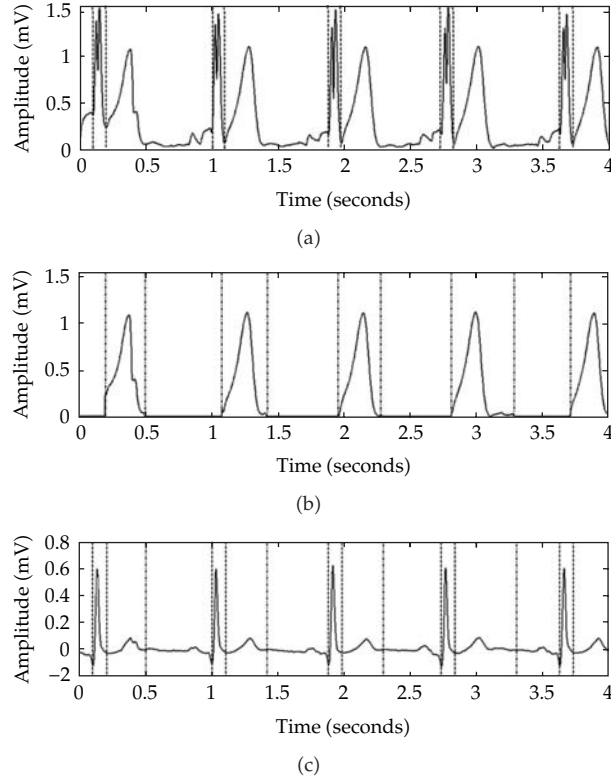


**Figure 3:** Detection of the QRS complex (depicted by the dashed line) and  $T$  wave (depicted by the dashed dotted line). (a) the detected QRS complex region on the magnitude of the dVCG signal, (b) the detected  $T$  wave region, (c) the detected QRS complex and  $T$  wave region on the signal of lead II.

were extracted from the dVCG data. Three features arose from the 3D space (depicted in Figure 2(a)), seven came from each QRS vector loop (depicted in Figure 2(b)) and  $T$  vector loop, and the others were the differential or proportional values obtained from the QRS and  $T$  vector loops.

To separate the QRS and  $T$  vector loops, we needed to detect the QRS complex and  $T$  wave. To detect the QRS complex, we used the QRS detection algorithm developed by Hamilton and Tompkins [20]. To detect the  $T$  wave, we used the QRS complex and the magnitude of the dVCG. As shown in Figure 3(a), the shape of the magnitude of the dVCG was segmented into the QRS complex and  $T$  wave regions. Therefore, we could easily separate the  $T$  wave interval by excluding the QRS region in the magnitude of the dVCG. The data shown in Figure 3(b) were achieved by calculating the region over a specific threshold after detecting the QRS complex region. Figure 3(c) shows the QRS complex and the  $T$  wave region of the signal from lead II.

### 2.3.1. Feature Extraction from the dVCG in 3D Space

Equation (2.6) shows the dVCG represented as vector

$$\overrightarrow{dVCG_i} = X_i \overrightarrow{a_X} + Y_i \overrightarrow{a_Y} + Z_i \overrightarrow{a_Z}, \quad (2.7)$$

where  $\vec{a}_X$ ,  $\vec{a}_Y$ , and  $\vec{a}_Z$  are unit vectors with directions along the  $X$ ,  $Y$ , and  $Z$  axes, respectively. The magnitude of  $\vec{dVCG}_i$  is  $|\vec{dVCG}_i| = \sqrt{X_i^2 + Y_i^2 + Z_i^2}$ . If this value becomes the largest value when  $i = p$ , then the maximum value ( $VCG_{\text{peak}}$ ), its azimuth ( $VCG_{\text{azimuth}}$ ), and its elevation ( $VCG_{\text{elevation}}$ ) angle are as shown in the following equation and Figure 2(a):

$$\begin{aligned} VCG_{\text{peak}} &= \sqrt{X_p^2 + Y_p^2 + Z_p^2}, \\ VCG_{\text{azimuth}} &= \tan^{-1}\left(\frac{Y_p}{X_p}\right), \\ VCG_{\text{elevation}} &= \tan^{-1}\left(\frac{Z_p}{Y_p}\right). \end{aligned} \quad (2.8)$$

### 2.3.2. Feature Extraction from the QRS Vector Loop

When points on the QRS vector loop are represented as vectors on the  $XY$  plane, the relationship is as shown in the following equation:

$$\vec{QRS}_i = X_i \vec{a}_X + Y_i \vec{a}_Y. \quad (2.9)$$

The magnitude of  $\vec{QRS}_i$  is  $|\vec{QRS}_i| = \sqrt{X_i^2 + Y_i^2}$ . If this value becomes the largest when  $i = p$ , then the maximum ( $QRS_{\text{peak}}$ ) and the azimuth ( $QRS_{\text{angel}}$ ) angle are as follows:

$$\begin{aligned} QRS_{\text{peak}} &= \sqrt{X_p^2 + Y_p^2}, \\ QRS_{\text{angel}} &= \tan^{-1}\left(\frac{Y_p}{X_p}\right). \end{aligned} \quad (2.10)$$

The area of a polygon whose vertices,  $QRS_i$ , have the coordinates  $(X_i, Y_i)$  for  $1 \leq i \leq k$  can be calculated using (2.11) [19]

$$\begin{aligned} QRS_{\text{area}} &= \frac{1}{2}(X_1 Y_2 - X_2 Y_1) + \cdots + \frac{1}{2}(X_{k-1} Y_k - X_k Y_{k-1}) + \frac{1}{2}(X_k Y_1 - X_1 Y_k) \\ &= \frac{1}{2} \sum_{i=1}^k (X_i Y_{i+1} - X_{i+1} Y_i). \end{aligned} \quad (2.11)$$

In the summation, we assume that  $X_{k+1} = X_1$  and  $Y_{k+1} = Y_1$ . The term  $QRS_{\text{maxdist}}$  represents the maximum distance between each pair of points on the QRS vector loop. If two points on the QRS vector loop are  $(X_i, Y_i)$  and  $(X_j, Y_j)$ , then the distance between them is given in

$$d(i, j) = \sqrt{(X_i - X_j)^2 + (Y_i - Y_j)^2}. \quad (2.12)$$

If this distance is at its maximum when  $i = p, j = q$ , then the maximum distance ( $QRS_{\text{maxdist}}$ ) and its angle ( $QRS_{\text{maxang}}$ ) are shown as follows:

$$\begin{aligned} QRS_{\text{maxdist}} &= d(i, j)|_{i=p, j=q} = d(p, q) = \sqrt{(X_p - X_q)^2 + (Y_p - Y_q)^2}, \\ QRS_{\text{maxang}} &= \tan^{-1} \left( \frac{Y_p - Y_q}{X_p - X_q} \right). \end{aligned} \quad (2.13)$$

Additionally,  $QRS_{\text{mindist}}$  is the length of the minor axis in the QRS vector loop. Namely,  $QRS_{\text{mindist}}$  is the maximum distance between the two points, where the line perpendicular to the line connecting the two points  $(X_p, Y_p)$  and  $(X_q, Y_q)$  from the previous equation meets the QRS vector loop. The six features mentioned above are depicted in Figure 2(b).

The term  $QRS_{\text{lwratio}}$  is the ratio of the major and minor axis on the QRS vector loop. This is represented by

$$QRS_{\text{lwratio}} = \frac{QRS_{\text{maxdist}}}{QRS_{\text{mindist}}}. \quad (2.14)$$

### 2.3.3. Feature Extraction from the T Vector Loop

Similar to the cases of the QRS vector loop, the features related to the T vector loop are  $T_{\text{peak}}$ ,  $T_{\text{angle}}$ ,  $T_{\text{area}}$ ,  $T_{\text{maxdist}}$ ,  $T_{\text{maxang}}$ ,  $T_{\text{mindist}}$ , and  $T_{\text{lwratio}}$ .

From these two sets of features, four additional features are acquired using the following equations:

$$\begin{aligned} QRST_{\text{diffang}} &= QRS_{\text{angle}} - T_{\text{angle}}, \\ QRST_{\text{diffarea}} &= QRS_{\text{area}} - T_{\text{area}}, \\ QRST_{\text{ratioarea}} &= \frac{QRS_{\text{area}}}{T_{\text{area}}}, \\ QRST_{\text{ratiopeak}} &= \frac{QRS_{\text{peak}}}{T_{\text{peak}}}. \end{aligned} \quad (2.15)$$

## 2.4. Personal Identification Using SVM and Relief-F

Support vector machines are learning machines based on recent advances in statistical learning theory [21, 22]. Geometrically speaking, SVMs try to maximize the margin, which is the distance between the separating hyperplane and the closest data samples (the support vectors) belonging to the different classes. For multiple class problems, pairwise classification is commonly employed, which builds  $c(c-1)/2$  binary classifiers (one versus one) and takes a majority-voted class as a winner, where  $c$  is the number of target classes [23].

To overcome the “curse of dimensionality” or to analyze the effect of each feature on classification, various feature selection methods have been introduced in the machine-learning field. Among these, the Relief-F algorithm has been successfully used in many feature selection tasks [24]. A key idea in Relief-F is estimating the power of each feature

by increasing the interclass difference and the intraclass similarity. The algorithm initially looks for the  $k$  nearest hits (samples with the same class label) and misses (samples with a different class label) for a randomly selected sample. Then, it updates the following weight for each feature,  $f$ , with respect to the difference between the feature values of the selected data and nearest ones

$$w(f) = P(\text{different value of } f | \text{different class}) - P(\text{different value of } f | \text{same class}). \quad (2.16)$$

In this study, the feature selection method by the Relief-F algorithm was adopted to improve the computational efficacy and remove possible redundant features that do not contribute to the classification performance. In addition, we used a linear SVM with a pairwise coupling method as a classifier in our experiments and compared the 10-fold cross validation accuracy by eliminating the lowest-ranked features one-by-one based on the Relief-F algorithm. We took advantage of the work of Witten and Frank [25] and Chang and Lin [26] for the Relief-F method and SVM learning.

### 3. Experimental Results

We used a dataset of Lee et al. [11] to evaluate our method and compared our proposed method with that of Lee et al. These standard 12-lead ECG data were acquired for ten healthy volunteers using a CardioTouch (Bionet Co., Korea) with a sampling speed of 500 samples per second. Each recording was 10 s long and was performed when the subject was at rest. The data collection was done for three months, and almost one hundred of recordings were done per subject.

To compare our proposed method and the previous dVCG method, we extracted 21 features from dVCG<sub>12-lead</sub> (dVCG derived from a standard 12-lead system) and dVCG<sub>limb-lead</sub> (dVCG derived from limb-lead system), respectively. These two sets of 21 features extracted from dVCG<sub>12-lead</sub> and dVCG<sub>limb-lead</sub> were ranked using the Relief-F algorithm, and the results are shown in Table 1. Note that the notation  $w(f)$  is the output from the Relief-F algorithm, which means the relative importance of the features in terms of the ability for increasing the interclass difference and the intraclass similarity.

For the 12-lead system, the foremost values were the angle of the maximum peak value in the  $T$  vector loop and the angle of the major axis in the  $T$  vector loop. Next were the values of the length and the angle of the major axis in the QRS vector loop, followed by the length of the minor axis in the QRS vector loop and the size of the QRS vector loop. The difference between the size of the QRS and  $T$  vector loops came next.

In the case of the limb-lead system, the highest values were the maximum peak value in 3D space of the dVCG and the area of the QRS vector loop, along with the difference between the area of the QRS and  $T$  vector loops. The length of the minor axis in the QRS vector loop and the maximum peak value in the  $T$  vector loop came next.

For two sets of 21 features, we performed a classification using a linear SVM with pairwise coupling method and compared the 10-fold cross validation accuracy by eliminating the lowest ranked features one-by-one. The results of the classification performance using the extracted features from a standard 12-lead and limb-lead system are denoted by the dashed and solid lines, respectively, in Figure 4.

**Table 1:** Rank for each set of 21 features extracted from dVCGs based on a standard 12-lead and limb-lead ECG, respectively.

Rank	12-Lead System		Limb-Lead System	
	$w(f)$	Feature	$w(f)$	Feature
1	0.26028	$T_{\text{angle}}$	0.29471	$VCG_{\text{peak}}$
2	0.25459	$T_{\text{maxang}}$	0.22822	$QRS_{\text{area}}$
3	0.24278	$QRS_{\text{maxdist}}$	0.22220	$QRST_{\text{diffarea}}$
4	0.17459	$QRS_{\text{maxang}}$	0.20969	$QRS_{\text{mindist}}$
5	0.16736	$QRS_{\text{mindist}}$	0.20752	$T_{\text{peak}}$
6	0.16552	$QRS_{\text{area}}$	0.18580	$T_{\text{maxang}}$
7	0.16499	$QRST_{\text{diffarea}}$	0.18002	$T_{\text{angle}}$
8	0.16268	$VCG_{\text{peak}}$	0.17490	$QRS_{\text{maxdist}}$
9	0.14688	$QRS_{\text{peak}}$	0.16626	$T_{\text{maxdist}}$
10	0.14518	$VCG_{\text{elevation}}$	0.14507	$QRST_{\text{ratiopeak}}$
11	0.11549	$QRS_{\text{lwratio}}$	0.12638	$QRST_{\text{diffang}}$
12	0.11397	$QRST_{\text{diffang}}$	0.11331	$QRS_{\text{lwratio}}$
13	0.10033	$T_{\text{area}}$	0.10956	$QRS_{\text{maxang}}$
14	0.09135	$T_{\text{maxdist}}$	0.10570	$QRS_{\text{peak}}$
15	0.08369	$VCG_{\text{azimuth}}$	0.07650	$VCG_{\text{azimuth}}$
16	0.07818	$T_{\text{peak}}$	0.07066	$QRS_{\text{angle}}$
17	0.06905	$T_{\text{mindist}}$	0.06596	$VCG_{\text{elevation}}$
18	0.05022	$QRS_{\text{angle}}$	0.05100	$T_{\text{lwratio}}$
19	0.03320	$QRST_{\text{ratiopeak}}$	0.03715	$T_{\text{area}}$
20	0.02709	$T_{\text{lwratio}}$	0.02179	$T_{\text{mindist}}$
21	0.00263	$QRST_{\text{ratioarea}}$	0.00091	$QRST_{\text{ratioarea}}$

The recognition rate using 21 features extracted from the standard 12-lead system was 99.52%, and the rate decreased as the number of features decreased. When we used only eight features, the recognition rate was 99.19%. In the case of features extracted from limb-lead system, the recognition rate of 99.53% was achieved using all 21 features and a recognition rate of 99.37% was achieved using only the top eight ranked features. These results show that when using the dVCG derived from limb leads only, we can produce an acceptable recognition rate.

#### 4. Discussion and Conclusions

The recording of the standard 12-lead ECG to identify a person is not readily applicable in a real environment due to the inconvenience of connecting many electrodes. To solve this problem, we have studied the feasibility of personal identification based on the dVCG derived from limb leads only.

We extracted 21 features from dVCG and performed feature selection using the Relief-F algorithm to analyze the effect of each feature. Although there were differences in rank order, seven out of the eight top-ranked features in a standard 12-lead system were also top-ranked in the limb-lead system with the exception being the angle of the major axis in the QRS vector loop. The results also show that the Relief-F algorithm is a suitable algorithm

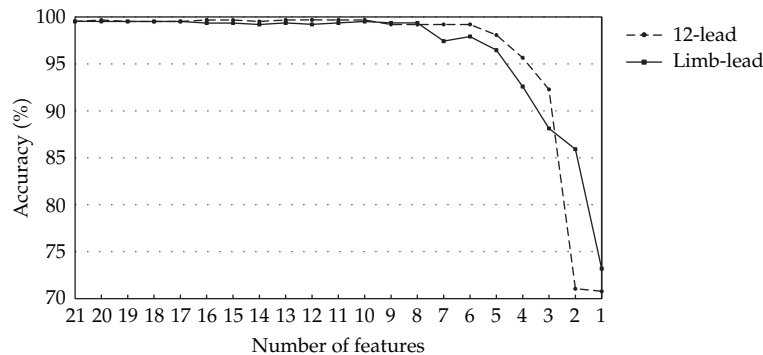


**Figure 4:** Comparison of classification performances between the method using a standard 12-lead system and our proposed method using the limb-lead system.

for sorting the ranks among the features since the recognition rates do not fluctuate and gradually decrease as the number of features decreases.

To identify a person, we used a linear SVM as a classifier and calculated the 10-fold cross validation accuracy. The results of the comparison between the dVCG from the limb-lead ECG and 12-lead ECG indicate that it is possible to identify a person using only a limb-lead system with three electrodes instead of the standard 12 leads.

Further studies should investigate the stability of the dVCG with a subject's various physical condition changes such as exercising, drinking, and smoking. Additionally, a large dataset including these various conditions should be used for its validation.

## Acknowledgment

This paper was supported by the research fund of Hanyang University (HY-2007-I).

## References

- [1] W. Zhao, R. Chellappa, P. J. Phillips, and A. Rosenfeld, "Face recognition: a literature survey," *ACM Computing Surveys*, vol. 35, no. 4, pp. 399–458, 2003.
- [2] L. F. Chen, H. Y. M. Liao, J. C. Lin, and C. C. Han, "Why recognition in a statistics-based face recognition system should be based on the pure face portion: a probabilistic decision-based proof," *Pattern Recognition*, vol. 34, no. 7, pp. 1393–1403, 2001.
- [3] A. Park and T. J. Hazen, "ASR dependent techniques for speaker identification," in *Proceedings of the 7th International Conference on Spoken Language Processing (ICSLP '02)*, pp. 1337–1340, 2002.
- [4] Y. Qiao, Z. Li, Q. Wang, Y. Zeng, and K. Liang, "Identification of palm print using dermatoglyphics analysis and detection system," *Medical Engineering and Physics*, vol. 27, no. 3, pp. 229–235, 2005.
- [5] A. Muroň, P. Koiš, and J. Pospíšil, "Identification of persons by means of the Fourier spectra of the optical transmission binary models of the human irises," *Optics Communications*, vol. 192, no. 3–6, pp. 161–167, 2001.
- [6] D. W. John, N. M. Orlans, and P. T. Higgins, *Biometrics—Identify Assurance in the Information Age*, McGraw-Hill, New York, NY, USA, 2003.
- [7] L. Biel, O. Pettersson, L. Philipson, and P. Wide, "ECG analysis: a new approach in human identification," *IEEE Transactions on Instrumentation and Measurement*, vol. 50, no. 3, pp. 808–812, 2001.
- [8] T. W. Shen, W. J. Tompkins, and Y. H. Hu, "One-lead ECG for identity verification," in *Proceedings of the 2nd Joint Conference of the IEEE Engineering in Medicine and Biology Society and the Biomedical Engineering Society*, pp. 62–63, October 2002.



- [9] M. Kyoso and A. Uchiyama, "Development of an ECG identification system," in *Proceedings of the 23rd Annual International Conference of the IEEE Engineering in Medicine and Biology Society*, pp. 3721–3723, October 2001.
- [10] S. A. Israel, J. M. Irvine, A. Cheng, M. D. Wiederhold, and B. K. Wiederhold, "ECG to identify individuals," *Pattern Recognition*, vol. 38, no. 1, pp. 133–142, 2005.
- [11] J. S. Lee, B. H. Cho, Y. J. Chee, I. Y. Kim, and S. I. Kim, "A new approach for personal identification based on dVCG," *IEICE Transactions on Information and Systems*, vol. E91-D, no. 4, pp. 1201–1205, 2008.
- [12] J. Carlson, R. Havmøller, A. Herreros, P. Platonov, R. Johansson, and B. Olsson, "Can orthogonal lead indicators of propensity to atrial fibrillation be accurately assessed from the 12-lead ECG?" *Europace*, vol. 7, no. 2, pp. S39–S48, 2005.
- [13] I. Christov, I. Jekova, and G. Bortolan, "Premature ventricular contraction classification by the Kth nearest-neighbours rule," *Physiological Measurement*, vol. 26, no. 1, pp. 123–130, 2005.
- [14] P. Dilaveris, A. Pantazis, E. Gialafos, J. Gialafos, P. Toutouzas, and C. Stefanadis, "Assessment of ventricular repolarization alterations in subjects with early repolarization," *International Journal of Cardiology*, vol. 96, no. 2, pp. 273–279, 2004.
- [15] L. Edenbrandt, A. Jakobsson, E. Lindvall, P. O. Bitzén, and O. Pahlm, "Increased prevalence of large bites in 12-lead vectorcardiograms of diabetic patients," *Journal of Electrocardiology*, vol. 30, no. 2, pp. 91–95, 1997.
- [16] L. Edenbrandt and O. Pahlm, "Vectorcardiogram synthesized from a 12-lead ECG: superiority of the inverse Dower matrix," *Journal of Electrocardiology*, vol. 21, no. 4, pp. 361–367, 1988.
- [17] G. E. Dower, H. B. Machado, and J. A. Osborne, "On deriving the electrocardiogram from vectorcardiographic leads," *Clinical Cardiology*, vol. 3, no. 2, pp. 87–95, 1980.
- [18] S. E. Fischer, S. A. Wickline, and C. H. Lorenz, "Novel real-time R-wave detection algorithm based on the vectorcardiogram for accurate gated magnetic resonance acquisitions," *Magnetic Resonance in Medicine*, vol. 42, no. 2, pp. 361–370, 1999.
- [19] D. Zwillinger, *Standard Mathematical Tables and Formulae*, Chapman & Hall/CRC, Boca Raton, Fla, USA, 31st edition, 2003.
- [20] P. S. Hamilton and W. J. Tompkins, "Quantitative investigation of QRS detection rules using the MIT/BIH arrhythmia database," *IEEE Transactions on Biomedical Engineering*, vol. 33, no. 12, pp. 1157–1165, 1986.
- [21] V. N. Vapnik, *The Nature of Statistical Learning Theory*, Springer, New York, NY, USA, 1995.
- [22] C. J. C. Burges, "A tutorial on support vector machines for pattern recognition," *Data Mining and Knowledge Discovery*, vol. 2, no. 2, pp. 121–167, 1998.
- [23] T. Hastie and R. Tibshirani, "Classification by pairwise coupling," *The Annals of Statistics*, vol. 26, no. 2, pp. 451–471, 1998.
- [24] I. Kononenko, "Estimating attributes: analysis and extensions of relief," in *Proceedings of the European Conference on Machine Learning (ECML '94)*, pp. 171–182, Catania, Italy, April 1994.
- [25] I. H. Witten and E. Frank, *Data Mining: Practical Machine Learning Tools and Techniques*, Morgan Kaufman, San Francisco, Calif, USA, 2nd edition, 2005.
- [26] C. C. Chang and C. J. Lin, "LIBSVM: a library for support vector machines," 2001, <http://www.csie.ntu.edu.tw/~cjlin/libsvm>.

## Research Article

# Monitoring Personalized Trait Using Oscillometric Arterial Blood Pressure Measurements

**Young-Suk Shin**

*Department of Information and Communication Engineering, Chosun University, 375 Seosuk-dong, Dong-gu, Gwangju 501-759, Republic of Korea*

Correspondence should be addressed to Young-Suk Shin, ysshin@chosun.ac.kr

Received 1 October 2011; Accepted 29 November 2011

Academic Editor: Pedro Serranho

Copyright © 2012 Young-Suk Shin. This is an open access article distributed under the Creative Commons Attribution License, which permits unrestricted use, distribution, and reproduction in any medium, provided the original work is properly cited.

The blood pressure patterns obtained from a linearly or stepwise deflating cuff exhibit personalized traits, such as fairly uniform peak patterns and regular beat geometry; it can support the diagnosis and monitoring of hypertensive patients with reduced sensitivity to fluctuations in Blood Pressure (BP) over time. Monitoring of personalized trait in Oscillometric Arterial Blood Pressure Measurements (OABPM) uses the Linear Discriminant Analysis (LDA) algorithm. The representation of personalized traits with features from the oscillometric waveforms using LDA algorithm includes four phases. Data collection consists of blood pressure data using auscultatory measurements and pressure oscillations data obtained from the oscillometric method. Preprocessing involves the normalization of various sized oscillometric waveforms to a uniform size. Feature extraction involves the use of features from oscillometric amplitudes, and trait identification involves the use of the LDA algorithm. In this paper, it presents a novel OABPM-based blood pressure monitoring system that can monitor personalized blood pressure pattern. Our approach can reduce sensitivity to fluctuations in blood pressure with the features extracted from the whole area in oscillometric arterial blood pressure measurement. Therefore this technique offers reliable blood pressure patterns. This study provides a cornerstone for the diagnosis and management of hypertension in the foreseeable future.

## 1. Introduction

Blood pressure (BP) is a vital sign, which along with body temperature, heart rate, and respiratory rate provides various physiological statistics about the body. Small changes in the BP over a period of time can provide clues about cardiovascular and respiratory abnormalities in a patient. Oscillometry is one of the widely used methods to determine the blood pressure [1–7]. The oscillometric method of measuring blood pressure uses the amplitude of cuff pressure oscillations from a linearly or stepwise deflating cuff and is given as two values, the systolic and diastolic pressures. The cuff pressure oscillations consist of waveforms. The systolic

pressure is the pressure associated with contraction of the heart, and indicates the maximum amount of work per stroke needed for the heart to pump blood through the arteries [8]. In contrast, diastolic pressure is the pressure in the large arteries during relaxation of the heart left ventricle [9]. The diastolic pressure indicates the amount of pressure that the heart must overcome in order to generate the next beat [8].

There have been ongoing studies to develop reliable measurements of blood pressure [3–7]. These researches have focused on improving the accuracy of blood pressure measurements. However, a large number of cardiovascular diseases such as arrhythmia can make it difficult to obtain accurate blood pressure measurements [3]. To determine the true BP level, many BP measurements need to be taken over a long period of time and problems affected by the white-coat effect have to be solved. The white-coat effect is usually defined as the difference between the BP measured at home and at the office. White-coat effect can be influenced by anxiety, a hyperactive alerting response, or a conditioned response. The white-coat effect typically causes the office BP to be higher than the home BP and is present in a high percentage of hypertensive patients [10]. If there are personalized traits in blood pressure measurements, problems such as noises caused by cardiovascular diseases like arrhythmia or problems of the white-coat effect may be overcome. Therefore, this study proposes the oscillometric measurement-based automatic blood pressure pattern identification system to explore personalized traits prior to obtaining reliable blood pressure measurements. The proposed approach demonstrates the feasibility of personalized trait identification with 85 people.

This paper aims to explore blood pressure pattern identification to find personalized traits in oscillometric arterial blood pressure measurements using the linear discriminant Analysis (LDA) algorithm. Section 2 introduces a review of related work. Section 3 develops a representation of personalized traits with features from the oscillometric waveforms. It consists of four steps. The first step introduces the database used for this research. The second step presents a preprocessing technique for obtaining uniform sized oscillation waves, and the third step develops a personalized traits representation via oscillations of amplitude features from uniform sized oscillation waves. The fourth step describes data reduction and feature extraction using LDA in the appearance-based approach. Section 4 presents the performance of the blood pressure patterns identification model via the LDA algorithm. Finally, this study discusses the advantages and applications of personalized trait monitoring.

## 2. Related Work

Blood pressure best predicts cardiovascular risk. Therefore, a variety of studies have been proposed to improve the accuracy of blood pressure measurements [3–7, 11–14]. Many studies use the oscillometric method to measure the blood pressure [1–7, 11, 12]. The oscillometric method is used to find the peak values of the oscillation waveform, which are determined as the oscillation amplitudes obtained from the pressure of the linearly deflating cuff. This method has virtually no complications and needs less expertise; it is less unpleasant and painful for the patient. In [1–7, 11, 12], blood pressure measurements based on the oscillometric method typically only use single-point estimates for both systolic blood pressure and diastolic blood pressure. Recently, BP measurements in [13, 14] were introduced: the confidence interval estimate of the systolic blood pressure and diastolic blood pressure. In [13], the confidence interval estimate performed well only when sample size is large. The confidence interval estimate used in [14] requires independent and identically distribution of data. But these methods also have to measure single-point estimates for systolic and diastolic blood pressure and can reflect on sensitivity to fluctuations in BP measurements.

In this paper, we have attempted to extract personalized blood pressure patterns of oscillation amplitudes rather than measure single-point estimates for systolic and diastolic blood pressure. During feature extraction, we focus on the more uniform features of the oscillation amplitudes in each person.

### **3. Methodology**

This section describes a new blood pressure patterns identification technique to find personalized traits in oscillometric arterial blood pressure measurements using the LDA algorithm. This work consists of four steps. First, data collection is described. Second, oscillometric waveforms of various sizes are normalized to a uniform size. Third, features based on the oscillation amplitudes are developed. Finally, the LDA algorithm is applied to identify blood pressure patterns.

#### **3.1. Data Collection**

Experimental data has been provided by the blood pressure research team of the University of Ottawa in Canada. The database consists of blood pressure data using auscultatory measurements and pressure oscillations data obtained from the oscillometric method. The blood pressure data measured using the auscultatory method was obtained by two trained nurses. The oscillometric method is similar to the auscultatory technique, but it uses a pressure sensor instead of a stethoscope to record the pressure oscillations within the cuff. This method requires an external inflatable cuff, which can be placed around the left wrist at heart level. The cuff is inflated starting from below the diastolic pressure until the cuff pressure exceeds the systolic pressure. The cuff pressure is first increased until it exceeds the systolic pressure and then deflated until it reaches certain pressures at fixed or variable intervals [7].

The database consists of a total of 425 ( $85 \times 5$ ) records with five recordings per subject from 85 male and female subjects. Subjects met various blood pressure criteria: 10% of participants had BP below 100 mmHg systolic, 10% had BP above 140 mmHg systolic, 10% had BP below 60 mmHg diastolic, 10% had BP above 100 mmHg diastolic, and the remainder had BP distributed between these outer limits. The subjects' ages ranged from 10 to 80 years. Subjects were allowed to relax in a waiting room area for 15 minutes and the measurement room was organized to be conducive to accurate blood pressure measurements. The subjects were told not to talk or move during the readings. Five records per subject were acquired, and measurements were repeated for one minute with a one-minute rest period. Figure 1 shows one example of an oscillation pattern extracted from the cuff pressure acquired from the oscillometric method.

#### **3.2. Preprocessing**

The number of oscillation waveforms extracted from the cuff pressure varies according to physiology, geometry of the heart, hypertension, gender, and age (see Table 1). Table 1 shows a partial example of varying number of oscillation waveforms extracted from the cuff pressure. The systolic and diastolic pressures are the average values acquired by two nurses with auscultatory measurements. We can find a similar number of oscillation waveforms in 5 measurements of the same subject. That is, the same person can have similar number of oscillation waveforms. We attempt to use normalization to reduce variations of corresponding

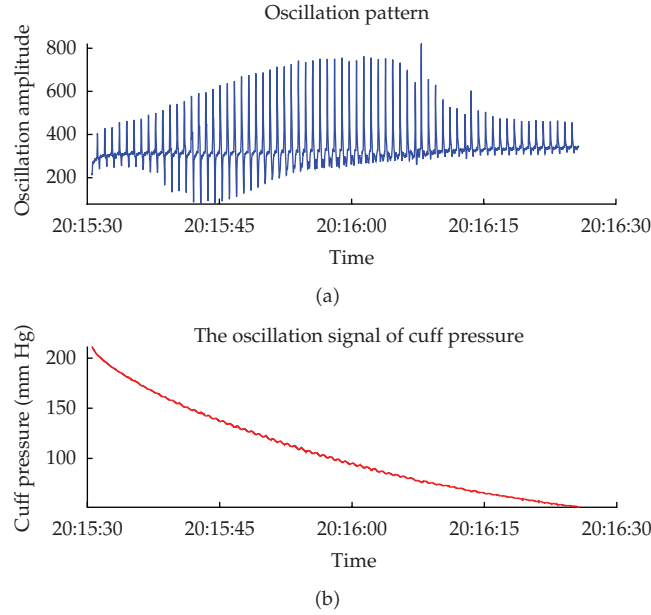


**Figure 1:** Oscillation pattern extracted from the cuff pressure with the oscillometric method.

oscillation waveforms for different oscillation waveforms of the same person. A blood pressure pattern means a varying number of oscillation waveforms in one record for one-minute. Training set is defined as  $X$ . Given the training set  $X = \{W_i\}_{i=1}^N$ , containing  $N$  blood pressure patterns where each blood pressure pattern  $W_i = \{W_{ij}\}_{j=1}^{N_i}$  consists of a number of oscillation waveforms  $W_{ij}$ , the normalization is applied as follows:

$$\varphi = \sqrt{\sum_{j=1}^{N_i} (W_{ij})^2}, \quad (3.1)$$

$$W_i^* = \frac{W_i}{\varphi}.$$

### 3.3. Feature Extraction

The proposed feature extraction technique extracts features of mean amplitude (MA), maximum positive amplitude (MPA), and maximum negative amplitude (MNA) based on database with the number of oscillation waveforms.

To implement the proposed approach, we segment a normalized oscillation pattern into 29-sample windows (at least including a single beat in the minimum oscillation waveforms) to obtain the feature windows. That is, a blood pressure pattern is divided into 29 sections and each divided section has to include at least a single heartbeat. In this study, 29 sections are defined for including at least a single heart beat on the training set,  $X$ . Blood pressure patterns larger than the minimum number of oscillation waveforms in a blood pressure pattern represent multiple heart beats within a given window. One-feature window means one section in 29 sections. Figure 2 shows four heart beats detected within a given

**Table 1:** Oscillation waveforms of various sizes extracted from the cuff pressure.

Subjects	age	Gender	Reading number	Number of oscillation waveforms acquired from cuff pressure for oscillometric method	Blood pressure by auscultatory method	Note
S1	50	Male	1	4591	Systolic 127	Diastolic 98
			2	4679	128	98
			3	4684	126	98
			4	4705	126	98
			5	4698	125	99
S2	22	Female	1	3457	113	67
			2	3499	104	68
			3	3530	112	66
			4	3551	104	61
			5	3523	108	65
S3	54	Female	1	3721	145	88
			2	3845	142	83
			3	3892	143	84
			4	3935	140	80
			5	3979	135	78
S4	34	Male	1	8401	131	82
			2	8500	131	86
			3	8746	130	79
			4	8808	131	78
			5	8948	130	82
S5	36	Male	1	3957	109	67
			2	4069	106	71
			3	4159	104	72
			4	4220	103	71
			5	4218	108	70
S6	43	Female	1	3991	109	69
			2	4106	112	69
			3	4041	109	70
			4	4139	112	69
			5	4100	114	71

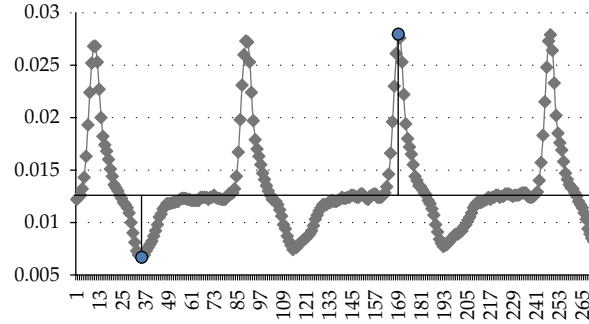


**Figure 2:** Four heartbeats detected in the segmented one-feature window from one subject.

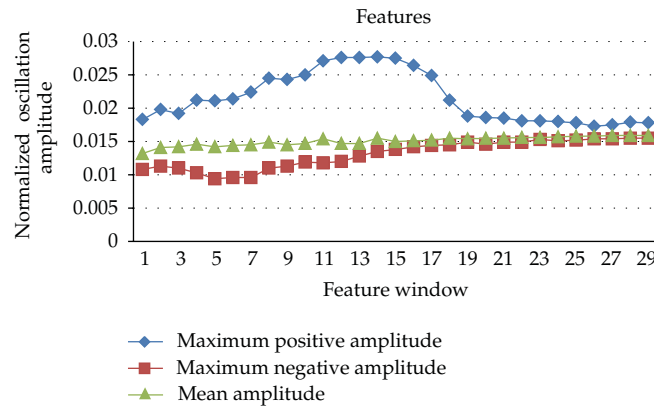
window. We extract three features from the oscillation amplitudes in the segmented feature window: mean amplitude, maximum positive amplitude, and maximum negative amplitude. The circle marks of Figure 2 display the maximum positive and negative amplitudes extracted in the segmented feature window. We define the following for three features; MA means the averaged oscillation amplitudes in the segmented one-feature window; MPA means the amplitude of the maximum upper pulse from the oscillations in the segmented one-feature window; MNA describes the amplitude of the maximum lower pulse from the oscillations in the segmented one-feature window.

Figure 3 shows the feature extraction results of one subject with the mean amplitude and maximum positive and negative amplitudes in each feature window. The mean amplitude can reduce noise signals within the feature window, and the maximum positive and negative amplitudes exhibit personalized traits in the period of high or low cuff pressure. Figures 4 and 5 show the feature extraction results of six subjects in Table 1 with maximum positive and negative amplitudes in 29 feature windows, respectively. Figures 4 and 5 show the averaged results of five readings obtained from the oscillometric blood pressure measurements of each subject. Subjects S2, S5, and S6 of Figures 4 and 5 are normal (BP:  $<120/80$  mmHg), whereas blood pressure subjects S1 and S4 are prehypertensive (BP:  $120/80$  to  $139/89$  mmHg) and S3 is stage 1 hypertensive (BP:  $140/90$  to  $160/100$  mmHg) blood pressure subject. In Figures 4 and 5, stage 1 hypertensive or prehypertensive subjects display a steep-slope pattern in front of the feature windows compared to normal subjects. Especially, older subjects show higher amplitudes based on the MPA features. In the MNA features, stage 1 hypertensive or prehypertensive subjects show lower amplitudes compared to normal subjects.

### 3.4. Identification

Linear discriminant analysis is used for data reduction and feature extraction in the appearance-based approach. LDA searches for feature vectors in the fundamental space that best discriminates among classes [15]. LDA describes a linear combination of feature vectors that produces the largest mean differences between the target classes. Features of the heartbeat applied for human identification from electrocardiogram (ECG) [16–18] are similar to features extracted from oscillometric arterial blood pressure measurements. Features extracted from oscillometric measurements are classified with an appearance-based approach based on LDA. Appearance-based approach is usually taken by different two-dimensional views





**Figure 3:** Features extracted with mean amplitude and maximum positive and negative amplitudes in the segmented feature windows from one subject.

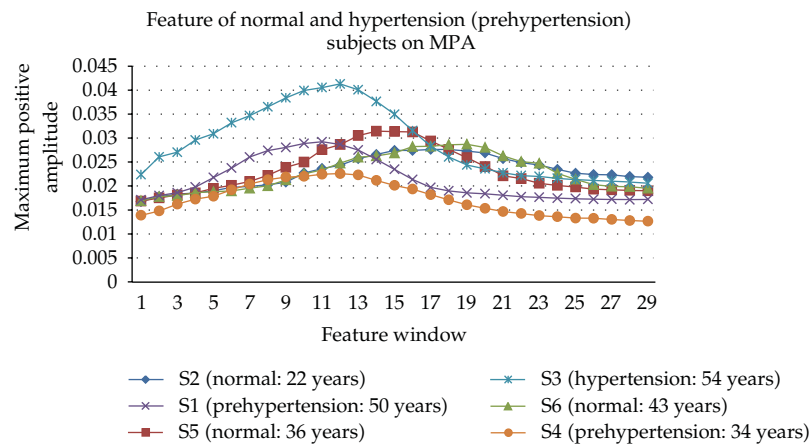


**Figure 4:** Features extracted with maximum positive amplitude averaged from five readings in the feature windows for normal and hypertension (prehypertension) subjects with respect to age.

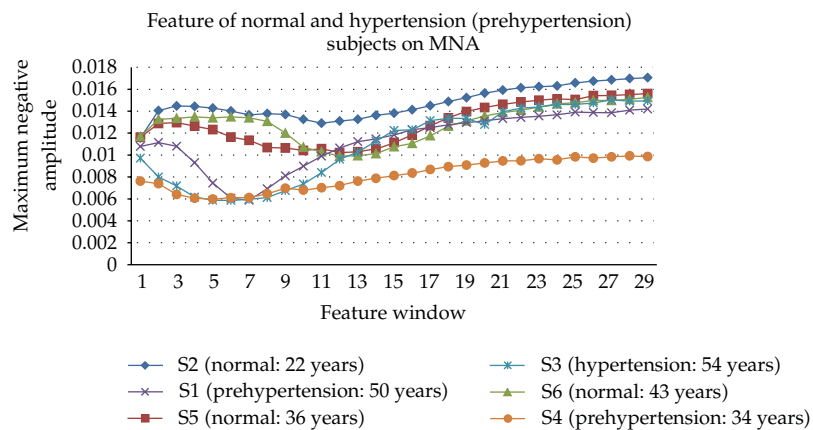


**Figure 5:** Features extracted with maximum negative amplitude averaged from five readings in the feature windows for normal and hypertension (prehypertension) subjects with respect to age.

of the object of interest. These methods based on the applied features can be subdivided into two approaches: local and global approaches. This study applies global appearance-based method. The main idea is to project the original input data onto a suitable lower-dimensional subspace that represents the data best for a specific work. Selecting optimization criteria for the projected data is the goal to best identify personalized trait.

Given a training set  $X = \{W_i^*\}_{i=1}^C$ , containing  $C$  classes with each class  $W_i^* = \{w_{ij}^*\}_{j=1}^{C_i}$ , consisting of a number of features,  $w_{ij}^*$ , there are a total of  $N = \sum_{i=1}^C C_i$  oscillation patterns. We define two measures for all samples of all classes.  $S_{WT}$  is defined as within-class scatter matrices of the training feature set.  $S_{BT}$  is defined as between-class scatter matrices of the training feature set.  $S_{WT}$  and  $S_{BT}$  are given as

$$S_{WT} = \frac{1}{N} \sum_{i=1}^c \sum_{j=1}^{C_i} (w_{ij}^* - \mu_i)(w_{ij}^* - \mu_i)^T, \quad (3.2)$$

$$S_{BT} = \frac{1}{N} \sum_{i=1}^c (\mu_i - \mu)(\mu_i - \mu)^T.$$

In (3.2),  $w_{ij}^*$  denotes the  $j$ th sample of class  $i$ ,  $c$  is the number of classes,  $\mu_i$  is the mean of class  $i$ , and  $c_i$  denotes the number of samples in class  $i$  and  $\mu$  is the mean of all classes. The LDA approach [19] finds a set of basis vectors described by  $\varphi$  that maximizes the ratio between  $S_{BT}$  and  $S_{WT}$ :

$$\varphi = \arg \max \frac{|\varphi^T S_{BT} \varphi|}{|\varphi^T S_{WT} \varphi|}. \quad (3.3)$$

One method is to assume that  $S_{WT}$  is nonsingular and the basis vectors  $\varphi$  correspond to the first  $N$  eigenvectors with the largest eigenvalues of  $S_{WT}^{-1} S_{BT}$ . LDA-based feature representation,  $y = \varphi^T w^*$ , is produced by projecting the normalized input features ( $w^*$ ) from the oscillation amplitudes onto the subspace spanned by the  $N$  eigenvectors.

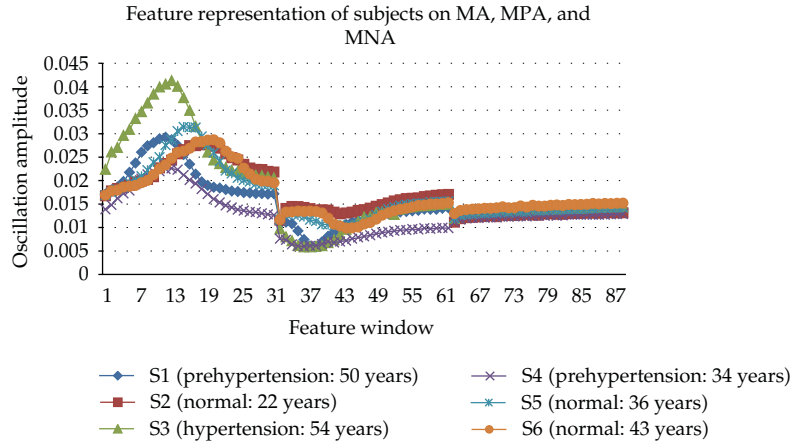
## 4. Experimental Results

To evaluate the performance of our approach, we conducted our experiments with the pressure oscillations data (measured using oscillometric method) provided by the blood pressure research team of the University of Ottawa in Canada. For the experiment, we used 425 records with five readings per subject obtained from 85 subjects; the training set consisted of 255 records with three readings per subject obtained from 85 subjects; the testing set consisted of the remaining 170 data readings excluded from the training set, two readings per subject obtained from 85 subjects. The blood pressure data measured using the auscultatory method provided indirect information for analyzing the subjects recognized by the oscillometric method in our experiment.

The experimental results were evaluated with the performance of LDA by using the nearest neighbor algorithm. The Euclidean distance was used for the similarity measure. To find the optimal LDA-based features, our implementation used the five sets of features from Figure 3 to test their discrimination power. One set included all of the features, whereas

**Table 2:** Subsets of features extracted using the oscillometric method.

Subset	Feature
I	Mean amplitude (MA)
II	Maximum positive amplitude (MPA)
III	Maximum negative amplitude (MNA)
IV	MPA + MNA
V	MA + MPA + MNA

**Figure 6:** Features extracted with mean amplitude and maximum positive and negative amplitudes in the feature windows from normal and hypertension (prehypertension) subjects.

the other four sets included a subset of these, as shown in Table 2. Subset IV concatenates the features of the maximum positive and negative amplitudes, and subset V concatenates the features of the mean amplitudes and maximum positive and negative amplitudes into one vector.

Figure 6 shows the feature extraction results obtained from six subjects in Table 1 and the mean amplitudes and maximum positive and negative amplitudes are concatenated into one vector. S2, S5, and S6 are normal blood pressure subjects, and S1, S3, and S4 are prehypertension or hypertensive blood pressure subjects. This shows the averaged results of the five readings for the oscillometric blood pressure measurements obtained from each subject. The feature windows describe feature windows 1 to 29 extracted from the maximum positive amplitudes, feature sections 30 to 57 extracted from the maximum negative amplitudes, and feature sections 58 to 87 extracted from the mean amplitude. The stage 1 hypertensive subject (S3) displays steeper maximum positive amplitude than that of the normal subjects. Prehypertensive or stage 1 hypertensive subjects generally display lower maximum negative amplitude than that of normal subjects. This shows that the averaged features of the five readings taken from each subject are plotted in a personalized uniform pattern. The results of the final LDA-based experiments are listed in Table 3. We can see that using all of the features provides the best blood pressure pattern identification rate, and subset IV shows good performance, while subset I shows the worst performance. LDA does not go beyond 85 for the dimensionality of the LDA space. Since we use 85 classes, this gives us an upper bound of 85-dimensional LDA space.

**Table 3:** Experimental results of LDA.

Subset	Recognition rate (%)
I	34.30
II	67.44
III	72.09
IV	93.02
V	94.70

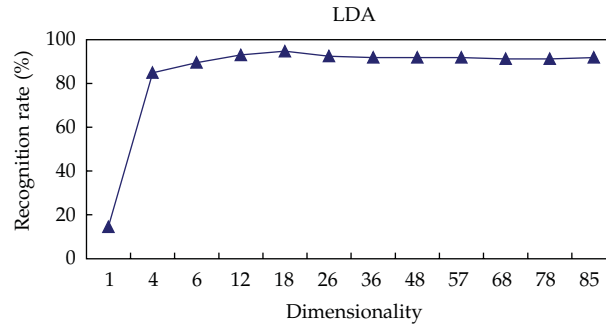
**Figure 7:** LDA recognition performance according to dimensionality via LDA algorithm with nearest neighbor classifier.

Figure 7 shows the recognition results based on the dimensionality that yields the best identification rate. We achieved the best blood pressure pattern identification rate of 94.7% for the first 18 eigenvectors. Thus, the first 18 eigenvectors are estimated to the optimal decision boundary to best identify personalized trait using LDA in this study.

## 5. Discussion

This study aimed to explore a new blood pressure patterns identification model for personalized traits monitoring of oscillometric arterial blood pressure measurements using the linear discriminant analysis algorithm. A blood pressure patterns identification model was used for the oscillometric arterial blood pressure measurements, which successfully discriminated personalized traits for the LDA algorithm. Our best recognition result showed a recognition rate of 94.7% for the first 18 eigenvectors. This means that the optimal LDA-based 18 eigenvectors in oscillometric arterial blood pressure measurements can effectively represent personalized traits.

The personalized traits of the oscillometric arterial blood pressure measurements can be represented for the features extracted from the whole domain of one oscillation pattern. Especially, the integration of the three feature streams extracted from each segmented feature window for the whole domain of one oscillation pattern enhances the recognition performance. In our experiment, the integration of the feature streams extracted with the maximum positive and negative amplitudes largely improved the recognition rate. In the three feature streams, while the maximum positive and negative amplitude feature streams showed strong effects on the recognition performance, the mean amplitude showed a weak effect. We propose that the maximum positive and negative amplitude features can effectively represent personalized traits of oscillometric arterial blood pressure measurement.

Features extracted from each segmented feature window in the oscillometric method may support the monitoring and diagnosis of hypertensive patients because stage 1 hypertensive or prehypertensive subjects display a steep-slope pattern in front of the feature windows compared to normal subjects.

Our approach offers a simple and inexpensive means of monitoring personalized trait with blood pressure patterns in oscillometric arterial blood pressure measurement. Based on these results, this study has established a new blood pressure monitoring system for health care monitoring in oscillometric arterial blood pressure measurements. Our research has the potentiality for the diagnosis and management of hypertension and provides a foundation of a new biometric modality using blood pressure patterns.

## Acknowledgments

This study was supported by research fund from Chosun University, 2011. The author wishes to acknowledge the data support of the blood pressure research team of the University of Ottawa in Canada.

## References

- [1] L. A. Geddes, M. Voelz, and C. Combs, "Characterization of the oscillometric method for measuring indirect blood pressure," *Annals of Biomedical Engineering*, vol. 10, no. 6, pp. 271–280, 1982.
- [2] J. C. T. B. Moraes, M. Cerulli, and P. S. Ng, "Development of a new oscillometric blood pressure measurement system," in *Proceedings of the 26th IEEE Computers in Cardiology Conference*, pp. 467–470, September 1999.
- [3] C. T. Lin, S. H. Liu, J. J. Wang, and Z. C. Wen, "Reduction of interference in oscillometric arterial blood pressure measurement using fuzzy logic," *IEEE Transactions on Biomedical Engineering*, vol. 50, no. 4, pp. 432–441, 2003.
- [4] T. J. Dorsett, "Application of a prediction and smoothing algorithm to non-invasive blood pressure measurement," in *Proceedings of the 13th Annual International Conference of the IEEE Engineering in Medicine and Biology Society*, pp. 468–469, November 1991.
- [5] K. G. Ng and C. F. Small, "Survey of automated noninvasive blood pressure monitors," *Journal of Clinical Engineering*, vol. 19, no. 6, pp. 452–475, 1994.
- [6] T. J. Brinton, B. Cotter, M. T. Kailasam et al., "Development and validation of a noninvasive method to determine arterial pressure and vascular compliance," *American Journal of Cardiology*, vol. 80, no. 3, pp. 323–330, 1997.
- [7] S. Colak and C. Isik, "Blood pressure estimation using neural networks," in *Proceedings of the IEEE International Conference on Computational Intelligence for Measurement Systems and Applications*, pp. 14–16, Boston, Mass, USA, 2007.
- [8] E. P. Dutton, "Heartbook, a guide to prevention and treatment of cardiovascular disease. The American heart association," vol. 116, pp. 132–136, 1980.
- [9] N. Kaplan, *Clinical Hypertension*, Williams and Wilkins, Baltimore, Md, USA, 3rd edition, 2005.
- [10] T. G. Pickering, N. H. Miller, G. Ogedegbe, L. R. Krakoff, N. T. Artinian, and D. Goff, "Call to action on use and reimbursement for home blood pressure monitoring: a joint scientific statement from the American heart association, american society of hypertension, and preventive cardiovascular nurses association," *Journal of Cardiovascular Nursing*, vol. 23, no. 4, pp. 299–323, 2008.
- [11] M. Forouzanfar, H. R. Dajani, V. Z. Groza, M. Bolic, and S. Rajan, "Oscillometric blood pressure estimation using principal component analysis and neural networks," in *2009 IEEE Toronto International Conference on Science and Technology for Humanity (TIC-STH '09)*, pp. 981–986, September 2009.
- [12] S. Chen, V. Z. Groza, M. Bolic, and H. R. Dajani, "Assessment of algorithms for oscillometric blood pressure measurement," in *Proceedings of the IEEE Instrumentation and Measurement Technology Conference*, pp. 1763–1767, May 2009.
- [13] L. R. Krakoff, "Confidence limits for interpretation of home blood pressure recordings," *Blood Pressure Monitoring*, vol. 14, no. 4, pp. 172–177, 2009.

- [14] S. Lee, M. Bolic, V. Z. Groza, H. R. Dajani, and S. Rajan, "Confidence interval estimation for oscillometric blood pressure measurements using bootstrap approaches," *IEEE Transactions on Instrumentation and Measurement*, vol. 60, no. 10, pp. 3405–3415, 2011.
- [15] K. Fukunaga, *Introduction to Statistical Pattern Recognition*, Academic Press, 2nd edition, 1990.
- [16] Y. Wang, F. Agraftioti, D. Hatzinakos, and K. N. Plataniotis, "Analysis of human electrocardiogram for biometric recognition," *EURASIP Journal on Advances in Signal Processing*, vol. 2008, Article ID 148658, 11 pages, 2008.
- [17] S. A. Israel, J. M. Irvine, A. Cheng, M. D. Wiederhold, and B. K. Wiederhold, "ECG to identify individuals," *Pattern Recognition*, vol. 38, no. 1, pp. 133–142, 2005.
- [18] C. C. Chiu, C. M. Chuang, and C. Y. Hsu, "A novel personal identity verification approach using a discrete wavelet transform of the ECG signal," in *Proceedings of the International Conference on Multimedia and Ubiquitous Engineering (MUE '08)*, pp. 201–206, April 2008.
- [19] P. N. Belhumeur, J. P. Hespanha, and D. J. Kriegman, "Eigenfaces vs. fisherfaces: recognition using class specific linear projection," *IEEE Transactions on Pattern Analysis and Machine Intelligence*, vol. 19, no. 7, pp. 711–720, 1997.

## Research Article

# Qualitative and Computational Analysis of a Mathematical Model for Tumor-Immune Interactions

**F. A. Rihan,<sup>1</sup> M. Safan,<sup>2</sup> M. A. Abdeen,<sup>3</sup> and D. Abdel Rahman<sup>1</sup>**

<sup>1</sup> *Department of Mathematical Sciences, Faculty of Science, United Arab Emirates University, Al-Ain 17551, United Arab Emirates*

<sup>2</sup> *Department of Mathematics, Faculty of Science, Mansoura University, Mansoura 35516, Egypt*

<sup>3</sup> *Department of Mathematics, Faculty of Science, Helwan University, Cairo 11790, Egypt*

Correspondence should be addressed to F. A. Rihan, frihan@uaeu.ac.ae

Received 7 July 2011; Revised 15 October 2011; Accepted 28 October 2011

Academic Editor: Pedro Serranho

Copyright © 2012 F. A. Rihan et al. This is an open access article distributed under the Creative Commons Attribution License, which permits unrestricted use, distribution, and reproduction in any medium, provided the original work is properly cited.

We provide a family of ordinary and delay differential equations to model the dynamics of tumor-growth and immunotherapy interactions. We explore the effects of adoptive cellular immunotherapy on the model and describe under what circumstances the tumor can be eliminated. The possibility of clearing the tumor, with a strategy, is based on two parameters in the model: the rate of influx of the effector cells and the rate of influx of IL-2. The critical tumor-growth rate, below which endemic tumor does not exist, has been found. One can use the model to make predictions about tumor dormancy.

## 1. Introduction

Cancer is one of the most difficult diseases to be treated clinically, and one of the main causes of death. It is the second fatal disease after the cardiovascular diseases. The World Health Organization estimates that the annual cancer-induced mortality number exceeds six million people. Accordingly, the fight against cancer is of major public health interest. For this and other economy-related reasons, a great research effort is being devoted to understand the dynamics of cancer and to predict the impact of any changes on the system reactors. Hence, mathematical models are required to help design therapeutic strategies.

In cancer modeling, we have to care about the scaling problem, where the class of equations, used to describe the model, are to be determined. Indeed, there are three natural scales, which are connected to the different stages of the disease and have to be identified. The first is the subcellular (or molecular) scale, where we focus on studying the alterations in the genetic expressions of the genes contained in the nucleus of a cell, as a result of some



special signals, which are received by the receptors on the cell surface and transmitted to the cell nucleus. The second is the cellular scale, which is an intermediate level between the molecular and the macroscopic scale. The third is the macroscopic scale, where we deal with heterogeneous tissues. In the heterogeneous tissues, some of the layers (the external proliferating layer, the intermediate layer, and the inner zone with necrotic cells) constituting the tumor may occur as islands, leading to a tumor comprised of multiple regions of necrosis, engulfed by tumor cells in a quiescent or proliferative state [1]. In case of macroscopic scale, we focus on the interaction between the tumor and normal cells (e.g., immune cells and blood vessels) in each of the three layers. For more details about description of the scaling problem and the passage from each scale to another, we refer to Bellomo et al. [1, 2].

A great research effort is being devoted to understand the interaction between the tumor cells and the immune system. Mathematical models, using ordinary, partial, and delay differential equations [3], play an important role in understanding the dynamics and tracking tumor and immune populations over time. Although the theoretical study of tumor immune dynamics has a long history [4, 5], the multifaceted nature of cancer requires sophisticated, nonlinear mathematical models to capture more realistic growth dynamics.

Many mathematical models have been proposed to model the interactions of cytotoxic T lymphocyte (CTL) response and the growth of an immunogenic tumor (see, e.g., [6–11]). The model by Kuznetsov et al. [7] takes into account the penetration of the tumor cells by the effector cells, which simultaneously causes the inactivation of effector cells. However, the model of Matzavinos et al. [9] describes the growth of a solid tumor in the presence of an immune system response, with special focus on the attack of tumor cells by the tumor-infiltrating cytotoxic lymphocytes (TICLs) in a small, multicellular tumor, without necrosis and at some stages prior to angiogenesis. The analysis shows that the TICLs can play an important role in the control of cancer dormancy.

The treatment of cancer is then one of the most challenging problems of modern medicine. The treatment should satisfy two basic conditions: first, it should destroy cancer cells in the entire body. Second, it should distinguish between cancerous and healthy cells. Other treatments such as surgery and/or chemoand radiotherapies have played key roles in treatment [12], but in many cases they do not represent a cure. Immunotherapy seems to be the method that best fulfils both of these requirements [7, 13, 14].

Numerous research papers have been made to explore the effects of the immune system in eliminating the tumor cells in the host, by stimulating the host's own immune response to kill cancer cells [15]. When tumor cells appear in a body, the immune system tries to identify and then eliminate them. Immunotherapy refers to the use of cytokines usually together with Adoptive Cellular Immunotherapy (ACI). Cytokines are protein hormones that mediate both natural and specific immunity. They are produced mainly by activated T cells (lymphocytes) during cellular-mediated immunity. Interleukin-2 (IL-2) is the main cytokine responsible for lymphocyte activation, growth, and differentiation. IL-2 has been shown to enhance Cytotoxic T Cells (CTL) activity at different disease stages. However, ACI refers to the injection of cultured immune cells that have antitumor reactivity into tumor bearing host. This interaction is analyzed and studied in various levels of biomathematical researches. They commonly focused on the models on ODEs over time. For example, in 1985, DeBoer et al. [4] suggested a mathematical model which contains eleven ordinary differential equations with five algebraic equations to describe antitumor response with IL-2 taken into account. A simple version of this model is proposed by Kirschner and Panetta [14]. The model is only based on three differential equations. Further analysis by several authors has also been done; see [5, 6, 16–18].

Immunotherapy models and their predictions have been extensively studied in [9, 14, 19]. In [14], Kirschner et al. explored the role of cytokine in the disease dynamics and studied the long-term tumor recurrence and short-term tumor oscillations. However, in [19] Kuznetsov and Knott presented a mathematical model for the growth and suppression of the tumor. They showed that the model can describe the regrowth of a dormant tumor by two distinct mechanisms. One explanation for the tumor regrowth is based on a single clone model, while the other is based on a two-clone model. They fitted their ODE models to the data and obtained several curves for the tumor regrowth. They compared their predicted results with clinical and experimental observations, where both results confirm that intensive limited-term immunotherapy does not provide complete tumor elimination. The simulations show that medium-term control of cancer is exhibited when long-life immune memory cells are activated, but long-term control results from reducing the cancer growth rate.

In this paper, we investigate mathematical models for the dynamics between tumor cells, immune-effector cells, and the cytokine interleukin-2 (IL-2). It is worth stressing that we operate at a supermacroscopic scale, namely, by ordinary differential equations. However, the link to lower cellular scale is represented by the delay. The delay differential equations have long been used in modeling cancer phenomena [20–26]. It should be noted that the heterogeneity, mutations, and link with the lower molecular scale are neglected. These topics are documented in [17, 27, 28].

The organization of this paper is as follows: in Section 2, we provide different models, using ODEs and DDEs, with interaction functions in the Lotka-Volterra form to describe the response of the effector cells to the growth of tumor cells. In Section 3, we study the local stability of the steady states for tumor-free and endemic persistence. Bifurcation analysis for a three-equations model and finding regions of existence of the equilibria are discussed in Section 4. In Section 5, we discuss the conditions that ensure tumor-clearance possibilities and conclude in Section 6.

## 2. The Model

The model of Kuznetsov et al. [7] describes the response of the effector cells (ECs) to the growth of tumor cells (TCs). In this model, it has been taken into account the penetration of TCs by ECs, which simultaneously causes the inactivation of ECs. It is assumed that interactions between ECs and TCs are in vitro such that  $E$ ,  $T$ ,  $C$ ,  $E^*$ , and  $T^*$  denote the local concentrations of ECs, TCs, EC-TC conjugates, inactivated effector cells, and “lethally hit” TCs, respectively. The rate of binding of ECs to TCs and the rate of separation of ECs from TCs without damaging them are denoted by  $k_1$  and  $k_{-1}$ , respectively. The rate at which EC-TC integrations program for lysis is denoted by  $k_2$ , while the rate at which EC-TC interaction inactivate ECs is denoted by  $k_3$ . The model takes the form

$$\frac{dE}{dt} = s + F(C, T) - d_1 E - k_1 ET + (k_{-1} + k_2)C,$$

$$\frac{dT}{dt} = aT(1 - bT) - k_1 ET + (k_{-1} + k_3)C,$$

$$\frac{dC}{dt} = k_1 ET - (k_{-1} + k_2 + k_3)C,$$

$$\begin{aligned}
\frac{dE^*}{dt} &= ak_3C - d_3E^*, \\
\frac{dT^*}{dt} &= k_2C - d_3T^*.
\end{aligned}
\tag{2.1}$$

Here, the parameter  $s$  represents the normal rate (not increased by the presence of the tumor) of the flow of adult ECs into the tumor site and  $F(C, T)$  describes the accumulation of ECs in the tumor site, while  $d_1$ ,  $d_2$ , and  $d_3$  are the coefficients of the processes of destruction and migration of  $E$ ,  $E^*$ , and  $T^*$ , respectively. The maximal growth of tumor is represented by the coefficient  $a$ , and  $b$  is the environment capacity. It was suggested in [7] that the function  $F$  takes the form

$$F(C, T) = F(E, T) = \frac{pET}{r + T}, \tag{2.2}$$

where  $p$  and  $r$  are positive constants. This term is the Michaelis-Menten form to indicate the saturated effects of the immune response.

The idea in this paper is to simplify the above model and reduce it into a two- or three-equation model to describe the interactions of three types of cell populations: the activated immune-system cells,  $E(t)$  (or effector cells such as cytotoxic T-cells, macrophages, and natural killer cells that are cytotoxic to the tumor cells); the tumor cells,  $T(t)$ ; the concentration of IL-2 in the single tumor-site compartment,  $I_L(t)$ . The above model can then be governed by the following three equations (see [14]):

$$\begin{aligned}
\frac{dE}{dt} &= \bar{c}T - \bar{\mu}_1E + \bar{\theta}_1EI_L + \bar{s}_1, \\
\frac{dT}{dt} &= \bar{r}_2T(1 - \bar{b}T) - \bar{\alpha}ET, \\
\frac{dI_L}{dt} &= \bar{\theta}_2ET - \bar{\mu}_2I_L + \bar{s}_2,
\end{aligned}
\tag{2.3}$$

with initial conditions  $E(0) = E_0$ ,  $T(0) = T_0$ ,  $I_L(0) = I_{L0}$ , where  $\bar{c}$  is the antigenicity rate of the tumor,  $\bar{s}_1$  is the external source of the effector cells, with rate of death  $\bar{\mu}_1$ , whereas the parameter  $\bar{r}_2$  incorporates both multiplication and death of tumor cells. The maximal carrying capacity of the biological environment for tumor cell is  $\bar{b}^{-1}$ ,  $\bar{\theta}_1$  is considered as the cooperation rate of effector cells with Interleukin-2 parameter,  $\bar{\alpha}$  is the rate of tumor cells, and  $\bar{\theta}_2$  is the competition rate between the effector cells and the tumor cells. External input of IL-2 into the system is  $\bar{s}_2$ , and the rate loss parameter of effector cells is  $\bar{\mu}_2$ .

### 2.1. Nondimensionalization

System (2.3) is an example of *stiff* (One definition of the stiffness is that the global accuracy of the numerical solution is determined by stability rather than local error and implicit methods are more appropriate for it.) model, in the sense that it has properties that make it slow and expensive to solve using *explicit* numerical methods. Stiffness often appear due

to the differences in speed between the fastest and slowest components of the solutions, and stability constraints. The efficient use of reliable numerical methods, that is based in general on implicit formulae, for dealing with stiff problems involves a degree of sophistication not necessarily available to nonspecialists [29]. In addition, the state variables of these types of models are very sensitive to small perturbations (or changes) in the parameters occurring in the model. Consequently, the parameter estimates are also sensitive to the noisy data and observations. To ease the analysis and stability of the steady states with meaningful parameters and less sensitive (or robust) model, we nondimensionalize the bilinear model (2.3), by taking the following rescaling:

$$\begin{aligned} x &= \frac{E}{E_0}, & y &= \frac{T}{T_0}, & z &= \frac{I_L}{I_{L_0}}, & \theta_1 &= \frac{\bar{\theta}_1 I_{L_0}}{t_s}, & \theta_2 &= \frac{\bar{\theta}_2 E_0 T_0}{t_s I_{L_0}}, \\ \mu_1 &= \frac{\bar{\mu}_1}{t_s}, & \mu_2 &= \frac{\bar{\mu}_2}{t_s}, & b &= \bar{b} T_0, & c &= \frac{\bar{c} T_0}{t_s E_0}, & \alpha &= \frac{\bar{\alpha} E_0}{t_s}, \\ \tau &= t_s t, & r_2 &= \frac{\bar{r}_2}{t_s}, & s_1 &= \frac{\bar{s}_1}{t_s E_0}, & s_2 &= \frac{\bar{s}_2}{t_s I_{L_0}}. \end{aligned} \quad (2.4)$$

Therefore, after the above substitution into (2.3) and replacing  $\tau$  by  $t$ , the model becomes

$$\begin{aligned} \frac{dx}{dt} &= cy - \mu_1 x + \theta_1 xz + s_1, \\ \frac{dy}{dt} &= r_2 y(1 - by) - \alpha xy, \\ \frac{dz}{dt} &= \theta_1 xy - \mu_2 z + s_2, \end{aligned} \quad (2.5)$$

with initial conditions  $x(0) = x_0$ ,  $y(0) = y_0$ , and  $z(0) = z_0$ . Here  $x(t)$ ,  $y(t)$ , and  $z(t)$  denote the dimensionless density of ECs, TCs, and IL-2, respectively. In model (2.5), there are four possible cases of treatments, according the values of  $s_1$  and  $s_2$ : (i) notreatment case ( $s_1 = s_2 = 0$ ), (ii) adoptive cellular immunotherapy case ( $s_1 > 0$ ,  $s_2 = 0$ ), (iii) interleukin-2 case ( $s_1 = 0$ ,  $s_2 > 0$ ), (iv) and immunotherapy with both adoptive cellular immunotherapy (ACI) and IL-2 ( $s_1 > 0$ ,  $s_2 > 0$ ).

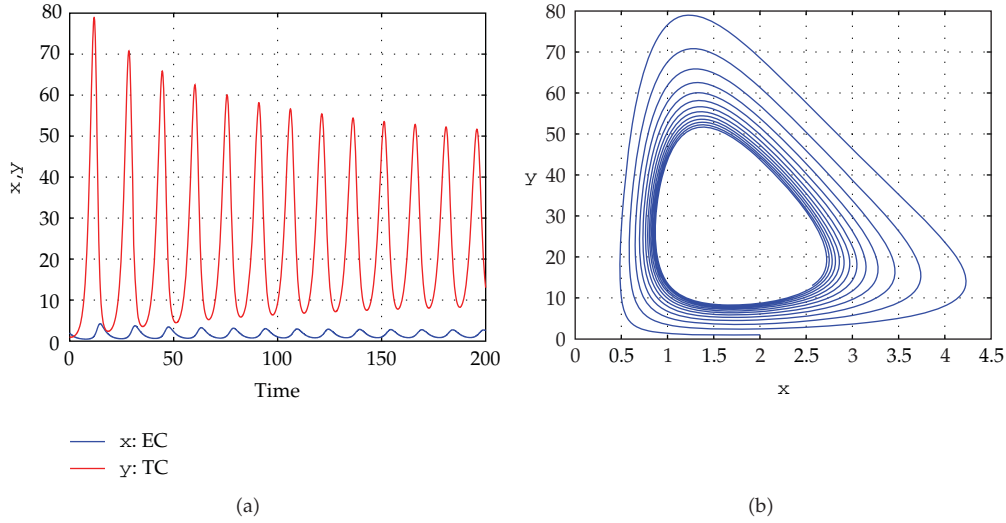
Yafia [10] considered system (2.5) in the absence of immunotherapy with IL-2,

$$\begin{aligned} \frac{dx}{dt} &= \omega xy - \mu x + s, \\ \frac{dy}{dt} &= r y(1 - by) - xy, \end{aligned} \quad (2.6)$$

where  $\omega$  is immune response to the appearance of the TCs,  $s$  has the same meaning of  $s_1$ ,  $r$  has the meaning of  $r_2$ , and  $\mu$  has the meaning of  $\mu_1$  in the above model. If we consider a time

**Table 1:** The nondimensionalization parameters of bilinear model (2.5).

$c = 5/18$	$\mu_1 = 1/6$	$\theta_1 = 1/18000000$
$r_2 = 1$	$b = 1/1000$	
$\mu_2 = 500/9$	$\theta_2 = 250/9$	

**Figure 1:** Solution of the DDEs (2.7) when  $\omega = 0.01184$ ,  $\mu = 0.3747$ ,  $s = 0.1181$ ,  $r = 1.636$ ,  $b = 0.002$ , and  $\tau = 0.8$ . This shows an unstable endemic equilibrium.

delay  $\tau > 0$  in (2.6) due to the time-lag in the interaction between ECs and TCs, the model takes the form

$$\begin{aligned}
 \frac{dx}{dt} &= \omega x(t)y(t-\tau) - \mu x(t) + s, \\
 \frac{dy}{dt} &= ry(t-\tau)(1 - by(t)) - x(t)y(t).
 \end{aligned}
 \tag{2.7}$$

In this model, we only consider the time delay in the dependent variable  $y$  (representing tumor) of the nonlinear term. Of course other models assume time delays in both variables  $x$  and  $y$  [6]. Further models that consider time delays when modeling tumor growth are discussed in [30–32]. To solve model (2.7), we should provide an initial function with initial function  $y(t) = \varphi(t)$ ,  $t \in [-\tau, 0]$  instead of the initial value  $y(0)$  at  $t = 0$  (see [3]). It has been shown that model (2.7) has visible and bounded solution (see [6, 11]). When the time delay is included in the simplified model (2.6), the state of returning tumor cells can be observed, as DDE models have richer dynamics than do ODE models; see the graphs displayed in Figures 1, 2, and 3. We next study the stability of the steady states of the above models, according the values of the parameters given in Table 1.

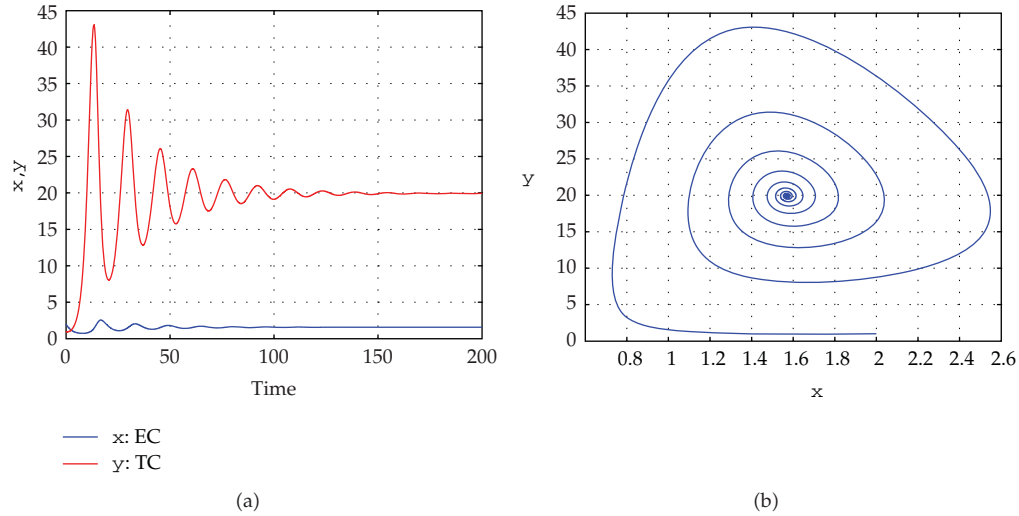


**Figure 2:** Solution of the DDEs (2.7) when  $\omega = 0.01184$ ,  $\mu = 0.3747$ ,  $s = 0.2181$ ,  $r = 1.636$ ,  $b = 0.002$  and  $\tau = 0.8$ . This shows a stable endemic equilibrium.

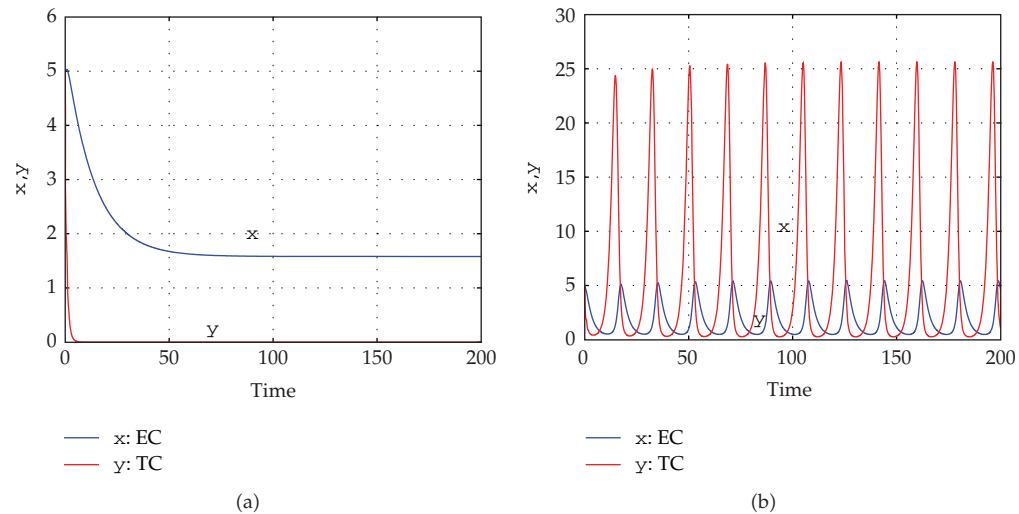


**Figure 3:** Solution of the DDEs (2.7) when  $\omega = 0.04184$ ,  $\mu = 0.03747$  (a), and  $\mu = 0.3747$  (b),  $s = 0.2181$ ,  $r = 1.636$ ,  $b = 0.002$ , and  $\tau = 0.8$ . The tumor-free equilibrium is asymptotically stable in the left banner and unstable in the right banner.

### 3. Steady States and Stability

The solutions of practical interest should have nonnegative population  $x$ ,  $y$ , and  $z$ . However, it is hard to find a closed analytical solution for the above nonlinear models, instated we can study their qualitative behavior by studying the stability of the steady states. We then assume that the parameters occuring in the models are also nonnegative.

### 3.1. Tumor-Free Equilibrium and Its Stability

To ease the analysis, we start with the 2-population model (2.6). The steady states of the reduced model (2.6) are the intersection of the null-clines  $dx/dt = 0$  and  $dy/dt = 0$ . If  $y = 0$ , the free tumor equilibrium is at  $(\bar{x}, \bar{y}) = (s/\mu, 0)$ . This steady state always exists, since  $s/\mu > 0$ . It is clear that the tumor-free equilibrium  $E_0 = (x^*, y^*) = (s/\mu, 0)$  of the model (2.6) is asymptotically stable if  $r\mu < s$  and unstable if  $r\mu > s$ . Whoever, when we consider the DDEs model, the characteristic equation of the linearized model of (2.7) at  $E_0 = (s/\mu, 0)$  takes the form

$$(\lambda + r) \left( \lambda - e^{-\lambda\tau} + \frac{s}{\mu} \right) = 0. \quad (3.1)$$

When  $\tau = 0$ , it is clear that  $E_0$  is asymptotically stable when  $r\mu < s$  and unstable otherwise. However, if  $\tau > 0$ , (3.1) has a negative real root  $\lambda = -r$  and roots of

$$\lambda - e^{-\lambda\tau} + \frac{s}{\mu} = 0. \quad (3.2)$$

Putting  $\lambda = \xi i$  in (3.2) and separating real and imaginary parts yields

$$\xi^2 = \left[ r^2 - \left( \frac{s}{\mu} \right)^2 \right]. \quad (3.3)$$

Therefore, when  $|r\mu| < |s|$  there are no positive real root  $\xi$ . This shows that all the roots of (3.1) have negative real parts and  $E_0$  is asymptotically stable.

In case of the three-equation model (2.5), and at the equilibrium points, we have

$$\begin{aligned} 0 &= cy - \mu_1 x + \theta_1 xz + s_1, & 0 &= r_2 y(1 - by) - \alpha xy, \\ 0 &= \theta_2 xy - \mu_2 z + s_2. \end{aligned} \quad (3.4)$$

Putting  $y = 0$  yields the tumor-free equilibrium, namely,

$$E_0 = \left[ \frac{s_1 \mu_2}{\mu_1 \mu_2 - \theta_1 s_2}, 0, \frac{s_2}{\mu_2} \right]. \quad (3.5)$$

It is clear that the infection-free equilibrium  $E_0$  exists if and only if  $s_2 < \mu_1 \mu_2 / \theta_1$ . Therefore, we restrict our analysis to the case where  $s_2 < \mu_1 \mu_2 / \theta_1$ . To study its stability, we consider the corresponding Jacobian matrix

$$J_{E_0} = \begin{bmatrix} -\mu_1 + \theta_1 s_2 / \mu_2 & c & \theta_1 s_1 \mu_2 / (\mu_1 \mu_2 - \theta_1 s_2) \\ 0 & r_2 - \alpha s_1 \mu_2 / (\mu_1 \mu_2 - \theta_1 s_2) & 0 \\ 0 & \theta_2 s_1 \mu_2 / (\mu_1 \mu_2 - \theta_1 s_2) & -\mu_2 \end{bmatrix}. \quad (3.6)$$



It has the eigenvalues  $-\mu_1 + \theta_1 s_2 / \mu_2$ ,  $r_2 - \alpha s_1 \mu_2 / (\mu_1 \mu_2 - \theta_1 s_2)$ , and  $-\mu_2$ . Therefore,  $E_0$  is locally asymptotically stable if and only if  $r_2 < \alpha s_1 \mu_2 / (\mu_1 \mu_2 - \theta_1 s_2)$ , while otherwise it is an unstable saddlepoint.

### 3.2. Endemic Equilibrium and Its Stability

Consider again the two-equation model (2.6). If  $y \neq 0$ , the steady states are obtained by solving  $\omega r b y^2 - r(\omega + \mu b)y + \mu r - s = 0$ . In this case, we have two endemic equilibria  $P_1 = (x_1, y_1)$  and  $P_2 = (x_2, y_2)$ , where

$$\begin{aligned} x_1 &= \frac{-r(b\mu - \omega) - \sqrt{\Delta}}{2\omega}, & y_1 &= \frac{r(b\mu + \omega) + \sqrt{\Delta}}{2rb\omega}, \\ x_2 &= \frac{-r(b\mu - \omega) + \sqrt{\Delta}}{2\omega}, & y_2 &= \frac{r(b\mu + \omega) - \sqrt{\Delta}}{2rb\omega}, \end{aligned} \quad (3.7)$$

with  $\Delta = r^2(b\mu - \omega)^2 + 4\omega r b \mu > 0$ . The Jacobian matrix of the system (2.6) at the endemic equilibrium  $P_1$  is

$$J_{\text{endemic}} = \begin{bmatrix} \omega y_1 - \mu & \omega x_1 \\ -y_1 & r - 2br y_1 - x_1 \end{bmatrix}. \quad (3.8)$$

**Proposition 3.1.** *If the endemic equilibrium  $P_1$  exists and has nonnegative coordinates, then  $\text{tr}(J_{\text{endemic}}) > 0$  and  $P_1$  is unstable.*

*Proof.* Since

$$\text{tr}(J_{\text{endemic}}) = \frac{\omega^2 - \omega(rb + b\mu) - rb^2\mu}{2b\omega} + \frac{\omega - rb}{2rb\omega} \sqrt{r^2(b\mu + \omega)^2 - 4rb\omega(r\mu - s)}, \quad (3.9)$$

then inequality  $\text{tr}(J_{\text{endemic}}) > 0$  is true if

$$r \left[ \omega^2 - \omega(rb + b\mu) - rb^2\mu \right] > (rb - \omega) \sqrt{r^2(b\mu + \omega)^2 - 4rb\omega(r\mu - s)}. \quad (3.10)$$

Therefore, when  $r\mu < s$  and  $\omega < -b\mu$ , we have  $\omega^2 - \omega b(r + \mu) - r\mu b^2 > 0$  and hence both sides of the inequality are positive. Therefore, if the point  $P_1$  exists and has nonnegative coordinates, then  $\text{tr}(J_{\text{endemic}}) > 0$  and the point  $P_1$  is unstable whenever  $\omega < -b\mu$  and  $r\mu < s$ .  $\square$

Similarly, it is easy to prove the following proposition.

**Proposition 3.2.** *If the point  $P_2$  exists and has nonnegative coordinates, then it is asymptotically stable.*

We extend the above analysis to the case of the three-equation model (2.5). The tumor-persistent solutions are obtained by putting  $y \neq 0$  and omitting  $x$  and  $z$  in (3.4) to get a scalar equation in the variable  $y$  which reads

$$F(r_2, y) = C_3 y^3 + C_2 y^2 + C_1 y + C_0 = 0, \quad (3.11)$$

where

$$\begin{aligned} C_3 &= \theta_1 \theta_2 r_2^2 b^2 > 0, \\ C_2 &= -2\theta_1 \theta_2 b r_2^2 < 0, \\ C_1 &= r_2^2 \theta_1 \theta_2 + r_2 b (\mu_1 \mu_2 - s_2 \theta_1) \alpha + c \mu_2 \alpha^2, \\ C_0 &= \alpha [r_2 (\theta_1 s_2 - \mu_1 \mu_2) + \mu_2 s_1 \alpha]. \end{aligned} \quad (3.12)$$

Since  $s_2 < \mu_1 \mu_2 / \theta_1$ , then the coefficient  $C_1$  is always positive, while the coefficient  $C_0$  can take positive and negative values depending on the values of the model parameters. Also, (3.11) is well defined for all  $y \in [0, 1/b]$ . Its left-hand side is a polynomial of degree three, and its zeros are not easy to be obtained in a closed-form. However, some conditions in the parameters occur in the model to ensure the existence of its solutions could be deduced. Equation (3.11) can also be seen as a bifurcation equation in  $r_2$  and  $y$ , where we keep all other parameters fixed. Once a solution  $y > 0$  of this equation has been obtained, we could find positive  $x$  and  $z$  from the other equations in (3.4). Therefore, there is a one-to-one correspondence between the solutions of (3.11) and the endemic stationary solutions. For more insights, we next study the bifurcation analysis.

#### 4. Bifurcation Analysis of Model (2.5)

The *bifurcation analysis* gives a deeper analysis about the model. It answers the query that “how does the behavior of the solutions change as parameters change.” We restrict ourselves to only study the bifurcation analysis of ODEs models rather than DDEs models.

##### 4.1. Bifurcation Points for the Parameter $r_2$

In this subsection, we then analyze the bifurcation so that the tumor growth rate  $r_2$  acts as a bifurcation parameter. Therefore, to find the bifurcation point(s), we put  $y = 0$  in (3.11) to get  $r_2 = \alpha \mu_2 s_1 / (\mu_1 \mu_2 - \theta_1 s_2) := \bar{r}_2$ . Hence, there is only one transcritical bifurcation point at

$$(\bar{r}_2, \bar{y}) = \left( \frac{\alpha \mu_2 s_1}{\mu_1 \mu_2 - \theta_1 s_2}, 0 \right). \quad (4.1)$$

Now, we compute the direction of bifurcation at  $(\bar{r}_2, 0)$  so that

$$\left. \frac{dy}{dr_2} \right|_{(\bar{r}_2, 0)} = - \left. \frac{F_{r_2}}{F_y} \right|_{(\bar{r}_2, 0)}, \quad (4.2)$$

where

$$F_{r_2}|_{(\bar{r}_2, 0)} = -\alpha(\mu_1\mu_2 - \theta_1s_2) < 0, \quad F_y|_{(\bar{r}_2, 0)} = \left( c + bs_1 + \frac{\theta_1\theta_2\mu_2s_1^2}{(\mu_1\mu_2 - \theta_1s_2)^2} \right) \mu_2\alpha^2 > 0. \quad (4.3)$$

Hence, the bifurcation at the point  $(\bar{r}_2, 0)$  is forward, irrespective of the values of the model-parameters. We notice that the model we consider here has only one bifurcation point  $(\bar{r}_2, 0)$  at which the bifurcation is forward.

#### 4.2. Bifurcation Diagrams for the Parameter $\alpha$

The parameter  $\alpha$  is very important in the model that plays an effective role to define cancer behavior. We investigate numerically, in this subsection, the bifurcation of the model for the parameter  $\alpha$ . We consider the four cases: no treatment case ( $s_1 = s_2 = 0$ ), adoptive cellular immunotherapy case ( $s_1 > 0, s_2 = 0$ ), interleukin-2 case ( $s_1 = 0, s_2 > 0$ ), and immunotherapy with both ACI and IL-2 case ( $s_1 > 0, s_2 > 0$ ).

If we solve  $F(y, \alpha) = F(\alpha, y) = 0$  in  $\alpha$ , we have

$$\begin{aligned} \alpha_+ &= \frac{r_2b(y - 1/b)}{2\mu_2(cy + s_1)} \left[ (\theta_1s_2 - \mu_1\mu_2) + \sqrt{(\mu_1\mu_2 - s_2\theta_1)^2 - 4\theta_1\theta_2\mu_2y(cy + s_1)} \right], \\ \alpha_- &= \frac{r_2b(y - 1/b)}{2\mu_2(cy + s_1)} \left[ (\theta_1s_2 - \mu_1\mu_2) - \sqrt{(\mu_1\mu_2 - s_2\theta_1)^2 - 4\theta_1\theta_2\mu_2y(cy + s_1)} \right]. \end{aligned} \quad (4.4)$$

To plot  $(\alpha, y)$  in the interval  $0 < y < 1/b$ , under the conditions that

$$\begin{aligned} (\mu_1\mu_2 - s_2\theta_1)^2 - 4\theta_1\theta_2\mu_2y(cy + s_1) &> 0, \\ -4\theta_1\theta_2c\mu_2y^2 - 4\theta_1\theta_2\mu_2s_1y + (\mu_1\mu_2 - s_2\theta_1)^2 &> 0, \end{aligned} \quad (4.5)$$

we have

$$y^2 + \frac{s_1}{c}y - \frac{(\mu_1\mu_2 - s_2\theta_1)^2}{4\theta_1\theta_2c\mu_2} < 0. \quad (4.6)$$

Then

$$\frac{1}{2} \left[ \frac{-s_1}{c} - \sqrt{\left(\frac{s_1}{c}\right)^2 + \frac{(\mu_1\mu_2 - s_2\theta_1)^2}{\theta_1\theta_2c\mu_2}} \right] < y < \frac{1}{2} \left[ \frac{-s_1}{c} + \sqrt{\left(\frac{s_1}{c}\right)^2 + \frac{(\mu_1\mu_2 - s_2\theta_1)^2}{\theta_1\theta_2c\mu_2}} \right]. \quad (4.7)$$

For  $0 < y < y_+$ , where

$$y_+ = \frac{1}{2} \left[ \frac{-s_1}{c} + \sqrt{\left(\frac{s_1}{c}\right)^2 + \frac{(\mu_1\mu_2 - s_2\theta_1)^2}{\theta_1\theta_2c\mu_2}} \right], \quad (4.8)$$

we have two cases  $y_+ < 1/b$  or  $y_+ > 1/b$ . The graphs in Figure 4, which are obtained numerically, display the bifurcation diagrams for different cases, where (i)  $s_1 = s_2 = 0$ , (ii)  $s_1 = 10, s_2 = 0$ , (iii)  $s_1 = 0, s_2 = 40$ , and (vi)  $s_1 = 10, s_2 = 40$ .

Given the threshold point  $(\alpha, y) = (\alpha^*, 0)$ , the tumor clearance condition is  $\alpha > \alpha^*$ , where

$$\alpha^* = \frac{(\mu_1\mu_2 - \theta_1s_2)r_2}{\mu_2s_1}. \quad (4.9)$$

Therefore, when  $s_1 > 0$ , then  $\alpha^* > 0$  and  $\alpha \propto 1/s_1$ . Thus, we can arrive to tumor clearance quickly when the value of  $s_1$  increases. We notice from Figure 4 that the locations of saddle node bifurcation points **A** and **B** bridge the one-positive equilibrium to the three-positive equilibria. The supercritical Hopf bifurcation point **C** joints between existence of stable limit cycles and nonexistence of limit cycles. The transcritical bifurcation point **D** at  $(\alpha, y) = (\alpha^*, 0)$  bridges the one-positive equilibrium and no positive equilibria.

### 4.3. Regions of Existence of the Equilibria

In addition to the tumor-free equilibrium, (3.11) may have one to three persistent-tumor equilibria, depending on the values of the model-parameters. However, before we proceed we provide the following proposition, which is helpful in the analysis.

**Proposition 4.1.** *Equation (3.11) does not have two persistent-tumor equilibria if  $r_2 < \bar{r}_2$ , where  $\bar{r}_2$  is given in (4.1).*

*Proof.* Since the bifurcation direction at the point  $(\bar{r}_2, 0)$  is always forward, then (3.11) has two positive roots, for  $r_2 < \bar{r}_2$ , if and only if  $F(\bar{r}_2, y) = y(\bar{c}_3y^2 + \bar{C}_2y + \bar{C}_1) = 0$  has two positive zeros, where

$$\begin{aligned} \bar{C}_2 &= \frac{-2}{b}\bar{C}_3 = -2b\theta_1\theta_2\left(\frac{\mu_2s_1\alpha}{\mu_1\mu_2 - \theta_1s_2}\right)^2, \\ \bar{C}_1 &= \theta_1\theta_2\left(\frac{\mu_2s_1\alpha}{\mu_1\mu_2 - \theta_1s_2}\right)^2 + \mu_2\alpha^2(bs_1 + c\mu_2). \end{aligned} \quad (4.10)$$

However,  $\bar{C}_2^2 - 4\bar{C}_1\bar{C}_3 = -4\bar{C}_3\mu_2\alpha^2(bs_1 + c\mu_2) < 0$ . Therefore, the proof is complete.  $\square$

Now, to find the conditions, on the model parameters, being required for the existence of the persistent equilibria, we make the use of both Descant's rule of signs and the Sturm sequence [33]. In (3.11), it is clear that the coefficients  $C_3$ ,  $C_2$ , and  $C_1$  have fixed signs, while the coefficient  $C_0$  can take positive or negative values. Hence, the number of feasible tumor-persistent equilibria (on the interval  $y \in [0, 1/b]$ ) depends on the difference

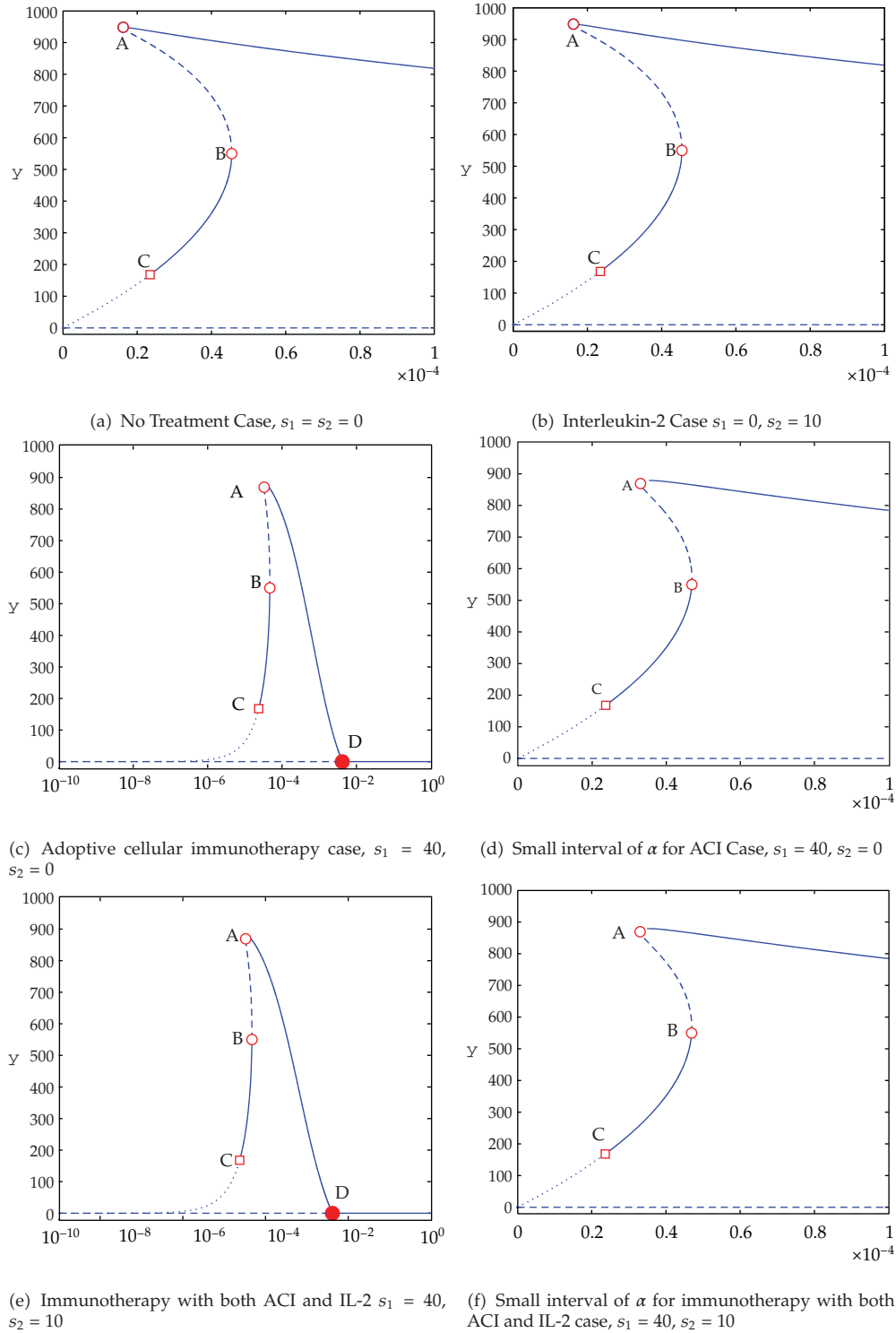


**Figure 4:** shows the bifurcation diagrams for the bilinear model (2.5) for the parameter  $\alpha$ : [—] represents the stable equilibrium, [- - -] represents the unstable equilibrium, [ $\cdots$ ] is the stable limit cycles, while [o] is the saddle node bifurcation. [•] is the transcritical bifurcation and [□] the supercritical Hopf bifurcation. The values of parameters are given in Table 1.

**Table 2:** The number of positive steady states (SS) is determined by the signs of the coefficients (3.11) and the signs of the quantities  $R$ ,  $S$ , and  $T$  from the Sturm sequence. Blank entries correspond to coefficients which may take positive, negative, or zero values.

SS	$C_0$	$R$	$S$	$T$
0	+		-	-
1	-			-
3	-	+	-	+

between the number of sign changes at  $y = 0$  and at  $y = 1/b$  in the Sturm sequence  $\{P_0(y), P_1(y), P_2(y), P_3(y)\}$ , such that

$$\begin{aligned}
 P_0(y) &= F(y) = C_3 y^3 + C_2 y^2 + C_1 y + C_0, \\
 P_1(y) &= F'(y) = 3C_3 y^2 + 2C_2 y + C_1, \\
 P_2(y) &= \frac{2}{9} R y + \frac{1}{9} S, \quad P_3(y) = T, \quad \text{where } R = (C_2^2 - 3C_1 C_3)/C_3, \\
 S &= (C_2 C_1 - 9C_0 C_3)/C_3, \quad T = \frac{R}{3} - 3C_3 \left( \frac{S}{2R} - \frac{C_2}{3C_3} \right)^2.
 \end{aligned} \tag{4.11}$$

Hence the number of sign changes depends on the sign of the coefficient  $C_0$  and the remainders  $R$ ,  $S$ , and  $T$ . Table 2 shows the conditions required for the existence of persistent-tumor equilibria as well as their numbers, where we take into account that  $C_0 > 0$  implies  $S < 0$ .

We may note that the tumor-persistent equilibria do not exist for  $C_0 > 0$ , while one or three equilibria exist depending on the other relevant quantities. The interest is to find the area where the tumor-free equilibrium is a global attractor. Based on Proposition 4.1 and Table 2, this area is determined by  $C_0 > 0$  that is equivalent to

$$r_2 < \frac{\mu_2 s_1 \alpha}{\mu_1 \mu_2 - \theta_1 s_2} := r_2^*, \tag{4.12}$$

where  $r_2^*$  is the *critical growth rate of the tumor cell population*, separating between nonexistence and existence of positive endemic equilibria.

If we consider the general case of immunotherapy with both ACI and IL-2 treatments, then according to the conditions given in Table 2 and data displayed in Figure 4, then Figure 5 displays six stability regions in terms of the two parameters  $\alpha$ ,  $r_2$  (according to the number of positive equilibria and the limit cycles). However, Figure 6 shows phase spaces for different equilibria where there are stable steady states, unstable steady states, stable manifold, unstable manifold and initial conditions. For example, Figure 6(f) shows the trajectories where there are three tumor-persistent equilibria for which two of them are locally stable and one, lying in between, for tumor-free equilibrium, is unstable (that correspond to region 3.b in Figure 5). Figure 6(e) shows the trajectories where there are three tumor-persistent equilibria for which one of them is locally stable, one is stable limit cycles, and one, lying in between, for tumor-free equilibrium is unstable (that correspond to region 3.a in Figure 5).

## 5. Tumor-Clearance Possibilities

Let us introduce the following definition to facilitate the analysis.

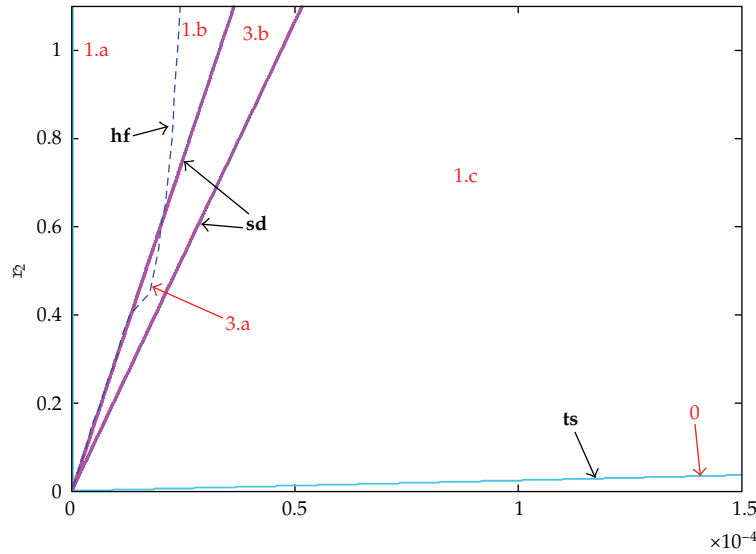


**Figure 5:** The two-dimensional transition structure as a function of  $\alpha$  (the tumor cell is predated by effector cells rate) and  $r_2$  (the maximal growth rate of the tumor cells population): **sd** is the saddle node bifurcation, **ts** is the transcritical bifurcation, and **hf** is the supercritical Hopf bifurcation. (Immunotherapy with both ACI and IL-2 Case; see Table 1 and  $s_1 = 40$ ,  $s_2 = 10$ .).

*Definition 5.1.* The threshold parameter  $\mathcal{R}_0$  (the minimum tumor-clearance parameter) is the parameter that has the property that if  $\mathcal{R}_0 < 1$ , then the endemic tumor does not exist, while if  $\mathcal{R}_0 > 1$  the tumor persists (see [34]).

The parameter  $\mathcal{R}_0$  can then be expressed in terms of the ratio between the tumor-growth rate and the critical tumor-growth rate separating between nonexistence and existence of endemic tumor. Now, for the three-equations model, the tumor-free equilibrium is the unique equilibrium if and only if  $r_2 < r_2^*$ , where it is also locally asymptotically stable. Therefore, the minimum tumor-clearance parameter is  $\mathcal{R}_0 = r_2 / r_2^*$  and clearing the tumor requires the achievement of the inequality  $\mathcal{R}_0 < 1$ . It is equivalent to the following set of inequalities:

$$s_1 > \frac{\mu_1 \mu_2 - \theta_1 s_2}{\mu_2 \alpha} r_2 := s_1^*, \quad s_2 < \frac{\mu_1 \mu_2}{\theta_1} := s_2^*. \quad (5.1)$$

Hence clearing the tumor depends mainly on the concentration of treatments: the external source of effector cells  $s_1$  and the treatment  $s_2$ , which represents the external input of IL-2. If  $s_2 = 0$ , then the tumor can be cleared by treatment with adoptive cellular immunotherapy alone,  $s_1 > (\mu_1 / \alpha) r_2$ . However, for  $s_1 = 0$ , then the inequality  $r_2 < r_2^*$  cannot be held and therefore, it is impossible to treat cancer by IL-2 alone. However, a strategy based on using both adoptive immunotherapy and IL-2 with concentrations  $s_2 < s_2^*$  and  $s_1 > s_1^*$  could be used to clear the tumor; see Figure 7. We arrive to the following corollary.

**Corollary 5.2.** *In the tumor-clearance problem, we have the following three cases:*

- (i) if  $s_1 = 0$ , the tumor could never be cleared,



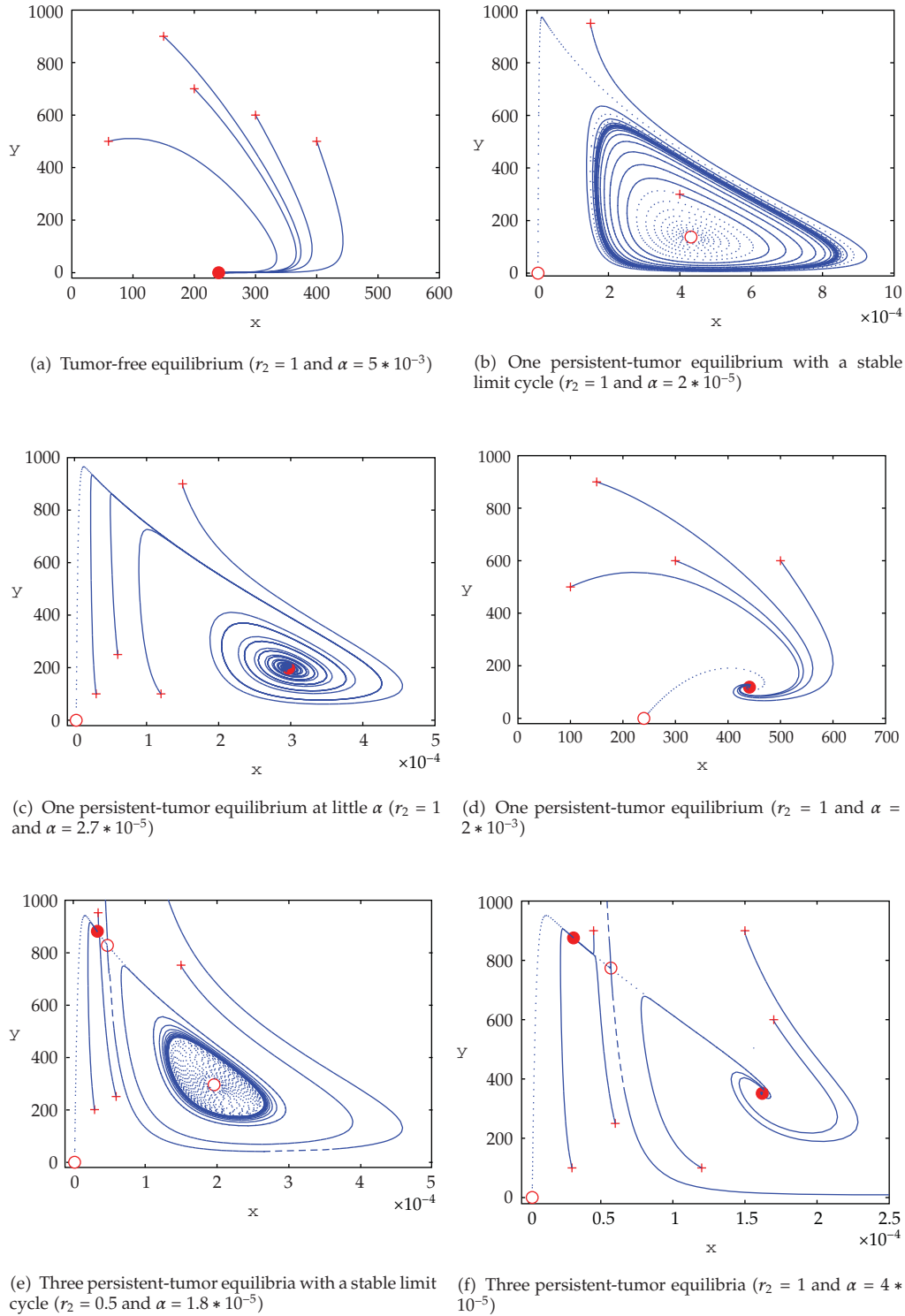


**Figure 6:** The phase spaces at different equilibria where stable steady states [●], unstable steady states [○], stable manifold [---], unstable manifold [...], and initial conditions [+], exist. (with immunotherapy with both ACI and IL-2, see Table 1 and  $s_1 = 40$ ,  $s_2 = 10$ ).

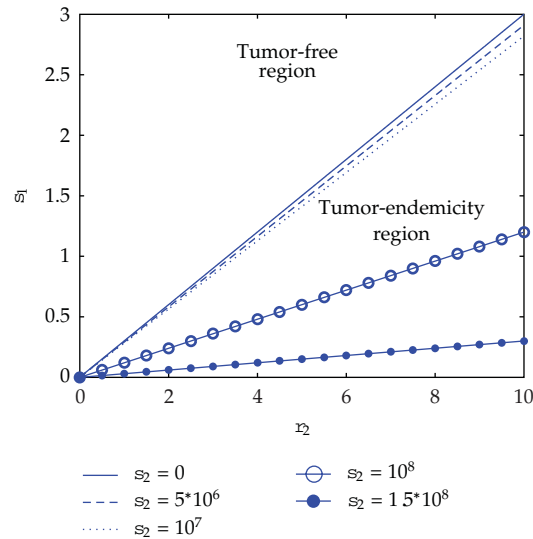


**Figure 7:** The critical  $s_1^*$  as a function of  $r_2$  for several levels of  $s_2$ . For values of  $s_1$  above the threshold  $s_1^*$ , the tumor cells do not exist (with  $\alpha = 0.5556$ ), see Table 1.

- (ii) if  $s_2 = 0$ , the tumor could be cleared by adding an external source of effector cells with concentration slightly above  $s_1^* = (\mu_1/\alpha)r_2$ ,
- (iii) if  $s_1 \neq 0$  and  $s_2 \neq 0$ , then the tumor could be cleared with concentrations  $s_2 < \mu_1\mu_2/\theta_1$  and  $s_1 > ((\mu_1\mu_2 - \theta_1s_2)/\mu_2\alpha)r_2$ .

## 6. Summary and Conclusion

In this paper, we introduced a family of differential models (ODEs and DDEs) to describe the dynamics of cancer. The ODEs models model cancer at supermacroscopic, in the sense that they describe the interaction between the tumor cells and the normal (immune) cells [1]. However, the DDEs models link it with the lower cellular scale. The qualitative and evolution of the models have been displayed with different values of the parameters  $\alpha$  (the rate of tumor cells predated by the effector cells) and  $r_2$  (the maximal growth rate of the tumor cells population). Although the underlying models are simple, they display very rich dynamics and give a good picture for the phenomena of real interaction of tumor growth and immunotherapy. The minimum tumor-clearance parameter  $\mathcal{R}_0$  has been expressed in terms of the ratio between the tumor-growth rate and the critical tumor-growth rate. The cases at which the tumor can be cleared are summarized in Corollary 5.2. The obtained results can help to gain a better understanding of interaction mechanisms and make predictions, determine and evaluate control strategies, and convey more general insight to biologists.

The numerical simulations (have been obtained by semi-implicit RK methods [29]) demonstrate that the system with time delay exhibits richer complex dynamics, such as quasiperiodic and chaotic patterns, compared with models without memory or after-effect. The steady states of DDEs models are similar to the steady states of ODEs models. We shall extend this work to investigate the qualitative behavior and bifurcation analysis of more sophisticated models of DDEs in modeling tumor-immune interactions with immunotherapy

and control functionals to maximize the effector cells and interleukin-2 concentration and to minimize the tumor cells.

## Acknowledgments

The authors would like to thank the referees and Professor Pedro Serranho for their valuable comments on the paper. The first author should thank Emirates Foundation for partially funding this research.

## References

- [1] N. Bellomo, N. K. Li, and P. K. Maini, "On the foundations of cancer modelling: selected topics, speculations, and perspectives," *Mathematical Models & Methods in Applied Sciences*, vol. 18, no. 4, pp. 593–646, 2008.
- [2] N. Bellomo, A. Bellouquid, J. Nieto, and J. Soler, "Multiscale biological tissue models and flux-limited chemotaxis for multicellular growing systems," *Mathematical Models & Methods in Applied Sciences*, vol. 20, no. 7, pp. 1179–1207, 2010.
- [3] F. Rihan, "Delay differential models in dynamic diseases," in *Proceedings of the International Conference on Bioinformatics and Computational Biology*, vol. 2, pp. 73–79, Honolulu, Hawaii, USA, 2010.
- [4] R. J. DeBoer, P. Hogeweg, F. Dullens, R. D. Weger, and W. DenOtter, "Macrophage T lymphocyte interactions in the antitumor immune response: a mathematical model," *Journal of Immunology*, vol. 134, no. 4, pp. 2748–2758, 1985.
- [5] C. DeLisi and A. Riscigno, "Immune surveillance and neoplasia. I. A minimal mathematical model," *Bulletin of Mathematical Biology*, vol. 39, no. 2, pp. 201–221, 1977.
- [6] M. Gałach, "Dynamics of the tumor-immune system competition the effect of time delay," *International Journal of Applied Mathematics and Computer Science*, vol. 13, no. 3, pp. 395–406, 2003.
- [7] V. A. Kuznetsov, I. A. Makalkin, M. A. Taylor, and A. S. Perelson, "Nonlinear dynamics of immunogenic tumors: parameter estimation and global bifurcation analysis," *Bulletin of Mathematical Biology*, vol. 56, no. 2, pp. 295–321, 1994.
- [8] V. A. Kuznetsov, "Mathematical modeling of the development of dormant tumors and immune stimulation of their growth," *Cybernetics and Systems Analysis*, vol. 23, no. 4, pp. 556–564, 1987.
- [9] A. Matzavinos, M. A. J. Chaplain, and V. A. Kuznetsov, "Mathematical modelling of the spatio-temporal response of cytotoxic T-lymphocytes to a solid tumour," *Mathematical Medicine and Biology*, vol. 21, no. 1, pp. 1–34, 2004.
- [10] R. Yafia, "Hopf bifurcation analysis and numerical simulations in an ODE model of the immune system with positive immune response," *Nonlinear Analysis*, vol. 8, no. 5, pp. 1359–1369, 2007.
- [11] R. Yafia, "Hopf bifurcation in differential equations with delay for tumor-immune system competition model," *SIAM Journal on Applied Mathematics*, vol. 67, no. 6, pp. 1693–1703, 2007.
- [12] L. G. de Pillis, W. Gu, and A. E. Radunskaya, "Mixed immunotherapy and chemotherapy of tumors: modeling, applications and biological interpretations," *Journal of Theoretical Biology*, vol. 238, no. 4, pp. 841–862, 2006.
- [13] B. Joshi, X. Wang, S. Banerjee, H. Tian, A. Matzavinos, and M. A. J. Chaplain, "On immunotherapies and cancer vaccination protocols: a mathematical modelling approach," *Journal of Theoretical Biology*, vol. 259, no. 4, pp. 820–827, 2009.
- [14] D. Kirschner and J. C. Panetta, "Modeling immunotherapy of the tumor—immune interaction," *Journal of Mathematical Biology*, vol. 37, no. 3, pp. 235–252, 1998.
- [15] D. Liu, S. Ruan, and D. Zhu, "Bifurcation analysis in models of tumor and immune system interactions," *Discrete and Continuous Dynamical Systems*, vol. 12, no. 1, pp. 151–168, 2009.
- [16] J. C. Arciero, T. L. Jackson, and D. E. Kirschner, "A mathematical model of tumor-immune evasion and siRNA treatment," *Discrete and Continuous Dynamical Systems*, vol. 4, no. 1, pp. 39–58, 2004.
- [17] N. Bellomo and M. Delitala, "From the mathematical kinetic, and stochastic game theory to modelling mutations, onset, progression and immune competition of cancer cells," *Physics of Life Reviews*, vol. 5, no. 4, pp. 183–206, 2008.
- [18] O. Isaeva and V. Osipov, "Modelling of anti-tumor immune response: immunocorrective effect of weak centimeter electromagnetic waves," *Journal of Mathematical Methods in Medicine*, vol. 10, no. 3, pp. 185–201, 2009.

- [19] V. A. Kuznetsov and G. D. Knott, "Modeling tumor regrowth and immunotherapy," *Mathematical and Computer Modelling*, vol. 33, no. 12-13, pp. 1275–1287, 2001.
- [20] M. Bodnar, U. Foryś, and J. Poleszczuk, "Analysis of biochemical reactions models with delays," *Journal of Mathematical Analysis and Applications*, vol. 376, no. 1, pp. 74–83, 2011.
- [21] U. Foryś, "Multi-dimensional Lotka-Volterra systems for carcinogenesis mutations," *Mathematical Methods in the Applied Sciences*, vol. 32, no. 17, pp. 2287–2308, 2009.
- [22] U. Foryś, M. Bodnar, and J. Poleszczuk, "Negativity of delayed induced oscillations in a simple linear DDE," *Applied Mathematics Letters*, vol. 24, no. 6, pp. 982–986, 2011.
- [23] J. Miekisz, J. Poleszczuk, M. Bodnar, and U. Forys, "Stochastic models of gene expression with delayed degradation," *Bulletin of Mathematical Biology*, vol. 73, no. 9, pp. 2231–2247, 2011.
- [24] M. J. Piotrowska and U. Foryś, "Analysis of the Hopf bifurcation for the family of angiogenesis models," *Journal of Mathematical Analysis and Applications*, vol. 382, no. 1, pp. 180–203, 2011.
- [25] M. Piotrowska and U. Forys, "The nature of hopf bifurcation for the gompertz model with delays," *Mathematical and Computer Modelling*, vol. 54, pp. 9–10, 2011.
- [26] J. Poleszczuk, M. Bodnar, and U. Foryś, "New approach to modeling of antiangiogenic treatment on the basis of Hahnfeldt et al. model," *Mathematical Biosciences and Engineering*, vol. 8, no. 2, pp. 591–603, 2011.
- [27] E. Gabetta and E. Regazzini, "About the gene families size distribution in a recent model of genome evolution," *Mathematical Models & Methods in Applied Sciences*, vol. 20, no. 6, pp. 1005–1020, 2010.
- [28] J. Paulsson, "Models of stochastic gene expression," *Physics of Life Reviews*, vol. 2, no. 2, pp. 157–175, 2005.
- [29] F. A. Rihan, E. H. Doha, M. I. Hassan, and N. M. Kamel, "Numerical treatments for Volterra delay integro-differential equations," *Computational Methods in Applied Mathematics*, vol. 9, no. 3, pp. 292–308, 2009.
- [30] M. Bodnar and U. Foryś, "Behaviour of solutions to Marchuk's model depending on a time delay," *International Journal of Applied Mathematics and Computer Science*, vol. 10, no. 1, pp. 97–112, 2000.
- [31] M. Bodnar and U. Foryś, "Periodic dynamics in a model of immune system," *Applicationes Mathematicae*, vol. 27, no. 1, pp. 113–126, 2000.
- [32] H. M. Byrne, "The effect of time delays on the dynamics of avascular tumor growth," *Mathematical Biosciences*, vol. 144, no. 2, pp. 83–117, 1997.
- [33] R. Beaumont and R. Pierce, *The Algebraic Foundations of Mathematics*, Addison-Wesely, Reading, Mass, USA, 1963.
- [34] M. Safan, H. Heesterbeek, and K. Dietz, "The minimum effort required to eradicate infections in models with backward bifurcation," *Journal of Mathematical Biology*, vol. 53, no. 4, pp. 703–718, 2006.

## Research Article

# Modeling of Brain Shift Phenomenon for Different Craniotomies and Solid Models

**Alvaro Valencia,<sup>1</sup> Benjamin Blas,<sup>1</sup> and Jaime H. Ortega<sup>2</sup>**

<sup>1</sup> Department of Mechanical Engineering, Universidad de Chile, Beauchef 850, Santiago, Chile

<sup>2</sup> Department of Mathematical Engineering and Center for Mathematical Modeling, Universidad de Chile, Av. Blanco Encalada 2120, Santiago, Chile

Correspondence should be addressed to Alvaro Valencia, [alvalenc@ing.uchile.cl](mailto:alvalenc@ing.uchile.cl)

Received 15 July 2011; Revised 4 October 2011; Accepted 20 October 2011

Academic Editor: Venky Krishnan

Copyright © 2012 Alvaro Valencia et al. This is an open access article distributed under the Creative Commons Attribution License, which permits unrestricted use, distribution, and reproduction in any medium, provided the original work is properly cited.

This study investigates the effects of different solid models on predictions of brain shift for three craniotomies. We created a generic 3D brain model based on healthy human brain and modeled the brain parenchyma as single continuum and constrained by a practically rigid skull. We have used elastic model, hyperelastic 1st, 2nd, and 3rd Ogden models, and hyperelastic Mooney-Rivlin with 2- and 5-parameter models. A pressure on the brain surface at craniotomy region was applied to load the model. The models were solved with the finite elements package ANSYS. The predictions on stress and displacements were compared for three different craniotomies. The difference between the predictions of elastic solid model and a hyperelastic Ogden solid model of maximum brain displacement and maximum effective stress is relevant.

## 1. Introduction

Neurosurgery requires high levels of accuracy due to the complexity of the brain. To do this, surgeons have preoperative images that identify the exact area of operation. However, during craniotomy, a change on loading condition occurs, that causes brain deformation. The deformations carry a margin of error in the surgery area. The phenomenon known as brain shift deformations will be studied in this work. We note that the brain shift is a negative effect that occurs in the surgical opening of the skull (craniotomy). Brain shift is produced by a pressure difference on the brain induced in the region of the craniotomy. This changes the position of the pathology and healthy tissues from the calculated with high-quality preoperative radiographic images.

The most surgical navigation systems use 3D preoperatively acquired data and register it to the patient coordinate system. This assumes that the brain is rigid and is a source of error in the exact determination of tumor position.

There are several factors that determinate the magnitude of brain shift produced by a craniotomy: gravity, mechanical tissue properties, loss of brain-spinal fluid, anatomical constraints, intracranial pressure, and patient variability.

A current challenge is the determination of stress and displacements in a solid model of the brain subject to a craniotomy. The geometry of the brain is very complex, and the characteristics of the tissue are not easy to measure and model. The results of the solid model will help to correct the position of the brain for the surgical navigator system.

Most solid brain models use elastic model [1] in order to model the deformations and stress of the brain tissue. Using an elastic solid model, the Young modulus does not affect the displacement field if the gravity is not considered [2].

The effects of considering hyperelastic model of brain have been considered in few works in the literature. The use of nonlinear solid model made it possible to obtain very good predictions of deformation of ventricles and tumor [3]. The same authors have supposed that the brain deformations depend very weakly on the constitutive model and mechanical properties of the brain tissues, and therefore simple hyperelastic model can be used [4].

Several authors propose the use of the linear elasticity to model the stress and deformations of the brain tissue [5–7]. The linear elasticity considers the determination of some parameters as the elasticity modulus ( $E$ ), the shear modulus, or second Lamé's parameter ( $\mu, \lambda$ ) among others. The models consider just one brain tissue, isotropic and incompressible, which is a simplification. Then, they assume that the brain is immersed into the cerebrospinal liquid which is contained by the rigid skull. It is clear that this liquid produces a pressure on the brain tissue. The skull is considered as an extremely rigid structure which is nondeformable. The elasticity modulus is similar to the human bones, that is the elasticity modulus of the skull is  $6.5 \text{ GN/m}^2$  and the Poisson constant of the skull is 0.22.

The skull is a rigid structure, which contains three elements, the brain tissue (86%), blood (4%), and cerebrospinal liquid (CRL, 10%). The interaction among these elements produces a pressure called intracranial pressure. Normally, this pressure in a health adult is around 10 mmHg (1332.8 Pa) and must not be higher than 15 mmHg. The density of the CRL is  $1007 \text{ kg/m}^3$ . Furthermore, the brain tissue corresponds only to the 2% of the total weight but is the element with highest intracranial volume. The weight of the brain is between 1300 and 1600 gr, and its volume is around 1000 to 1500 cc. Its density is closer to the water density, that is  $1040 \text{ kg/m}^3$ .

We can see that, about the properties of the brain tissue, in particular, the values of the elasticity constants, there are several differences among the authors [8, 9].

It is important to remark that the linear elasticity has a suitable behavior for small deformations, and it is clear from several authors that the relationship between stress and deformation for soft tissue is not linear [10, 11].

In the present investigation, we report the effects of hyperelastic solid models on maximal displacement and effective stress of the brain. We have calculated the brain shift for three craniotomies.

## 2. Mathematical Models

The linear elasticity theory is the study of linear elastic solids undergoing small deformations. The linearity means that the components of the stress tensor are a linear combination of the deformations.

The relationship that defines each element of the strain tensor is shown in (2.1). This tensor is known as infinitesimal tensor of Green-Cauchy:

$$\varepsilon_{ij} = \frac{1}{2} \left( \frac{\partial u_i}{\partial x_j} + \frac{\partial u_j}{\partial x_i} \right), \quad (2.1)$$

with  $i, j = 1, 2, 3$ .

The constitutive equations of linear elasticity for an elastic solid are represented by generalized Hooke's law:

$$\sigma_{ij} = C_{ijkl} \varepsilon_{kl}, \quad (2.2)$$

where  $i, j = 1, 2, 3$ .

However, if the material is assumed homogeneous and isotropic, we obtain the constitutive equation of Lamé-Hooke.

### 2.1. Constitutive Equation of Lamé-Hooke

It is well known that, considering a homogeneous and isotropic material, we obtain the Lamé-Hooke constitutive equations. That means that the components of the elastic tensor depend on two particular constants of each material, these constants are the so-called Lamé modulus  $(\lambda, \mu)$ . The relation between the elastic coefficients and the Lamé modulus is the following:

$$C_{ijkl} = \lambda \delta_{ij} \delta_{kl} + \mu (\delta_{ik} \delta_{jl} + \delta_{il} \delta_{jk}). \quad (2.3)$$

Finally, after some simplifications, we have

$$\sigma_{ij} = \lambda \delta_{ij} \varepsilon_{kk} + 2\mu \varepsilon_{ij}, \quad (2.4)$$

where  $\varepsilon_{kk}$  is the trace of the deformation tensor.

### 2.2. Nonlinear Elasticity

The nonlinear elasticity is an observed phenomenon in elastomeric material (rubber) and porous media. The origin of both materials is different, for instance, the elastomeric materials, which are polymers, can be synthetic or natural rubber, and, on the other hand, porous media exist in the nature in form of organic materials, vegetal and animal tissue. The main characteristic of this material is their deformation capacity, which can arrive from 200% to 300%. Nevertheless, these large deformations can be recovered, and the material comes back to its natural state. It is important to note that the human tissues behave as a nonlinear elastic material.



In what follows, we will present some ideas on the nonlinear elastic models. Firstly, we will define the relationship between the strains and the displacement vector, which is defined in (2.5), which is a nonlinear relationship:

$$\varepsilon_{ij} = \frac{1}{2} \left( \frac{\partial u_i}{\partial x_j} + \frac{\partial u_j}{\partial x_i} + \frac{\partial u_k}{\partial x_i} \frac{\partial u_k}{\partial x_j} \right), \quad (2.5)$$

with  $i, j = 1, 2, 3$ .

From the above equation, we can obtain the strain tensor or Green-Lagrange strain tensor. This tensor helps to quantify the length changes of the material and the variation of the angle between the material fibers.

The deformation energy is a useful function in order to define a hyperelastic material. This function gives a relation between the stored energy with the strain and deformations generated in the solid. Moreover, its derivatives with respect to stretch give us the stress produced for the applied force (Cauchy stress). In order to compute the deformation energies, it is necessary to introduce the deformation gradient

$$[F] = \begin{pmatrix} \frac{\partial x}{\partial X} & \frac{\partial x}{\partial Y} & \frac{\partial x}{\partial Z} \\ \frac{\partial y}{\partial X} & \frac{\partial y}{\partial Y} & \frac{\partial y}{\partial Z} \\ \frac{\partial z}{\partial X} & \frac{\partial z}{\partial Y} & \frac{\partial z}{\partial Z} \end{pmatrix}. \quad (2.6)$$

This tensor represents the variation of a deformed material point with respect to its initial state. To simplify the computations, it is interesting to obtain the Green-Cauchy left deformation tensor ( $[B]$ ) and the Green-Cauchy right deformation tensor ( $[C]$ ), both can be recovered from the deformation gradient tensor, and the Green-Cauchy invariant deformation tensor can be easily obtained:

$$\begin{aligned} [B] &= [F][F]^T, \\ [C] &= [F]^T[F]. \end{aligned} \quad (2.7)$$

The deformation energy of the material is a function of the invariants of the left Green-Cauchy deformation tensor ( $[B]$ ). If we assume isotropy of the material, the energy depends on the first three invariants of the tensor

$$W = W(I_1, I_2, I_3). \quad (2.8)$$

The invariants for an isotropic material are as follows.

First Invariant:

$$I_1 = \text{tr}(B). \quad (2.9)$$

Second Invariant:

$$I_2 = \frac{1}{2} \left( \text{tr}(B)^2 - \text{tr}(B^2) \right). \quad (2.10)$$

Third Invariant:

$$I_3 = \det(B). \quad (2.11)$$

If the normal forces are parallel to the principal direction of the material, we have that the invariants only depend on the principal elongations of the solid. It is important to remark that this condition can occur in every isotropic material, and this is due to that in all directions the measurements are equal.

The principal stretches are defined as the quotient between the final length and the initial length in the direction of the deformation. The invariants are functions of the principal stretches:

$$\begin{aligned} I_1 &= \lambda_1^2 + \lambda_2^2 + \lambda_3^2, \\ I_2 &= \lambda_1^2 \lambda_2^2 + \lambda_2^2 \lambda_3^2 + \lambda_1^2 \lambda_3^2, \\ I_3 &= \lambda_1^2 \lambda_2^2 \lambda_3^2, \end{aligned} \quad (2.12)$$

where  $\lambda_1$ ,  $\lambda_2$ , and  $\lambda_3$  are the stretch in the principal directions.

If we suppose that the solid is almost incompressible or with a high compression modulus, the deformation energy depends only on the first and second invariant, since the third invariant verifies  $I_3 = 1$ . The Cauchy strains are calculated from the derivative with respect to the deformations of the deformation energy, that is,

$$\sigma_{ij} = -p\delta_{ij} + \frac{\partial W}{\partial I_1} B_{ij} + \frac{\partial W}{\partial I_2} B_{ij}^{-1}, \quad (2.13)$$

where  $p$  represents the pressure produced in the principal directions.

In what follows, we will present several solid models, such as, their deformation energies and principal stress obtained under different assumptions as hyperelasticity, isotropy, incompressibility and, under uniaxial tension. For the uniaxial tension, we have that

$$\begin{aligned} \lambda_1 &= \lambda, \\ \lambda_2 &= \lambda_3 = \frac{1}{\sqrt{\lambda}}. \end{aligned} \quad (2.14)$$

Thus, we obtain that

$$\begin{aligned} I_1 &= \lambda^2 + 2\lambda^{-1}, \\ I_2 &= 2\lambda + \lambda^{-2}. \end{aligned} \quad (2.15)$$

In what follows, we will describe some different hyperelastic models used for brain tissue modeling.

### 2.2.1. Neo-Hooke Material Model

In this case, the deformation energy model is given by

$$W = C_1(I_3 - 3), \quad (2.16)$$

where  $C_1$  is a given constant. The stress in the direction of the principal stretch is

$$\sigma = C_1 \left( 2\lambda - \frac{2}{\lambda^2} \right). \quad (2.17)$$

### 2.2.2. Mooney-Rivlin Material Model

In this case, the deformation energy model, with 5 parameters, is the following:

$$w = C_1(I_1 - 3) + C_2(I_2 - 3) + C_3(I_1 - 3)^2 + C_4(I_1 - 3)(I_2 - 3) + C_5(I_2 - 3)^2, \quad (2.18)$$

where  $C_1$  to  $C_5$  are material constants. In this case, the stress direction for the principal stretch corresponds to

$$\begin{aligned} \sigma = & C_1 \left( 2\lambda - \frac{2}{\lambda^2} \right) + C_2 \left( 2 - \frac{2}{\lambda^3} \right) + 2C_3 \left( \lambda^2 + \frac{2}{\lambda} - 3 \right) \left( 2\lambda - \frac{2}{\lambda^2} \right) \\ & + C_4 \left( \left( 2\lambda - \frac{2}{\lambda^2} \right) \left( 2\lambda + \frac{1}{\lambda^2} - 3 \right) + \left( \lambda^2 + \frac{2}{\lambda} - 3 \right) \left( 2 - \frac{2}{\lambda^3} \right) \right) \\ & + 2C_5 \left( 2\lambda + \frac{1}{\lambda^2} - 3 \right) \left( 2 - \frac{2}{\lambda^3} \right). \end{aligned} \quad (2.19)$$

### 2.2.3. Odgen Material Model

In this case, the deformation energy is given by

$$W = \sum_{k=1}^n \frac{\mu_k}{\alpha_k} \left( \lambda^{\alpha_k} + \left( \frac{1}{\sqrt{\lambda}} \right)^{\alpha_k} - 2 \right), \quad (2.20)$$

where  $\alpha_k$  and  $\mu_k$  are constants of the material. The stress direction of the principal stretch is

$$\sigma = \sum_{k=1}^n \mu_k \left( \lambda^{\alpha_k-1} + (\lambda)^{-0.5\alpha_k-1} \right). \quad (2.21)$$

From the Cauchy tensor, it is possible to compute the equivalent stresses. The equivalent stress. is computed using the Von Misses formula:

$$\sigma_{vm} = \sqrt{\frac{(\sigma_1 - \sigma_2)^2 + (\sigma_2 - \sigma_3)^2 + (\sigma_1 - \sigma_3)^2}{2}}, \quad (2.22)$$

where  $\sigma_1$ ,  $\sigma_2$ , and  $\sigma_3$  are the principal stresses.

The equivalent strain is defined as

$$\varepsilon_{eq} = \frac{1}{\sqrt{2}(1 + \nu_{eq})} \left[ (\varepsilon_x - \varepsilon_y)^2 + (\varepsilon_y - \varepsilon_z)^2 + (\varepsilon_z - \varepsilon_x)^2 + \frac{3}{2} (\gamma_{xy}^2 + \gamma_{yz}^2 + \gamma_{xz}^2) \right]^{1/2}, \quad (2.23)$$

where  $\varepsilon$  and  $\gamma$  are the components of the deformation tensor of Hencky.

### 3. Numerical Methods

#### 3.1. Modeling of the Brain Shift

In order to make the numerical simulations of the brain shift, we will consider the experimental data of Mehdizadeh et al. [8]. In the experiments, the gray matter is obtained from the parietal lobe and the white matter is obtained from the corpus callosum from a one-year-old bovine. The tissue obtained corresponds to discs of 15 mm diameter and 5 mm of height. The tests were realized with a uniform rate of deformation of 1 mm/min in order to avoid inertial forces. The used machine was a dynamic testing machine, Hct/25–400 with servo hydraulic valve PID controller. The elastic modulus obtained was  $E = 24.6$  kPa and  $\nu = 0.49$ . For the Neo-Hooke model, the constant is  $C_1 = 7903$  Pa.

To study the hyperelastic solids, we use the data obtained for the gray matter. The curve for the uniaxial traction for the gray matter is showed in Figure 1.

The cerebral cortex consists of gray matter, and this region is the most affected by brain shift. Also, the ratio of the volume of grey matter to white matter in the cerebral hemisphere for a 20-year-old man is 1.3 [12]. The mechanical properties of gray and white matters measured by Mehdizadeh et al. [8] show differences for gray matter, true Young modulus of 24.6 kPa and, for the white matter, true Young modulus of 19 kPa have been derived. On the other hand, it is practically impossible to build a simple solid model considering the real white and gray matter distribution in a human brain. Considering these reasons, we have used the mechanical properties of gray matter for the complete brain model. Due to the facts that the larger brain displacements are near brain surface and the brain cortex is composed only principally of gray matter, the model predicts brain shift with acceptable precision.

The Odgen material model was studied considering the first, second, and third order. The Mooney-Rivlin model was studied considering two of its forms, with two and five parameters (see Tables 1 and 2).

#### 3.2. CAD Geometry

To quantify accurately the deformations and stresses produced in the phenomenon of brain shift during a brain craniotomy, the CAD model of brain is relevant. The CAD geometry used in the present work is an approximation with characteristics similar to a real brain. We modeled the characteristics of a healthy male brain of 35 years. The brain is approximately a ball whose surface geometry is characterized by irregular folds, see Figure 2. In this area circulate most of the blood vessels, veins, and arteries. The width of the brain is variable; however, the average value is 140 mm. The average length is 170 mm. The height of the brain varies with respect to the observed cross-section up to 120 mm. Considering the above measures as a reference and using MRI images of the brain, a CAD 3D is generated.

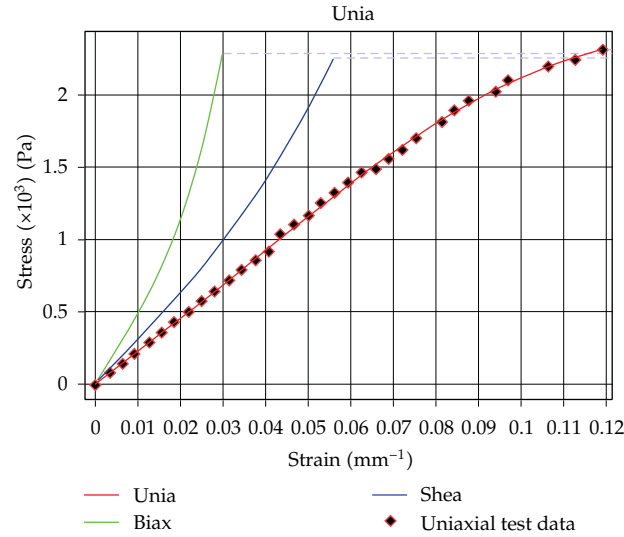


**Figure 1:** Stress-strain curves for gray matter.

**Table 1:** Odgen constants.

	First order	Second order	Third order
$\mu_1$ [Pa]	8743	629,5	423.62
$\alpha_1$	1.8127	10.499	9.8787
$\mu_2$ [Pa]	—	657.22	445.45
$\alpha_2$	—	10.188	10.213
$\mu_3$ [Pa]	—	—	459.1
$\alpha_3$	—	—	10.156

**Table 2:** Mooney-Rivlin constants.

	MR 2 parameters [Pa]	MR 5 parameters [Pa]
$C_1$	3922.2	-620.52
$C_2$	30.838	4466.1
$C_3$	—	$3.85E + 06$
$C_4$	—	$-8.71E + 06$
$C_5$	—	$4.93E + 06$

The CAD software used is solid edge, as it provides the necessary tools to model complex nonparameterized curves. The methodology is to build a hemisphere from the outer contours of the brain. To obtain these, contours are sectioned in coronal three-dimensional models, then the contours are drawn to generate the solid model. Once the model is built in, with the option Mirror, the second hemisphere is created ensuring the model symmetry. The last step is to use the option Swept Protrusion to create the final CAD model of the brain. The model obtained is showed in Figure 3.

The cerebral cortex is characterized as a cortical layer with a convoluted topology, Figure 2. This complex geometry is modeled as simple hemisphere as in all previously reported investigations about brain shift, see Wittek et al. [3, 4]. The model must be relatively

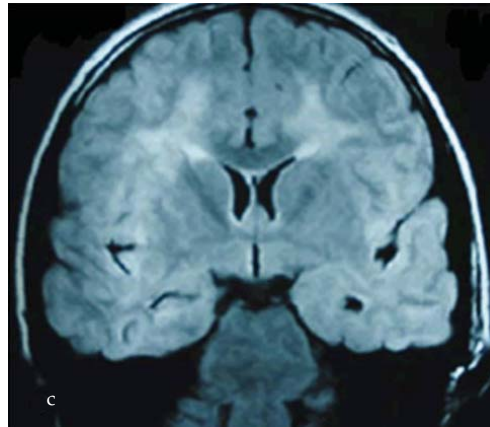


**Figure 2:** Coronal view of the brain.

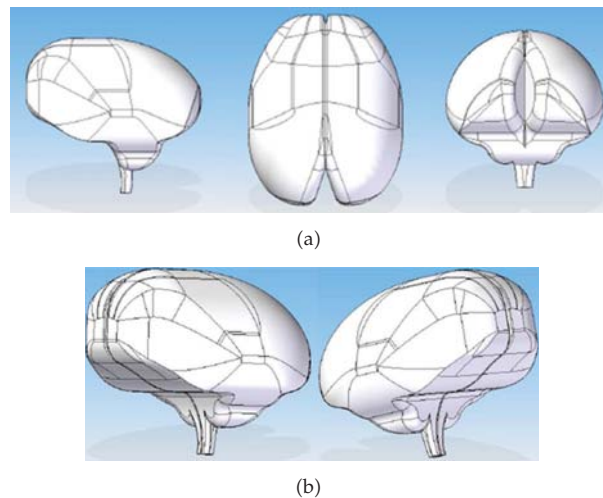


**Figure 3:** Principal and Isometric views of the brain model.

simple to be used as predictive tool for the clinicians with a minimum error. The comparison of model predictions with clinical results of brain shift ensures that the approximation of the complex brain structure is correct for the goal of the present model. We will try to use this model in brain surgery to predict brain shift after clinical validation in the future; for this reason, the model must produce computational results in short time. Models that consider the topology of cerebral cortex as highly convoluted sheet for investigation of the gray matter deformation have been reported by Chung et al. [13]. However, the model is too complex to be applied during a surgery.

The skull is made similarly to the brain. To do this, we use the option Offset tool in the CAD software. The goal is to keep the skull around the brain model but with a separation between these elements. According to what was observed in the MRI images of the middle-aged male patient, the gap between the elements was determined. Figure 4 shows the process of generating the skull geometry.

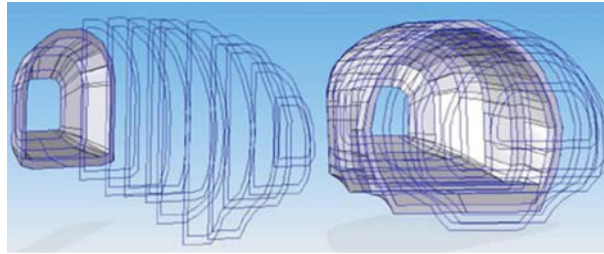


Figure 4: Design for the skull model.

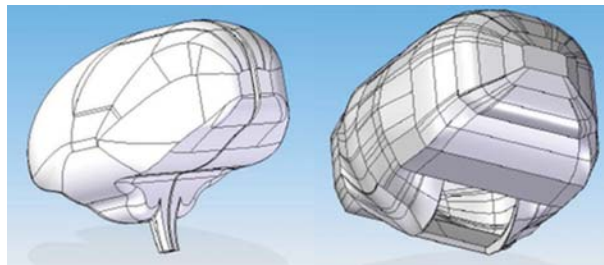


Figure 5: Views of the brain and skull model.

Figure 5 shows a view of the brain and the skull used in the present investigation. Although the models are a simplification of the real, it is important to note that they retain morphological similarity.

In the present investigation, we do not consider the cerebrospinal fluid CSF and the brain can be deformed in this space. In a brain craniotomy, CSF is extracted during surgery, and, therefore, this model restriction has low effect on brain displacement. The subarachnoid space between brain and skull is small compared with nominal brain diameter, also variation of model distance between brain and skull was considered as second-order effect. The present brain model intends to describe a methodology to predict brain shift.

### 3.3. Boundary Conditions

For the simulation of the brain shift effects, we consider two boundary conditions.

Fix of spinal cord: in order to limit movement of the brain and allow greater deformations only in the area affected by the change in pressure.

Pressure variation in area of operation: intracranial pressure caused by brain, blood, and CSF is approximately 770 mmHg. The atmospheric pressure is 760 mmHg. Upon opening the skull, there is trickle of CSF and blood, mainly affecting the operation area and leaving it exposed to atmospheric pressure. This condition results in a negative pressure in the opening area equivalent to 10 mmHg or 1333 Pa.

Figure 6 shows the application of the pressure boundary conditions for the different craniotomies. Figure 6 shows the skull with the brain inside, and indicated with red color the region where the pressure boundary condition is applied in each case.



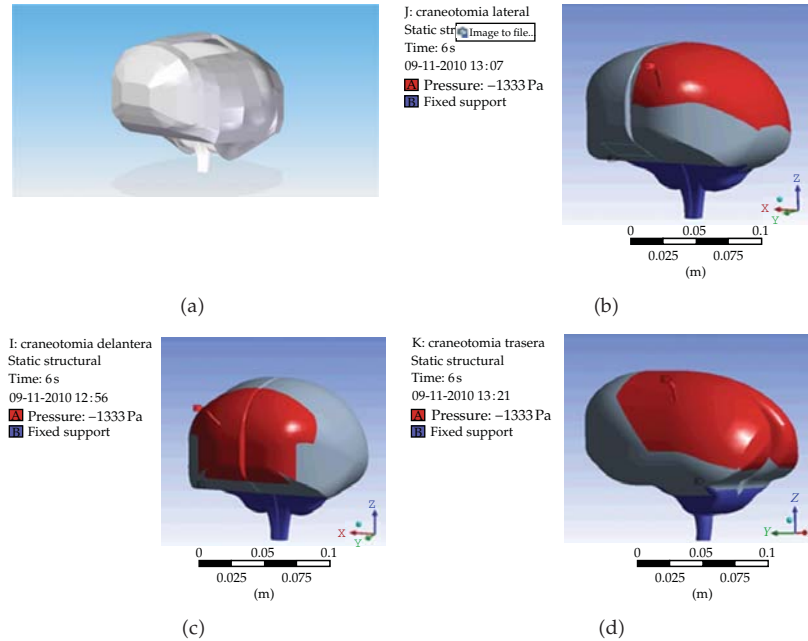


**Figure 6:** Boundary condition for parietal, frontal, and posterior craniotomy.

The region size to apply the pressure boundary condition in the three brain craniotomies was very difficult to choose. The first idea was to apply the pressure on the same area for the three cases; however, personal communications with neuroradiologists from the Instituto de Neurocirugia Asenjo, that help us in this project, indicated that the affected area is different for the three investigated craniotomies. The red areas showed in Figure 6 show the chosen areas to apply the pressure boundary condition. The areas were not the same for the three cases, because the goal was to try to reproduce clinical results.

For the brain shift, the small distance between skull and the brain is the most relevant parameter that induces pressure differences on brain surface. During a craniotomy, CSF moves outside the skull and CSF flow does not produce pressure difference on brain surface.

### 3.4. Computational Method

The model was solved by a commercial finite element package ANSYS v12.1. The finite element method (FEM) is used to solve the governing equations. The FEM discretizes the computational domain into finite elements that are interconnected by element nodal points. We have used the static structural formulation with a maximum time of 6 s. Incompressible material behavior may lead to some difficulties in numerical simulation, such as volumetric locking, inaccuracy of solution, checkerboard pattern of stress distributions, or divergence. We used the mixed  $u$ - $P$  elements available in ANSYS to overcome these problems.

The unstructured grids were composed of tetrahedral SOLID187 with 10 nodes available in ANSYS. Figure 7 shows the details of the three different grids used for the parietal, posterior, and frontal craniotomies. For the parietal craniotomy, the grid was more refined in the middle brain region. For the frontal craniotomy, the grid was refined nearer than the frontal region of the brain.

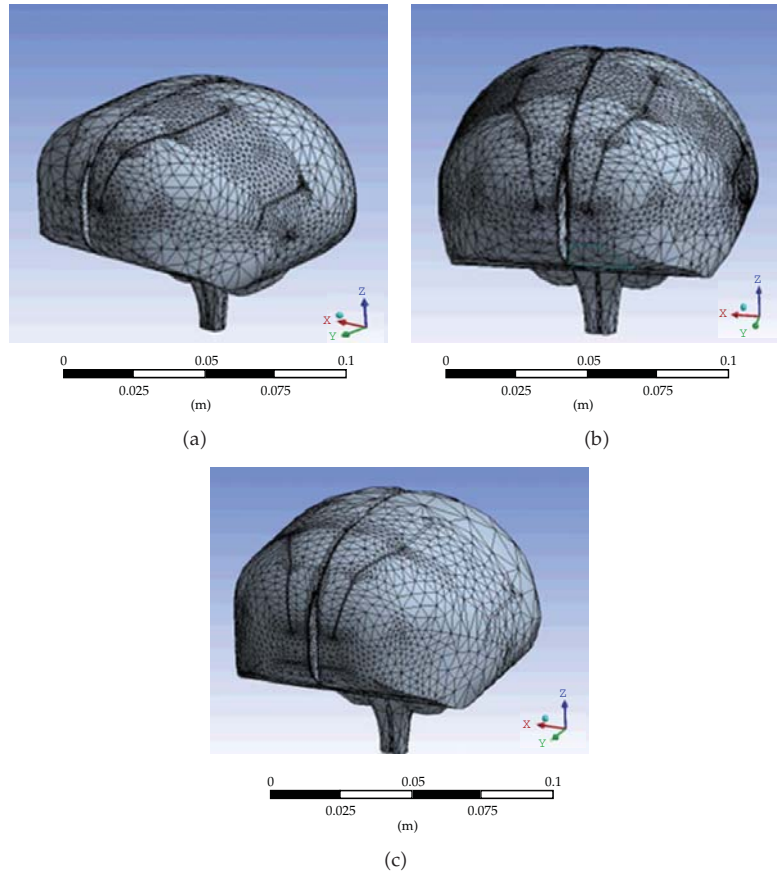


**Figure 7:** Isometric and superior views of the different computational grids of the brain model used for (a) parietal, (b) posterior, and (c) frontal craniotomy.

**Table 3:** Comparison of maximum displacement, strain, and stress for three different grid sizes.

Grid	Elements	Maximum displacement [mm]	Maximum equivalent strain %	Maximum equivalent stress [Pa]
1	49453	3.845	59.14	14527
2	34356	3.83	59.31	14591
3	11730	3.806	59.85	14724

The three grids used are similar, and the variations of element size in the brain depend also on model construction, see Figure 5.

Grid independence study was performed for three grid sizes; maximum displacement, equivalent strain, and equivalent stress were compared in Table 3. For the comparison, we have used the frontal craniotomy with the elastic brain. The differences between the results are very small. Therefore, the middle grid size was used to perform all the computational simulations. This test ensures that the grid density does not affect the expected results about brain shift.

**Table 4:** Comparison of maximum displacement and effective stress using seven brain models for a frontal pressure boundary condition without skull.

	Elastic	Neo-Hookean	Ogden 1	Ogden 2	Ogden 3	M-R 2	M-R 5
Maximum displacement [mm]	8.923	8.631	8.625	9.0894	9.0667	8.630	7.935
Maximum effective stress [Pa]	37045	16920	16401	47729	46639	16880	56375

#### 4. Results and Discussion

The predictions of maximum displacement and effective stress of brain under a pressure boundary condition similar to frontal craniotomy but without skull were compared for elastic, neo-Hookean, Ogden first-order, Ogden second-order, Ogden third-order, Mooney-Rivlin with two-parameter, and Mooney Rivlin with five-parameter models. The results are showed in Table 4. The low-order neo-Hookean model, the first-order Ogden model, and the Mooney-Rivlin model with two parameters predict similar displacement and effective stress. The elastic model predicts similar displacement as the high-order hyperelastic Ogden models; however, the prediction of maximum effective stress is 66% lower than the prediction of the second-order Ogden model.

The predictions of hyperelastic second-order Ogden and third-order Ogden models are similar. The Mooney-Rivlin model with five parameters predicts lower brain displacement compared with all models included in the elastic model and therefore is discarded. With these considerations, the hyperelastic second-order Ogden model is selected as adequate solid model for comparison with an elastic model for prediction of brain shift phenomena.

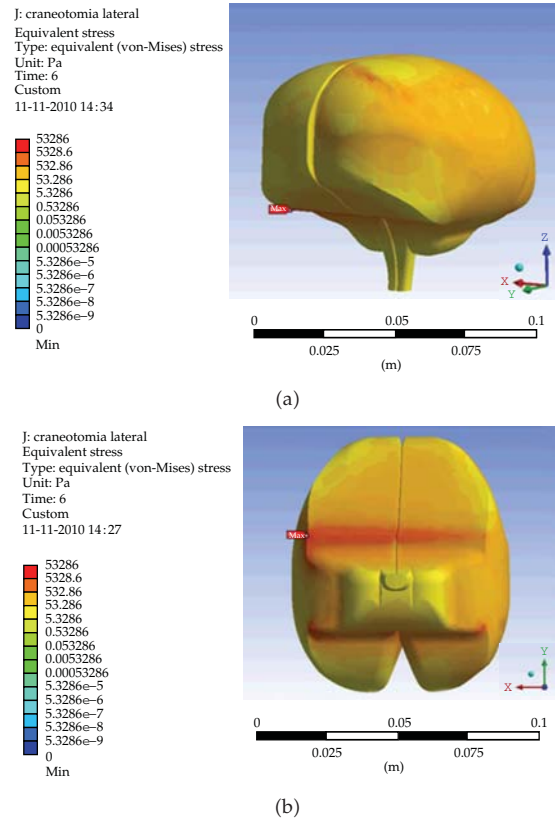
In this work, we have considered three brain craniotomies, a parietal, a posterior, and a frontal case as showed in Figure 6, and the maximum displacement and effective stress were investigated. The solid models of brain are the elastic and the hyperelastic second-order Ogden models.

Figure 8 shows in logarithmic scale the distribution of the effective stress for the parietal craniotomy, and an isometric and an inferior views of the brain are showed. The effective stress on brain surface shows large areas with values around 1000 Pa. The maximum effective stress is 53286 Pa. The maximum is on the brain base near the spinal cord, where the model is fixed.

Figure 9 shows in logarithmic scale the distribution of the effective stress for the posterior craniotomy, and an isometric and an inferior views of the brain are showed. The effective stress on brain surface shows large areas with values around 500 Pa. The maximum effective stress is now 38073 Pa. The maximum is on the brain base near the spinal cord, where the model is fixed. Areas on the brain base are under relatively high stress compared with the rest of brain.

Figure 10 shows in logarithmic scale the distribution of the effective stress for the frontal craniotomy, and an isometric and a inferior views of the brain are showed. The effective stress on brain surface shows large areas with values around 200 Pa. The maximum effective stress is now only 10049 Pa. The maximum is on the brain base near the spinal cord, where the model is fixed. Areas on the brain base are under relatively high stress compared with the rest of brain.

A comparison between the three craniotomies shows that the parietal produces higher effective stress on brain than the posterior and frontal interventions. High stress values are distributed principally on brain base.



**Figure 8:** Effective stress for parietal craniotomy, hyperelastic second-order Ogden model.

Comparing the maximum effective stress for the frontal craniotomy with the data of Table 4 can be concluded that the effect of the skull is very important, and the stress for the craniotomy is considerably lower as the value obtained only with a pressure boundary condition. This indicates that modeling of brain shift must consider the skull to obtain more realistic values. Ji et al. [5] reported the relevance of brain-skull contact in the determination of brain shift compensation.

The maximum effective stress is high compared with the values of the stress strain curve showed in Figure 1; therefore, the use of hyperelastic model for the brain is relevant for better prediction of brain shift.

The distribution of brain displacement for parietal craniotomy calculated with the hyperelastic second-order Ogden model is showed in Figure 11. Figure 11 shows the displacement of brain surface and the displacement in a plane through the craniotomy. The upper surface shows displacements around 7 mm. The brain area with large displacement is important. Also, in the brain center, the displacements are around 3 mm. Figure 11 shows the relevance of brain shift for parietal craniotomy.

Figure 11 shows that a part of the brain is displaced out of the skull in the craniotomy area. The zones with low displacement are near the spinal cord, due to the fix condition in this area. From a neurological point of view, this result is realistic. For the brain, the zone with maximum stress does not coincide with the location of maximum brain shift or brain displacement.

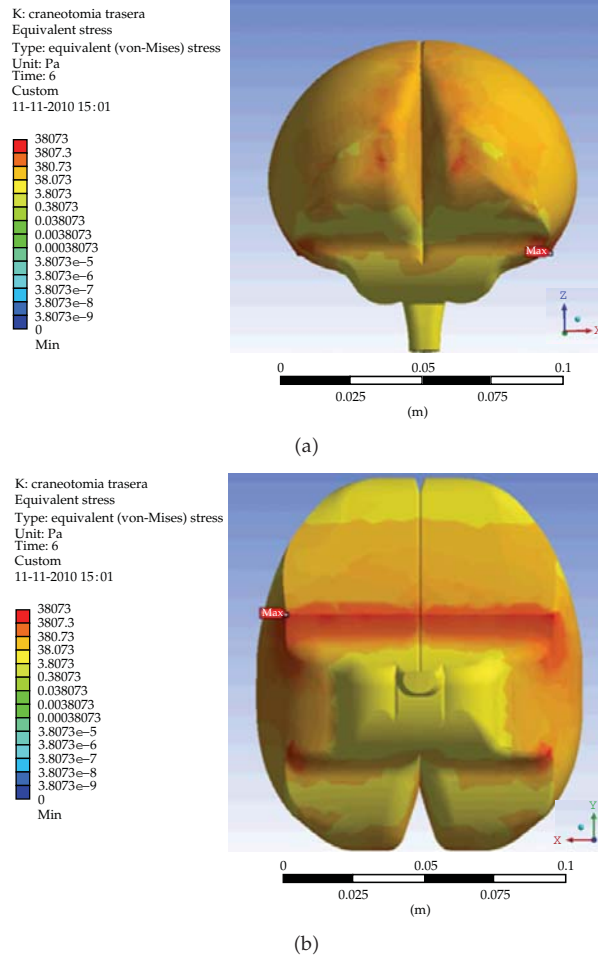


**Figure 9:** Effective stress for posterior craniotomy, hyperelastic second-order Ogden model.

The distribution of brain displacement for the posterior craniotomy calculated with the hyperelastic second-order Ogden model is showed in Figure 12. The figure shows the displacement of brain surface and the displacement in a middle brain plane. The frontal region shows displacements around 12 mm. The brain area with large displacement is important. Also, in the brain center, the displacements are around 5 mm. Figure 12 shows the relevance of brain shift for posterior craniotomy. The zones with low displacement are near the spinal cord, due to the fix condition in this area.

Finally, the distribution of brain displacement for the frontal craniotomy calculated with the hyperelastic second-order Ogden model is showed in Figure 13. The figure shows the displacement of brain surface and the displacement in a middle brain plane. The superior region shows displacements around 4 mm. The brain area with large displacement is important. Also, in the brain center, the displacements are around 2 mm. Figure 13 shows the relevance of brain shift for frontal craniotomy. The zones with low displacement are near the spinal cord, due the fix condition in this area. For the brain, the zone with maximum stress does not coincide with the location of maximum brain shift or brain displacement and a craniotomy.

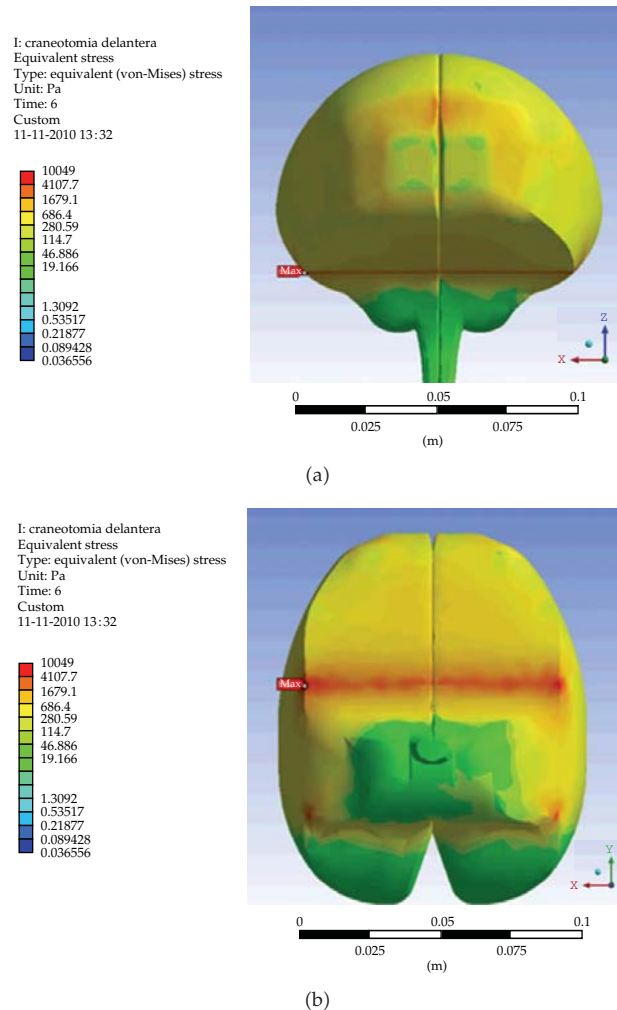


**Figure 10:** Effective stress for frontal craniotomy, hyperelastic second-order Ogden model.

Table 5 shows a comparison of maximum displacement and effective stress on brain modeled with the elastic model and the hyperelastic second-order Ogden model. For the displacement, the elastic model predicts values 10%, 13%, and 8% lower for the parietal, posterior, and frontal craniotomies, compared with the prediction of Ogden model. These differences are relevant in neurosurgery.

The prediction of maximum effective stress with the elastic model is 53%, 62% lower for the parietal and posterior craniotomies, compared with the predictions with the hyperelastic Ogden model. For the frontal craniotomy, the elastic model predicts a maximum effective stress 45% higher than the Ogden model.

The predictions on maximum equivalent strain show also important differences between the elastic and hyperelastic models in the three craniotomies. The elastic model is valid only for small deformations, and therefore it cannot be applied to this problem that produces large deformations. The formulation of the hyperelastic model is for large deformations, and therefore this model produces more realistic results. The small

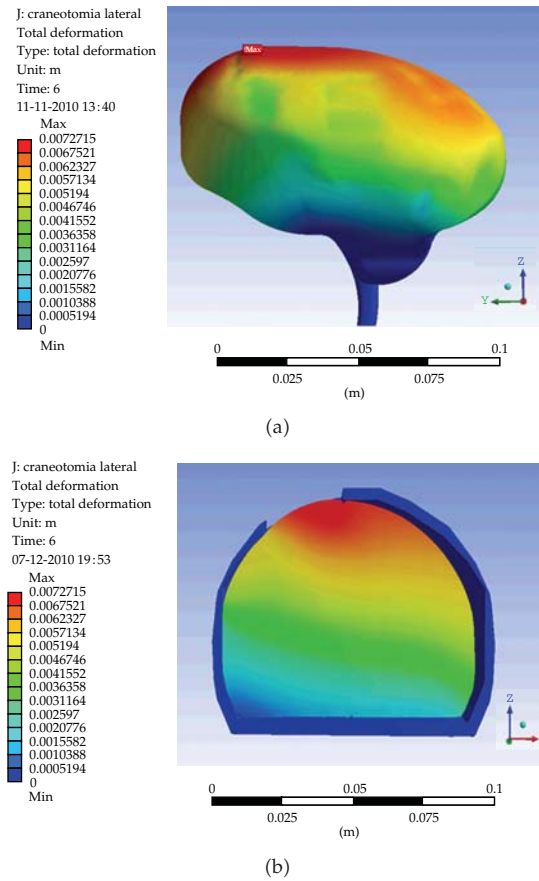


**Figure 11:** Brain displacement for parietal craniotomy, hyperelastic second-order Ogden model.

**Table 5:** Comparison of maximum displacement, equivalent strain, effective stress, and principal stress for parietal, posterior, and frontal craniotomies.

Craniotomy	Model	Maximum displacement [mm]	Maximum equivalent strain (%)	Maximum effective stress [Pa]	Maximum principal stress [Pa]
Parietal	Elastic	6.546	102	25145	40670
	hyperelastic Ogden	7.271	38	53286	57168
Posterior	Elastic	10.766	59	14388	32029
	hyperelastic Ogden	12.341	32	38073	41139
Frontal	Elastic	3.830	59	14591	14651
	hyperelastic Ogden	4.177	23	10049	10880

displacements formulation is exact for deformations lower than 2%, because this value is lower than the deformations present in the present investigation; all the simulations presented in Table 5 were made using the large deformation formulation.



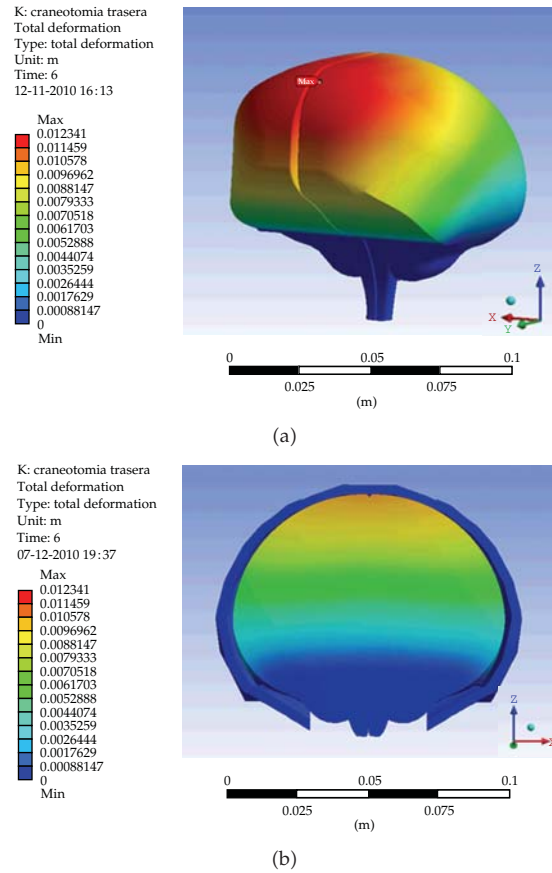


**Figure 12:** Brain displacement for posterior craniotomy, hyperelastic second-order Ogden model.

The differences between the maximum effective stress and the maximum principal stress with the hyperelastic model in the three craniotomies are small indicating good convergence for this model. On the contrary, the elastic model shows large differences between both stresses indicating convergence problems for this problem with large deformations.

Soza et al. [14] have reported for a parietal craniotomy an average brain shift of 8.9 mm, that is similar to the maximum deformation obtained in the present investigation of 7 mm, considering that the solid models and the brain geometry were different. For a posterior craniotomy, Clatz et al. [15] reported brain shift up to 14 mm for several patients, and the present hyperelastic second-order Ogden model predicts for this case a brain shift of 12 mm. Both comparisons show that the present methodology has a potential to be applied in neurosurgery to correct the position of a brain tumor after the craniotomy and make the intervention more precise.

## 5. Conclusions

A solid model to study the brain shift phenomena was applied to parietal, frontal, and posterior craniotomies. Maximum displacements from 4 mm to 12 mm were found for the different craniotomies. The hyperelastic second-order Ogden solid model was found that

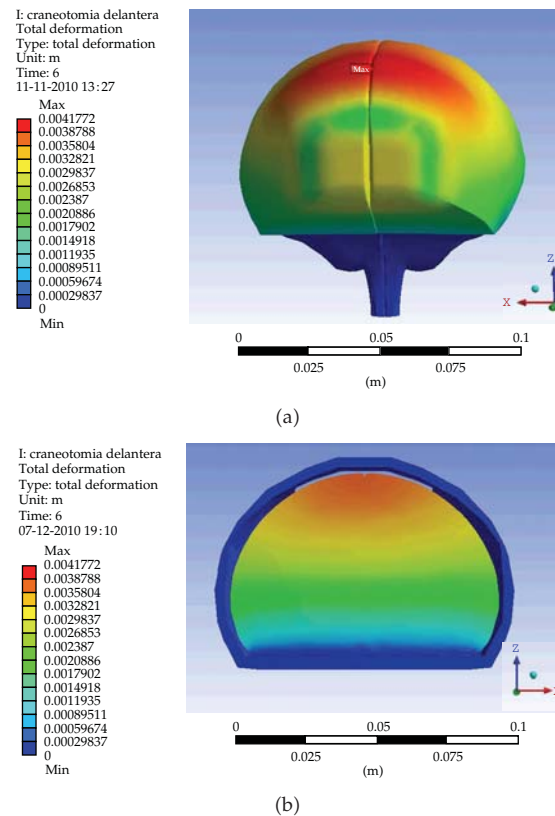


**Figure 13:** Brain displacement for frontal craniotomy, hyperelastic second-order Ogden model.

predicts the best results. Elastic solid model should not be used with large strains as in this problem. A correct model must include the skull. The methodology developed in the present investigation can help to more precise clinical interventions.

## Acknowledgments

This work was partially supported by Grants 1070148, 1110008, and 1111012 of FONDECYT, D0111035 of FONDEF, and PFB03 2007 CMM CONICYT, Chile. The authors want to thank the neurosurgeons of the Instituto de Neurocirugía Asenjo, Santiago, for the relevant information provided to their investigation.

## References

- [1] L. Vigneron, R. Boman, J. Ponthot, P. Robe, S. Warfield, and J. Verly, "Enhanced FEM-based modeling of brain shift deformation in image-guided neurosurgery," *Journal of Computational and Applied Mathematics*, vol. 234, no. 7, pp. 2046–2053, 2010.
- [2] O. Skrinjar, A. Nabavi, and J. Duncan, "Model-driven brain shift compensation," *Medical Image Analysis*, vol. 6, no. 4, pp. 361–373, 2002.
- [3] A. Wittek, K. Miller, R. Kikinis, and S. Warfield, "Patient-specific model of brain deformation: application to medical image registration," *Journal of Biomechanics*, vol. 40, no. 4, pp. 919–929, 2007.

- [4] A. Wittek, G. Joldes, M. Couton, S. Warfield, and K. Miller, "Patient-specific non-linear finite element modelling for predicting soft organ deformation in real-time; Application to non-rigid neuroimage registration," *Progress in Biophysics and Molecular Biology*, vol. 103, no. 2-3, pp. 292–303, 2010.
- [5] S. Ji, D. Roberts, A. Hartov, and K. Paulsen, "Brain-skull contact boundary conditions in an inverse computational deformation model," *Medical Image Analysis*, vol. 13, no. 4, pp. 659–672, 2009.
- [6] G. Joldes, A. Wittek, and K. Miller, "Computation of intra-operative brain shift using dynamic relaxation," *Computer Methods in Applied Mechanics and Engineering*, vol. 198, no. 41–44, pp. 3313–3320, 2009.
- [7] P. Dumpuri, R. Thompson, B. Dawant, A. Cao, and M. Miga, "An atlas-based method to compensate for brain shift: preliminary results," *Medical Image Analysis*, vol. 11, no. 2, pp. 128–145, 2007.
- [8] S. Mehdizadeh, M. Khoshgoftar, S. Najarian, F. Farmanzad, and S. Hooshiar, "Comparison between brain tissue gray and white matters in tension including necking phenomenon," *American Journal of Applied Sciences*, vol. 5, no. 12, pp. 1701–1706, 2008.
- [9] K. Miller and K. Chinzei, "Simple validation of biomechanical models of brain tissue," *Journal of Biomechanics*, vol. 31, supplement 1, p. 104, 1998.
- [10] K. Miller, "Constitutive model of brain tissue suitable for finite element analysis of surgical procedures," *Journal of Biomechanics*, vol. 32, no. 5, pp. 531–537, 1999.
- [11] K. Miller and K. Chinzei, "Mechanical properties of brain tissue in tension," *Journal of Biomechanics*, vol. 35, no. 4, pp. 483–490, 2002.
- [12] A. K. Miller, R. L. Alston, and J. A. Corsellis, "Variation with age in the volumes of grey and white matter in the cerebral hemispheres of man: measurements with an image analyser," *Neuropathology and Applied Neurobiology*, vol. 6, no. 2, pp. 119–132, 1980.
- [13] M. K. Chung, K. J. Worsley, S. Robbins et al., "Deformation-based surface morphometry applied to gray matter deformation," *NeuroImage*, vol. 18, no. 2, pp. 198–213, 2003.
- [14] G. Soza, R. Grosso, U. Labsik et al., "Fast and adaptive finite element approach for modeling brain shift," *Computer Aided Surgery*, vol. 8, no. 5, pp. 241–246, 2003.
- [15] O. Clatz, H. Delingette et al., "Robust non rigid registration to capture brain shift from intra operative MRI," *IEEE Transactions on Medical Imaging*, vol. 24, pp. 1417–1427, 2005.

## Research Article

# Dynamical Models for Infectious Diseases with Varying Population Size and Vaccinations

**Peilin Shi and Lingzhen Dong**

*Department of Mathematics, Taiyuan University of Technology, Taiyuan, Shanxi 030024, China*

Correspondence should be addressed to Lingzhen Dong, [linzhen.dong@yahoo.com.cn](mailto:linzhen.dong@yahoo.com.cn)

Received 24 July 2011; Accepted 13 October 2011

Academic Editor: Venky Krishnan

Copyright © 2012 P. Shi and L. Dong. This is an open access article distributed under the Creative Commons Attribution License, which permits unrestricted use, distribution, and reproduction in any medium, provided the original work is properly cited.

We formulate and discuss models for the spread of infectious diseases with variable population sizes and vaccinations on the susceptible individuals. First, we assume that the susceptible individuals are vaccinated continuously. We establish the threshold-like results for the existence and global stability of the disease-free and the endemic equilibriums for these systems. Especially, we prove the global stability of the endemic equilibriums by converting the systems into integrodifferential equations. Second, we suppose that vaccinations occur once per time period. We obtain the existence and global stability of the disease-free periodic solutions for such systems with impulsive effects. By a useful bifurcation theorem, we acquire the existence of the endemic periodic solutions when the disease-related deaths do not occur. At last, we compare the results with vaccinations and without vaccinations and illustrate our results by numerical simulations.

## 1. Introduction

Confidence that the infectious diseases would soon be eliminated was created by the improved sanitation, effective antibiotics and vaccination programs in the 1960s, but it collapsed now. Human and animal invasions of new ecosystems, global warming, environmental degradation, and increased international travels provide many opportunities for the spread and the eruption of infectious diseases. It is clear that new infectious diseases are emerging, and some eliminated diseases are reemerging since the infectious agents' evolvement and adaptation to the environment. Moreover, these infectious diseases lead to terrible suffering and mortality. Consequently, infectious diseases are receiving more and more attention in developing countries, even in the developed countries.

The emerging and reemerging of infectious diseases have been studied by many scientists in different fields. Mathematical models are important tools to analyze and control the spread of infectious diseases. Hethcote [1] gives a review on the mathematics of infectious diseases. Most models for the transmission of infectious diseases descend from the

pioneering work of Kermack-McKendrick on SIR (susceptible-infectious-removal), in which vital dynamics (birth and death) is negligible for the short incubation of infectious diseases. The possible and realistic situations would be to discuss epidemic models with varying population size, which may refer to Mena-Lorca and Hethcote [2], Anderson and May [3], Gao and Hethcote [4], Li and Graef [5], and Brauer and Driessche [6]. Thresholds are obtained which determine whether the diseases die out or break out. The existence and stability of equilibrium points are investigated for each model, but there is still some work to do. Such as in [4], the global stability of the endemic equilibrium points was not obtained. We complete this in the present paper.

Vaccination programs have been applied to prevent and control the yield and spread of infectious diseases, which achieved a lot. Models with vaccination are constructed and analyzed by Shulgin et al. [7], Stone et al. [8], Li and Ma [9], Greenhalgh and Das [10] and Greenhalgh [11]. Some useful results are obtained, and results with vaccination and without vaccination are compared. But they assumed that the susceptible is vaccinated continuously. In fact, it would be more realistic and reasonable that the susceptible is assumed to be vaccinated in a single pulse or at fixed moments. In this paper, we consider not only a constant flow of new members into the susceptible but also vaccinating continuously and impulsively on the susceptible. We will investigate the dynamical behaviors of these epidemic models, which are described by continuous or impulsive differential equations. The models of infectious diseases with impulsive effects had been discussed in [12], where the birth, rather than the vaccination, is assumed to be impulsive.

We denote by  $S(t)$  the number of members of a population who are susceptible to an infection at time  $t$ ,  $I(t)$  the number of members who are infective at time  $t$ , and  $R(t)$  the number of members at time  $t$  who have been removed as the result of recovery from the infection with temporary immunity against reinfection. The total population size at time  $t$  is represented by  $N(t)$  with  $N(t) = S(t) + I(t) + R(t)$ . In addition, basic hypotheses are needed to formulate our models:

- (1) there is a constant flow of  $A$  new members into the susceptible in unit time;
- (2) a fraction  $p \geq 0$  of the susceptible is vaccinated in unit time or in a single pulse once per time period, which will enter directly into the removal owing to obtaining the immunity;
- (3) there is a constant per capita natural death rate  $d > 0$  in each group;
- (4) a fraction  $\alpha \geq 0$  of the infective dies from the infection, and a fraction  $\gamma \geq 0$  of the infective recovers in unit time;
- (5) a fraction  $\delta \geq 0$  of the removal loses their immunity and becomes the susceptible in unit time;
- (6) the force of the infection is  $\beta I$ , where  $\beta$  is the effective per capita contact rate of the infective individuals and the incidence rate is  $\beta SI$ .

In the next section, an SIR model with variable population size and continuous vaccination is analyzed. The existence and stability of the equilibrium points for this model are discussed. The global stability of the disease-free equilibrium is proved by differential comparison theorem, and the global stability of the endemic equilibrium is obtained by converting the system into an integrodifferential equation. In Section 3, we consider an impulsive differential epidemic model, of which the stability and the existence of disease-free periodic solution are discussed. Further, the existence of endemic periodic solution is also studied for such a system

with  $\alpha = 0$ , which implies that the disease-related deaths are not considered. At last, we give some examples to illustrate our results by numerical simulation.

## 2. An SIR Model with Continuous Vaccination

In this section, we discuss the disease transmission model, which is described by

$$\begin{aligned}\dot{S}(t) &= A - dS - \beta SI + \delta R - pS, \\ \dot{I}(t) &= \beta SI - (\gamma + \alpha + d)I, \\ \dot{R}(t) &= \gamma I - (\delta + d)R + pS.\end{aligned}\tag{2.1}$$

Denoting  $N = S + I + R$ , and adding these three equations, we have

$$\dot{N} = A - dN - \alpha I.\tag{2.2}$$

Therefore, we may obtain system (2.3), which is equivalent to system (2.1), and consider the following system:

$$\begin{aligned}\dot{N}(t) &= A - dN - \alpha I, \\ \dot{I}(t) &= \beta(N - I - R)I - (\gamma + \alpha + d)I, \\ \dot{R}(t) &= pN + (\gamma - p)I - (d + \delta + p)R.\end{aligned}\tag{2.3}$$

For nonnegative initial conditions  $(N(0), I(0), R(0))$ , it is easily known that  $N(t), I(t)$ , and  $R(t)$  remain nonnegative, and the total population size  $N(t)$  is ultimately upper bounded by  $A/d$ . Moreover, we have

$$\begin{aligned}N(t) &= N(0)e^{-dt} + \frac{A}{d}(1 - e^{-dt}) - \alpha \int_0^t e^{-d(t-s)} I(s) ds, \\ R(t) &= R(0)e^{-(d+\delta+p)t} + (\gamma - p) \int_0^t e^{-(d+\delta+p)(t-s)} I(s) ds + p \int_0^t e^{-(d+\delta+p)(t-s)} N(s) ds \\ &= \frac{Ap}{d(d+\delta+p)} + \left[ \frac{pN(0)}{p+\delta} - \frac{Ap}{d(p+\delta)} \right] e^{-dt} + \left[ R(0) - \frac{pN(0)}{p+\delta} - \frac{Ap}{d(d+\delta+p)} + \frac{Ap}{d(p+\delta)} \right] \\ &\quad \times e^{-(d+\delta+p)t} - \frac{\alpha p}{p+\delta} \int_0^t e^{-d(t-s)} I(s) ds + \left( \gamma - p + \frac{\alpha p}{p+\delta} \right) \int_0^t e^{-(d+\delta+p)(t-s)} I(s) ds.\end{aligned}\tag{2.4}$$

Substituting them into the second equation of (2.3), then

$$\begin{aligned} I(t) = & \beta I \left\{ \frac{A(d+\delta)}{d(d+\delta+p)} + \left[ \frac{\delta N(0)}{p+\delta} - \frac{A\delta}{d(p+\delta)} \right] e^{-dt} - \left( \gamma - p + \frac{\alpha p}{p+\delta} \right) \int_0^t e^{-(d+\delta+p)(t-s)} I(s) ds \right. \\ & \left. - I(t) - \frac{\alpha\delta}{p+\delta} \int_0^t e^{-d(t-s)} I(s) ds - \left[ R(0) - \frac{pN(0)}{p+\delta} - \frac{Ap}{d(d+\delta+p)} + \frac{Ap}{d(p+\delta)} \right] e^{-(d+\delta+p)t} \right\} \\ & - (\gamma + \alpha + d)I. \end{aligned} \quad (2.5)$$

With respect to equilibriums of (2.3), we have the following.

**Theorem 2.1.** *There only exists the disease-free equilibrium  $E^0(N^0, 0, R^0)$ , which is globally asymptotically stable if  $A\beta(\delta+d) < d(\gamma+\alpha+d)(d+\delta+p)$ . Here,  $N^0 = A/d$  and  $R^0 = Ap/(d(d+\delta+p))$ .*

*Proof.* The existence and uniqueness of the disease-free equilibrium  $E^0$  for system (2.3) are easily obtained if inequality  $A\beta(\delta+d) < d(\gamma+\alpha+d)(d+\delta+p)$  holds. Next, we first discuss the local stability of  $E^0$ . The Jacobian matrix of system (2.3) at a point  $E(N, I, R)$  is

$$J(E) = \begin{bmatrix} -d & -\alpha & 0 \\ \beta I & \beta(N-R-2I) - (\gamma+\alpha+d) & -\beta I \\ p & \gamma-p & -(d+\delta+p) \end{bmatrix}. \quad (2.6)$$

Thus,

$$J(E^0) = \begin{bmatrix} -d & -\alpha & 0 \\ 0 & \frac{A\beta(d+\delta)}{d(d+\delta+p)} - (\gamma+\alpha+d) & 0 \\ p & \gamma-p & -(d+\delta+p) \end{bmatrix}, \quad (2.7)$$

and  $J(E^0)$  has three eigenvalues with negative real part if inequality  $A\beta(\delta+d) < d(\gamma+\alpha+d)(d+\delta+p)$  is true, which shows that the disease-free equilibrium  $E^0$  is locally stable.

Further, we assume  $\gamma \leq p$ . It is easily known that for any  $\varepsilon_1 > 0$ , that there exists  $T_1 > 0$  such that

$$N(t) \leq \frac{A}{d} + \varepsilon_1, \quad t > T_1. \quad (2.8)$$

Hence, we obtain from the third equation of (2.3) that

$$\dot{R}(t) < p \left[ \frac{A}{d} + \varepsilon_1 \right] - (d+\delta+p)R, \quad t > T_1. \quad (2.9)$$



Then, for any  $\varepsilon_2 > 0$ , there exists  $T_2 > T_1$  such that

$$R(t) \leq \frac{Ap}{d(\delta + d + p)} + \varepsilon_1 + \varepsilon_2, \quad t > T_2. \quad (2.10)$$

Therefore, we have

$$\dot{S}(t) < \frac{A(d + \delta)(d + p)}{d(d + \delta + p)} + \delta(\varepsilon_1 + \varepsilon_2) - (d + p)S, \quad t > T_2. \quad (2.11)$$

This shows that for any  $\varepsilon_3 > 0$ , there exists  $T_3 > T_2$  such that

$$S(t) < \frac{A(d + \delta)}{d(d + \delta + p)} + \frac{\delta(\varepsilon_1 + \varepsilon_2)}{d + p} + \varepsilon_3, \quad t > T_3. \quad (2.12)$$

Moreover, we have

$$\dot{I}(t) \leq I \left[ \frac{A\beta(d + \delta)}{d(d + \delta + p)} + \frac{\delta(\varepsilon_1 + \varepsilon_2) + (d + p)\varepsilon_3}{d + p} - (\gamma + \alpha + d) \right], \quad t > T_3. \quad (2.13)$$

By the assumption of  $A\beta(\delta + d) < d(\gamma + \alpha + d)(d + \delta + p)$ , we may choose  $\varepsilon_1, \varepsilon_2$ , and  $\varepsilon_3$ , are small enough such that

$$\frac{\beta A(d + \delta)}{d(d + \delta + p)} + \frac{\delta(\varepsilon_1 + \varepsilon_2) + (d + p)\varepsilon_3}{d + p} - (\gamma + \alpha + d) < 0, \quad t > T_3. \quad (2.14)$$

Therefore, we obtain

$$\lim_{t \rightarrow +\infty} I(t) = 0. \quad (2.15)$$

This leads to

$$\lim_{t \rightarrow +\infty} N(t) = \frac{A}{d} = N^0, \quad \lim_{t \rightarrow +\infty} R(t) = \frac{Ap}{d(d + \delta + p)} = R^0. \quad (2.16)$$

If  $\gamma \geq p$ , we obtain from (2.5)

$$\begin{aligned} I(t) \leq \beta I \left\{ \frac{A(d + \delta)}{d(d + \delta + p)} + \left[ \frac{\delta N(0)}{p + \delta} - \frac{A\delta}{d(p + \delta)} \right] e^{-dt} \right. \\ \left. - \left[ R(0) - \frac{pN(0)}{p + \delta} - \frac{Ap}{d(d + \delta + p)} + \frac{Ap}{d(p + \delta)} \right] e^{-(d + \delta + p)t} - \frac{(\gamma + \alpha + d)}{\beta} \right\}. \end{aligned} \quad (2.17)$$

Since  $\lim_{t \rightarrow +\infty} e^{-dt} = 0$ ,  $\lim_{t \rightarrow +\infty} e^{-(d+\delta+p)t} = 0$ , and  $A\beta(\delta + d) < d(\gamma + \alpha + d)(d + \delta + p)$ , then there exists  $q > 0$  and  $T > 0$  such that

$$\dot{I}(t) \leq -q\beta I, \quad t > T. \quad (2.18)$$

Thus, we prove that (2.15) is held. Further, (2.16) is obtained.  $\square$

**Theorem 2.2.** *The unstable disease-free equilibrium  $E^0$  and the local stable endemic equilibrium  $E^*(N^*, I^*, R^*)$  of system (2.3) coexist if  $A\beta(\delta + d) > d(\gamma + \alpha + d)(d + \delta + p)$  holds. Here,*

$$N^* = \frac{A - \alpha I^*}{d}, \quad I^* = \frac{A(\delta + d) - d(d + \delta + p)S^*}{(\gamma + \alpha + d)(\delta + p) - \gamma\delta}, \quad R^* = \frac{pS^* + \gamma I^*}{d + \delta}, \quad S^* = \frac{\gamma + \alpha + d}{\beta}. \quad (2.19)$$

*Proof.* It is easily known that system (2.3) has unique positive equilibrium  $E^*(N^*, I^*, R^*)$  except the disease-free equilibrium  $E^0(N^0, 0, R^0)$  if inequality  $A\beta(\delta + d) > d(\gamma + \alpha + d)(d + \delta + p)$  holds.

Moreover, we may obtain the Jacobian matrix of (2.3) at equilibrium  $E^*$  as

$$J(E^*) = \begin{bmatrix} -d & -\alpha & 0 \\ \beta I^* & -\beta I^* & -\beta I^* \\ p & \gamma - p & -(d + \delta + p) \end{bmatrix}. \quad (2.20)$$

The characteristic equation of  $J(E^*)$  is given by

$$\lambda^3 + Q_1\lambda^2 + Q_2\lambda + Q_3 = 0, \quad (2.21)$$

and the coefficients  $Q_i$  ( $i = 1, 2, 3$ ) are

$$\begin{aligned} Q_1 &= \beta I^* + 2d + \delta + p, \\ Q_2 &= \beta I^*(2d + \gamma + \alpha + \delta) + d(d + \delta + p), \\ Q_3 &= \beta I^*[d(\gamma + d + \delta) + \alpha(d + \delta)]. \end{aligned} \quad (2.22)$$

Clearly,  $Q_i > 0$  ( $i = 1, 2, 3$ ) and  $Q_1Q_2 > Q_3$ . By Routh-Hurwitz criterion, there exist three eigenvalues with negative real part for Jacobian matrix  $J(E^*)$ , which shows that equilibrium  $E^*$  is locally stable.  $\square$

Further, we study the global stability of  $E^*$ .

**Theorem 2.3.** *If  $(\gamma - p)(p + \delta) + \alpha p > 0$  is held besides  $A\beta(\delta + d) > d(\gamma + \alpha + d)(d + \delta + p)$ , then the positive equilibrium  $E^*$  of (2.3) is globally asymptotically stable.*

*Proof.* Since  $I^* > 0$ , we may make the change of variable  $I(t) = I^* e^{y(t)}$ , thus

$$\dot{y}(t) = \frac{\dot{I}(t)}{I(t)}, \quad y(t) = \ln \frac{I(t)}{I^*}, \quad (2.23)$$

and (2.5) is equivalent to

$$\begin{aligned} \dot{y}(t) = \beta \left\{ \frac{A(d+\delta)}{d(d+\delta+p)} + \left[ \frac{\delta N(0)}{p+\delta} - \frac{A\delta}{d(p+\delta)} \right] e^{-dt} - \left( \gamma - p + \frac{\alpha p}{p+\delta} \right) I^* \int_0^t e^{-(d+\delta+p)(t-s)} e^{y(s)} ds \right. \\ \left. - I^* e^{y(t)} - \frac{\alpha\delta}{p+\delta} I^* \int_0^t e^{-d(t-s)} e^{y(s)} ds - \left[ R(0) - \frac{pN(0)}{p+\delta} - \frac{Ap}{d(d+\delta+p)} + \frac{Ap}{d(p+\delta)} \right] \right. \\ \left. \times e^{-(d+\delta+p)t} \right\} - (\gamma + \alpha + d). \end{aligned} \quad (2.24)$$

Further, we define  $g(y) = e^y - 1$  and

$$a(s) = \begin{cases} 0, & s \leq 0, \\ \beta I^* \left[ 1 + \frac{\alpha\delta}{p+\delta} \int_0^s e^{-du} du + \left( \gamma - p + \frac{\alpha p}{p+\delta} \right) \int_0^s e^{-(d+\delta+p)u} du \right], & s > 0, \end{cases} \quad (2.25)$$

so that  $a(s)$  has a jump  $\beta I^*$  at  $s = 0$  and  $\dot{a}(s) = \beta I^* [\alpha\delta/(p+\delta)e^{-ds} + (\gamma - p + \alpha p/(p+\delta))e^{-(d+\delta+p)s}] > 0$  for  $s > 0$  if  $(\gamma - p)(p+\delta) + \alpha p > 0$ , then

$$\begin{aligned} \int_0^t g(y(t-s)) da(s) = \beta I^* \left[ \frac{\alpha\delta}{p+\delta} \int_0^t e^{-d(t-u)} e^{y(u)} du + \frac{(\gamma - p)(p+\delta) + \alpha p}{p+\delta} \int_0^t e^{-(d+\delta+p)(t-u)} e^{y(u)} du \right] \\ - \beta I^* \left[ \frac{\alpha\delta}{p+\delta} \frac{1 - e^{-dt}}{d} + \frac{(\gamma - p)(p+\delta) + \alpha p}{p+\delta} \frac{1 - e^{-(d+\delta+p)t}}{d + \delta + p} \right]. \end{aligned} \quad (2.26)$$

Hence, system (2.3) is reduced to a single integrodifferential equation

$$\dot{y}(t) = - \int_0^t g(y(t-s)) da(s) - h(y(t)) + f(t). \quad (2.27)$$

Here,  $h(y) = \beta I^*(e^y - 1)$  and

$$\begin{aligned} f(t) = \beta \left\{ \left[ \frac{\delta N(0)}{p+\delta} - \frac{A\delta}{d(p+\delta)} + \frac{\alpha\delta I^*}{d(p+\delta)} \right] e^{-dt} \right. \\ \left. - \left[ R(0) - \frac{pN(0)}{p+\delta} - \frac{Ap}{d(d+\delta+p)} + \frac{Ap}{d(p+\delta)} + \frac{((\gamma - p)(p+\delta) + \alpha p)I^*}{(d+\delta+p)(p+\delta)} \right] e^{-(d+\delta+p)t} \right\} \\ + \left\{ \frac{A\beta(d+\delta)}{d(d+\delta+p)} - \frac{\alpha\delta\beta I^*}{d(p+\delta)} - \frac{((\gamma - p)(p+\delta) + \alpha p)\beta I^*}{(d+\delta+p)(p+\delta)} - \beta I^* - (\gamma + \alpha + d) \right\}. \end{aligned} \quad (2.28)$$

With the equilibrium condition of (2.3),  $f(t)$  can be simplified as

$$f(t) = \beta \left\{ \left[ \frac{\delta N(0)}{p + \delta} - \frac{A\delta}{d(p + \delta)} + \frac{\alpha \delta I^*}{d(p + \delta)} \right] e^{-dt} - \left[ R(0) - \frac{pN(0)}{p + \delta} - \frac{Ap}{d(d + \delta + p)} + \frac{Ap}{d(p + \delta)} + \frac{((\gamma - p)(p + \delta) + \alpha p)I^*}{(d + \delta + p)(p + \delta)} \right] e^{-(d + \delta + p)t} \right\}, \quad (2.29)$$

which is negative exponential.

Obviously, the equilibrium  $I^*$  of (2.5) corresponds to the equilibrium  $y(t) \equiv 0$  of (2.27). According to Theorem 18.2.3 of Gripenberg et al. [13], since  $a(s)$  is of strong positive type ([14, 15]),  $g(y)$  is continuous and  $\int_0^y g(y)dy \rightarrow \infty$  as  $|y| \rightarrow \infty$ ,  $h(y)$  is also continuous and  $g(y)h(y) \geq 0$  for  $-\infty < y < +\infty$ ,  $f(t)$ , and  $\dot{f}(t)$  are in  $L^2(0, \infty)$ , it follows that every bounded solution of (2.27) satisfies  $\lim_{t \rightarrow \infty} g(y(t)) = 0$ . Owing to  $g(y) = 0$  only for  $y = 0$ , this implies that every solution of (2.27) tends to zero as  $t \rightarrow \infty$  and therefore the equilibrium  $I^*$  of (2.5) is globally asymptotically stable. As (2.5) is equivalent to system (2.3), the unique positive equilibrium  $(N^*, I^*, R^*)$  of (2.3) is globally asymptotically stable.  $\square$

It is similar to the classical SIR models that there exists the threshold quantity and it is given by  $R_1 = A/d \cdot \beta/(\gamma + \alpha + d) \cdot (\delta + d)/(\delta + d + p)$  for the model (2.1). If  $R_1 < 1$ , then system (2.1) has only the globally asymptotically stable disease-free equilibrium. This shows that the epidemic disease will die out. Otherwise, if  $R_1 > 1$ , system (2.1) has a locally stable positive equilibrium except disease-free equilibrium. Moreover, the global asymptotical stability of positive equilibrium is obtained under the assumption of  $(\gamma - p)(p + \delta) + \alpha p > 0$ . This reveals a fact that the disease may be “invaded” or always exists in the population forever. According to the expression of  $R_1$ , it is the convenient and important policy to control the occurrence of the disease that the flow of the members decreases, the vaccinated members increase, and the infectious period shortens.

### 3. An SIR Model with Impulsive Vaccinations

In this section, the assumption that the susceptible is vaccinated continuously is replaced by the assumption that the susceptible is vaccinated impulsively, that is, the susceptible is vaccinated at the fixed moments. At the moment  $n\tau$ , the vaccinated susceptible will enter directly to the removal owing to acquiring the temporary immunity, which leads to the following system:

$$\begin{aligned} \dot{S}(t) &= A - dS - \beta SI + \delta R, & \dot{I}(t) &= \beta SI - (\gamma + \alpha + d)I, & \dot{R}(t) &= \gamma I - (\delta + d)R, & t \neq n\tau, \\ S(n\tau^+) &= (1 - p)S(n\tau), & I(n\tau^+) &= I(n\tau), & R(n\tau^+) &= R(n\tau) + pS(n\tau), \end{aligned} \quad (3.1)$$

where  $\tau > 0$  is the vaccinated period. Clearly, system (3.1) is equivalent to the system

$$\begin{aligned} \dot{S}(t) &= A - dS - \beta SI + \delta(N - S - I), & \dot{I}(t) &= \beta SI - (\gamma + \alpha + d)I, & \dot{N}(t) &= A - dN - \alpha I, \\ & & & & t &\neq n\tau, \\ S(n\tau^+) &= (1 - p)S(n\tau), & I(n\tau^+) &= I(n\tau), & N(n\tau^+) &= N(n\tau). \end{aligned} \quad (3.2)$$

Let  $I = 0$ , then system (3.2) is simplified as

$$\begin{aligned} \dot{S}(t) &= A - (d + \delta)S + \delta N, & \dot{N}(t) &= A - dN, & t &\neq n\tau, \\ S(n\tau^+) &= (1 - p)S(n\tau), & N(n\tau^+) &= N(n\tau). \end{aligned} \quad (3.3)$$

**Lemma 3.1.** *Consider the following system:*

$$\dot{x}(t) = a - bx(t), \quad t \neq n\tau, \quad x(n\tau^+) = (1 - p)x(n\tau). \quad (3.4)$$

Then there exists a positive periodic solution  $x^*(t)$ , which is globally attractive. Here  $x^*(t) = a/b(1 - (p(e^{-b(t-n\tau)})/(1 - (1 - p)e^{-b\tau})))$  for  $n\tau < t \leq (n + 1)\tau$ .

The proof is so simple that we omit it.

By Lemma 3.1, we can easily know that there exists a positive periodic solution  $(\tilde{S}(t), \tilde{N}(t))$  for system (3.3), and their expression is

$$\begin{aligned} \tilde{S}(t) &= \frac{A}{d} \left( 1 - \frac{pe^{-(d+\delta)(t-n\tau)}}{1 - (1-p)e^{-(d+\delta)\tau}} \right), & \tilde{N}(t) &= \frac{A}{d}, & t &\neq n\tau, \\ \tilde{S}(n\tau^+) &= \frac{A}{d} \left[ \frac{(1-p)(1 - e^{-(d+\delta)\tau})}{1 - (1-p)e^{-(d+\delta)\tau}} \right]. \end{aligned} \quad (3.5)$$

This indicates that system (3.2) has a disease-free periodic solution  $(\tilde{S}(t), 0, \tilde{N}(t))$  with period  $\tau$ , and its local stability may be determined by considering the behavior of small-amplitude perturbation of the solution. Define  $(S(t), I(t), N(t)) = (\tilde{S}(t) + x(t), y(t), \tilde{N}(t) + z(t))$ , then these may be written

$$\begin{bmatrix} x(t) \\ y(t) \\ z(t) \end{bmatrix} = \Phi(t) \begin{bmatrix} x(0) \\ y(0) \\ z(0) \end{bmatrix}, \quad (3.6)$$

where  $\Phi(t)$  satisfies

$$\frac{d\Phi(t)}{dt} = \begin{bmatrix} -(d + \delta) & -(\delta + \beta\tilde{S}(t)) & \delta \\ 0 & \beta\tilde{S}(t) - (\gamma + \alpha + d) & 0 \\ 0 & -\alpha & -d \end{bmatrix} \Phi(t) \quad (3.7)$$

with  $\Phi(0) = I$ , the identity matrix. The resetting impulsive conditions of (3.2) become

$$\begin{bmatrix} x(n\tau^+) \\ y(n\tau^+) \\ z(n\tau^+) \end{bmatrix} = \begin{bmatrix} 1-p & 0 & 0 \\ 0 & 1 & 0 \\ 0 & 0 & 1 \end{bmatrix} \begin{bmatrix} x(n\tau) \\ y(n\tau) \\ z(n\tau) \end{bmatrix}. \quad (3.8)$$

Hence, if all eigenvalues  $\mu_j (j = 1, 2, 3)$  of the monodromy matrix  $M$ ,

$$M = \begin{bmatrix} 1-p & 0 & 0 \\ 0 & 1 & 0 \\ 0 & 0 & 1 \end{bmatrix} \Phi(\tau) = \begin{bmatrix} (1-p)e^{-(d+\delta)\tau} & (1-p)a_{12}(\tau) & (1-p)a_{13}(\tau) \\ 0 & e^{-(\gamma+\alpha+d)\tau+\beta\int_0^\tau \tilde{S}(t)dt} & 0 \\ 0 & a_{32}(\tau) & e^{-d\tau} \end{bmatrix}, \quad (3.9)$$

have absolute value less than one, then the  $\tau$ -periodic solution  $(\tilde{S}(t), 0, \tilde{N}(t))$  is locally stable. Actually,  $a_{12}(\tau)$ ,  $a_{13}(\tau)$ , and  $a_{32}(\tau)$  need not to be solved out, and we have  $\mu_1 = (1-p)e^{-(d+\delta)\tau}$ ,  $\mu_2 = e^{-(\gamma+\alpha+d)\tau+\beta\int_0^\tau \tilde{S}(t)dt}$ , and  $\mu_3 = e^{-d\tau}$ . Therefore, if  $-(\gamma + \alpha + d)\tau + \beta\int_0^\tau \tilde{S}(t)dt < 0$ , which is equivalent to  $A/d \cdot \beta/(\gamma + \alpha + d) \cdot (1 - p(e^{(d+\delta)\tau} - 1)/((d + \delta)(e^{(d+\delta)\tau} - 1 + p)\tau)) < 1$ , then  $|\mu_j| < 1$  ( $j = 1, 2, 3$ ) holds. And we have the following.

**Theorem 3.2.** *If inequality  $A/d \cdot \beta/(\gamma + \alpha + d) \cdot (1 - p(e^{(d+\delta)\tau} - 1)/((d + \delta)(e^{(d+\delta)\tau} - 1 + p)\tau)) < 1$  holds, then there exists a disease-free periodic solution  $(\tilde{S}(t), 0, \tilde{N}(t))$  for (3.2), which is locally stable. Moreover, it is globally asymptotically stable.*

*Proof.* Denote that  $R_2 = A/d \cdot \beta/(\gamma + \alpha + d) \cdot (1 - p(e^{(d+\delta)\tau} - 1)/((d + \delta)(e^{(d+\delta)\tau} - 1 + p)\tau))$ . In fact, we only prove that  $\lim_{t \rightarrow \infty} S(t) = \tilde{S}(t)$ ,  $\lim_{t \rightarrow \infty} I(t) = 0$ , and  $\lim_{t \rightarrow \infty} \tilde{N}(t) = A/d$  for  $R_2 < 1$ .

For every solution  $(S(t), I(t), N(t))$  of (3.2) with positive initial value  $(S(0^+), I(0^+), N(0^+))$ , it is clear that  $\dot{N}(t) \leq A - dN$ , which leads to

$$N(t) \leq \frac{A}{d} + \varepsilon_1, \quad t > m\tau. \quad (3.10)$$

Here,  $\varepsilon_1 > 0$  may be arbitrary small, and a positive integer  $m$  may be large enough. Hence, we have

$$\begin{aligned} \dot{S}(t) &\leq \frac{A}{d}(d + \delta) + \delta\varepsilon_1 - (d + \delta)S, \quad m\tau \leq n\tau < t \leq (n + 1)\tau, \\ S(n\tau^+) &= (1 - p)S(n\tau). \end{aligned} \quad (3.11)$$

Furthermore, we consider the system

$$\begin{aligned} \dot{S}_1(t) &= \frac{A}{d}(d + \delta) + \delta\varepsilon_1 - (d + \delta)S_1, \quad m\tau \leq n\tau < t \leq (n + 1)\tau, \\ S_1(n\tau^+) &= (1 - p)S_1(n\tau). \end{aligned} \quad (3.12)$$

Therefore, we have  $S(t) \leq S_1(t)$ , and  $S_1(t)$  is the solution of (3.12) with the initial value  $S_1(m\tau^+) = S(m\tau^+)$ . In addition, for system (3.12), it is easily known that there exists a positive

periodic solution  $\widetilde{S}_1(t)$ , and every solution with positive initial value  $S_1(0^+) > 0$  is globally attractive by Lemma 3.1. Here,

$$\begin{aligned}\widetilde{S}_1(t) &= \left( \frac{A}{d} + \frac{\delta \varepsilon_1}{d + \delta} \right) \left( 1 - \frac{pe^{-(d+\delta)(t-n\tau)}}{1 - (1-p)e^{-(d+\delta)\tau}} \right), \quad n\tau < t \leq (n+1)\tau, \\ \widetilde{S}_1(n\tau^+) &= \left( \frac{A}{d} + \frac{\delta \varepsilon_1}{d + \delta} \right) \frac{(1-p)e^{-(d+\delta)\tau}}{1 - (1-p)e^{-(d+\delta)\tau}}.\end{aligned}\quad (3.13)$$

Thus, for an arbitrary small  $\varepsilon_2 > 0$ , there exists a positive integer  $m_1 > m$  such that

$$S_1(t) < \widetilde{S}_1(t) + \varepsilon_2, \quad t \geq m_1\tau. \quad (3.14)$$

As a result, we have

$$\dot{I}(t) < [\beta(\widetilde{S}_1(t) + \varepsilon_2) - (\gamma + \alpha + d)]I, \quad t \geq m_1\tau. \quad (3.15)$$

So,

$$0 \leq I(t) \leq I(m_1\tau^+)e^{\int_{m_1\tau}^t [\beta(\widetilde{S}_1(t) + \varepsilon_2) - (\gamma + \alpha + d)]dt}, \quad t \geq m_1\tau. \quad (3.16)$$

Since  $R_2 < 1$  holds, we may choose  $\varepsilon_1$  and  $\varepsilon_2$  small enough such that  $\int_0^\tau [\beta(\widetilde{S}_1(t) + \varepsilon_2) - (\gamma + \alpha + d)]dt < 0$ , which leads to

$$\lim_{t \rightarrow \infty} I(t) = 0. \quad (3.17)$$

And since

$$N(t) = N(0)e^{-dt} + \frac{A}{d}(1 - e^{-dt}) - \alpha \int_0^t e^{-d(t-s)} I(s) ds, \quad (3.18)$$

by (3.17), we have

$$\lim_{t \rightarrow \infty} N(t) = \frac{A}{d}. \quad (3.19)$$

Therefore, for an arbitrary small  $\varepsilon_3 > 0$ , there exists a positive integer  $m_2 (> m_1)$  such that

$$0 < I(t) < \varepsilon_3, \quad 0 < \frac{A}{d} - \varepsilon_3 < N(t) < \frac{A}{d} + \varepsilon_3, \quad t \geq m_2\tau. \quad (3.20)$$



Then, we have

$$\begin{aligned}\dot{S}(t) &> \left[ \frac{A(d+\delta)}{d} - 2\delta\varepsilon_3 \right] - (d+\delta+\beta\varepsilon_3)S, \quad m_2\tau < n\tau < t \leq (n+1)\tau, \\ S(n\tau^+) &= (1-p)S(n\tau), \quad n\tau > m_2\tau.\end{aligned}\quad (3.21)$$

Considering the system

$$\begin{aligned}\dot{S}_2(t) &= \left[ \frac{A(d+\delta)}{d} - 2\delta\varepsilon_3 \right] - (d+\delta+\beta\varepsilon_3)S_2, \quad m_2\tau < n\tau < t \leq (n+1)\tau, \\ S_2(n\tau^+) &= (1-p)S_2(n\tau), \quad n\tau > m_2\tau,\end{aligned}\quad (3.22)$$

we have  $S(t) \geq S_2(t)$ , where  $S_2(t)$  is the solution of (3.22) with initial value  $S_2(m_2\tau^+) = S(m_2\tau^+)$ . Denote that  $\widetilde{S}_2(t)$  is the globally asymptotically attractive and positive periodic solution; thus, for an arbitrary small number  $\varepsilon_4 > 0$ , there is a positive integer  $m_3$  such that

$$\widetilde{S}_2(t) - \varepsilon_4 < S_2(t) < \widetilde{S}_2(t) + \varepsilon_4, \quad t \geq m_3\tau, \quad (3.23)$$

and since  $S(t) > S_2(t)$ , we may get

$$\widetilde{S}_2(t) - \varepsilon_4 < S(t), \quad t \geq m_3\tau. \quad (3.24)$$

Let  $\varepsilon = \min\{\varepsilon_1, \varepsilon_2, \varepsilon_3, \varepsilon_4\}$  and  $M = \max\{m_2, m_3\}$ , then for  $t > M\tau$ , we have

$$\widetilde{S}_2(t) - \varepsilon < S(t) < \widetilde{S}_1(t) + \varepsilon. \quad (3.25)$$

And since  $\widetilde{S}_1(t)$  and  $\widetilde{S}_2(t)$  will approach the positive periodic solution  $\widetilde{S}(t)$  of system (3.3) for  $\varepsilon \rightarrow 0$ , therefore, we have

$$\lim_{t \rightarrow \infty} S(t) = \widetilde{S}(t). \quad (3.26)$$

Thus, the global stability of the boundary periodic solution  $(\widetilde{S}(t), 0, A/d)$  has been proven. This indicates that the disease-free periodic solution  $(\widetilde{S}(t), 0, \widetilde{R}(t))$  of (3.1) is also globally asymptotically stable.  $\square$

Clearly, if  $A/d \cdot \beta/(\gamma + \alpha + d) < 1$  holds, then  $R_2 < 1$  is true. So, we have the following.

**Corollary 3.3.** *If  $A/d \cdot \beta/(\gamma + \alpha + d) < 1$  holds, then system (3.2) has a unique disease-free periodic solution  $(\widetilde{S}(t), 0, \widetilde{N}(t))$  for arbitrary  $p > 0$  and  $\tau > 0$ , which is globally asymptotically stable.*

In the following, one only considers the case:  $A/d \cdot \beta/(\gamma + \alpha + d) > 1$ .

Denote  $f(\tau) \triangleq (A\beta/d - (\gamma + \alpha + d))\tau + A\beta/d \cdot p / (d + \delta) \cdot (1 - \exp(-(d + \delta)\tau)) / (\exp((d + \delta)\tau) - 1 + p)$ . Notice that the function satisfies  $f(\tau)$  is continuous on  $[0, +\infty)$ ,  $f(0) = 0$ ,  $f(+\infty) = +\infty$ ,  $f'(0) = -( \gamma + \alpha + d ) < 0$ ,  $f'(+\infty) = A\beta/d - (\gamma + \alpha + d) > 0$ ; moreover,  $f''(\tau) = (d + \delta)p^2 e^{(d + \delta)\tau} A\beta/d \cdot (e^{(d + \delta)\tau} + 1 - p) / (e^{(d + \delta)\tau} - 1 + p)^3 > 0$ . Then one has the following.

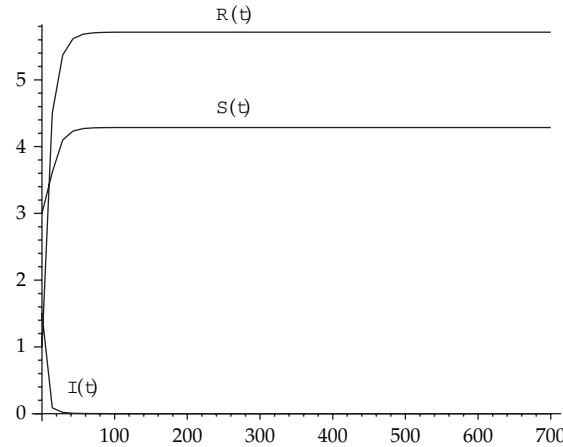


Figure 1

**Lemma 3.4.** If  $A/d \cdot \beta/(\gamma + \alpha + d) > 1$ , then there exists and only exists a root  $\tau_0$  in  $(0, +\infty)$  for function  $y = f(\tau)$ , and  $f(\tau) < 0$  for  $\tau < \tau_0$  and  $f(\tau) > 0$  for  $\tau > \tau_0$ .

Noting that  $f(\tau) < 0$  is equivalent to  $R_2 < 1$ , one has the following.

**Corollary 3.5.** For system (3.2), if  $A/d \cdot \beta/(\gamma + \alpha + d) > 1$ , then there exists  $\tau_0 > 0$  such that system (3.2) has a unique disease-free periodic solution  $(\tilde{S}(t), 0, \tilde{N}(t))$  for  $\tau < \tau_0$ , which is globally asymptotically stable.

Now, we are in the position of studying the behaviors of (3.1) under the assumption of  $R_2 > 1$ . Here, we only discuss the existence of endemic periodic solution  $(S^*(t), I^*(t), R^*(t))$  of system (3.1) with  $\alpha = 0$ . From the viewpoint of biology, we neglect the death-related disease. At this time, system (3.1) can be rewritten as follows:

$$\begin{aligned} \dot{S}(t) &= A - dS - \beta SI + \delta(N - S - I), & \dot{I}(t) &= \beta SI - (\gamma + d)I & \dot{N}(t) &= A - dN, & t \neq n\tau, \\ S(n\tau^+) &= (1 - p)S(n\tau), & I(n\tau^+) &= I(n\tau), & N(n\tau^+) &= N(n\tau). \end{aligned} \quad (3.27)$$

If (3.27) has a periodic solution, it is certain that  $N(t) \equiv A/d$ . Then, we may change to consider the two-dimensional system (3.28), which is equivalent to (3.27).

$$\begin{aligned} \dot{S}(t) &= \frac{A}{d}(d + \delta) - (d + \delta)S - \delta I - \beta SI, & \dot{I}(t) &= \beta SI - (\gamma + d)I, & t \neq n\tau, \\ S(n\tau^+) &= (1 - p)S(n\tau), & I(n\tau^+) &= I(n\tau). \end{aligned} \quad (3.28)$$

Note that there exists a positive periodic solution  $S^\circ(t)$  of system

$$\begin{aligned} \dot{S} &= (d + \delta)\left(\frac{A}{d} - S\right), & t \neq n\tau, \\ S(n\tau^+) &= (1 - p)S(n\tau), \end{aligned} \quad (3.29)$$

where

$$\begin{aligned} S^\circ(t) &= \frac{A}{d} \left[ 1 - \frac{pe^{-(d+\delta)(t-n\tau)}}{1 - (1-p)e^{-(d+\delta)\tau}} \right], \quad n\tau < t \leq (n+1)\tau, \\ S^\circ(n\tau^+) &= \frac{A}{d} \left[ \frac{(1-p)(e^{(d+\delta)\tau} - 1)}{e^{(d+\delta)\tau} - 1 + p} \right], \end{aligned} \quad (3.30)$$

then system (3.28) has a boundary periodic solution  $\zeta(t) = (S^\circ(t), 0)$ . With bifurcation technique and the important Theorem [16], we may obtain the positive periodic solution  $(S^*(t), I^*(t))$  of (3.28). As

$$\begin{aligned} d'_0 &= 1 - \exp \int_0^\tau (\beta S^\circ(t) - (\gamma + d)) dt, \\ a'_0 &= 1 - (1-p) \exp \int_0^\tau (-(d + \delta)) dt > 0, \\ b'_0 &= -(1-p) \int_0^\tau \exp \left( \int_u^\tau -(d + \delta) dr \right) (-\beta S^\circ(u) - \delta) \exp \left( \int_0^u (\beta S^\circ(r) - (\gamma + d)) dr \right) \\ &\quad \times du > 0, \\ \frac{\partial^2 \Phi_2(\tau, X_0)}{\partial x_1 \partial x_2} &= \beta \tau \exp \int_0^\tau \frac{\partial F_2(\zeta(r))}{\partial x_2} dr > 0; \\ \frac{\partial^2 \Phi_2(\tau, X_0)}{\partial x_2^2} &= \beta \int_0^\tau \left\{ \int_0^u \left[ \exp \left( \int_p^u (-(d + \delta)) dr \right) (-\delta - \beta S^\circ(p)) \exp \left( \int_0^p (\beta S^\circ(r) - (\gamma + d)) dr \right) \right] dp \right\} \\ &\quad \times \left\{ \exp \left( \int_u^\tau (\beta S^\circ(r) - (\gamma + d)) dr \right) \right\} du < 0, \\ \frac{\partial^2 \Phi_2(\tau, X_0)}{\partial \bar{\tau} \partial x_2} &= (\beta S^\circ(\tau) - (\gamma + d)) \exp \left( \int_0^\tau (\beta S^\circ(r) - (\gamma + d)) dr \right); \\ \frac{\partial \Phi_1(\tau, X_0)}{\partial \bar{\tau}} &= S^\circ(\tau) > 0, \end{aligned} \quad (3.31)$$

and if we choose  $\tau_0$ , the unique root of  $d'_0 = f(\tau) = 0$ , to be the bifurcated parameter, then we can easily see that  $\partial^2 \Phi_2(\tau_0, X_0) / \partial \bar{\tau} \partial x_2 > 0$ . Further, we have  $B < 0$  and  $C > 0$ . According to the theorem of Lakmeche and Arino [16], the supercritical bifurcation occurs for system (3.28).

**Theorem 3.6.** *If  $\tau > \tau_0$  and is close to  $\tau_0$  enough, then there exists positive periodic solution  $(S^*(t), I^*(t))$  for system (3.28). Here,  $\tau_0$  is the root of  $d'_0 = 0$ .*

Further, one has the following.

**Corollary 3.7.** *For system (3.1), if  $\tau > \tau_0$  and is close to  $\tau_0$  enough, then there exists positive periodic solution  $(S^*(t), I^*(t), A/d - S^*(t) - I^*(t))$ . Here,  $\tau_0$  is defined in Theorem 3.6.*

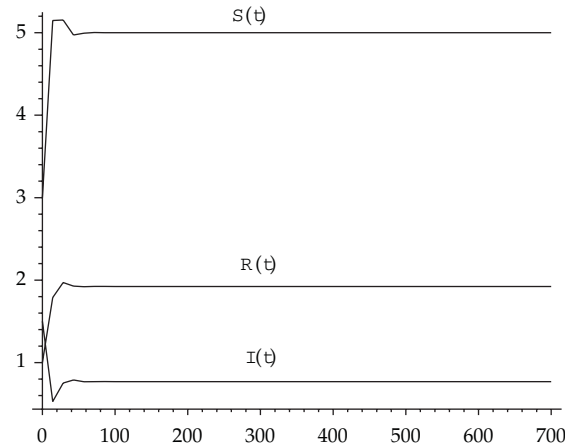


Figure 2

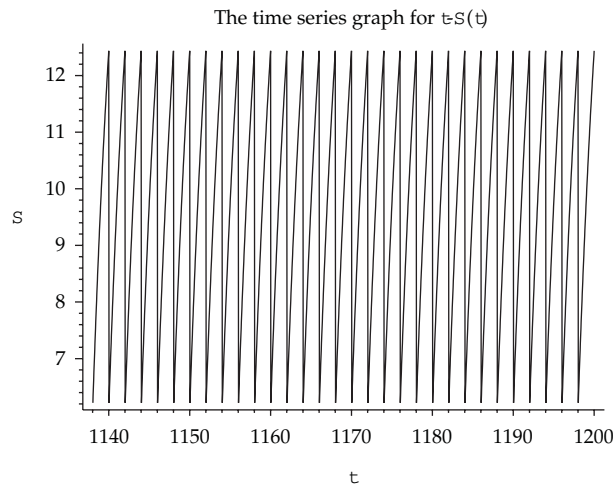


Figure 3

Thus, we complete the discussion on the epidemic model with impulsive vaccination. And we know that if the period of vaccination is smaller than  $\tau_0$ , the disease will die out forever, but once it is larger than  $\tau_0$ , the infectious disease is going to be the endemic disease.

#### 4. Discussion and Numerical Simulation

In this paper, we first assume that the susceptible is vaccinated continuously. The model is formulated by a continuous differential system. Similar to most models for the spread of infectious diseases, there is a threshold parameter  $R_1 = A/d \cdot \beta / (\gamma + \alpha + d) \cdot (\delta + d) / (\delta + d + p)$ . If  $R_1 < 1$ , the disease-free equilibrium is approached by all solutions; if  $R_1 > 1$ , the disease-free equilibrium is unstable and the endemic equilibrium exists, which is locally stable. Especially, we prove that the endemic equilibrium is globally asymptotically stable if  $(\gamma - p)(p + \delta) + \alpha p > 0$ .

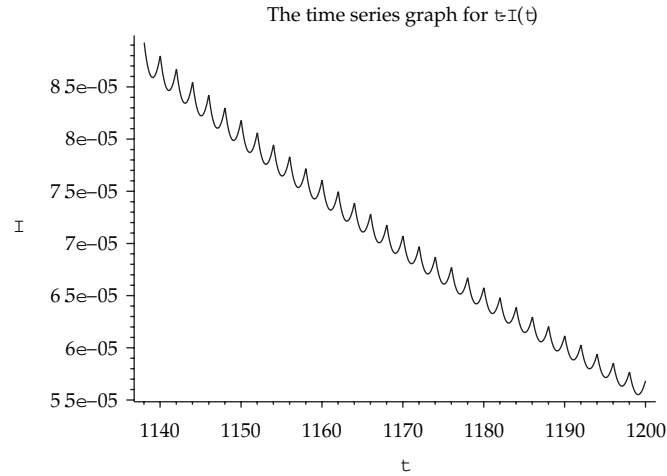


Figure 4

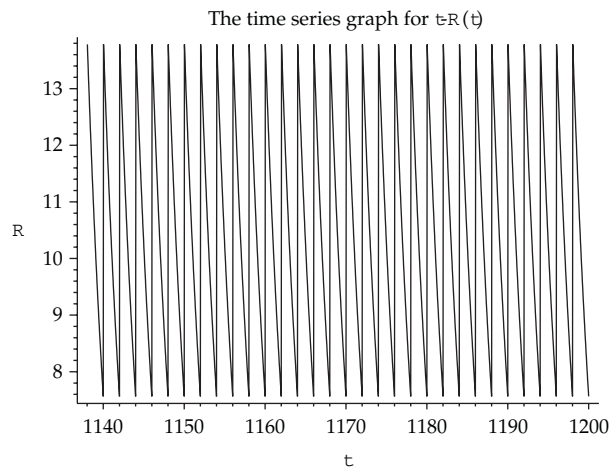


Figure 5

Obviously, there is a unique  $p_0$  such that  $R_1 = 1$ . If  $p$  exceeds  $p_0$ , then  $R_1 < 1$ , and if  $p$  is less than  $p_0$ , then  $R_1 > 1$ . We show that increasing the vaccinated members is helpful to control the spread of the infectious diseases.

Let  $A = 1$ ,  $d = 0.1$ ,  $\beta = 0.1$ ,  $\delta = 0.2$ ,  $p = 0.4$ ,  $\gamma = 0.1$ , and  $\alpha = 0.3$ , then we have  $R_1 < 1$ . By Theorem 2.1, we know that system (2.1) has a unique disease-free equilibrium  $E^0(S^0, 0, R^0)$  with  $S^0 = 4.285714286$ ,  $R^0 = 5.714285714$ , which is globally asymptotically stable. The time series of solutions with initial value  $[S(0) = 3, I(0) = 1.5, R(0) = 1]$  are given in Figure 1.

If we choose  $p := 0.1$ , then  $R_1 > 1$  and  $(\gamma - p)(p + \delta) + \alpha p > 0$ . By Theorem 2.2, there exists a globally asymptotically stable endemic equilibrium  $E^*(S^*, I^*, R^*)$  with  $S^* = 5.000000000$ ,  $I^* = 0.7692307692$ , and  $R^* = 1.923076923$ . Setting the initial values  $S(0) = 3$ ,  $I(0) = 1.5$ , and  $R(0) = 1$ , we draw the time series graph of the solution of (2.1) in Figure 2.

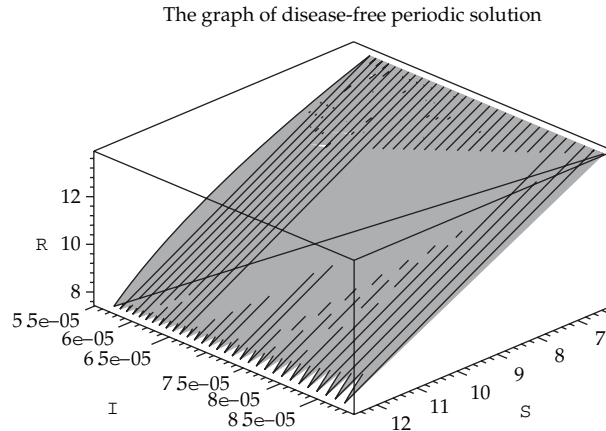


Figure 6

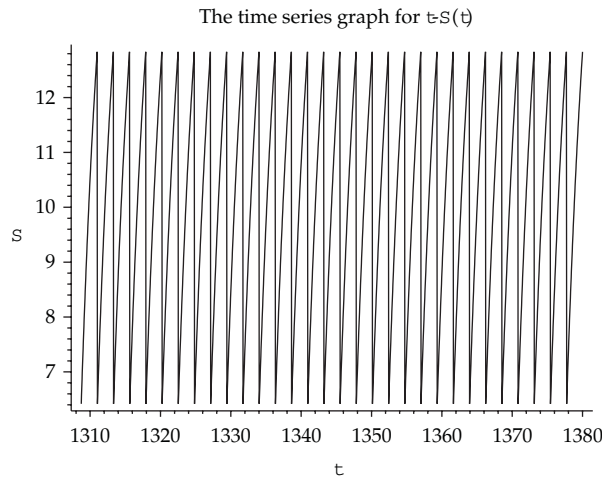


Figure 7

We continue to analyze our results. Let  $p = 0$ , that is, without vaccination on the susceptible. The model was discussed, and a threshold parameter  $R = A/d \cdot \beta/(\gamma + \alpha + d)$  was obtained for such a model in [4]. It is clear that  $R$  is identical to  $R_1$  with  $p = 0$ . In addition, in [4], the global stability of the endemic equilibrium was not proved. By our conclusion, we know that the endemic equilibrium is globally asymptotically stable if  $R_1 > 1$ , that is, we generalize the results in [4].

Second, the susceptible is supposed to be vaccinated at fixed moments. Such an epidemic model is described by an impulsive differential system, which also has a threshold parameter  $R_2$ . If  $R_2 < 1$ , the disease-free periodic solution is globally stable, while it is unstable for  $R_2 > 1$ . Clearly, if  $A/d \cdot \beta/(\gamma + \alpha + d) < 1$ , then  $R_2 < 1$ . Hence, there exists a unique globally asymptotically disease-free periodic solution. If  $A/d \cdot \beta/(\gamma + \alpha + d) > 1$ , then there exists a unique globally asymptotically disease-free periodic solution for  $\tau < \tau_0$ , and  $\tau_0$  is the root of  $R_2 = 1$ . With respect to the existence of positive periodic solution, we only consider

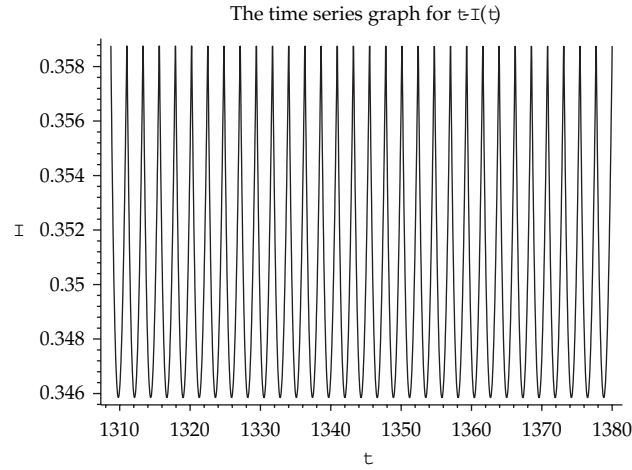


Figure 8

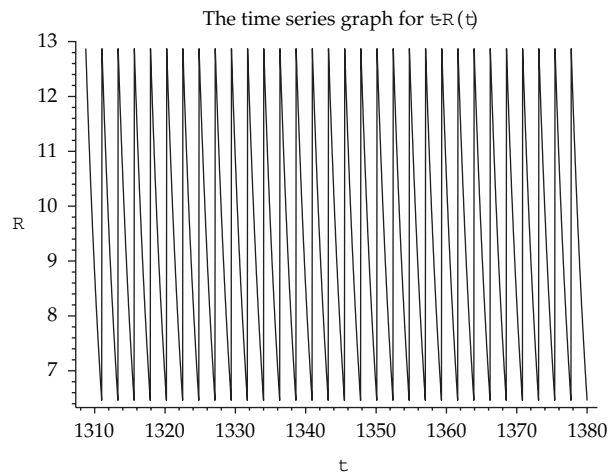


Figure 9

a simple model, in which  $\alpha = 0$ , that is, the disease-related death is neglected for the infective. The positive periodic solution exists if the vaccinated period  $\tau$  satisfies  $\tau > \tau_0$  and is close to the critical value  $\tau_0$  enough. It is implied that the epidemic disease may be controlled by shortening the vaccination period.

Let  $A = 2$ ,  $d = 0.1$ ,  $\beta = 0.02$ ,  $\delta = 0.2$ ,  $p = 0.5$ ,  $\gamma = 0.1$ ,  $\alpha = 0$  and  $\tau = 2$ . Then  $R_2 = 0.9636347352 < 1$  for impulsive system (3.1). Hence, there exists a disease-free periodic solution. Moreover, it is globally asymptotically stable. Figures 3, 4, and 5 are the time series of the solution with initial values  $S(0) = 5$ ,  $I(0) = 8$ , and  $R(0) = 5$ , and Figure 6 is the trajectory phase for it, which implies that this solution tends to the disease-free periodic solution  $(\tilde{S}(t), 0, \tilde{R}(t))$  with  $\tilde{S}(t) + \tilde{R}(t) = A/d = 20$ .

If we extend the period  $\tau$  of the vaccination and choose  $\tau = 2.3$ , then  $R_2 = 1.035848923 > 1$ . By Corollary 3.7, we know that there exists a positive periodic solution

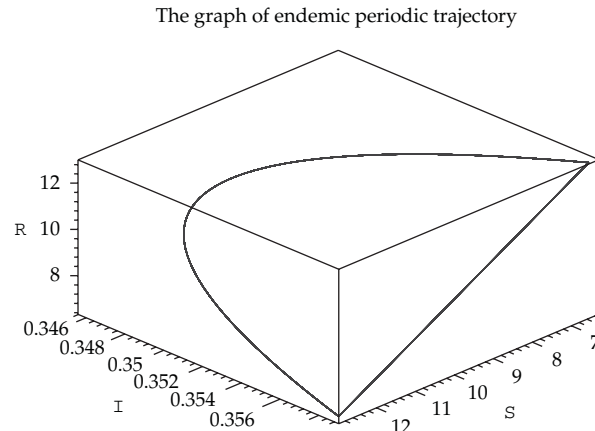


Figure 10

$(S^*(t), I^*(t), R^*(t))$  with period  $T = 2.3$ . We draw its time-series in Figures 7, 8, and 9. And the graph of its trajectory is drawn in Figure 10.

## Acknowledgments

This work is supported by the Natural Science Foundation of Shanxi Province [no. 20080110-02-2] and the Key Project of Chinese Ministry of Education [no. 210030], China.

## References

- [1] H. W. Hethcote, "The mathematics of infectious diseases," *SIAM Review*, vol. 42, no. 4, pp. 599–653, 2000.
- [2] J. Mena-Lorca and H. W. Hethcote, "Dynamic models of infectious diseases as regulators of population sizes," *Journal of Mathematical Biology*, vol. 30, no. 7, pp. 693–716, 1992.
- [3] R. M. Anderson and R. M. May, "Population biology of infectious diseases. Part I," *Nature*, vol. 280, no. 5721, pp. 361–367, 1979.
- [4] L. Q. Gao and H. W. Hethcote, "Disease transmission models with density-dependent demographics," *Journal of Mathematical Biology*, vol. 30, no. 7, pp. 717–731, 1992.
- [5] M. Y. Li, J. R. Graef, L. Wang, and J. Karsai, "Global dynamics of a SEIR model with varying total population size," *Mathematical Biosciences*, vol. 160, no. 2, pp. 191–213, 1999.
- [6] F. Brauer and P. van den Driessche, "Models for transmission of disease with immigration of infectives," *Mathematical Biosciences*, vol. 171, no. 2, pp. 143–154, 2001.
- [7] B. Shulgin, L. Stone, and Z. Agur, "Pulse vaccination strategy in the SIR epidemic model," *Bulletin of Mathematical Biology*, vol. 60, no. 6, pp. 1123–1148, 1998.
- [8] L. Stone, B. Shulgin, and Z. Agur, "Theoretical examination of the pulse vaccination policy in the SIR epidemic model," *Mathematical and Computer Modelling*, vol. 31, no. 4-5, pp. 207–215, 2000.
- [9] J. Li and Z. Ma, "Qualitative analyses of SIS epidemic model with vaccination and varying total population size," *Mathematical and Computer Modelling*, vol. 35, no. 11-12, pp. 1235–1243, 2002.
- [10] D. Greenhalgh and R. Das, "Modeling epidemics with variable contact rates," *Theoretical Population Biology*, vol. 47, no. 2, pp. 129–179, 1995.
- [11] D. Greenhalgh, "Some results for an SEIR epidemic model with density dependence in the death rate," *IMA Journal of Mathematics Applied in Medicine and Biology*, vol. 9, no. 2, pp. 67–106, 1992.
- [12] M. G. Roberts and R. R. Kao, "The dynamics of an infectious disease in a population with birth pulses," *Mathematical Biosciences*, vol. 149, no. 1, pp. 23–36, 1998.



- [13] G. Gripenberg, S.-O. Londen, and O. Staffans, *Volterra Integral and Functional Equations*, vol. 34 of *Encyclopedia of Mathematics and Its Applications*, Cambridge University Press, Cambridge, UK, 1990.
- [14] J. A. Nohel and D. F. Shea, "Frequency domain methods for Volterra equations," *Advances in Mathematics*, vol. 22, no. 3, pp. 278–304, 1976.
- [15] A. Halanay, "On the asymptotic behavior of the solutions of an integro-differential equation," *Journal of Mathematical Analysis and Applications*, vol. 10, pp. 319–324, 1965.
- [16] A. Lakmeche and O. Arino, "Bifurcation of non trivial periodic solutions of impulsive differential equations arising chemotherapeutic treatment," *Dynamics of Continuous, Discrete and Impulsive Systems*, vol. 7, no. 2, pp. 265–287, 2000.

## *Review Article*

# **Mathematical Issues in the Inference of Causal Interactions among Multichannel Neural Signals**

**Young-Jin Jung,<sup>1,2</sup> Kyung Hwan Kim,<sup>3</sup> and Chang-Hwan Im<sup>1</sup>**

<sup>1</sup> *Department of Biomedical Engineering, Hanyang University, Seoul 133-791, Republic of Korea*

<sup>2</sup> *Research Institute of Industrial Science, Hanyang University, Seoul 133-791, Republic of Korea*

<sup>3</sup> *Department of Biomedical Engineering, Yonsei University, Wonju 220-710, Republic of Korea*

Correspondence should be addressed to Chang-Hwan Im, ich@hanyang.ac.kr

Received 28 October 2011; Accepted 16 November 2011

Academic Editor: Kiwoon Kwon

Copyright © 2012 Young-Jin Jung et al. This is an open access article distributed under the Creative Commons Attribution License, which permits unrestricted use, distribution, and reproduction in any medium, provided the original work is properly cited.

Within the last few decades, attempts have been made to characterize the underlying mechanisms of brain activity by analyzing neural signals recorded, directly or indirectly, from the human brain. Accordingly, inference of functional connectivity among neural signals has become an indispensable research tool in modern neuroscience studies aiming to explore how different brain areas are interacting with each other. Indeed, remarkable advances in computational sciences and applied mathematics even allow the estimation of causal interactions among multichannel neural signals. Here, we introduce the brief mathematical background of the use of causality inference in neuroscience and discuss the relevant mathematical issues, with the ultimate goal of providing applied mathematicians with the current state-of-the-art knowledge on this promising multidisciplinary topic.

## **1. Introduction and Background**

Traditional functional neuroimaging studies have focused on the functional specification of brain areas. However, only a limited amount of information regarding the underlying neuronal mechanisms can be obtained when such spatial specification is studied. Recently, research interests have shifted toward describing how different brain areas interact with each other, with the hope of better understanding the functional organization of the cortical network [1–7]. Correlation [1, 2], coherence [3], phase locking value [4], mean phase coherence [5], and mutual information [6, 7] have been used to estimate functional interaction between multiple neural assemblies. These methods have been applied to signals obtained via many different functional neuroimaging modalities such as electroencephalography (EEG), local field potential (LFP), intracranial EEG (iEEG), magnetoencephalography (MEG), and functional magnetic resonance imaging (fMRI). Recent advances in neural signal analysis

have also enabled the estimation of direction of information flow between different cortical areas [8–12] even beyond conventional correlation-based functional connectivity analyses.

Over the past few decades, a number of measures for “directional” coupling between neural activities have been developed [8–13] and applied to various fields in both basic and clinical neuroscience [14–24]. Although a variety of causality estimators have been widely used for characterizing the mechanisms of neuronal networks, notable limitations and issues still exist that require intervention by applied mathematicians. For example, multivariate autoregressive (MVAR) model-based causality estimators do not accurately infer information flow between nonstationary and/or highly nonlinear neural signals. The determination of model order and the dependency on the analysis sample size are other issues that should be addressed in future studies. Furthermore, most non-MVAR-based causality estimators can only be used to infer causality between two signals, and thus need to be extended to the case of multichannel ( $\geq 3$ ) signal analyses [12, 13, 25].

Here, we introduce several mathematical signal analysis methods for estimating directional coupling between neural activities, all of which have been widely used in basic and applied neuroscience. Additionally, this paper attempts to illustrate the important mathematical issues that need to be addressed to improve the conventional causality estimators, with the aim to stimulate interest in this imperative multidisciplinary research topic among applied mathematicians.

## 2. MVAR-Based Causality Estimators

Recently, a number of causality estimation techniques have been developed to infer causality among multiple neural signal generators. The MVAR model—a linear multivariate time series model with a long history of application in econometrics [8]—has been frequently applied for causality estimations. The MVAR model is an extended version of the autoregressive (AR) model, a simple approach to time series characterization that assumes that for any given univariate time series, its consecutive measurements contain information regarding the process that generated it. The AR model can be implemented by modeling the current value of any variable as the weighted linear sum of its previous values. In the AR model, the value of a time series  $x$  at time  $t$ ,  $x_t$  can be estimated using:

$$x_t = \alpha_0 + \sum_{k=1}^p \alpha_k x_{t-k} + e_t, \quad (2.1)$$

where  $\alpha$ ,  $p$ , and  $e_t$  represent AR-matrix coefficients, the model order, and the uncorrelated Gaussian random process with a zero mean, respectively.

### 2.1. Granger Causality

Granger causality [8] has been proposed in the field of econometrics to quantify the causal relationship between two different time series. Specifically, this simple technique uses an MVAR model to linearly predict the future values of  $\mathbf{x}$  and  $\mathbf{y}$ , vectors of deterministic variables. The MVAR model attempts to estimate the value of  $x_t$  using:

$$x_t = \alpha_0 + \sum_{k=1}^p \alpha_k x_{t-k} + \sum_{k=1}^p \beta_k y_{t-k} + w_t, \quad (2.2)$$

where  $\alpha$  and  $\beta$  represent the AR-matrix coefficients and  $w_t$  the uncorrelated multivariate Gaussian random process with a zero mean. In contrast to (2.1), where the current value of a time series is estimated as the weighted sum of its previous values, the current value  $x_t$  in (2.2) is estimated using the previous values of two signal vectors  $\mathbf{x}$  and  $\mathbf{y}$ . We can judge whether there exists the Granger causality from  $\mathbf{y}$  to  $\mathbf{x}$  by inspecting whether the past information from both time series significantly improves the prediction of the future of  $\mathbf{x}$ , rather than using the past information from  $\mathbf{x}$  alone. In other words, if the prediction error for the MVAR model ( $w_t$ ) is smaller than that for the AR model ( $e_t$ ), it can be concluded that  $\mathbf{y}$  causes  $\mathbf{x}$ . In this way, Granger causality can be evaluated using

$$F \equiv \frac{(RSS_0 - RSS_1)/M}{RSS_1/(T - 2M - 1)}, \quad (2.3)$$

where

$$\begin{aligned} RSS_0 &= \sum_{i=1}^T e_i^2, \\ RSS_1 &= \sum_{i=1}^T w_i^2, \end{aligned} \quad (2.4)$$

where  $T$  represents the number of observations. To assess the statistical significance of the estimated Granger causality, the  $F$ -test with the null hypothesis,  $H_0: \beta_k = 0$  (i.e.,  $y_t$  does not influence the generation of  $x_t$ ) is generally used. If  $\beta_k = 0$  for all  $k = 1, 2, \dots, p$ , the Granger causality value  $F$  becomes zero as  $RSS_0$  equals  $RSS_1$ . Conversely, if the null hypothesis is rejected, that is,  $F$  is sufficiently large, it can be concluded that  $y_t$  causes  $x_t$ .

To test this hypothesis, a traditional  $F$ -test derived from an ordinary least squared regression for each equation can be used. To test the statistical significance of  $F$ , the cumulative  $F$  distribution is first estimated, after which the probability of the  $F$  value can be calculated by  $P_{GC} = 1 - \text{CDF}(F)$ , where CDF represents the cumulative distribution function and  $P_{GC}$  represents the probability of Granger causality. For example,  $P_{GC} = 1$  would indicate that no causal interaction exists between two time series, while  $P_{GC} = 0$  would signal a strong directional influence ( $y_t \rightarrow x_t$ ).

However, the MVAR model is problematic when estimating the appropriate model order  $p$ . Basically, most model order estimation methods are based on the maximum likelihood principle, which allows the determination of the highest possible model order in MVAR signal modeling. Akaike information criterion (AIC) [26] is also based on this concept and was the earliest method to estimate MVAR model orders. As AIC generally chooses larger than optimal model orders, the Bayesian information criterion (BIC) [27]—which is based on the Bayes estimator—was developed by Schwarz. The BIC generally penalizes free parameters more strongly than the AIC, and thus provides more accurate estimates of MVAR model orders. Although several modifications of the AIC and BIC have been recently developed [28–35], the estimation of accurate and reliable model orders remains an important issue.

## 2.2. Directed Transfer Function

Directed transfer function (DTF) is a widely used tool in identifying information flow between multichannel neural signals. Even though both Granger causality and DTF are based on MVAR modeling, the DTF procedure differs slightly from Granger causality. As described

above, Granger causality uses the variance of prediction errors to estimate the causal interaction, while DTF uses a matrix transfer function derived from MVAR model coefficients [9, 36]. In the framework of the MVAR model, a multivariate process of DTF can be described as a data vector  $X$  of  $N$  source signals:  $X_t = (X_1(t), X_2(t), \dots, X_N(t))^T$ . The MVAR model can then be constructed as

$$X_t = \sum_{k=1}^p A_k X_{t-k} + E_t, \quad (2.5)$$

where  $E_t$  represents a vector composed of white noise values at time  $t$ ,  $A_k$  is an  $N \times N$  matrix composed of the model coefficients, and  $p$  is the model order of MVAR. Note that (2.1) is a special case of (2.5) when  $N = 1$ . The MVAR model is then transformed into the frequency domain as follows:

$$X(f) = A^{-1}(f)E(f) = H(f)E(f), \quad (2.6)$$

where  $f$  denotes a specific frequency and the  $H(f)$  matrix represents the so-called transfer matrix, which is defined as

$$H(f) = A^{-1}(f) = \left( \sum_{k=0}^p A_k e^{-i2\pi f k \Delta t} \right)^{-1}, \quad A_0 = -I, \quad (2.7)$$

where  $I$  is the identity matrix.

The DTF can then be defined in terms of the elements of the transfer matrix  $H_{ij}$  as

$$\gamma_{ij}^2(f) = \frac{|H_{ij}(f)|^2}{\sum_{m=1}^k |H_{im}(f)|^2}, \quad (2.8)$$

where  $\gamma_{ij}^2(f)$  denotes the ratio between inflow from signal  $j$  to signal  $i$  and all inflows to signal  $i$  and  $k$  represents the number of signals. The DTF ratio  $\gamma_{ij}^2(f)$  ranges from 0 to 1, with values approaching to 1, suggesting that signal  $i$  is caused by signal  $j$ , whereas values approaching to 0 indicating that no information flow from signal  $j$  to signal  $i$  exists at a specific frequency.

### 2.3. Partial Directed Coherence

Partial directed coherence (PDC) was proposed by Baccalá and Sameshima as a frequency domain counterpart to Granger causality [11] and is based on a spectral representation of (2.5), defined as

$$A(f) = \sum_{k=0}^p A_k e^{-i2\pi f k \Delta t}, \quad (2.9)$$

$$\bar{A}(f) = I - A(f),$$

where  $I$  is an identity matrix [37]. The estimate of PDC from  $X_m$  to  $X_n$  is defined as

$$\text{PDC}_{X_n \leftarrow X_m}(f) = \frac{\bar{A}_{n,m}(f)}{\sqrt{\sum_{k=1}^Q |A_{n,k}(f)|^2}}, \quad (2.10)$$

where  $\bar{A}_{n,m}$  is the  $(n, m)$ -th element of  $\bar{A}$ .

## 2.4. Modified MVAR-Based Estimators

Although the MVAR-based causality estimators described above have been shown to be useful in many neuroscience problems, they are not applicable for all types of neural signals. For example, signals which have severely unbalanced model residual variances are not appropriate for PDC. Accordingly, several additional modified causality estimators, including generalized partial directed coherence [38, 39], Geweke's Granger causality [40, 41], Wiener Granger causality [42], and direct directed transfer function [43], were subsequently developed to broaden application.

The generalized partial directed coherence (gPDC) was first proposed by Baccalá et al. to circumvent the numerical problem associated with time series scaling [38], by which a variance stabilization of the frequency domain representation of lagged causality could be achieved [39]. The gPDC estimator is defined as

$$\pi_{ij}^{(w)}(f) = \frac{(1/\sigma_i)\bar{A}_{ij}(f)}{\sqrt{\sum_{k=1}^N (1/\sigma_k^2)\bar{A}_{kj}(f)\bar{A}_{kj}^*(f)}}, \quad (2.11)$$

where  $\sigma_i$  represents the variance of the  $i$ th input process. gPDC was modified from PDC to improve the identification of causal interactions between signals with severely unbalanced model residual variances [39].

The Geweke's Granger causality is derived from Geweke's formulation [40, 41] and is defined as

$$\begin{aligned} I_{k \rightarrow l}(f) &= \frac{(Z_{kk} - (Z_{lk}^2/Z_{ll}))|H_{lk}|^2}{|S_{ll}(f)|}, \\ I_{l \rightarrow k}(f) &= \frac{(Z_{ll} - (Z_{kl}^2/Z_{kk}))|H_{kl}|^2}{|S_{kk}(f)|}, \end{aligned} \quad (2.12)$$

where  $S_{kk}(f)$  and  $S_{ll}(f)$  represent the individual power spectra of sites  $k$  and  $l$ , respectively, and the expressions for  $H_{lk}$  can be found in (2.6).  $Z_{kk}$ ,  $Z_{ll}$ ,  $Z_{lk}$ , and  $Z_{kl}$  are elements of the covariance matrix  $Z$  for the noise vector of the bivariate model. Geweke's Granger causality at frequency  $f$  is expressed as the fraction of the total power at the frequency at one site that can be explained by the causal influence from the other. As seen in (2.12) and (15), Geweke's Granger causality can be evaluated solely using the bivariate model. Recently, Bressler and Seth [42] introduced Wiener-Granger causality and discussed its merits and limitations in various neuroscience applications [42].

The direct directed transfer function (dDTF) was proposed by Korzeniewska [43] for the analysis of direct information transfer among brain structures using local field potentials. To calculate the dDTF, partial coherence  $\chi_{ij}$  and full-band frequency DTF (ffDTF)  $\eta_{ij}$  were independently defined as

$$\begin{aligned}\chi_{ij}^2(f) &= \frac{M_{ij}^2(f)}{M_{jj}(f)M_{ii}(f)}, \\ \eta_{ij}^2(f) &= \frac{|H_{ij}(f)|^2}{\sum_f \sum_{m=1}^k |H_{im}(f)|^2},\end{aligned}\tag{2.13}$$

where  $M_{ij}$  represents the minor produced by removing the  $i$ th row and  $j$ th column of a spectral matrix  $S$ . In multivariate signals, partial coherences may provide more specific information regarding causal interactions among signals than ordinary coherences [44]. The value of dDTF is defined as the product of the above two variables and can be expressed as

$$\delta_{ij}(f) = \chi_{ij}^2(f)\eta_{ij}^2(f).\tag{2.14}$$

The dDTF method was proposed to circumvent some problems associated with DTF, specifically its inability to differentiate between the direct and indirect connections [43].

## 2.5. Examples of Practical Applications

To date, Granger causality has been extensively applied to the analysis of neural signals [45–58]. For examples, Hesse et al. used Granger causality to assess directed interdependencies between neural signal generators related to the Stroop task [45]. Seth also demonstrated that Granger causality may represent a useful tool for determining how interregional directional coupling is modulated by behavior [46]. Moreover, Sato et al. proposed a wavelet-based Granger causality, which they applied to fMRI signals [47]. Tang et al. applied both a blind source separation algorithm and Granger causality to the analysis of a high-density scalp EEG dataset and assessed the top-down and bottom-up influences [48]. Gow et al. demonstrated the potential value of combining Granger causality analyses with multimodal imaging to explore the functional architecture of cognition [49].

The DTF algorithm has also been extensively applied to various aspects within neuroscience, particularly to the analyses of electrophysiological signals such as EEG, MEG, and iEEG, because frequency-domain analysis is generally required in these modalities. Franaszczuk et al. first applied the DTF algorithm to the localization of ictal onset zones in temporal lobe epilepsy patients [59, 60]. Astolfi et al. demonstrated that the DTF algorithm could be used to assess the time-varying functional connectivity patterns from noninvasive EEG recordings in human [61]. Babiloni et al. investigated cortical causal interactions from combined high-resolution EEG and fMRI data and showed that DTF was able to unveil the direction of the information flow between the cortical regions of interest [62]. Kuś et al. attempted to characterize EEG activity propagation patterns in beta and gamma bands during finger movements, demonstrating that short-time DTF can successfully identify frequency selective information from EEGs [63]. Ding et al. and Wilke et al. also applied the DTF algorithm to EEG and iEEG signals acquired from intractable partial epilepsy patients

in order to better describe the structure of seizures in terms of space, time, and frequency [64, 65]. Kim et al. applied a source localization technique called FINEs in addition to DTF to iEEG signals and verified that directional connectivity analysis could be a useful tool to identify epileptogenic sources located outside of the iEEG electrodes [66].

As with DTF, PDC analyses have recently been applied to a variety of practical applications: Sun et al. demonstrated that PDC is a useful tool for evaluating changes in cortical interdependences in the context of different psychotic or mental states and can also be used to diagnose affective disorders [21]. Similarly, Zhang et al. used PDC to estimate cortical interactive networks during the mental rotation of Chinese characters, demonstrating different changes in cortical networks according to task difficulty [18]. Furthermore, Zhu et al. studied the effects of brain development and aging on cortical interactive network pattern, demonstrating that the PDC analysis of EEG is a powerful approach for characterizing brain development and aging [24].

### 3. Non-MVAR-Based Causality Estimators

#### 3.1. Transfer Entropy

Information theoretic measures have widely been utilized to quantify mutual dependence between time series. Although standard time-delayed mutual information can estimate mutual dependence between neural signals, it is not able to distinguish information flow [12]. To circumvent this issue, Schreiber developed a new causality estimator named transfer entropy (TE), on the basis of the entropy rate,

$$h_x = \langle -\log[P(x_{n+1} | x_n)] \rangle, \quad (3.1)$$

where  $\langle \cdot \rangle$  denotes an expectation value,  $P(x)$  represent the probability of  $x$ ,  $P(x_{n+1} | x_n)$  is the conditional probability of  $x_{n+1}$  given  $x_n$ , and  $n$  is the time sample position. To estimate the information flow, the conditional entropy rate of  $x_{n+1}$  given both  $y_n$  and  $x_n$

$$h_{x|y} = \langle -\log[P(x_{n+1} | x_n, y_n)] \rangle \quad (3.2)$$

has to be introduced. This indicated the average uncertainty about the future state ( $= x_{n+1}$ ) of  $x_{(t)}$ , conditional on the current state ( $= y_n$ ) of  $y_{(t)}$  as well as on its own current state ( $= x_n$ ). The transfer entropy can be defined as the difference between  $h_x$  and  $h_{x|y}$  [67], in the following form:

$$T_{y \rightarrow x} = \sum P(x_{n+1}, x_n, y_n) \log \frac{P(x_{n+1} | x_n, y_n)}{P(x_{n+1} | x_n)}, \quad (3.3)$$

where  $P(x_{n+1}, x_n, y_n)$  is the joint probability, evaluated by the sum of all available realizations of  $(x_{n+1}, x_n, y_n)$  in time series.

Many researchers now apply the TE algorithm to the field of neuroscience [67–71], as TE has been demonstrated to be more sensitive to nonlinear signal properties than the conventional MVAR-based causality estimators [69]. However, TE analyses are restricted to bivariate situations and require substantially more data samples than MVAR-based causality estimators.



### 3.2. Phase Slope Index

To robustly estimate the direction of information flow in multivariate time series, Nolte proposed a new causality estimator called phase slope index (PSI) [13], basic assumption of which states that mixing does not affect the imaginary part of the complex coherency of a multivariate times series [72]. Measured data  $Y_t$  are assumed to be a superposition of two sources  $X_t$  and additive noise  $E_t$

$$Y_t = X_t + BE_t, \quad (3.4)$$

where  $B$  represents a mixing matrix that merges the additive noise into the measurement channels. The measured data are then divided into  $K$  segments and used to calculate the cross-spectral density as follows:

$$S_{ij}(f) = \frac{1}{K} \sum_k z_i(f, k) z_j^*(f, k), \quad (3.5)$$

where  $z_i(f, k)$  represents the Fourier transform of the  $i$ th channel data and  $k$ th segment and  $S_{ij}$  is the cross-spectral matrix between  $i$ th and  $j$ th time series. PSI is defined as

$$\tilde{\Psi}_{ij} = \Im \left( \sum_{f \in F} C_{ij}^*(f) C_{ij}(f + \delta f) \right), \quad (3.6)$$

where

$$C_{ij}(f) = \frac{S_{ij}(f)}{\sqrt{S_{ii}(f) S_{jj}(f)}} \quad (3.7)$$

is the complex coherency,  $\delta f$  is the specific frequency resolution,  $F$  is the frequency band of interest, and  $\Im(\cdot)$  denotes the imaginary part. Finally, the PSI is normalized using its standard deviation and is expressed as

$$\Psi = \frac{\tilde{\Psi}}{\text{std}(\tilde{\Psi})}, \quad (3.8)$$

Nolte et al. presented several computer simulations, via which the relative performances of Granger causality and PSI were compared. In these simulations, PSI was found to perform better than Granger causality in inferring causal relationship between signals with nonlinear interactions. As the PSI is a nonparametric approach, it has several key advantages over conventional parametric approaches represented by the MVAR models. For instance, the PSI not only requires a lower computational load than the MVAR-based approaches, but it is also independent from the signal's stationarity. However, the PSI has a limitation in that it is also a pairwise metric of directional interactions and is thereby vulnerable to the ambiguity between direct and indirect influences [25].

### 3.3. Nonlinear Granger Causality

To estimate causal interactions between the nonlinear bivariate neural signals, nonlinear Granger causality (NGC) was developed [73, 74]. The basic concept of NGC is similar to TE in that NGC concludes that  $y_{(t)}$  does not cause  $x_{(t)}$  if the value of  $h_x$  in (3.1) is comparable to  $h_{x|y}$  in (3.2). Gourévitch [37] defined the nonlinear Granger causality as follows:

$$\text{NGC}_{x \leftarrow y} = \frac{C^2(x_{n+1}, x_n, y_n)}{C^2(x_n, y_n)} - \frac{C^2(x_{n+1}, x_n)}{C^2(x_n)}, \quad (3.9)$$

where  $C^2$  is the correlation integral of order 2. This correlation integral was proposed by Grassberger [75]. For any given vectorial signal dimension  $L$  and length of signal  $T$ , the correlation integral of order  $q$  is defined as

$$C^q(X) = \left( \frac{1}{T-L} \sum_{t=L+1}^T \left( \frac{1}{(T-L-1)} \sum_{s=L+1, s \neq t}^T 1_{\{\|X(t)-X(s)\| < r\}} \right)^{q-1} \right)^{1/(q-1)}, \quad (3.10)$$

where  $\|\cdot\|$  represents the maximum norm,  $1_A$  is 1 in a set  $A$ , 0 otherwise, and  $r$  is a positive scalar. The bivariate version for two signals  $X$  and  $Y$  of the same dimension  $L$  and the same length  $T$  is expressed as

$$C^2(X, Y) = \frac{1}{(T-L)(T-L-1)} \sum_{t=L+1}^T \sum_{s=L+1, s \neq t}^T 1_{\{\|X(t)-X(s)\| < r\}} 1_{\{\|Y(t)-Y(s)\| < r\}}. \quad (3.11)$$

### 3.4. Partial Nonlinear Granger Causality

Recently, Gourévitch et al. proposed a new method for estimating nonlinear causal interactions [37], termed partial nonlinear Granger causality (PNGC). The PNGC algorithm is able to estimate direct causality from  $X_m$  to  $X_n$  when  $Q$  signals are considered. PNGC is defined as

$$\text{PNGC}_{x_n \leftarrow x_m} = \frac{C^2(X_n^f, X_1^p, \dots, X_Q^p)}{C^2(X_1^p, \dots, X_Q^p)} - \frac{C^2(X_n^f, X_1^p, \dots, X_{m-1}^p, X_{m+1}^p, X_Q^p)}{C^2(X_1^p, \dots, X_{m-1}^p, X_{m+1}^p, X_Q^p)}, \quad (3.12)$$

Although PNGC showed promising results when applied to complex systems, it is still dependent on model order and scale [37]. Consequently, if nonlinearity is suspected, PNGC should be used only as a complementary tool.

## 4. Mathematical Issues in Causality Inference

### 4.1. Issues in MVAR-Based Causality Inference

The most popular causality estimators—GC [8], DTF [9], and PDC [11]—as well as their modifications are based on MVAR modeling of neural signals. The MVAR modeling is highly

dependent on the selection of model orders: too low order may not provide an exact expression of the signal feature, while too high model order may result in overfitting. Thus, the correct choice of an MVAR model orders is critically important for precise causality inference. Although several methods have been proposed to estimate proper model orders (like AIC [26], BIC [27], deviance information criterion (DIC) [33], minimum description length (MDL) [30], focused information criterion (FIC) [34], minimum message length (MML) [28], and others [29, 31, 33]) and some investigators have attempted to compare performances of different model order determination criteria [35, 76], no golden rule exists for the model order selection, and further research is clearly needed.

Moreover, MAVR-based causality estimators guarantee accurate causality inference only when datasets (signals) satisfy stationary conditions [9, 77], whereby their multivariate probability distribution is not affected by timeshift. At the very least, the mean, variance, and autocorrelation of multivariate time series should not vary over time. Unfortunately, these conditions cannot be satisfied in most cases, and thus, some mathematical transformations are often required to make the time series become roughly stationary. Nolte et al. demonstrated that MVAR-based approaches typically fail to estimate causal interactions between neuronal signals that are not stationary [13]. Although several stationary tests (e.g., unit root test [78] and Sargan and Bhargava test [79]) have been introduced to assess whether or not a time series is stationary, most were not verified in practical neural signals. In neuroscience applications, issues of stationarity also have to be carefully dealt with by considering an empirical appraisal of the participants' behavioral states [11].

Another critical limitation affecting the reliability of causality estimators is the linear modeling of neural signals [80]. Neural time-series signals can take several forms; for example, spikes, noisy signal, and highly correlated signals, may have a nonlinear form [37]. Accordingly, it is imperative to develop techniques for causality analysis that accommodate nonlinear time series, as most current studies on the causal network inference do not verify signal linearity, nor do they account for nonlinearity. Specifically, many MVAR-based models (such as PDC) are not robust to simple nonlinear linkage [37].

Generally, MVAR-based causality estimators require the appropriate selection of signal sample number. In one study, Schlögl assessed the dependency of several MVAR algorithms on the number of time samples, demonstrating that sufficient numbers of samples are required to obtain a reliable estimate of causal interactions among neural signals [81]. Moreover, Schlögl also showed causality inference to be highly dependent on both MVAR estimation methods as well as model order in cases with the same number of time samples. As the number of time samples is generally limited in most practical examples, a more systematic approach to reliably determine the number of time samples and appropriate MVAR estimators should be developed in future studies.

#### ***4.2. Issues in Non-MVAR-Based Causality Inference***

While most non-MVAR-based causality estimators, such as PNGC, nonlinear Granger causality, TE, and PSI, were introduced to circumvent the well-described problems of MVAR-based causality estimators, many can only be applied to causality inferences of bivariate neural signals. As such, further research is required to extend bivariate causality inferences to include multivariate (more than three) causality inference. Furthermore, a method for determining the proper model order in PNGC remains an ongoing problem [37], as with MVAR-based estimators.

## 5. Conclusion

Here, we summarized the mathematical techniques used in causality estimation, all of which have been extensively applied to infer causal relationships among multichannel neural signals. We also described the limitations of current methods and presented several ongoing problems, some of which may be of interest to applied mathematicians. We hope that this paper will serve as a useful guide for researchers in the field of applied mathematics and helps raise awareness of this important research topic.

## Author Contribution

Y.-J. Jung and K.-H. Kim are co-first authors and contributed equally to this work.

## Acknowledgments

This work was supported by the Original Technology Research Program for Brain Science through the National Research Foundation of Korea (NRF) Grant funded by the Ministry of Education, Science, and Technology (no. 2010-0018840).

## References

- [1] A. Aarabi, F. Wallois, and R. Grebe, "Does spatiotemporal synchronization of EEG change prior to absence seizures?" *Brain Research*, vol. 1188, no. 1, pp. 207–221, 2008.
- [2] G. Thut, D. Veniero, V. Romei, C. Miniussi, P. Schyns, and J. Gross, "Rhythmic TMS causes local entrainment of natural oscillatory signatures," *Current Biology*, vol. 21, no. 14, pp. 1176–1185, 2011.
- [3] G. Varotto, E. Visani, S. Franceschetti, G. Sparacino, and F. Panzica, "Spectral and coherence analysis of EEG during intermittent photic stimulation in patients with photosensitive epilepsy," *International Journal of Bioelectromagnetism*, vol. 11, no. 4, pp. 189–193, 2009.
- [4] J. P. Lachaux, E. Rodriguez, J. Martinerie, and F. J. Varela, "Measuring phase synchrony in brain signals," *Human Brain Mapping*, vol. 8, no. 4, pp. 194–208, 1999.
- [5] F. Mormann, K. Lehnertz, P. David, and C. E. Elger, "Mean phase coherence as a measure for phase synchronization and its application to the EEG of epilepsy patients," *Physica D: Nonlinear Phenomena*, vol. 144, no. 3, pp. 358–369, 2000.
- [6] S. Baillet, L. Garnero, G. Marin, and J. P. Hugonin, "Combined MEG and EEG source imaging by minimization of mutual information," *IEEE Transactions on Biomedical Engineering*, vol. 46, no. 5, pp. 522–534, 1999.
- [7] J. Jeong, J. C. Gore, and B. S. Peterson, "Mutual information analysis of the EEG in patients with Alzheimer's disease," *Clinical Neurophysiology*, vol. 112, no. 5, pp. 827–835, 2001.
- [8] C. W. J. Granger, "Investigating causal relations by econometric models and cross-spectral methods," *Econometrica*, vol. 37, no. 3, pp. 424–438, 1969.
- [9] M. J. Kaminski and K. J. Blinowska, "A new method of the description of the information flow in the brain structures," *Biological Cybernetics*, vol. 65, no. 3, pp. 203–210, 1991.
- [10] K. Sameshima and L. A. Baccalá, "Using partial directed coherence to describe neuronal ensemble interactions," *Journal of Neuroscience Methods*, vol. 94, no. 1, pp. 93–103, 1999.
- [11] L. A. Baccalá and K. Sameshima, "Partial directed coherence: a new concept in neural structure determination," *Biological Cybernetics*, vol. 84, no. 6, pp. 463–474, 2001.
- [12] T. Schreiber, "Measuring information transfer," *Physical Review Letters*, vol. 85, no. 2, pp. 461–464, 2000.
- [13] G. Nolte, A. Ziehe, V. V. Nikulin et al., "Robustly estimating the flow direction of information in complex physical systems," *Physical Review Letters*, vol. 100, no. 23, Article ID 234101, 2008.
- [14] J. Dauwels, K. Srinivasan, M. Ramasubba Reddy et al., "Slowing and loss of complexity in Alzheimer's EEG: two sides of the same coin?" *International Journal of Alzheimer's Disease*, pp. 1–10, 2011.

- [15] M. Grosse-Wentrup, B. Schölkopf, and J. Hill, "Causal influence of gamma oscillations on the sensorimotor rhythm," *NeuroImage*, vol. 56, no. 2, pp. 837–842, 2011.
- [16] K. Blinowska, R. Kus, M. Kaminski, and J. Janiszewska, "Transmission of brain activity during cognitive task," *Brain Topography*, vol. 23, no. 2, pp. 205–213, 2010.
- [17] A. Korzeniewska, C. M. Crainiceanu, R. Kuś, P. J. Franaszczuk, and N. E. Crone, "Dynamics of event-related causality in brain electrical activity," *Human Brain Mapping*, vol. 29, no. 10, pp. 1170–1192, 2008.
- [18] H. Zhang, Y. Sun, J. Yan et al., "Cortical interactive network during mental rotation of Chinese character," *Neuroscience Letters*, vol. 461, no. 2, pp. 185–189, 2009.
- [19] A. Korzeniewska, P. J. Franaszczuk, C. M. Crainiceanu, R. Kuś, and N. E. Crone, "Dynamics of large-scale cortical interactions at high gamma frequencies during word production: event related causality (ERC) analysis of human electrocorticography (ECoG)," *NeuroImage*, vol. 56, no. 4, pp. 2218–2237, 2011.
- [20] E. Başar, "The theory of the whole-brain-work," *International Journal of Psychophysiology*, vol. 60, no. 2, pp. 133–138, 2006.
- [21] Y. Sun, Y. Li, Y. Zhu, X. Chen, and S. Tong, "Electroencephalographic differences between depressed and control subjects: an aspect of interdependence analysis," *Brain Research Bulletin*, vol. 76, no. 6, pp. 559–564, 2008.
- [22] D. W. Gow and J. A. Segawa, "Articulatory mediation of speech perception: a causal analysis of multi-modal imaging data," *Cognition*, vol. 110, no. 2, pp. 222–236, 2009.
- [23] A. Sinai and A. Korzeniewska, "Event-related dynamics of brain oscillations," *Brain*, vol. 159, no. 6, pp. 275–295, 2006.
- [24] C. Zhu, X. Guo, Z. Jin et al., "Influences of brain development and ageing on cortical interactive networks," *Clinical Neurophysiology*, vol. 122, no. 2, pp. 278–283, 2011.
- [25] P. Rana, *Seizure Detection and Analysis Using Phase-Slope Index*, University Of Wisconsin, 2011.
- [26] H. Akaike, "A new look at the statistical model identification," *IEEE Transactions on Automatic Control*, vol. 19, pp. 716–723, 1974.
- [27] G. Schwarz, "Estimating the dimension of a model," *The Annals of Statistics*, vol. 6, no. 2, pp. 461–464, 1978.
- [28] C. S. Wallace and D. M. Boulton, "An information measure for classification," *The Computer Journal*, vol. 11, no. 2, pp. 185–194, 1968.
- [29] A. S. Holevo, "Bounds for the quantity of information transmitted by a quantum communication channel," *Problemy Peredachi Informatsii*, vol. 9, no. 3, pp. 3–11, 1973.
- [30] J. Rissanen, "Modeling by shortest data description," *Automatica*, vol. 14, no. 5, pp. 465–471, 1978.
- [31] E. J. Hannan and B. G. Quinn, "The determination of the order of an autoregression," *Journal of the Royal Statistical Society*, vol. 41, no. 2, pp. 190–195, 1979.
- [32] E. I. George, "The variable selection problem," *Journal of the American Statistical Association*, vol. 95, no. 452, pp. 1304–1308, 2000.
- [33] D. J. Spiegelhalter, N. G. Best, B. P. Carlin, and A. van der Linde, "Bayesian measures of model complexity and fit," *Journal of the Royal Statistical Society*, vol. 64, no. 4, pp. 583–639, 2002.
- [34] G. Claeskens and N. L. Hjort, "The focused information criterion," *Journal of the American Statistical Association*, vol. 98, no. 464, pp. 900–916, 2003.
- [35] O. I. Shittu and M. J. Asemota, "Comparison of criteria for estimating the order of autoregressive process: a Monte Carlo approach," *European Journal of Scientific Research*, vol. 30, no. 3, pp. 409–416, 2009.
- [36] M. Eichler, "On the evaluation of information flow in multivariate systems by the directed transfer function," *Biological Cybernetics*, vol. 94, no. 6, pp. 469–482, 2006.
- [37] B. Gourévitch, R. L. Bouquin-Jeannès, and G. Faucon, "Linear and nonlinear causality between signals: methods, examples and neurophysiological applications," *Biological Cybernetics*, vol. 95, no. 4, pp. 349–369, 2006.
- [38] L. A. Baccalá, K. Sameshima, and D. Y. Takahashi, "Generalized partial directed coherence," in *Proceedings of the 15th International Conference on Digital Signal Processing (DSP '07)*, no. 1–4, pp. 163–166, July 2007.
- [39] L. Faes and G. Nollo, "Extended causal modeling to assess partial directed coherence in multiple time series with significant instantaneous interactions," *Biological Cybernetics*, vol. 103, no. 5, pp. 387–400, 2010.
- [40] J. F. Geweke, "Measures of conditional linear dependence and feedback between time series," *Journal of the American Statistical Association*, vol. 79, no. 388, pp. 907–915, 1984.

- [41] S. Bressler, C. Richter, and Y. Chen, "Cortical functional network organization from autoregressive modeling of local field potential oscillations," *Statistics in Medicine*, vol. 26, no. 21, pp. 3875–3885, 2007.
- [42] S. L. Bressler and A. K. Seth, "Wiener-granger causality: a well established methodology," *NeuroImage*, vol. 58, no. 2, pp. 323–329, 2011.
- [43] A. Korzeniewska, M. Mańczakb, M. Kamiński, K. J. Blinowska, and S. Kasicki, "Determination of information flow direction among brain structures by a modified directed transfer function (dDTF) method," *Journal of Neuroscience Methods*, vol. 125, no. 1-2, pp. 195–207, 2003.
- [44] P. J. Franaszczuk, K. J. Blinowska, and M. Kowalczyk, "Biological cybernetics in the study of electrical brain activity," *Biological Cybernetics*, vol. 247, pp. 239–247, 1985.
- [45] W. Hesse, E. Möller, M. Arnold, and B. Schack, "The use of time-variant EEG Granger causality for inspecting directed interdependencies of neural assemblies," *Journal of Neuroscience Methods*, vol. 124, no. 1, pp. 27–44, 2003.
- [46] A. K. Seth, "Causal connectivity of evolved neural networks during behavior," *Computation in Neural Systems*, vol. 16, no. 1, pp. 35–54, 2005.
- [47] J. R. Sato, E. A. Junior, D. Y. Takahashi, M. de Maria Felix, M. J. Brammer, and P. A. Morettin, "A method to produce evolving functional connectivity maps during the course of an fMRI experiment using wavelet-based time-varying Granger causality," *NeuroImage*, vol. 31, no. 1, pp. 187–196, 2006.
- [48] A. Tang, M. T. Sutherland, P. Sun et al., "Top-down versus bottom-up processing in the human brain: distinct directional influences revealed by integrating SOBI and granger causality," *Independent Component Analysis and Signal Separation*, vol. 4666, pp. 802–809, 2007.
- [49] D. W. Gow, J. A. Segawa, S. P. Ahlfors, and F.-H. Lin, "Lexical influences on speech perception: a Granger causality analysis of MEG and EEG source estimates," *NeuroImage*, vol. 43, no. 3, pp. 614–623, 2008.
- [50] M. X. Cohen et al., "Top-down-directed synchrony from medial frontal cortex to nucleus accumbens during reward anticipation," *Human Brain Mapping*, vol. 33, no. 1, pp. 246–252, 2012.
- [51] J. Szaflarski, M. DiFrancesco, T. Hirschauer et al., "Cortical and subcortical contributions to absence seizure onset examined with EEG/fMRI," *Epilepsy and Behavior*, vol. 18, no. 4, pp. 404–413, 2010.
- [52] A. Özkaya and M. Korürek, "Estimating short-run and long-run interaction mechanisms in interictal state," *Journal of Computational Neuroscience*, vol. 28, no. 2, pp. 177–192, 2010.
- [53] C. Ligges, M. Ungureanu, M. Ligges, and B. Blanz, "Understanding the time variant connectivity of the language network in developmental dyslexia: new insights using Granger causality," *Journal of Neural Transmission*, vol. 117, no. 4, pp. 529–543, 2010.
- [54] L. Pollonini, S. Pophale, N. Situ et al., "Information communication networks in severe traumatic brain injury," *Brain Topography*, vol. 23, no. 2, pp. 221–226, 2010.
- [55] E. Sitnikova, "Thalamo-cortical mechanisms of sleep spindles and spike-wave discharges in rat model of absence epilepsy (a review)," *Epilepsy Research*, vol. 89, no. 1, pp. 17–26, 2010.
- [56] K. L. Anderson, R. Rajagovindan, G. A. Ghacibeh, K. J. Meador, and M. Ding, "Theta oscillations mediate interaction between prefrontal cortex and medial temporal lobe in human memory," *Cerebral Cortex*, vol. 20, no. 7, pp. 1604–1612, 2010.
- [57] L. Astolfi, J. Toppi, F. De Vico Fallani et al., "Neuroelectrical hyperscanning measures simultaneous brain activity in humans," *Brain Topography*, vol. 23, no. 3, pp. 243–256, 2010.
- [58] D. W. Gow, C. J. Keller, E. Eskandar, N. Meng, and S. S. Cash, "Parallel versus serial processing dependencies in the perisylvian speech network: a Granger analysis of intracranial EEG data," *Brain and Language*, vol. 110, no. 1, pp. 43–48, 2009.
- [59] P. J. Franaszczuk, G. K. Bergey, and M. J. Kaminski, "Analysis of mesial temporal seizure onset and propagation using the directed transfer function method," *Electroencephalography and Clinical Neurophysiology*, vol. 91, no. 6, pp. 413–427, 1994.
- [60] P. J. Franaszczuk and G. K. Bergey, "Application of the directed transfer function method to mesial and lateral onset temporal lobe seizures," *Brain Topography*, vol. 11, no. 1, pp. 13–21, 1998.
- [61] L. Astolfi, F. Cincotti, D. Mattia et al., "Assessing cortical functional connectivity by linear inverse estimation and directed transfer function: simulations and application to real data," *Clinical Neurophysiology*, vol. 116, no. 4, pp. 920–932, 2005.
- [62] F. Babiloni, F. Cincotti, C. Babiloni et al., "Estimation of the cortical functional connectivity with the multimodal integration of high-resolution EEG and fMRI data by directed transfer function," *NeuroImage*, vol. 24, no. 1, pp. 118–131, 2005.
- [63] R. Kuś, J. S. Ginter, and K. J. Blinowska, "Propagation of EEG activity during finger movement and its imagination," *Acta Neurobiologiae Experimentalis*, vol. 66, no. 3, pp. 195–206, 2006.



- [64] L. Ding, G. A. Worrell, T. D. Lagerlund, and B. He, "Ictal source analysis: localization and imaging of causal interactions in humans," *NeuroImage*, vol. 34, no. 2, pp. 575–586, 2007.
- [65] C. Wilke, W. van Drongelen, M. Kohrman, and B. He, "Neocortical seizure foci localization by means of a directed transfer function method," *Epilepsia*, vol. 51, no. 4, pp. 564–572, 2010.
- [66] J. S. Kim, C. H. Im, Y. J. Jung, E. Y. Kim, S. K. Lee, and C. K. Chung, "Localization and propagation analysis of ictal source rhythm by electrocorticography," *NeuroImage*, vol. 52, no. 4, pp. 1279–1288, 2010.
- [67] C. J. Honey and O. Sporns, "Dynamical consequences of lesions in cortical networks," *Human Brain Mapping*, vol. 29, no. 7, pp. 802–809, 2008.
- [68] C. J. Honey, R. Kötter, M. Breakspear, and O. Sporns, "Network structure of cerebral cortex shapes functional connectivity on multiple time scales," *Proceedings of the National Academy of Sciences of the United States of America*, vol. 104, no. 24, pp. 10240–10245, 2007.
- [69] M. Lungarella and O. Sporns, "Mapping information flow in sensorimotor networks," *PLoS Computational Biology*, vol. 2, no. 10, pp. 1301–1312, 2006.
- [70] L. Barnett and A. Barrett, "Granger causality and transfer entropy Are equivalent for gaussian variables," *Physical Review Letters*, vol. 103, no. 23, pp. 1–10, 2009.
- [71] G. Boris and J. Eggermont, "Evaluating information transfer between auditory cortical neurons," *Journal of Neurophysiology*, vol. 97, no. 3, pp. 2533–2543, 2007.
- [72] G. Nolte, O. Bai, L. Wheaton, Z. Mari, S. Vorbach, and M. Hallett, "Identifying true brain interaction from EEG data using the imaginary part of coherency," *Clinical Neurophysiology*, vol. 115, no. 10, pp. 2292–2307, 2004.
- [73] E. Baek and W. A. Brock, "A nonparametric test for independence of a multivariate time series," *Statistica Sinica*, vol. 2, no. 1, pp. 137–156, 1992.
- [74] C. Hiemstra and J. D. Jones, "Testing for linear and nonlinear granger causality in the stock price-volume relation," *Journal of Finance*, vol. 49, no. 5, pp. 1639–1664, 1994.
- [75] P. Grassberger, "Estimation of the Kolmogorov entropy from a chaotic signal," *Physical Review A: General Physics*, vol. 28, no. 4, pp. 2591–2593, 1983.
- [76] C. Porcaro, F. Zappasodi, P. M. Rossini, and F. Tecchio, "Choice of multivariate autoregressive model order affecting real network functional connectivity estimate," *Clinical Neurophysiology*, vol. 120, no. 2, pp. 436–448, 2009.
- [77] J. D. Hamilton, *Time Series Analysis*, vol. 48, no. 1, Princeton University Press, Princeton, NJ, USA, 1994.
- [78] D. A. Dickey and W. A. Fuller, "Distribution of the estimators for autoregressive time series with a unit root," *Journal of the American Statistical Association*, vol. 74, no. 366, pp. 427–431, 1979.
- [79] J. D. Sargan and A. Bhargava, "Testing residuals from least squares regression for being generated by the Gaussian random walk," *Econometrica: Journal of the Econometric Society*, vol. 51, no. 1, pp. 153–174, 1983.
- [80] D. Marinazzo, W. Liao, H. Chen, and S. Stramaglia, "Nonlinear connectivity by Granger causality," *NeuroImage*, vol. 58, no. 2, pp. 330–338, 2011.
- [81] A. Schlögl, "A comparison of multivariate autoregressive estimators," *Signal Processing*, vol. 86, no. 9, pp. 2426–2429, 2006.

## Research Article

# Scanning Reduction Strategy in MEG/EEG Beamformer Source Imaging

**Jun Hee Hong and Sung Chan Jun**

*School of Information and Communications, Gwangju Institute of Science and Technology,  
Gwangju 500-712, Republic of Korea*

Correspondence should be addressed to Sung Chan Jun, [scjun@gist.ac.kr](mailto:scjun@gist.ac.kr)

Received 20 August 2011; Accepted 18 September 2011

Academic Editor: Venky Krishnan

Copyright © 2012 J. H. Hong and S. C. Jun. This is an open access article distributed under the Creative Commons Attribution License, which permits unrestricted use, distribution, and reproduction in any medium, provided the original work is properly cited.

MEG/EEG beamformer source imaging is a promising approach which can easily address spatiotemporal multi-dipole problems without a priori information on the number of sources and is robust to noise. Despite such promise, beamformer generally has weakness which is degrading localization performance for correlated sources and is requiring of dense scanning for covering all possible interesting (entire) source areas. Wide source space scanning yields all interesting area images, and it results in lengthy computation time. Therefore, an efficient source space scanning strategy would be beneficial in achieving accelerated beamformer source imaging. We propose a new strategy in computing beamformer to reduce scanning points and still maintain effective accuracy (good spatial resolution). This new strategy uses the distribution of correlation values between measurements and lead-field vectors. Scanning source points are chosen yielding higher RMS correlations than the predetermined correlation thresholds. We discuss how correlation thresholds depend on SNR and verify the feasibility and efficacy of our proposed strategy to improve the beamformer through numerical and empirical experiments. Our proposed strategy could in time accelerate the conventional beamformer up to over 40% without sacrificing spatial accuracy.

## 1. Introduction

Magnetoencephalography (MEG) and electroencephalography (EEG) are noninvasive imaging technologies which provide functional information about human brain dynamics by providing millisecond temporal images over the entire brain. These technologies have been widely used to diagnose epilepsy and forward neuroscience research. Particularly, MEG/EEG source localization estimates current sources from measured spatiotemporal data. Inherently, MEG/EEG source localization is mathematically ill-posed; that is, it has no unique solution and is very sensitive to noise. For a couple of decades, many researchers have tried to develop methods to deal with these difficulties in calculation, resulting in extensive



research and commercialization of MEG/EEG source localization methods (see [1, 2] for a review).

In the early 1990s, beamformer techniques originated in the field of antenna signal processing [3]. Application in MEG/EEG source imaging soon followed. A beamformer represents a kind of linear spatial filter acting on spatial or spatiotemporal data within sensor space. It allows a neural signal produced only at designated source point to pass, filtering out signals originating from other source points. Therefore, even without a priori information on source quantity, beamformers can effectively image brain activities within a source space under the assumption that sources are uncorrelated [4–6]. Many varieties of beamformers have been investigated [7–10] and are roughly categorized into 2 classes: adaptive beamformers using measurement information, and nonadaptive beamformers independent of measurement information [11]. Among the variety of options, the minimum-variance (MV) beamformer has been most widely used and deeply investigated in regard to MEG/EEG source localization problems [5, 12–17].

Recently, source imaging has been gaining more attention on continuous MEG/EEG (unaveraged) and single-trial MEG/EEG data in understanding rapidly changing brain dynamics [18, 19]. This understanding can better facilitate real-time brain activity monitoring, neurofeedback, brain computer interface (BCI) [20–22], among others [23, 24]. Brain signals can usually be measured by means of MEG or EEG systems and their real-time interpretation can provide a variety of applications. Beamformer is a promising technique easily dealing with spatiotemporal multi-dipole source problems as well as being robust to noise. Regarding real-time source imaging, beamformer speed generally depends on the quantity of scanned source points, that is, the number of scanning points of interesting brain area. For this purpose, reducing beamformer scanning points (accelerating beamformer) without sacrifice of spatial resolution (accuracy) is greatly beneficial in real-time source imaging. In the present work, a procedure is proposed to accelerate beamformer as well as to maintain effective spatial resolution. Sensor measurements are composed of a (composite) linear combination of lead-field vectors (sensitivity of sensors to sources) at active points as well as noise [15]. For that reason, sensor measurements may produce relatively higher correlation values than correlation around inactive points. In the present paper, such reasoning is further investigated culminating in a proposal for reducing scanning points during beamformer source imaging.

This paper is an extended version of a short conference paper presented in BIOMAG 2010 [25] and is organized in sections. In Section 2, a conventional MV-beamformer is briefly explained. In Section 3 we follow with a theoretical proposal for reducing scanning regions and then discuss an effective strategy for computing the correlation distribution between measurement data and lead-field vectors. Next, both simulated and empirical experimental results are presented to verify the feasibility and efficacy of the proposed procedure. Lastly, we discuss other efforts in achieving accelerated beamformer.

## 2. Minimum-Variance (MV) Beamformer

Beamformer techniques are categorized into two classes: one is adaptive and the other is nonadaptive. A nonadaptive spatial filter is independent of the measurement, but an adaptive spatial filter depends on the measurement. Among beamformers, the minimum-variance (MV) beamformer is superior in accuracy to others [11] and has been widely used in MEG/EEG source imaging [10]. MV beamformers can be scalar type and vector

type. In the scalar type beamformers, the source orientation could be estimated to yield maximum source power (for details, see [10, 15]) or may be predetermined accordingly. On the contrary, the source orientation could be simultaneously estimated in the vector type beamformer (uses a set of three weights and each weight detects one component in Cartesian coordinate system) [4, 5, 26, 27]. Throughout this paper, MV vector type beamformer is used.

A vector type beamformer enables to estimate simultaneously source orientation and magnitude. A vector type spatial filter consists of a set of three weight vectors,  $w_x(\mathbf{r})$ ,  $w_y(\mathbf{r})$ , and  $w_z(\mathbf{r})$  depending on  $x$ ,  $y$ , and  $z$  components of the source vector, respectively. Denoting the weight matrix by  $\mathbf{W}(\mathbf{r}) = [w_x(\mathbf{r}); w_y(\mathbf{r}); w_z(\mathbf{r})]$ , vector-type beamformer is derived solving the following optimization:

$$\mathbf{W}(\mathbf{r}) = \text{argmin } \mathbf{W}^T \mathbf{C} \mathbf{W}, \quad \text{subject to } \mathbf{W}^T(\mathbf{r}) \mathbf{L}(\mathbf{r}) = \mathbf{I}, \quad (2.1)$$

where  $\mathbf{C} = \langle m(t)m^T(t) \rangle_t$  is measurement covariance matrix estimated by time average,  $\mathbf{L}(\mathbf{r}) = [l_x(\mathbf{r}); l_y(\mathbf{r}); l_z(\mathbf{r})]$  is the lead-field matrix representing the sensitivity of the whole sensor array to source activity at  $\mathbf{r}$ , and  $\mathbf{I}$  represents an identity matrix.  $l_\xi(\mathbf{r})$  is a lead-field vector of unit source activity oriented to  $\xi$ -axis at  $\mathbf{r}$ . The weight matrix and output power of this vector type spatial filter are expressed as follows:

$$\begin{aligned} \mathbf{W}(\mathbf{r}) &= \mathbf{C}^{-1} \mathbf{L}(\mathbf{r}) \left[ \mathbf{L}^T(\mathbf{r}) \mathbf{C}^{-1} \mathbf{L}(\mathbf{r}) \right]^{-1}, \\ \langle \hat{Q}(\mathbf{r}, t)^2 \rangle_t &= \left[ \mathbf{L}^T(\mathbf{r}) \mathbf{C}^{-1} \mathbf{L}(\mathbf{r}) \right]^{-1}. \end{aligned} \quad (2.2)$$

### 3. Scanning Reduction Strategy

#### 3.1. Definitions and Principles

In this section, a new strategy of reducing scanning points, thereby accelerating beamformer source imaging, is proposed without sacrificing accuracy. In beamformer source imaging, full source space scanning is necessary; sources are located on the brain's cortical area and thus all scanning of the brain may be time intensive but achieves whole brain images. On the other hand, partial scanning accelerates beamformer source imaging. Evidently, reducing the number of scanning source points while keeping scanning resolution can accelerate the source imaging process without losing spatial resolution significantly. Our proposed idea is reducing the scanning region (eventually reduce the number of scanning points) by using the correlation between measurement and lead-field vectors, defined as

$$p(\mathbf{r}, t) = \frac{m(t) \cdot l(\mathbf{r})}{\|m(t)\| \|l(\mathbf{r})\|}. \quad (3.1)$$

Here  $m(t)$  and  $l(\mathbf{r})$  represent the measurement vector at time  $t$  and the lead-field vector at  $\mathbf{r}$ , respectively. The inner product between  $m(t)$  and  $l(\mathbf{r})$  vector yields scalar value. At each source point  $\mathbf{r}$ , the root mean square (RMS) correlation is computed as follows:

$$p_{\text{rms}}(\mathbf{r}) = \sqrt{\frac{1}{K} \sum_{t=1}^K p(\mathbf{r}, t)^2}, \quad (3.2)$$

where  $K$  is the number of time points. In general, sensor measurements consist of a linear combination of (composite) lead-field vectors [15] at active points and noise:

$$\begin{aligned} m(t) &= \mathbf{L}s(t) + n(t) \\ &= \sum_{i=1}^{N_s} l(\mathbf{r}_i) s_i(t) + n(t) \cong \sum_{i_a=1}^{n_a} l(\mathbf{r}_{i_a}) s_{i_a}(t) + n(t), \quad n_a \ll N_s. \end{aligned} \quad (3.3)$$

Here  $s(t) = [s_1(t), s_2(t), \dots, s_{N_s}(t)]^T$  is a source vector representing a signed source magnitude at each scanning point  $\mathbf{r}_i$  and time  $t$ .  $\mathbf{L} = [l(\mathbf{r}_1), l(\mathbf{r}_2), \dots, l(\mathbf{r}_{N_s})]$  is a matrix consisting of all lead-field vectors, and  $n(t)$  is noise at time  $t$ , being commonly colored and independent of signal. Assuming that measurement is produced by a few significantly strong source activations (such case is common in BCI or spontaneous activity, evoked response activity, etc.), sources at most scanning points are inactive, yielding a negligibly small magnitude of  $s_i(t)$ , and only a few sources ( $n_a$  sources) are active, the corresponding  $s_i(t)$  yields significant magnitudes. A correlation value between  $m(t)$  and lead-field  $l(\mathbf{r})$  at scanning point  $\mathbf{r}$  is expressed as

$$m(t) \cdot l(\mathbf{r}) = \sum_{i_a=1}^{n_a} s_{i_a}(t) l(\mathbf{r}_{i_a}) \cdot l(\mathbf{r}) + n(t) \cdot l(\mathbf{r}). \quad (3.4)$$

Independence from noise on a signal yields that the 2nd term on the right side of (3.4) is negligible and thus the correlation value is mainly affected by the 1st term. When a scanning point is around an active source point, that is,  $\mathbf{r}$  is very close or equal to  $\mathbf{r}_{i_a}$ , then  $l(\mathbf{r}_{i_a}) \cdot l(\mathbf{r})$  gives a significant value. However, when the scanning point is away from all active points,  $l(\mathbf{r}_{i_a})$  and  $l(\mathbf{r})$  may be much less correlated, and thus  $l(\mathbf{r}_{i_a}) \cdot l(\mathbf{r})$  may yield a considerably smaller value in magnitude. Due to such arguments, the correlation value  $p(\mathbf{r}, t)$  may be more significant at active points than others. Overall, RMS correlation values at active points are likely to give more significant magnitude than inactive points. Furthermore, it was observed in Section 4.1 that RMS correlations tended to have higher values around active than inactive points. From such reasoning and observations, the following strategy is proposed.

- (i) Correlation values  $p(\mathbf{r}, t)$  for each scanning point  $\mathbf{r}$  in source space and time point  $t$  are computed using (3.1).
- (ii) RMS correlation values  $p_{\text{rms}}(\mathbf{r})$  at each scanning source point  $\mathbf{r}$  are eventually computed using (3.2).
- (iii) Scanning regions are reduced by selecting source points with higher RMS correlation values than given correlation thresholds. Correlation thresholds are estimated empirically for various SNRs via the Monte Carlo simulation, while corresponding criteria are formulated in a least square sense (optimization) at a later time.
- (iv) Beamformer is performed at such reduced source region.

### 3.2. Correlation Computing Strategy

To reduce scanning points, RMS correlation should be computed at every point within the source space. Computing RMS correlations across the entire source space, including a plenty of corresponding time points, may be time intensive. For example, about 500 time samples (2 second-long duration for a 250 Hz acquisition system) are naturally needed to update brain dynamics or decode user intention in existing BCI systems. As shown in (3.1), correlation value computation is necessary for all time points, thereby prolonging overall computation. Downsampling is a possible strategy, but it risks losing important information. Instead, the use of eigen temporal window (called ETWB) is proposed in this work.

By projecting a measurement matrix onto eigen-temporal space while ignoring negligibly small eigenvalues and corresponding eigenvectors, the number of time points is dramatically reduced, thereby reducing correlation computation time. Such a procedure is formulated as follows.

- (i) Spatiotemporal measurement matrix  $\mathbf{M} = [m(t_1); m(t_2); \dots; m(t_K)]$  of size  $S \times K$  can be decomposed by singular value decomposition (SVD) as follows:

$$\mathbf{M} = \begin{pmatrix} \vdots & \dots & \vdots \\ u_1 & \dots & u_K \\ \vdots & \dots & \vdots \end{pmatrix} \begin{pmatrix} \lambda_1 & 0 & 0 \\ 0 & \ddots & 0 \\ 0 & 0 & \lambda_S \end{pmatrix} \begin{pmatrix} \dots & v_1^T & \dots \\ \vdots & \vdots & \vdots \\ \dots & v_S^T & \dots \end{pmatrix} = \mathbf{U}\mathbf{\Sigma}\mathbf{V}^T, \quad (3.5)$$

$$\lambda_1 \geq \lambda_2 \geq \dots \geq \lambda_S.$$

- (ii) Projection matrix  $\mathbf{V}_{\text{ETWB}} = [v_1; v_2; \dots; v_J]$  is constructed using  $J$  significant temporal eigenvectors  $v_j$  (determined by the significance of corresponding eigenvalues) of measurement matrix  $\mathbf{M}$ . Threshold of eigenvalues or the number of eigenvalues  $J (\ll K)$  can be determined empirically.
- (iii) Projected measurement matrix  $\mathbf{M}_{\text{ETWB}}$  of size  $S \times J$  is defined to compute as follows:

$$\mathbf{M}_{\text{ETWB}} := \mathbf{M}\mathbf{V}_{\text{ETWB}}. \quad (3.6)$$

Reduction of the time dimensionality of the measurement matrix is thus ensured, thereby significantly reducing correlation computation time. Computing time of about 3 seconds is reduced to 0.7 seconds, which will be discussed later in this paper. The effectiveness of this strategy is demonstrated in the following section.

## 4. Results

### 4.1. Observation on Correlation Distribution

Correlation distribution between active and inactive points was investigated through numerical experiments in this section. A spherical homogeneous conductor head model with an 8.5 cm radius, centered at origin, was used for forward computing [28], while sensor geometry from a MEGVISION Yokogawa system with a 160-sensor gradiometer array was adopted. Two sources were assumed to be located within a box-shaped region defined by

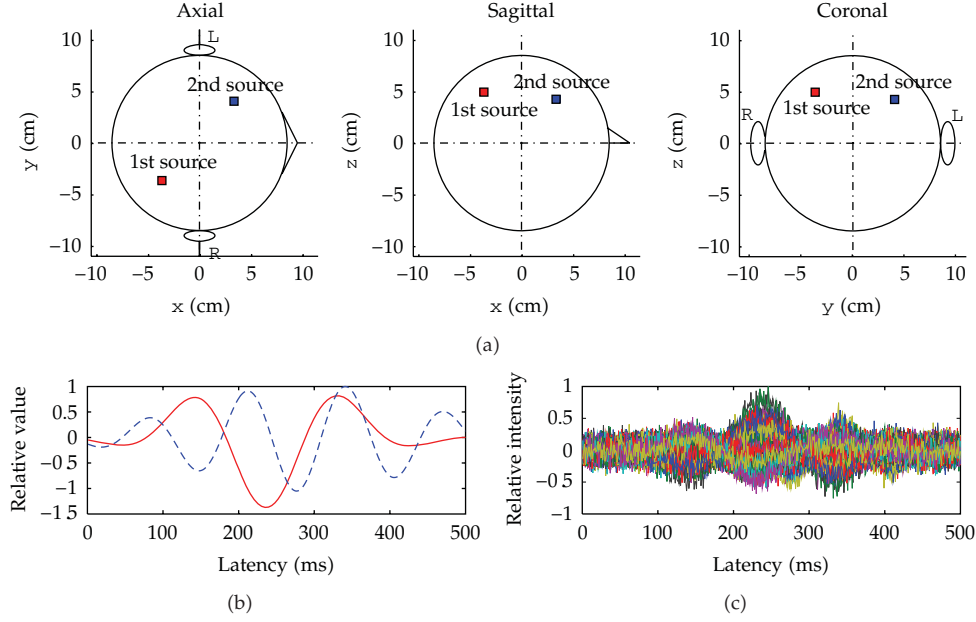


**Figure 1:** Two source locations and head geometry description (a), time courses of dipole sources, first with a solid and second with a dashed line (b), and over-plotted synthetic MEG measurement data (SNR of 1) for 160 sensors (c).

$-8.5 \leq x \leq 8.5$ ,  $-8.5 \leq y \leq 8.5$ , and  $-2.0 \leq z \leq 8.5$  (cm) with a total of 10,000 scanning points comprising equally spaced lattices. Such sources were located at  $(-3.7, -3.6, 5.0)$  and  $(3.3, 4.1, 4.3)$  cm, both directed to  $(1, 0, 0)$ . Synthetic data was generated by adding white Gaussian noise to calculated sensor values computed through a forward model. A synthetic magnetic field with 500 time samples was generated with an SNR of 1. The SNR was defined by  $\|\mathbf{S}\|_F^2 / \|\mathbf{N}\|_F^2$ , where  $\mathbf{S}$  and  $\mathbf{N}$  are signal and noise matrices, respectively, and  $\|\cdot\|_F$  is a Frobenius norm. Time courses for dipoles were provided as damping sinusoids with different wavelengths; these sources were almost uncorrelated. A detailed configuration description is shown in Figure 1. Numerical experiments were conducted on a workstation (2x AMD Opteron CPU 2.3 GHz, 64 bit OS, and 64 GB RAM).

Correlation of full-source space with 10,000 scanning points was computed to illustrate the distribution using (3.2). In Figure 2, three different views of correlation distribution such as  $xy$ -,  $xz$ -, and  $yz$ -plane projections are depicted. This  $xy$ -plane projection map and others were generated by  $p_{\text{rms}}(ix, iy) = \max_{iz} p_{\text{rms}}(ix, iy, iz)$  for each pixel point  $(ix, iy)$ . Figure 2 shows that correlation values produced around active rather than inactive points were relatively higher. Therefore, beamformer scanning within regions with relatively high correlation values seemed to be adequate in reconstructing source information. It is obvious from this observation that choosing a scanning region in the proposed manner can be a good strategy in accelerating beamformer.

#### 4.2. Correlation Threshold

In the previous section, correlation distribution was found to play a key role in getting a priori information on source locations. Intuitively, use of such correlation distribution can

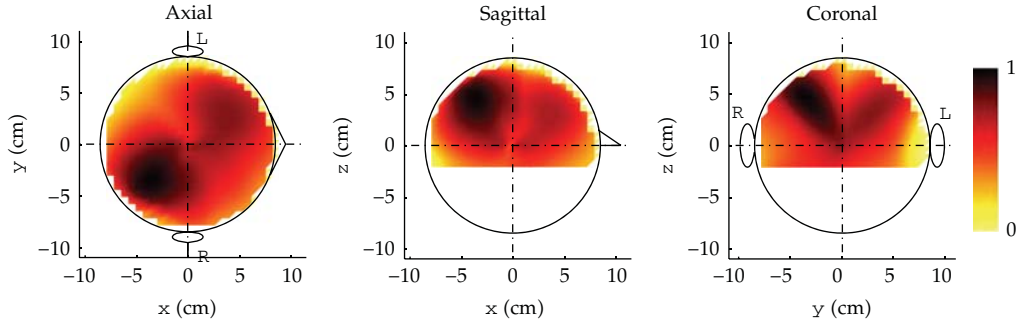


**Figure 2:** Correlation distribution for two dipole source problems on the entire source region of the brain. Darker color represents a higher correlation value.

accelerate beamformer source imaging when beamformer scanning is confined to regions with relatively high correlation values. To apply such a concept, proper correlation thresholds should be predetermined in a reasonable way. In general, correlation distribution may influence various factors such as source locations, source magnitudes, SNR, and sensor geometry. For simplicity, correlation threshold criterion is assumed to depend only on SNR; estimation is thus possible with information easily obtainable or observable. Under such consideration, the following formulation on correlation threshold  $\text{corr}_{\text{thresh}}(\text{SNR})$  is proposed:

$$\begin{aligned} \text{corr}_{\text{thresh}}(\text{SNR}) &:= \bar{m} + \bar{\sigma} \cdot a(\text{SNR}), \\ \bar{m} &:= \text{mean}\{p_{\text{rms}}(\cdot)\}, \quad \bar{\sigma}^2 := \text{var}\{p_{\text{rms}}(\cdot)\}. \end{aligned} \quad (4.1)$$

Here  $\bar{m}$  and  $\bar{\sigma}$  are the first- (mean) and second- (standard deviation) order statistics of RMS correlation values, which are easily estimated. Further,  $a(\text{SNR})$  is a nonlinear function depending on SNR and should be determined with more caution. In order to estimate  $a(\text{SNR})$  effectively, a Monte Carlo simulation study was executed. For a great number of simulated data with various SNRs (with real noise), proper  $a(\text{SNR})$  values were computed and fitted to the given model in a least square sense—assuming that correlation values at active source points are higher than thresholds. From our experience, the following simple logarithmic model was ideally adopted in the present work:

$$a(\text{SNR}) = \max\{\alpha \log(\beta \cdot \text{SNR}), 0\}. \quad (4.2)$$

Correlation threshold criterion  $\text{corr}_{\text{thresh}}(\text{SNR})$  was estimated through the Monte Carlo simulation study. The Monte Carlo simulation was conducted with 200 randomly distributed dipole sources at random orientations across the entire brain. For each dipole (fully correlated source between lead-field vector  $l(\mathbf{r})$  and measurement  $m(t)$ ), five different empirical noise realizations and 15 different SNRs (between 0.01 and 8) were generated by noise power control. Hence, a total of 15,000 single dipole problems were generated in estimating the correlation threshold. Estimated optimal parameters ( $\alpha$  and  $\beta$ ) for such ETWB strategy are as follows:

$$a(\text{SNR}) \approx \max\{0.214 \log(11.309 \cdot \text{SNR}), 0\}. \quad (4.3)$$



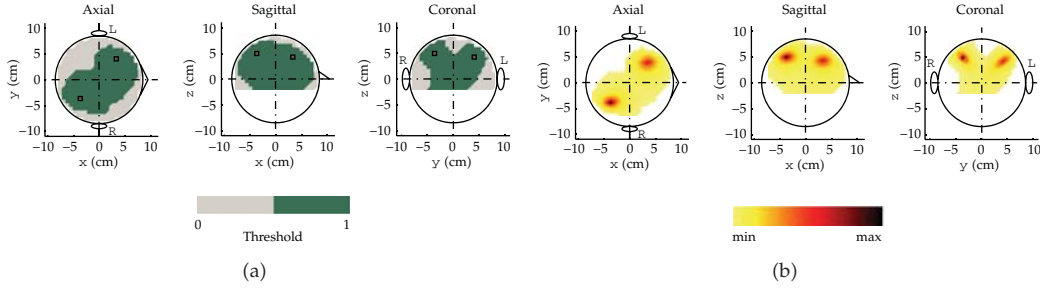


**Figure 3:** SNR = 1: beamformer source reconstruction results using the ETWB strategy. (a) Reduced scanning region (darker shaded region) with a higher correlation value than the predetermined threshold value in (4.1). (b) Beamformer source imaging in the region with reduced scanning.

Empirical MEG noise used in the Monte Carlo simulation study was acquired under the following experimental paradigm.

Empirical MEG data was collected from a healthy male volunteer (24-year-old) who participated after appropriate informed consent was acquired. During spontaneous activity with eyes closed in a magnetically shielded room, an acquisition period of 120 seconds was launched. Data was digitized at 2 kHz with the online lowpass filter set at 500 Hz, postprocessing digital filter applied from 1 to 100 Hz, excluding 50 Hz due to electrical power conditions. Data was collected from a whole-head gradiometer system with 160 channels (MEGVISON Yokogawa system).

Our proposed threshold criterion was generated from a single dipole simulation study; thus other possible source configurations are not sure to be perfectly accounted for. Nevertheless, it was found that our proposal proved quite effective throughout the work.

#### 4.3. Experimental Results: Simulated Data

In this section, investigation into the degree of acceleration and reduction of scanning points resulting from our proposed ETWB strategy was studied. For this purpose, beamformer and proposed scanning reduction strategy was integrated to apply to a simulated two dipole problem, which was generated in Section 4.1. For effective inversion of data covariance and higher output SNR [10], the inversion of data covariance matrix  $(\mathbf{C} + \epsilon \mathbf{I})^{-1}$  in place of  $\mathbf{C}^{-1}$  was used, where  $\epsilon$  and  $\mathbf{I}$  are a regularization factor and an identity matrix, respectively [29]. Regularization factor  $\epsilon$  is estimated by  $\epsilon = \max\{\lambda_1, \lambda_2, \dots, \lambda_S\} \cdot 10^{-5}$ , where  $\lambda_i$ ,  $\{i = 1, 2, \dots, S\}$  is the eigenvalue of the data covariance  $\mathbf{C}$ . We tested beamformer using the ETWB strategy addressed in Section 3.1. Reconstructed source imaging by this method is illustrated in Figure 3. According to (4.1), the correlation threshold was properly chosen in reducing source scanning regions. In the ETWB strategy, significant eigenvectors were chosen explaining the amount of information, up to 70%, from measurement matrix  $\mathbf{M}$ . Thus, approximately one fifth of 500 total time samples were selected to create an eigen-temporal projection matrix  $\mathbf{V}_{\text{ETWB}}$ .

Figure 3 shows which particular region has higher correlation values than threshold, and beamformer in the reduced region resulted in images being identical to the beamformer source imaging with the entire source space scanning. In this experiment, the number of

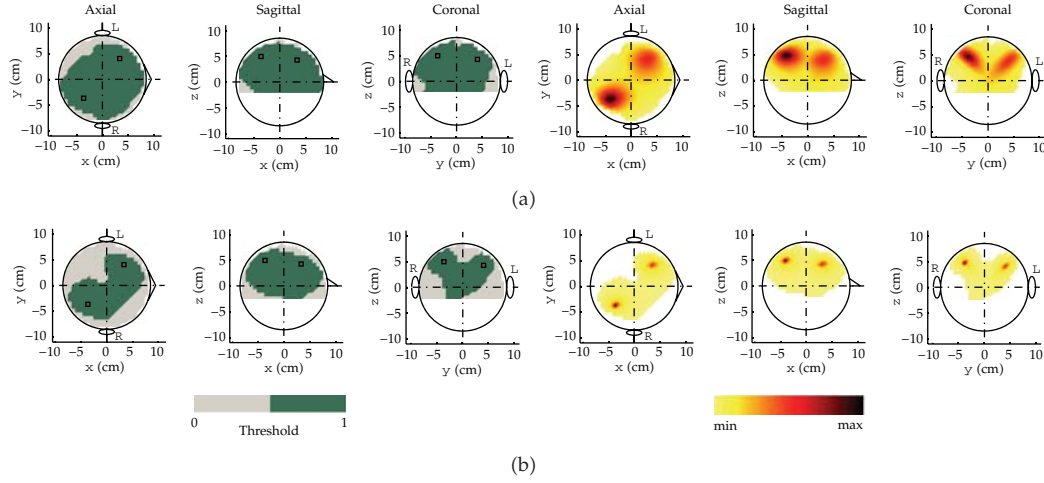


**Figure 4:** Reduced scanning regions (left) by our proposed beamformer and reconstructed images (right) over simulated data with different SNRs. (a) SNR: 0.1. (b) SNR: 4.

scanning points was reduced to about 3,000, that is, about one third of the total original scanning points of 10,000. Total elapsed time of beamformer was about 0.53 seconds, even including correlation computation, while conventional beamformer time (full-brain scan) was about 1.03 seconds.

#### Source Imaging Effect on SNR

Conventional full-scan beamformer was compared with reduced scanning beamformer using the proposed strategy to determine how much scanning reduction was attained over different SNRs (0.1 or 4). The reduced scanning regions by ETWB strategy are illustrated in Figure 4. The same ETWB strategy as in previous experiments was used. For simulated data with SNR 0.1, Figure 4(a) shows the results from the reduced scanning region using the ETWB strategy and the reconstructed image from beamformer. Computation time for the conventional beamformer was about 1.03 seconds over the entire region of 10,000 points. Conversely, our proposed strategy took about 0.6 seconds, and scanning points were reduced up to about 4,400 points.

With regards to high SNR 4, the same experiment was conducted. Figure 4(b) shows the results from the reduced scanning region using the ETWB strategy for processing simulated data. In this case, computation time for beamformer using our proposed strategy was about 0.37 seconds, and scanning points were reduced to about 2,300 points. Such results show that our proposed strategy can accelerate beamformer while maintaining spatial resolution of source images with respect to SNRs. As previously mentioned in the initial simulation (SNR = 1), the number of significant eigenvectors needed for the ETWB strategy was about one fifth of the total time points.

#### Source Imaging Effect on Source Correlation

In this section, the performance of our proposed beamformer was investigated over different source correlations between two dipole sources. It is known that beamformer performance



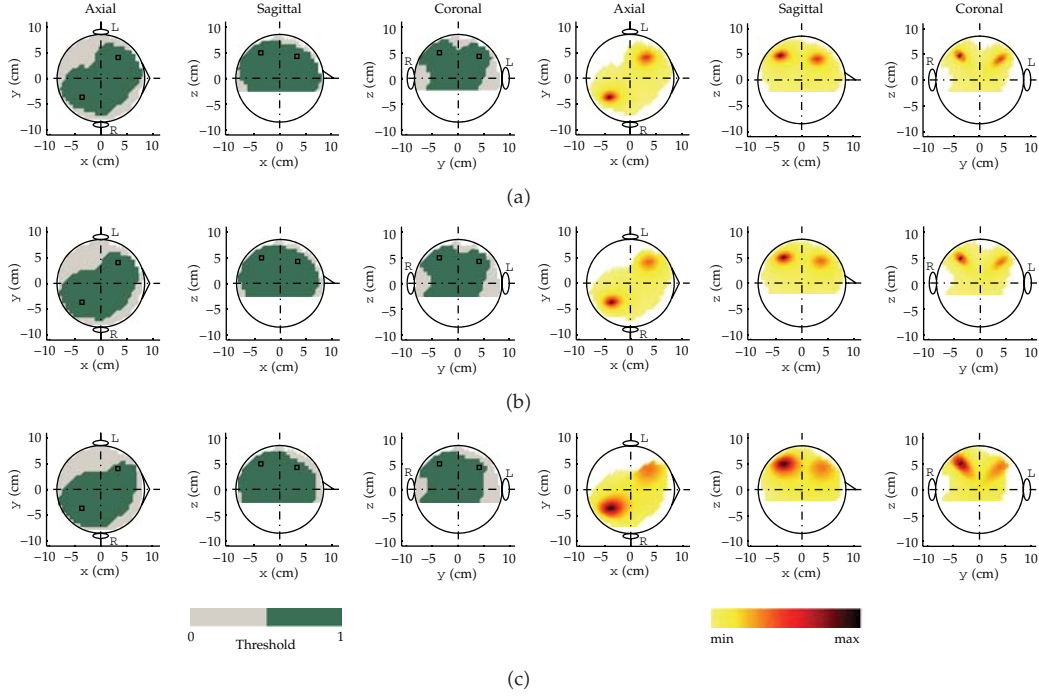


**Figure 5:** Reduced scanning regions (left) by our proposed strategy and reconstructed images (right). All other configurations (source locations, time courses, and SNR (=1)) are the same as in Figure 1. (a) Correlation: 0.1. (b) Correlation: 0.6. (c) Correlation: 0.9.

degrades for heavily correlated sources. To investigate how much our proposed method relatively effects source correlation, simulated data was generated under the same configurations as in Section 4.1, except for different source correlations such as 0.1, 0.6, and 0.9. To generate simulated data with different source correlations, the time course of the second dipole source was made using the formula:  $\hat{w}_2(t) = (1 - \xi)w_1(t) + \xi w_2(t)$ , where  $w_1(t)$  and  $w_2(t)$  represent the first and second time courses of the sources, respectively. The parameter  $\xi$  controls the degree of the correlation between  $w_1(t)$  and  $w_2(t)$ . Figure 5 shows the reduced scanning regions by our proposed strategy and reconstructed source imaging of beamformer. As correlation increases, sources get more broadly reconstructed; thereby spatial resolution is poorer. However, reduced scanning regions seem to be almost same; therefore, there is no significant effect on scanning reduction of correlation between sources.

#### Source Imaging Effect on Source Depth and Extended Source Model

In general, as brain sources are activated far away from the sensor surface of the MEG/EEG system, it is dramatically less sensitive to those sources and localization accuracy gets worse. In this section, the performance of beamformer using our proposed strategy is investigated as sources gradually move away from the sensor surface. For this investigation, the same source configuration as in Figure 1 was used except for the depth of one source. Three source depths (z-coordinate), 5.0, 2.9, and 0.8 cm, were considered. Figure 6 shows the reduced scanning regions by our proposed strategy over varying source depths. Obviously, as the source is located deeper, the source signal gets weaker; thus it is harder to reconstruct deep sources

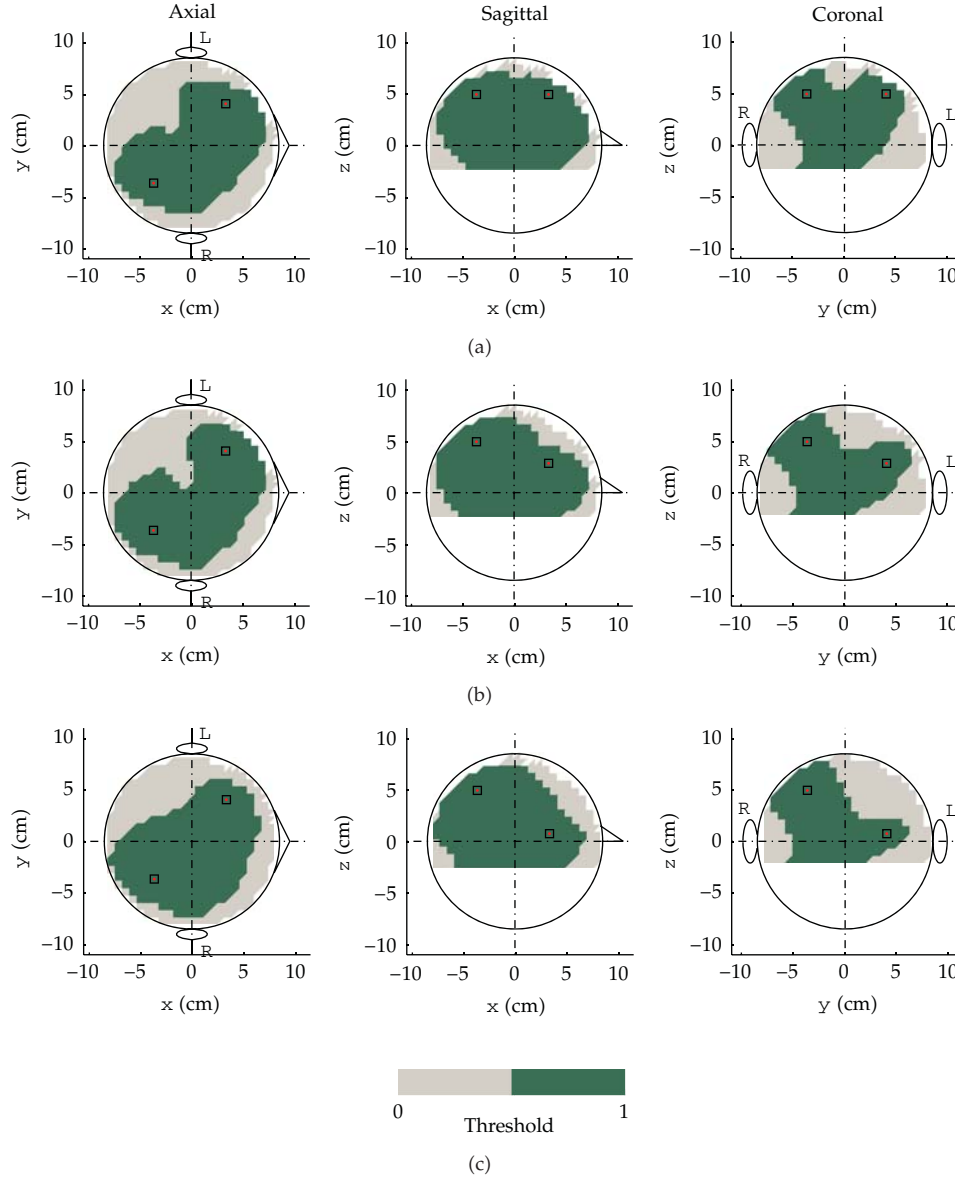


**Figure 6:** Reduced scanning regions by our proposed beamformer over varying source depths. Source configuration is the same as in Figure 1, except for the depth ( $z$ -coordinate) of one source. (a) Depth:  $z = 5.0$  cm. (b) Depth:  $z = 2.9$  cm. (c) Depth:  $z = 0.8$  cm.

by our proposed beamformer. The reduced scanning region got slightly narrower since SNR gets smaller, but it is not significantly noticeable.

Further, the performance of our proposed beamformer was tested on extended source models. Extended sources were generated for three different source span diameters: 0, 2.0, and 5.0 cm. Here the source with a 0 cm span diameter means a dipole source. Extended sources were generated on the plane ( $z = 5.0$  cm) parallel to the  $xy$ -plane. Each center of the extended sources is located on  $(-3.7, -3.6, 5.0)$  cm. All dipole sources within extended

source regions were oriented to the same direction. Expectedly, there was no big variation on different span diameters, but extended sources with span diameter 5.0 cm seemed slightly broad spread. However, reduction of scanning regions was almost unchanged (not shown).

### *Comparison on Computing Time*

So far, many kinds of simulated data over different SNRs, different source depths, different source correlations as well as different extended source spans have been tested to compare reduced scanning beamformer using our proposed strategy to conventional full-scan beamformer. Overall, our proposed beamformer shows its relative acceleration in time and yields comparable in accuracy to the conventional beamformer. Figure 7 depicts comparative computational time over numerous simulated problems, which were generated as follows.

- (i) For single dipole problem, 1,000 dipoles were randomly distributed within the spherical head model. For each dipole, 7 single dipole problems with different SNRs (between 0.01 and 8) were generated by adding white Gaussian noise, thus yielding 7,000 single dipole problems. Particularly, for different diameter of source simulation, 6 different diameters of source (between 0 and 50 mm) at each source were considered. Thus 6,000 single source problems were generated with keeping SNR of 1 in this case.
- (ii) For two-dipole problem, 1,000 pairs of two dipoles were randomly chosen among 1000 dipoles generated in single dipole problems. For each pair, two-dipole problems were generated with 7 different SNRs (between 0.01 and 8), 7 different source correlation coefficients (between 0 and 1), and 6 different interdistance between two sources (between 0 and 100 mm). Hence, total 294,000 two-dipole problems were generated to test.

For each problem, the number of scanning point and computational time were estimated. Evidently, computational time is linearly proportional to the reduced scanning points. In our proposed strategy, we found that averaged correlation computing time including SVD computation was about 0.15 seconds, which was added to computational time. The averaged computational time of the conventional beamformer was about 1.035 seconds. Each point in Figure 7 represents an averaged computing time with standard deviation over all corresponding simulated problems.

Figure 7(a) shows that our strategy speeds up as SNR gets higher. It means that reduction rate of scanning points is higher as SNR goes higher. Further, computational time has no noticeable difference as extent of source and source correlation vary (Figures 7(b) and 7(c)). However, computational time over inter-source distance seems slight difference (Figure 7(d)). As two sources get far, computational time increases slightly, but not substantial.

It is remarkable that correlation computation time did not change with respect to SNRs; however, we found that computation time of SVD varied slightly over SNRs. We guess that such small variation of SVD computing time may stem from different matrix characteristics. Total original scanning points amounted to 10,000 and the temporal size of the measurement matrix was 500. Figure 7(a) shows that beamformer utilizing our proposed ETWB strategy computed significantly quicker than the conventional beamformer, yielding about 30–60% improvement. These experiments demonstrate how the beamformer with our strategy was effective in accelerating beamformer source imaging.

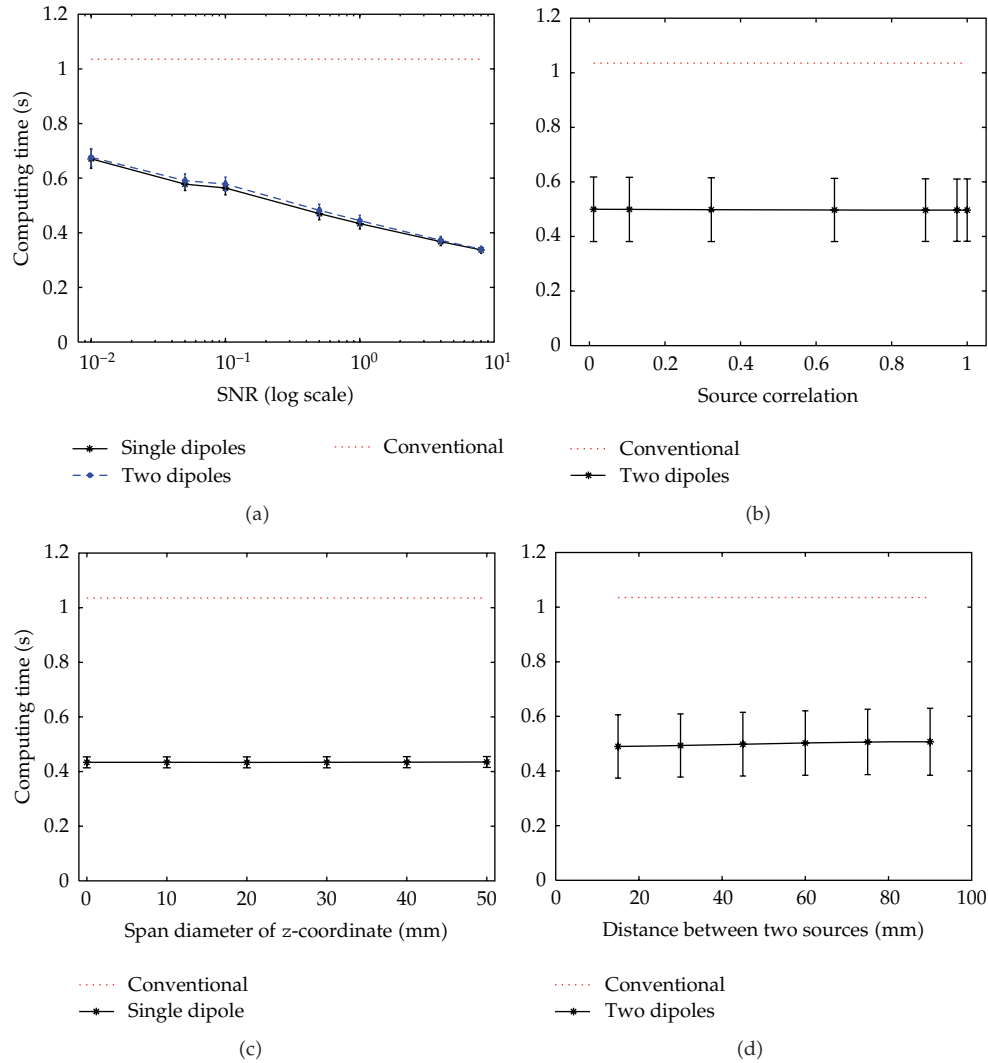


**Figure 7:** Comparative computational time of our proposed strategy and conventional beamformer over different problems varying SNR, source correlation, diameter of source, and distance between two sources. Each problem requires a total of 10,000 scanning points and has temporal window of 500 time samples. Each point is the averaged computational time with standard deviation.

#### 4.4. Experimental Results: Empirical Data

In the present section, reduced scanning beamformer with our proposed strategy was applied to empirical MEG data. Four kinds of empirical MEG datasets were acquired on a whole-head gradiometer MEGVISION Yokogawa system with 160 channels—median nerve stimulations (right hand/left hand) and auditory stimulations (left ear/right ear). Experimental paradigm is detailed as follows.

A healthy male volunteer (24-year-old) participated in the MEG measurement after appropriate informed consent. First, the somatosensory electrostimulation median nerve of his right/left hand was stimulated and all measurements were

done in a magnetically shielded room. During measurement, the subject was instructed to keep his eyes closed.

A 2.9 (right)/3.5 (left) mA current and a 2 Hz sampling were applied with 0.3-millisecond current pulses. Interstimulus-interval (ISI) was randomized with 0.5 s duration. Second, the auditory stimulation of his right/left ear was stimulated with eyes closed. A 80 dB sound pressure and a 2 Hz sampling were applied with 40 ms plateau with 10 ms rise and falls. Also, ISI was randomized with a 2 s duration (random 50%, 1–3 s). Data were digitized at 2 kHz, lowpass filtered at 500 Hz as well as postprocessed via a digital filter at 1–100 Hz (median nerve stimulation)/1–50 Hz (auditory stimulation), excluding 50 Hz due to electrical power conditions. In the case of median nerve stimulation, a total 399 (right-hand)/418 (left-hand) single trials were acquired. Total 73 (right-ear)/70 (left-ear) single trials were obtained in the case of auditory simulations.

Each collected single trial data (unaveraged) with 0–250 millisecond (time-locked, 500 time samples) time window after stimulation onset were analyzed. Such analysis can better facilitate real-time brain activity monitoring for neurofeedback and brain computer interface (BCI) [23], among others. For single trial analysis, the reduced scanning beamformer with our proposed strategy and the conventional full-scan beamformer were used. We used entire the source region consisting of a total of 8,640 scanning points and a temporal window with 500 samples corresponding to a duration of 250 milliseconds. The correlation threshold was accordingly determined through formula defined in (4.1). Eigen-temporal projection matrix  $V_{ETWB}$  was estimated as having explained 70% of the measurement matrix information. To compare source reconstruction performance, all of each single trial was reconstructed and their source information (number of scanning points  $\times$  number of time samples  $\times$  number of trials) was averaged over the trials. Also, total computing time elapsed for single trial analysis was measured over different datasets and two kinds of beamformers. Figure 8 shows the averaged-over-trial-reconstructed source power maps of both conventional full-scan beamformer and reduced scanning beamformer with our proposed strategy for median nerve stimulation data (right and left). To verify the capability of our proposed reduced scanning beamformer, we attempted single-trial analysis for empirical data. Both beamformers were applied to compare and averaged source power maps over trial were generated by considering zero power out of the reduced scanning region. Since each trial has different reduced scanning region based on correlation threshold, averaged-over-trial source power map was seen in the whole region.

Beamformer source imaging for averaged median nerve stimulation data yielded focused source activity in the upper contralateral posterior central sulcus (not shown here), which is relevant to existing literature (see [30] and therein). As illustrated in Figure 8, strong source activity appeared in the upper contralateral area and most mildly active sources seemed scattered around strong source activity, which is relevant to beamformer results (not shown) for averaged median nerve stimulation data. Evidently, both beamformers showed almost identical results, thereby reduced scanning beamformer being comparable in accuracy to the conventional one. However, significant improvement in computing time was achieved in the reduced scanning beamformer with our proposed strategy, and comparative total elapsed computing time for each experiment was tabulated in Table 1.

These results tell that overall improvement in computing time of reduced scanning beamformer with our proposed strategy is over 40%. In conclusion, our proposed reduced

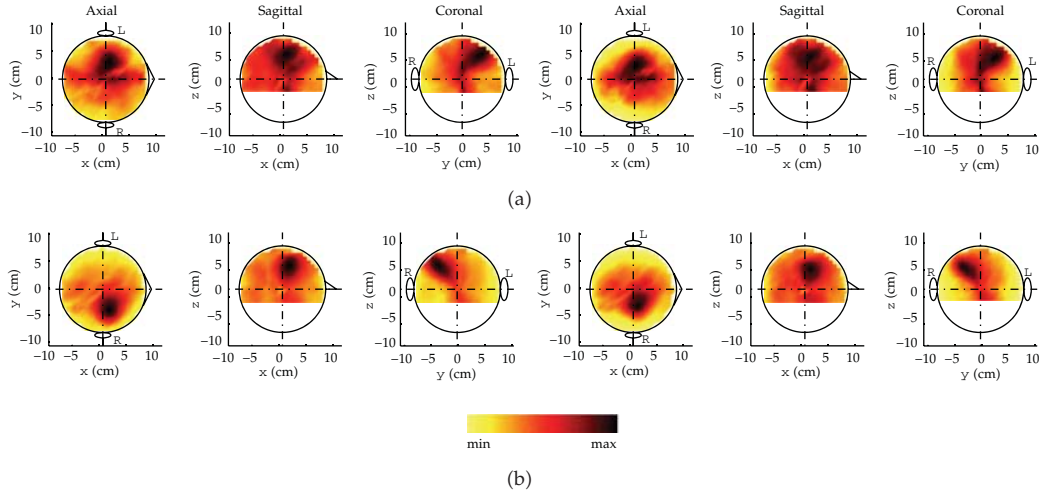


**Figure 8:** Averaged-over-trial-reconstructed source power maps of both conventional beamformer (left) and reduced scanning beamformer with our proposed strategy (right) for empirical median nerve stimulation data. (a) Right-hand movement. (b) Left-hand movement.

**Table 1:** Comparative total computing time (in seconds) of single trial analysis for different empirical data between conventional full-scan beamformer and reduced scanning beamformer with our proposed strategy. Source region with a total of 8,640 scanning points and a temporal window of 500 time samples were used. Experiments were conducted on a PC (Intel Core 2 Duo CPU 2.4 GHz, 32 bit OS, and 4 GB RAM).

Experiment (No. of trials)	Elapsed time of beamformer imaging (sec)		Improvement (%)
	Full-scan	Reduced scanning	
Median-right (399)	723.3	418.8	42.1
Median-left (418)	760.6	430.2	43.4
Auditory-right (73)	132.1	74.7	43.5
Auditory-left (70)	126.9	72.1	43.2

scanning beamformer is feasible and very applicable in accelerating the conventional beamformer.

## 5. Discussion

### 5.1. Other Possible Accelerating Strategies

In this work, one beamformer using ETWB strategy was proposed to reduce the beamformer scanning regions by computing correlation distribution, thereby accelerating beamformer. Similar to the ETWB strategy, another strategy is possibly proposed by doing eigen-temporal projection and in addition doing eigen-spatial projection. We call this strategy eigen-spatiotemporal window-based method (we call it ESTWB). The discarding of relatively insignificant sensor information via the ESTWB strategy seems more efficient in relation to computation time while the ETWB strategy will inherently provide a more accurate correlation distribution as well as yielding more reliable beamformer source imaging. In addition to



ETWB and ESTWB strategies, temporal downsampling is another idea; however, it possibly loses useful information.

Computing correlation in (3.1) and (3.2) amounts to a spatial matched filter when normalization term of measurement vector  $m(t)$  in (3.1) is dropped. So, it is not surprising that correlation behaves like another spatial filter, thereby yielding rough less accurate but fast spatial imaging. This information is used for prescreening to determine final scanning region of more elegant spatial filter, that is, MV beamformer. Such argument gives more general perspective in developing speeding-up strategies of scanning methods. Any hybrid between a fast scanning method and an accurate scanning method can be possible when they can yield synergy effect due to reasonable combination strategies.

Furthermore, there exist other strategies to speed up scanning methods. One can consider downsampling in spatial scanning to reduce computation effort. It is commonly applicable in scanning methods like beamformer. When our strategy would be applied together, scanning methods should be boosted easily. Another easy strategy is to increase computational resources such as parallel computing to use many personal computers at the same time. This provides powerful computing ability; thus tens to hundreds of times improvement would be possible. Certainly, such a strategy demands a relatively high cost; thus, it may be not easily affordable to most investigators. It is noted that our proposed strategy of simple consideration of correlation distribution can be achieved on a single personal computer.

## ***5.2. Applicability of Our Proposed Strategy***

As discussed in Section 4.1, simple description and observation of correlation distribution around active and inactive sources motivated us to conduct this kind of investigation. For a few strong brain sources being well separated, our strategy is favorably relevant. However, for many sources, the correlation threshold may become lower due to more mixed source intercorrelations; thus, scanning points will be slightly reduced and our proposed correlation threshold criterion may not be effective in such cases. Nevertheless, real-time brain activity monitoring systems (or BCI systems) are usually designed to find relatively rapidly changing source information (or discriminative information among different conditions); thus, a few strong sources may be accountable and helpful for providing such information.

In real-time monitoring or BCI systems, seamless monitoring or control decision is of great importance. In reality, most systems have some delay coming from computation implicitly required to do any defined action; however, such delay is reasonably small or one may design the system to have delay constant or within an affordable bound; thus it looks real-time system to user. Particularly, source imaging analysis introduced in these systems may not avoid significant delay incurring from intense computation. However, well-designed system to hide such significant delay may be possible. For example, assuming that every 1-second-long window data is collected to analyze and source imaging requires 1 second, such system may be designed that data is analyzed to give final result to the system during system being collected next 1 second-long data; then system continues to do the same procedure. This system can achieve seamless procedure (it looks real-time system from user) with constant delay of 1 second. From this perspective on real-time monitoring or BCI systems, the faster source imaging can achieve the higher monitoring scan or decision rate. Therefore, our proposed strategy yielding about 40% speed-up of source imaging is well applicable in this reasoning.



On the other hand, in BCI systems, one could define a region-of-interest (ROI) manually [23, 24] or by elegant procedures [31, 32]. Source imaging on such ROI could increase the spatial specificity or enhance SNR in source space [31]. Furthermore, it is possible to achieve far more accelerated source imaging than whole brain source imaging. To achieve real-time source activity monitoring or source information-based BCI [20, 22–24], naturally higher spatial resolved imaging within ROI is beneficial in such development. However, it requires more computation time. Our proposed strategy can be still applicable on ROI in the same manner. Furthermore, single-trial analysis using fast beamformer has been beneficial in developing many applications [18, 19]. Accordingly, our proposed method was applied to single-trial data, such as empirical median nerve stimulation and auditory stimulation, as discussed in Section 4.4. It revealed several dynamic activation regions, usually not visible during averaged data analysis (not shown here). Such single-trial analysis and online BCI application will be investigated in more detail and reported in a subsequent paper.

### 5.3. Other Issues

Through the Monte Carlo simulation, our correlation threshold criterion, depending on SNR, was formulated in a least square sense. This criterion was dependent on sensor configuration (geometry); so it should be reestimated under other sensor configurations. Factors other than SNR may have some effects on correlation thresholds. Accordingly, more thorough research is currently under investigation.

Even though the conventional vector-type MV-beamformer among the beamformer variants was adopted in this work, scalar-type or other nonadaptive beamformers are similarly applicable. Furthermore, this strategy is very straightforward for EEG or simultaneous MEG/EEG data application, and subsequent work on simultaneous MEG/EEG beamformers [33] is currently under investigation.

## Acknowledgments

This work was supported by a KRF grant (KRF-331-2008-1-D00768), NRF grant (NRF-2010-32A-B00283), the PLSI supercomputing resources of KISTI, the BioImaging Research Center at GIST, and the National IT Industry Promotion Agency (NIPA-2011-C1090-1131-0006). The authors appreciate Dr. Haruta at Yokogawa Electric Corp for his assistance with MEG data acquisition.

## References

- [1] M. Hämäläinen, R. Hari, R. J. Ilmoniemi, J. Knuutila, and O. V. Lounasmaa, "Magnetoencephalography—theory, instrumentation, and applications to noninvasive studies of the working human brain," *Reviews of Modern Physics*, vol. 65, no. 2, pp. 413–497, 1993.
- [2] S. Baillet, J. C. Mosher, and R. M. Leahy, "Electromagnetic brain mapping," *IEEE Signal Processing Magazine*, vol. 18, no. 6, pp. 14–30, 2001.
- [3] B. D. Van Veen and K. M. Buckley, "Beamforming: a versatile approach to spatial filtering," *IEEE ASSP Magazine*, vol. 5, no. 2, pp. 4–24, 1988.
- [4] K. Sekihara, S. S. Nagarajan, D. Poeppel, and A. Marantz, "Performance of an MEG adaptive-beamformer technique in the presence of correlated neural activities: effects on signal intensity and time-course estimates," *IEEE Transactions on Biomedical Engineering*, vol. 49, no. 12, pp. 1534–1546, 2002.

- [5] B. D. Van Veen, W. Van Drongelen, M. Yuchtman, and A. Suzuki, "Localization of brain electrical activity via linearly constrained minimum variance spatial filtering," *IEEE Transactions on Biomedical Engineering*, vol. 44, no. 9, pp. 867–880, 1997.
- [6] M. J. Brookes, C. M. Stevenson, G. R. Barnes et al., "Beamformer reconstruction of correlated sources using a modified source model," *NeuroImage*, vol. 34, no. 4, pp. 1454–1465, 2007.
- [7] M. X. Huang, J. J. Shih, R. R. Lee et al., "Commonalities and differences among vectorized beamformers in electromagnetic source imaging," *Brain Topography*, vol. 16, no. 3, pp. 139–158, 2004.
- [8] K. Nazarpour, Y. Wongsawat, S. Sanei, S. Orintara, and J. A. Chambers, "A robust minimum variance beamforming approach for the removal of the eye-blink artifacts from EEGs," in *Proceedings of the 29th Annual International Conference of IEEE, Engineering in Medicine and Biology Society (EMBS '07)*, pp. 6211–6214, Lyon, France, August 2007.
- [9] K. Nazarpour, Y. Wongsawat, S. Sanei, J. A. Chambers, and S. Orintara, "Removal of the eye-blink artifacts from EEGs via STF-TS modeling and robust minimum variance beamforming," *IEEE Transactions on Biomedical Engineering*, vol. 55, no. 9, pp. 2221–2231, 2008.
- [10] K. Sekihara and S. S. Nagarajan, *Adaptive Spatial Filters for Electromagnetic Brain Imaging*, Springer, Berlin, Germany, 2008.
- [11] K. Sekihara, M. Sahani, and S. S. Nagarajan, "Localization bias and spatial resolution of adaptive and non-adaptive spatial filters for MEG source reconstruction," *NeuroImage*, vol. 25, no. 4, pp. 1056–1067, 2005.
- [12] J. Gross and A. A. Ioannides, "Linear transformations of data space in MEG," *Physics in Medicine and Biology*, vol. 44, no. 8, pp. 2081–2097, 1999.
- [13] A. Hillebrand, K. D. Singh, I. E. Holliday, P. L. Furlong, and G. R. Barnes, "A new approach to neuro-imaging with magnetoencephalography," *Human Brain Mapping*, vol. 25, no. 2, pp. 199–211, 2005.
- [14] S. Robinson and J. Vrba, "Functional neuroimaging by synthetic aperture magnetometry (SAM)," in *Recent Advances in Biomagnetism*, T. Yoshimoto, M. Kotani, S. Kuriki, H. Karibe, and N. Nakasato, Eds., pp. 302–305, Tohoku University Press, Sendai, Japan, 1999.
- [15] K. Sekihara, S. S. Nagarajan, D. Poeppel, A. Marantz, and Y. Miyashita, "Application of an MEG eigenspace beamformer to reconstructing spatio-temporal activities of neural sources," *Human Brain Mapping*, vol. 15, no. 4, pp. 199–215, 2002.
- [16] M. E. Spencer, R. Leahy, J. Mosher, and P. Lewis, "Adaptive filters for monitoring localized brain activity from surface potential time series," in *Proceedings of the IEEE 26th Asilomar Conference on Signals, Systems and Computers*, vol. 1, pp. 156–161, Pacific Grove, Calif, USA, October 1992.
- [17] O. Steinsträter, S. Sillekens, M. Junghoefer, M. Burger, and C. H. Wolters, "Sensitivity of beamformer source analysis to deficiencies in forward modeling," *Human Brain Mapping*, vol. 31, no. 12, pp. 1907–1927, 2010.
- [18] M. Besserve, K. Jerbi, F. Laurent, S. Baillet, J. Martinerie, and L. Garnero, "Classification methods for ongoing EEG and MEG signals," *Biological Research*, vol. 40, no. 4, pp. 415–437, 2008.
- [19] P. Poolman, R. M. Frank, P. Luu, S. M. Pederson, and D. M. Tucker, "A single-trial analytic framework for EEG analysis and its application to target detection and classification," *NeuroImage*, vol. 42, no. 2, pp. 787–798, 2008.
- [20] M. Ahn, J. H. Hong, and S. C. Jun, "Source space based brain computer interface," in *Proceedings of the 17th International Conference on Biomagnetism Advances in Biomagnetism (Biomag '10)*, vol. 28, part 12, pp. 366–369, April 2010.
- [21] B. Blankertz, R. Tomioka, S. Lemm, M. Kawanabe, and K. R. Müller, "Optimizing spatial filters for robust EEG single-trial analysis," *IEEE Signal Processing Magazine*, vol. 25, no. 1, pp. 41–56, 2008.
- [22] M. Congedo, F. Lotte, and A. Lécuyer, "Classification of movement intention by spatially filtered electromagnetic inverse solutions," *Physics in Medicine and Biology*, vol. 51, no. 8, pp. 1971–1989, 2006.
- [23] B. Kamousi, Z. Liu, and B. He, "Classification of motor imagery tasks for brain-computer interface applications by means of two equivalent dipoles analysis," *IEEE Transactions on Neural Systems and Rehabilitation Engineering*, vol. 13, no. 2, pp. 166–171, 2005.
- [24] H. Yuan, A. Doud, A. Gururajan, and B. He, "Cortical imaging of event-related (de)synchronization during online control of brain-computer interface using minimum-norm estimates in frequency domain," *IEEE Transactions on Neural Systems and Rehabilitation Engineering*, vol. 16, no. 5, pp. 425–431, 2008.
- [25] J. H. Hong and S. C. Jun, "Speeding-up MEG beamforming source imaging by correlation between measurement and lead-field vector," in *Proceedings of the 17th International Conference on Biomagnetism Advances in Biomagnetism (BIOMAG '10)*, vol. 28, part 5, pp. 148–151, April 2010.

- [26] K. Sekihara, S. S. Nagarajan, D. Poeppel, A. Marantz, and Y. Miyashita, "Reconstructing spatio-temporal activities of neural sources using an MEG vector beamformer technique," *IEEE Transactions on Biomedical Engineering*, vol. 48, no. 7, pp. 760–771, 2001.
- [27] K. Sekihara, S. S. Nagarajan, D. Poeppel, and A. Marantz, "Performance of an MEG adaptive-beamformer source reconstruction technique in the presence of additive low-rank interference," *IEEE Transactions on Biomedical Engineering*, vol. 51, no. 1, pp. 90–99, 2004.
- [28] J. Sarvas, "Basic mathematical and electromagnetic concepts of the biomagnetic inverse problem," *Physics in Medicine and Biology*, vol. 32, no. 1, pp. 11–22, 1987.
- [29] P. C. Hansen, *Rank-Deficient and Discrete Ill-Posed Problems: Numerical Aspects of Linear Inversio*, SIAM Monographs on Mathematical Modeling and Computation, Society for Industrial and Applied Mathematics, Philadelphia, Pa, USA, 1998.
- [30] S. C. Jun, J. S. George, J. Paré-Blagoev et al., "Spatiotemporal Bayesian inference dipole analysis for MEG neuroimaging data," *NeuroImage*, vol. 28, no. 1, pp. 84–98, 2005.
- [31] M. Congedo, "Subspace projection filters for real-time brain electromagnetic imaging," *IEEE Transactions on Biomedical Engineering*, vol. 53, no. 8, Article ID 1658157, pp. 1624–1634, 2006.
- [32] T. E. Ozkurt, M. Sun, W. Jia, and R. J. Sclabassi, "Spatial filtering of MEG signals for user-specified spherical regions," *IEEE Transactions on Bio-Medical Engineering*, vol. 56, no. 10, pp. 2429–2438, 2009.
- [33] S. Ko and S. C. Jun, "Beamformer for simultaneous magnetoencephalography and electroencephalography analysis," *Journal of Applied Physics*, vol. 107, p. 09B315, 2010.